Au(hkl): Surface X-ray Diffraction Studies at the Electrochemical Interface

By

Joshua James Fogg

Oliver Lodge Laboratory, Department of Physics

University of Liverpool

Thesis submitted in accordance with the requirements of the University of Liverpool for the degree of Doctor in Philosophy

September 2018

Abstract

In-situ surface x-ray diffraction (SXRD) measurements have been performed to develop an increased understanding of electrocatalytic reactions and electrodeposition processes occurring on gold single crystal surfaces. The surfaces of gold exhibit a rich physical behaviour that is interesting not only from a structural perspective but also for applications in areas such as heterogeneous catalysis and electrocatalysis. The surface reconstructions of Au(111) and Au(100) have been found to undergo a potential dependent in plane surface compression in alkaline solution that is remarkably similar despite the underlying geometry. The compressibility is linked to the charge on the surface Au atoms with a simple free electron model. The surface compression and the reversible lifting of the reconstructions are determined by the interplay between surface charge and the adsorption of hydroxide species. Carbon monoxide adsorption is shown to supress both the potential-induced changes in surface compression and the lifting of the reconstruction leading to the promotion of electrocatalytic reactivity. Measurements of the Au(111)/Pb UPD system in acidic solution reveal a substitutional Au/Pb surface alloy of the ratio ~ 4:1 that forms at intermediate coverages of Pb during the stripping of Pb from the Au(111) electrode surface. Investigations into the adsorption of Acetonitrile (AcN) on the Au(111) electrode surface in sulphuric acid solution find that AcN has an enhancing effect on the adsorption of sulphate molecules. In the potential regions where sulphate is not adsorbed onto the Au(111) AcN is shown to weakly interact with the Au(111) electrode surface. The interaction between Cu and AcN ions in sulphuric acid solution and its effect on the Au(111)/Cu UPD process were investigated. AcN was shown to form a $[Cu(C_2H_3N)_4]^+$ complex with copper that enhances the the deposition of copper on the Au(111) surface and suppress the characteristic honeycomb $(\sqrt{3}x\sqrt{3})R30°$ structure in sulphuric acid.

Acknowledgements

First, I would like to thank my supervisor Prof. C. A. Lucas for introducing me to the field of surface x-ray diffraction and its combination with electrochemistry, his patience and support (and pints!) throughout my PhD.

A big thank you to my secondary supervisor Dr. Yvonne Gründer, your insights have been invaluable over the last four years. Another big thank you to Paul Thompson for all his help with experiments, advice and welcoming me to Grenoble with a heavy drinking session that I still laugh about to this day. Kevin McCormick and Keith Williams deserve a mention for all their hard work building the electrochemical cells and crystal collets.

Many thanks to Gary Harlow and Elizabeth Cocklin for making me feel welcome in the group and showing me the ropes. Liz, you still owe me that karaoke night! A thank you to the other members of the group for all their support sessions, scientific discussions and sanity checks, in no particular order: Nikolas Antonatos, Lisa Rhodes-Martin, Lena Reichenbach and Jack William Beane. Graeme O'Dowd deserves a mention for the nights out and putting up with me as a housemate for so long.

Pete, Beth and Liam, I hope you know how invaluable you are. Thank you for the drinking sessions and lending an ear.

Stephanie, although you still think a synchrotron is some kind of transformer, thank you for your patience and sticking with me through the years.

I would like to thank my mum, Lindsey Heywood, for putting up with me during my write up over the last 6 months. Finally, my nana and grandad, Joan and Terry Kershaw. Thank you, without your unwavering support this thesis would not exist.

Contents

1 **Introduction** 1

2 **Theoretical Principles** 4

2.1 Introduction 4

2.2 The Electrode/Electrolyte Interface 4

2.2.1 *Electrode Reactions* 4

2.2.2 *Underpotential Deposition* 6

2.2.3 *The Electrochemical Double Layer* 6

2.2.4 *Cyclic Voltammetry* 7

2.3 X-Ray Diffraction 10

2.3.1 *Crystallographic Definitions* 10

2.3.2 *Kinematical X-ray Diffraction* 11

2.3.3 *Surface X-ray Diffraction* 18

2.3.4 *Modelling Surface Structure* 19

2.3.5 *Reciprocal Lattice for the Low-Index fcc Metal Surfaces* 21

2.3.6 *Additional contributions to the scattered intensity* 25

2.4 X-ray Voltammetry 29

3 **Experimental Techniques** 30

3.1 Sample Preparation 30

3.2 Electrochemistry 31

3.3 Synchrotrons and Beamlines 36

3.4 Diffractometers 38

3.5 Data Acquisition and Extraction 41

3.5.1 *Rocking Scans* 41

3.5.2 *Stationary Scans* 42

3.5.3 *Reciprocal Space Scan* 43

3.6 Data Analysis 43

3.6.1 *Correction Factors* 43

3.6.2 *Non-Linear Least Squares Fitting* 44

4 **The Au(hkl) Surface Reconstructions and the Effect of CO on the Surface/Electrolyte interface** 45

4.1 Introduction 45

4.1.1 *The Au(hkl) Surface Reconstructions* 46

4.2 Experimental 50

4.3 0.1M KOH 51

4.3.1 *Au(111)* 51

4.3.2 *Au (100)* 56
4.3.3 *Au(110)* 59
4.3.4 *Au(111) and Au(100) in 0.1 M KOH* 61
4.4 Au(*hkl*): the CO effect 63
5 **Formation of an Au/Pb Surface Alloy in the Au(111)/Pb UPD system** 72
5.1 Introduction 72
5.2 Experimental 75
5.2 Characterisation of the Pb/Au(111) UPD system 75
5.4 Formation of an Au/Pb surface alloy 78
5.5 Au(100) in 0.1 M KOH +1 mM $PbCO_3$ 85
5.6 Conclusions and Summary 89
6 **The Adsorption of Acetonitrile at the Au(111)/Electrolyte Interface** 90
6.1 Introduction 90
6.2 Experimental 94
6.3 Au(111) in H2SO4 95
6.4 Cu UPD on Au(111) in H_2SO_4 103
6.5 Conclusions and summary 115
7 Conclusion and Future Outlook 117

1 Introduction

The discipline of electrochemistry is becoming increasingly important as the need for harnessing and storing energy grows. To develop a real understanding of the electrocatalytic reactions occurring at the solid/liquid interface, the atomic scale characterisation of model catalytic surfaces is essential. These reactions involve the transfer of charge across the interface between an electrode surface and an ionic solution (the electrolyte). The kinetics of the reaction are heavily dependent on the composition and surface atomic structure of the electrode. Cyclic Voltammetry (CV) measures the current flowing between a working electrode surface and a secondary electrode as a function of the applied electrode potential and is the primary measurement used in many electrochemical studies. The measurement yields a wealth of information in terms of the potential dependence of certain electrochemical reactions occurring at the electrode/electrolyte interface. However, as the measurable quantity of CV is the current flow, it is unclear as to the nature of the structural changes occurring on the surface key to understanding the processes that occur. Therefore, to gain a more complete picture, voltammetry must be combined with surface sensitive spectroscopic techniques if the interfacial region is to be investigated.

Many of the techniques commonly used to investigate surfaces, such as Low Energy Electron Diffraction (LEED) and X-ray Photoelectron Spectroscopy (XPS), rely on ultra-high vacuum (UHV) and the free movement of electrons. In the past numerous approaches have been taken towards the study of the electrochemical interface, both *in-situ* and *ex-situ*, with the tendency to focus more on the use of *ex-situ* techniques. The theory behind *ex-situ* techniques is that when the electrode is transferred from the electrochemical cell to the UHV chamber, part of the double layer structure that forms at the interface remains intact[1]. While this approach has had some success [2–5], there remains a doubt as to what the effect of the loss of potential control and the electrolyte is which means there is never complete confidence that the interface is equivalent to its electrochemical counterpart. *In-situ* techniques have the benefit of enabling continuous potential control of the electrode/electrolyte interface during the structural or chemical examination. However, the experimental difficulties of *in-situ* techniques stem from the inherent nature of the electrochemical interface being a buried interface, making electron probe techniques unsuitable for direct studies due to electron absorption in the liquid overlayer. The development of experimental techniques such as optical spectroscopy, scanning probe microscopy and diffraction techniques summarised in [6] have overcome this problem.

1 Introduction

The principle technique used throughout this thesis is *in-situ* surface x-ray diffraction (SXRD). SXRD is capable of simultaneously providing information about the electrode surface and the electrolyte above it, as well as correlating the observed current in the voltammetry with the atomic structure of the electrode surface under reaction conditions. Chapter 2 describes the theoretical principles underpinning the work completed here. This begins with an overview of the development of the model for the solid-liquid interface over the past 150 years and a basic description of the CV technique employed to study the interface. This is followed by a description of the scattering techniques used to characterise the electrode surfaces, beginning with the elastic scattering from a single electron and then building up to the case of scattering from a 3D crystal; with a focus on the scattering due to the surface, e.g. Crystal Truncation Rods (CTRs). The contributions to the scattering from the electrolyte are described before finally briefly describing X-ray Voltammetry (XRV), an extremely useful technique that combines x-ray diffraction techniques with CV measurements.

Chapter 3 provides an overview of the considerations required for an *in-situ* SXRD experiment. A description of the sample preparation, the experimental equipment and instrumentation used is provided. The data acquisition procedure is outlined, and the necessary correction factors and fitting procedures are described.

Chapter 4 details an investigation into the potential dependent behaviour of the surface reconstructions of the low-index faces of gold in alkaline solution. Surface x-ray diffraction techniques are also used to explore the potential dependence of adsorbed CO on the Au(111) and Au(100) crystal surfaces. Surface reconstruction is where the outermost atomic layer assumes a periodicity different to that expected from termination of the bulk crystal lattice in a particular orientation. The ability of Au surfaces to reconstruct has been of great interest since its discovery in the UHV environment. It was revealed in subsequent experiments that these reconstructed surfaces could be formed in an electrochemical environment and the ability to control the nature of the electrode surface by the application of applied potential was also demonstrated. Gold has been shown to have a surprisingly high activity in electrocatalysis and heterogeneous catalysis studies[7]. However, the driving force behind such behaviour is largely unknown. In recent years it has been shown that adsorbed CO acts as a promoter for the electro-oxidation of certain alcohols on the hexagonal reconstructions of Au(111) and Au(100) [8].

Chapter 5 provides an *in-situ* investigation into the underpotential deposition (UPD) of Pb on the Au(111) surface in 0.1 M $HClO_4$ solution. Underpotential deposition is a phenomenon that indicates the onset of deposition of metal adatoms on a foreign metal substrate in potential ranges positive of the Nernst potential. Such phenomena allow for precise and reproducible

control of surface coverage and the study of the electronic and structural properties of the metallic adlayer[9]. The UPD of Pb on Au(111) electrodes is an extensively studied system, alloying/de-alloying process taking place during the deposition/stripping of Pb[10]. This chapter details a series of measurements at various stages of the Pb stripping process to identify the nature of the suspected surface alloy.

Chapter 6 details an *in-situ* investigation into the structure of the electrochemical double layer of Au(111) in various concentrations of Acetonitrile (AcN) in 0.1 M H_2SO_4. The effect of AcN on the Au(111)/$CuSO_4$ UPD system is also explored. Acetonitrile, is interesting for studying adsorption processes as the electrode is expected to have an altered reactivity when compared to that of AcN-free metal surfaces [11] due to the surface being chemically modified, a process known as reactive chemisorption. Acetonitrile is known to weakly adsorb on Au(111) in aqueous media[12]however, the structure of the electrochemical double layer in this system is unknown. In addition, the electrochemical reactivity of a metal electrode and the formation of metal adlayers via UPD can be significantly affected by the presence of small organic molecules.

2 Theoretical Principles

2.1 Introduction

When a particle of sufficiently high energy passes through ordered matter, the resulting scattering that occurs is known as diffraction. The experiments discussed in this work utilise x-ray diffraction, in conjunction with electrochemical techniques, to understand the electrochemical reactions occurring on the well-defined surfaces of fcc single crystal metals. The intensity of the scattered x-ray beam from a surface is approximately 10^6 times weaker than that of the bulk and thus synchrotron radiation is required to probe the surface. In this chapter the theoretical principles behind x-ray diffraction are built up.

2.2 The Electrode/Electrolyte Interface

2.2.1 Electrode Reactions

Electrode reactions involve a transfer of electrons and it is this charge transfer that is measured in potential sweep experiments e.g. Cyclic Voltammetry. Such a transfer of electrons are oxidation-reduction or redox reactions. Oxidation is the reaction that involves the loss of one or more electrons. In the case where the reverse occurs, i.e. one or more electrons are gained, the reaction is known as reduction. These reactions are shown in equations (2.1) and (2.2) respectively. For a reaction to occur there must be a way of balancing charge transfer. Therefore, a functioning electrochemical cell must have at least two electrodes, where the second electrode acts as a source/sink for electrons. As such in an electrochemical cell, two half reactions occur, oxidation occurs at the anode and reduction occurs at the cathode.

$$R = O^+ + ne^- \quad \textbf{(2.1)}$$

$$O^+ + ne^- = R \quad \textbf{(2.2)}$$

Where O is the oxidised species, R is the reduced species and ne^- is the number of electrons transferred between them. As stated above, the basic electrochemical cell consists of at least

two electrodes. These electrodes also act as a path for the electrons to flow from the anode to the cathode through wires external to the cell. The current through such an external circuit, *i,* is given by:

$$i = AI \tag{2.3}$$

Where A is the electrode area and I is the current density. By measuring the current, the charge transfered, q, can be extracted. Using Faraday's law, the number of moles, m, of the starting product in the reaction can be found:

$$q = \int_0^s i\, dt = mnF \tag{2.4}$$

Where *t* is time, *n* is the number of electrons transferred per molecule of reactant and *F* is the Faraday constant[13]. If the net change in free energy is negative the reactions will take place spontaneously. Assuming this is not the case the reaction must be driven by an applied potential between the two electrodes. The potential must be greater than the difference between the reversible potentials of the reactions at the anode and cathode. Therefore, the Gibbs free energy of the reactions taking place in the cell can be related to the cell potential:

$$\Delta G = -nFE_{cell} \tag{2.5}$$

Where E_{cell} is the sum of the potentials for each half reaction occurring at the cathode and anode. If the reaction is under standard conditions the relation becomes:

$$\Delta G^0 = -nFE_{cell}^0 \tag{2.6}$$

$$\Delta G = \Delta G^0 + RT\, ln \frac{a_{ox}}{a_{red}} \tag{2.7}$$

Where *R* is the gas constant (~8.3 J K^{-1} mol^{-1}), T is the absolute temperature and a_{ox}/a_{red} are the activity of the reductant and the oxidant.

Substituting the Gibbs free energy:

$$-nFE = -nFE^0 + RT\,ln\frac{a_{ox}}{a_{red}} \quad \textbf{(2.8)}$$

Dividing both sides by -nF:

$$\Delta E = \Delta E^0 + \frac{RT}{nF} ln\frac{a_{ox}}{a_{red}} \quad \textbf{(2.9)}$$

This is the Nernst equation which relates the equilibrium potential *E* to the standard electrode potential E^0 and to the activities of the electroactive species which, under equilibrium condition, are the same as their values in the bulk solution[14].

2.2.2 Underpotential Deposition

At potentials positive of that predicted by the Nernst equation (the Nernst potential) for bulk deposition processes, a phenomenon referred to as Underpotential Deposition occurs as discussed herewith. In solution metallic cations exist with a surrounding solvation shell. When the electrode surface possesses a net negative excess charge, these cations can be adsorbed onto the surface which, depending on the electrode potential, can be reduced to lower oxidation states or discharged completely. This allows for the formation of metal atoms on the surface in monolayer/sub-monolayer quantities and is known as Underpotential Deposition (UPD). This type of deposition arises from a difference in the chemical potential of the electroactive species in the bulk solution and that adsorbed on the electrode surface. This arises from stronger interactions between the electrode and deposited metal than the metal and the bulk metal[14]. It is of interest because the resulting properties of the UPD layer, and by extension the electrode, differ significantly to those of the original electrode material. Furthermore, UPD allows for the precise and reproducible control of the surface coverage and thus the study of the relation of surface coverage with its electronic properties and structure[9]. The UPD of metals on to gold single crystal surfaces is studied in chapters 5 and 6.

2.2.3 The Electrochemical Double Layer

Over a period of approximately 100 years, the current model for the electrode/electrolyte interface has been developed[14]. The first model for the solid/liquid interface assumed that no Faradaic processes occur at the interface, (i.e. no transfer of electrons between electrode and electrolyte). In this model it is assumed that electrical neutrality is upheld by an equal and opposite charge density from the electrolyte, balancing the excess charge density at the surface of the electrode[1]. These two opposing layers of charge were referred to as the

electrochemical double layer. A later model by Gouy and Chapman proposed the free movement of the charged ions in solution. In this model, ion concentration is highest near to the electrode and decreases with increasing distance to neutrality, where it is effectively the bulk electrolyte. Modifications to the Guoy-Chapman model by Stern[15] introduced a plane of closest approach accounting for the finite size of ions. A second plane of closest approach for ions with solvation shells was finally introduced in the Grahame model[16]. Grahame proposed that despite the closest zone of approach is mainly occupied by solvent molecules, some ionic or uncharged species may be able to penetrate into this region. This could occur even if the ion had no solvation shell or had recently lost its solvation shell when it approached the electrode surface. In this instance ions in contact with the surface are 'specifically adsorbed' as the interaction occurs for only certain ions or molecules irrespective of the charge on the ion. By including both specifically and non-specifically adsorbed ions, it is possible to model the bonding of the solute species to the surface. Once the surface was modelled the current responses of the electrode-electrolyte interface were able to be understood and thus allowed for the gathering of meaningful data during experiments such as cyclic voltammetry. A schematic of the model is presented in Figure 2.1.

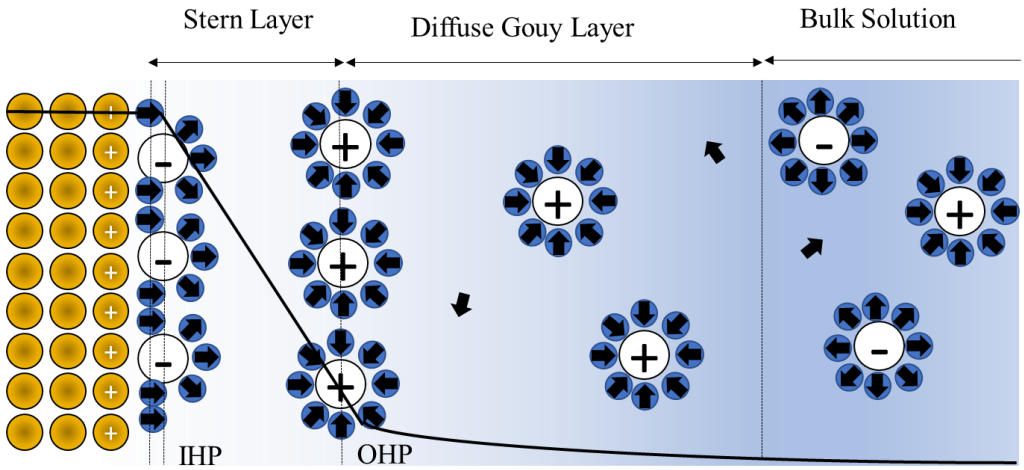

Figure 2.1: Schematic diagram of the electrode/electrolyte interface and double layer model. Arrows indicate the direction of the orientation of the solvent molecules. In this diagram, IHP and OHP represent the inner and outer Helmholtz planes respectively[6]. The solid black line represents the potential drop across the interface in the case of fully solvated anions.

2.2.4 Cyclic Voltammetry

Cyclic Voltammetry (CV) is one of the most fundamental methods of studying electrochemical systems through the interpretation of current and voltage measurements. CV measures the electric current as a function of the applied potential as it is continuously scanned between two points at a constant sweep rate. Electrons transfer at the surface, resulting from the oxidation/reduction of species induced by this potential cycling, are observed as peaks in the

'cyclic voltammogram' at potentials dependent on the system. Furthermore, peaks in the CV can arise due to the adsorption/desorption of ionic species from the solution on to the electrode surface in addition to ordering/disordering of adsorbate layers or structural transitions within the electrode surface layer itself (surface reconstruction).

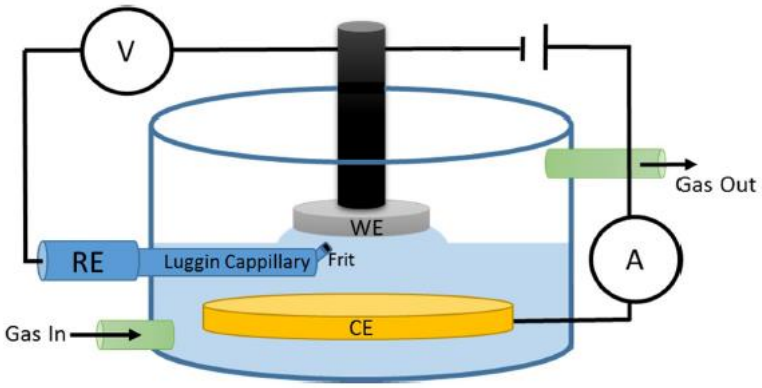

Figure 2.2: Schematic of the three-electrode electrochemical cell. The electrolyte forms a hanging meniscus with the working electrode surface ensuring the obtained CV is due to the reactions occurring on the well-defined single crystal surface. The electrolyte is deoxygenated by purging with N_2 gas.

A schematic of a three-electrode electrochemical cell is shown in Figure 2.2, with a hanging meniscus geometry typical of the type employed in CV experiments. The three electrodes used are denoted as the working, counter and reference electrodes (WE, CE and RE respectively), with the working electrode being the single crystal sample of interest. The working electrode surface forms a hanging meniscus with the electrolyte in this geometry so that the observed CV can be interpreted in terms of processes occurring at the well-defined surface. As the name implies, the reference electrode is used to provide a stable and fixed potential against which the potential of the working electrode can be measured. Reference electrodes that are commonly used for CV experiments include $Ag/AgCl^-$ and the reversible hydrogen electrode (RHE). In this work $Ag/AgCl^-$(3.5 M) electrodes were used for all measurements. The potential of the working electrode is held relative to the reference by a potentiostat, such that current flows between the counter and working electrodes. A graphical representation of the variation of the working potential with time $^{dV}/_{dt}$ in a CV experiment is shown in Figure 2.3(a). The potential is scanned at a constant rate (typically between 1 to 100 mV/s), from an initial value, E_1, to a second potential, E_2, and back again producing a triangular potential cycle. The potential limits E_1 and E_2 are typically measured relative to the reference electrode. Figure 2.3 (b), shows an example of a current response in the CV for a simple reversible one electron transfer reaction, $A^+_{(aq)} + e^-_{(metal)} \rightleftharpoons B_{(aq)}$. The nature of a reversible reaction means that as soon as sufficient potential is applied and thus reduction/oxidation becomes thermodynamically viable, the reaction will take place. This reaction can be described as fast

due to an equally large charge flowing in each direction at equilibrium and as such comes about by rapid electrode kinetics.

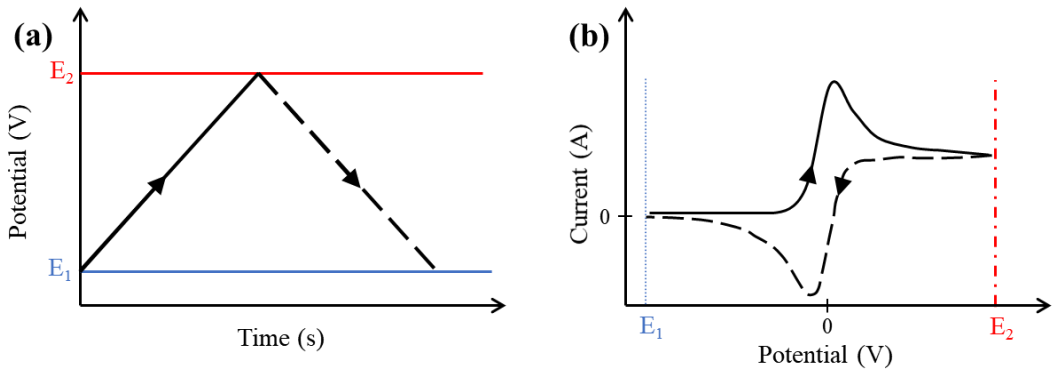

Figure 2.3: (a) Variation of potential with time in a cyclic voltammogram measurement. (b) An example of a current-potential curve obtained from a solution phase single electron transfer reaction.

As the potential is not great enough to induce a reaction initially, the CV shows that there is no current flowing as the potential is swept from E_1 to E_2. When sufficient potential is applied, the current increases and approaches a maximum due to the high concentrations of $A^+_{(aq)}$ in the diffusion layer. The maximum is reached as more of the reactant $A^+_{(aq)}$ is consumed and greater diffusion of $A^+_{(aq)}$ from the bulk is required. The current then decreases and becomes a constant at E_2 as the current becomes dominated by the diffusion rate. As the reverse potential sweep occurs back towards E_1, in the same manner as the positive sweep, there is an initial abundance of reactant in the surface layer. This time the reactant is $B_{(aq)}$ and the current tends towards a maximum before becoming dominated by the diffusion of $B_{(aq)}$ and the current finally returning to 0. In general, the current response is dependent on the reversibility of the electrochemical reaction[14]. In the case of a fully reversible reaction the measured current peak is equal in size and opposite in sign to that of the positive sweep. For an irreversible reaction the charge transferred is reduced and/or the peak position is shifted. CVs not only yield valuable information for the potentials at which reactions occur but also make it possible to calculate surface coverage by integration under the CV peaks. It is known that in CV an electron transfer takes place and usually the number of electrons is measurable. CV is usually paired with surface science techniques such as scanning probe microscopy and SXRD to give a more detailed view of the interface.

2.3 X-Ray Diffraction

This section begins by detailing relevant crystallographic definitions, thereafter, providing a basic description of x-ray scattering from surfaces. The derivations in this section closely follow that of the comprehensive treatments carried out in references[17–22].

2.3.1 Crystallographic Definitions

Crystal Lattice and Unit Cell

The atoms in a crystal exist in a periodic array with long range order that can be described in terms of a space lattice with a group of atoms, known as the *basis*, attached to each lattice point. The lattice is defined by three vectors **a**, **b** and **c**, such that a similar lattice point can be located via integer translations in these directions from any point in the lattice. A parallelepiped characterised by sides of length **a**, **b** and **c**, with angles α, β and γ between them defines the unit cell. A representation of the fcc crystal structure is shown in Figure 2.4a cubic lattice where **a**, **b** and **c** vectors are all equal and the angles between them are all equal to 90°. The basis consists of four atoms located at (0,0,0), (½, 0, ½), (0, ½, ½) and (½, ½, 0) in terms of the primitive lattice vectors (**a**, **b**, **c**).

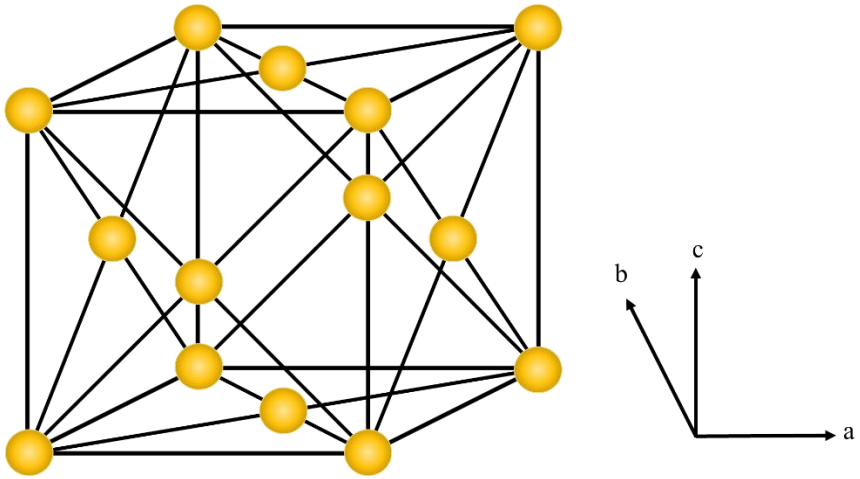

Figure 2.4: The face centred cubic (fcc) crystal structure. This is a four-atom basis cubic lattice. In this case a=b=c and the angles between them α=β=γ=90°

Crystal Planes and Miller Indices

To complete the crystal structure, the unit cell must be translated over all space in the three directions of the primitive unit cell. The 3D lattice has an infinite number of parallel 2D planes associated with it. Groups of planes are specified by *Miller Indices* with the notation (*hkl*). A specific plane's Miller indices are derived by finding the intercepts of the plane with the three axes in terms of primitive lattice vectors **a**, **b** and **c**. Multiplying the reciprocals of the

intercepts and by their lowest common factor yields the integer values for (*hkl*). Figure 2.5 displays the three lowest index planes for an fcc crystal. Directions in such cubic crystals are denoted [*hkl*] and are perpendicular to the plane denoted by (*hkl*). The inter-planer spacing, d_{hkl}, can be calculated using the Miller indices for parallel planes associated with a *cubic* lattice according to:

$$d_{hkl} = \frac{a_0}{\sqrt{h^2 + k^2 + l^2}} \tag{2.10}$$

Where a_0 is the cubic lattice parameter.

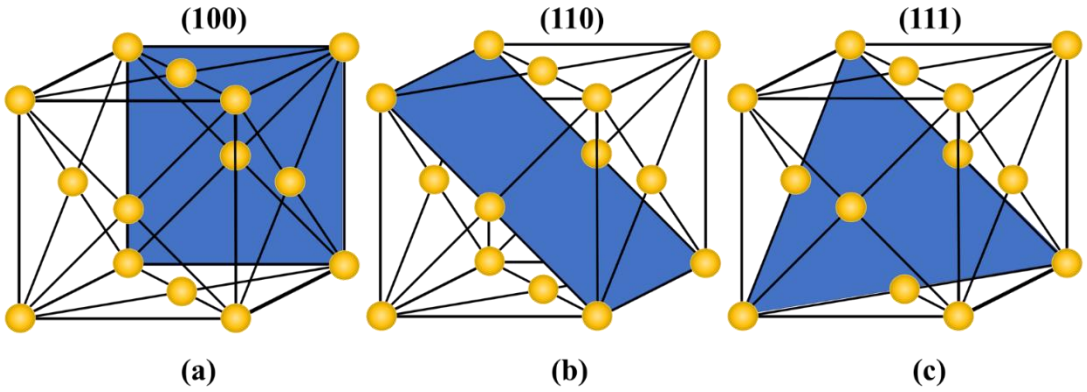

Figure 2.5: The 3 fcc crystal low-index planes: (a) (100), (b) (110) and (c) (111).

2.3.2 Kinematical X-ray Diffraction

The derivation of the scattering equations in this section assumes the interaction between the x-rays and the crystal is weak, therefore assuming the *kinematical approximation*. With this approximation, multiple scattering effects can be ignored in such a way that an individual scattering event can be considered as an elastic collision between the x-ray and an atomic electron, simplifying the description. The scattering formulae can then be formed in stages from a single electron and through to the bulk crystal, assuming the observed scattering is merely the sum of independent contributions from all individual electrons.

Classical Description of Diffraction

Starting with the classical interpretation of diffraction from parallel crystal atomic planes, the derivation of the Bragg law will be described. A schematic diagram of the scattering from two adjacent parallel planes separated by a distance d is shown in Figure 2.6(a). Assuming each plane of atoms scatters a small fraction of the incident x-rays, multiple layers of the bulk crystal therefore contribute to the observed diffraction. If the extra distance travelled by the

wave scattering from the lower plane ($2x$) is equal to an integer number of wavelength ($n\lambda$), maximum scattering is observed. Based on Figure 2.6(b), the distance x is equal to $d\ sin\ \theta$, so that Bragg's law can be stated as:

$$n\lambda = 2dsin\theta \qquad where\ n\ is\ an\ integer \geq 1$$

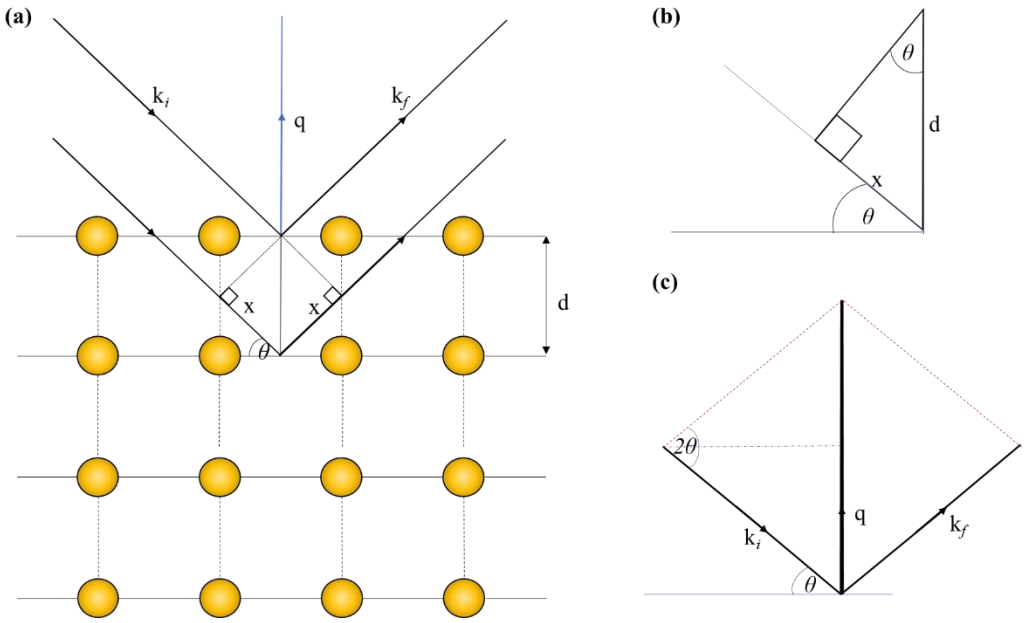

Figure 2.6: Diagrams showing the scattering from a series of parallel atomic planes separated by a distance d. The incident x-ray beam has a wavevector k_i and approaches the planes at an angle of incidence θ. The resulting scattered x-ray beam has a wavevector k_f.

While Braggs law provides the conditions for diffraction from parallel atomic planes, there is lack of information essential for structural analysis such as; consideration of the scattering power of the atoms comprising the crystal. The standard procedure for understanding the magnitude of the scattered intensity from a crystal starts with the scattering of one electron and builds up in stages: namely, scattering of the electrons belonging to an atom, the atoms in a unit cell and then finally, a crystal containing N unit cells in three dimensions.

Momentum Transfer

Momentum transfer (q) is the difference between the incoming (k_i) and outgoing wavevectors (k_f)where $\mathbf{q} = \mathbf{k_f} - \mathbf{k_i}$. A graphical representation of this is shown in Figure 2.6(c). In the case of elastic scattering, $|\mathbf{k_i}|=|\mathbf{k_f}|=|\mathbf{k}| = {}^{2\pi}/_{\lambda}$, . This relationship in combination with principles of trigonometry (Figure 2.6(c)) can be used to derive Bragg's law in terms of momentum transfer and the reciprocal vector such that:

$$|\boldsymbol{q}| = 2|\boldsymbol{k}|\, sin\left(\frac{1}{2}(2\theta)\right) = \frac{4\pi}{\lambda} sin\left(\frac{1}{2}(2\theta)\right) \tag{2.11}$$

Real Space vectors

A definition of the real space vectors as adapted from Robinson & Tweet [10] is shown in Figure 2.7. Using point O as the origin of the crystal, it can be said that point A is the origin of the *n*th unit cell, point B the *j*th atom of the nth unit cell and point C is the location of an electron belonging to the atom at point B. At a distance $\mathbf{R_0}$ from the crystal origin, the scattered x-rays are observed.

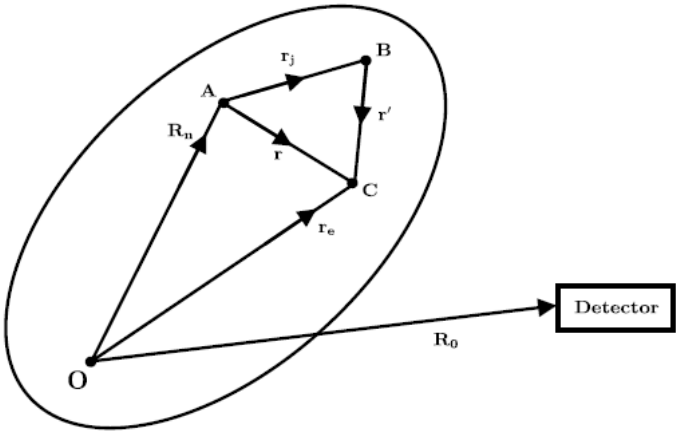

Figure 2.7: Real space vectors defining the position of an electron (C) belonging to the *j*th atom (B) of the *n*th unit cell (A). The origin of the unit cell is a distance R_n from the origin of the crystal and the scattering is observed at a distance R_0 away. Reproduced with permission from [17].

Scattering from a Single Electron

Scattering can be thought of most simply as the scattering from a free electron. The classical description of the scattering event states that the incident x-ray's electric field sets the electron into oscillation via exerted force. As a result, the electron radiates a spherical wave with a wavelength equal to that of the incident plane wave. The Thompson formula describes the amplitude, A_e, of the scattered wave from an electron at $\mathbf{r_e}$ as a function of the incident wave amplitude, A_i:

$$A_e e^{-i(k_f \cdot r_e)} = A_i \frac{e^2}{4\pi\epsilon_0 mc^2} \frac{1}{R_0} e^{-i(k_i \cdot r_e)} \tag{2.12}$$

Where *e* and *m* are the electron charge and mass respectively. The $1/R_0$ terms arises due to the incoming wave being plane polarised whereas the outgoing wave is spherical. The pre-factor to the spherical wave term is known as the Thompson scattering length, r_0, where:

$$r_0 = \frac{e^2}{4\pi\epsilon_0 mc^2} \tag{2.13}$$

Using ${e^a}/{e^b} = e^{(a-b)}$ and $\mathbf{q} = \mathbf{k_f} - \mathbf{k_i}$, equation (***2.13***) can be rearranged to yield the scattered amplitude in terms of the incident amplitude and the momentum transfer:

$$A_e = A_i \frac{r_0}{R_0} e^{-i(\boldsymbol{q}\cdot r_e)} \tag{2.14}$$

Scattering from an Atom

The scattering from an atom stems from the constructive interference of the spherical waves from each electron contained within the atom. Classically, each electron is defined as having an associated density distribution, $\rho(\boldsymbol{r'})$, where $\mathbf{r'}$ is the position of the electron shown in Figure *2.7*. The scattering amplitude of an atom, A_a, is given by substituting the electron position vector ($\mathbf{r_e} = \mathbf{R_n} + \mathbf{r_j} + \mathbf{r'}$) into equation (***2.14***) and summing the separate electron contributions. The summation becomes an integration over the atom such that:

$$A_e = A_i \frac{r_0}{R_0} \int_{-\infty}^{+\infty} \rho(\boldsymbol{r'})\, e^{-i\boldsymbol{q}\cdot(R_n + r_j + r')} \boldsymbol{d^3 r'}$$

$$= A_i \frac{r_0}{R_0} f(q) e^{-i\boldsymbol{q}\cdot(R_n + r_j)} \tag{2.15}$$

Where f(**q**) is the *atomic form factor* given by:

$$f(\boldsymbol{q}) = \int_{-\infty}^{+\infty} \rho(\boldsymbol{r'})\, e^{-i\boldsymbol{q}\cdot(r')} \boldsymbol{d^3 r'} \tag{2.16}$$

Equation (***2.16***) shows a **q** dependence on the atomic form factor in the cases where the x-ray energy is well below the atomic absorption edge of a particular element. The International Tables of Crystallography[23] contains tabulations of the atomic from factors of most elements and list the appropriate coefficients for the Cromer-Mann equation. When q is less than ~20 $Å^{-1}$, the Cromer-Mann equation provides a good approximation for the q dependence of atomic form factors:

$$f(\boldsymbol{q}) = \sum_{i=1}^{4} a_i \, e^{-b_i\left(\frac{q}{4\pi}\right)^2} + c \qquad \textbf{(2.17)}$$

However, in practice the form factor needs to account for the resonant effects of photon energies close to the absorption edges, referred to as anomalous dispersion. The so-called dispersion correction is then:

$$f(\boldsymbol{q}, E) = f(\boldsymbol{q}) + f'(E) + if''(E) \qquad \textbf{(2.18)}$$

Where $f(\boldsymbol{q}, E)$ is the corrected form factor, $f(\boldsymbol{q})$ is the uncorrected form factor and $f'(E)$ and $if''(E)$ are the real and imaginary parts of the dispersion correction respectively. The additional complex term, $if''(E)$, accounts for any shift in phase that occurs. Tabulations by Brennan and Cowan[24] show the energy dependence of the f' and f'' terms for most atoms and can be interpolated to find their values.

Scattering from a Unit Cell

By summing the contributions of all the atoms contained within a unit cell, the resulting scattering amplitude, A_u, can be obtained. The atoms within a unit cell do not necessarily have the same chemical element, this is accounted for via the use of a separate form factor, $f_j(\boldsymbol{q})$. A unit cell containing a number of atoms, N_c, has a scattering amplitude:

$$\begin{aligned} A_u &= A_i \frac{r_0}{R_0} \sum_{j=1}^{N_c} f_j(\boldsymbol{q}) e^{(i\boldsymbol{q}\cdot(R_n + r_j))} \\ &= A_i \frac{r_0}{R_0} F(\boldsymbol{q}) e^{(i\boldsymbol{q}\cdot R_n)} \end{aligned} \qquad \textbf{(2.19)}$$

Where F(**q**) is the *structure factor* given by

$$F(\boldsymbol{q}) = \sum_{j=1}^{N_c} f_j(\boldsymbol{q}) e^{(i\boldsymbol{q}\cdot r_j)} \qquad \textbf{(2.20)}$$

For which the value is dependent of the position of the atoms in the unit cell.

Scattering from a Crystal

By summing the contribution from each unit cell, the scattering from the crystal can be evaluated. The crystal is defined as consisting of N_1, N_2 and N_3 unit cells along the crystal axes directions **a**, **b** and **c**. Using the vector:

$$\boldsymbol{R_n} = n_1\boldsymbol{a} + n_2\boldsymbol{b} + n_3\boldsymbol{c} \qquad \textbf{(2.21)}$$

To give the position of each unit cell relative to the origin, the scattered amplitude is then given by:

$$A_c = A_i \frac{r_0}{R_0} F(\boldsymbol{q}) \sum_{n_1=0}^{N_1-1} \sum_{n_2=0}^{N_2-1} \sum_{n_3=0}^{N_3-1} e^{i(\boldsymbol{q}\cdot(n_1\boldsymbol{a}+n_2\boldsymbol{b}+n_3\boldsymbol{c}))} \qquad \textbf{(2.22)}$$

Equation 2.13 shows that the scattered amplitude is a combination of two factors; the structure factor, containing the chemical information, and the summation of the lattice of unit cells over three dimensions. To proceed further it is necessary to consider one of the independent terms from equation ***(2.22)***. A geometric progression from a one-dimensional crystal of N atoms, where x=**q·a,** such that

$$S_N(x) = \sum_{n=0}^{N-1} e^{ixn} \qquad \textbf{(2.23)}$$

$$= \frac{1 - e^{ixn}}{1 - e^{ix}}$$

$$= \frac{e^{ixn/2}\left(e^{-ixn/2} - e^{ixn/2}\right)}{e^{ix/2}(e^{-ix/2} - e^{ix/2})} \qquad \textbf{(2.24)}$$

In a diffraction experiment we are interested in the scattered intensity, the square modulus of $S_N(x)^*$ is proportional to the scattered intensity. Therefore, using $e^{i\theta} = \cos\theta + i\sin\theta$ and multiplying equation ***(2.24)*** by its complex conjugate the pre-factor becomes unity and the contribution to the scattered intensity is as follows:

$$|S_N(x)|^2 = \frac{sin^2(xN/2)}{sin^2(x/2)} \qquad \textbf{(2.25)}$$

This Equation is known as the *N-slit interference function*, its magnitude reaching some

maxima of N^2 separated by 2π in units of $\mathbf{q}\cdot\mathbf{a}$[17]**.** When ½ $\mathbf{q}\cdot\mathbf{a} = m\pi$, where *m* is an integer, the denominator goes to zero and the value of $|S_N(x)|^2$ is maximised. Extending this to three dimensions, i.e treating the other two components of the scattered intensity similarly, the scattered intensity from a large 3D crystal can be expressed as:

$$I(\boldsymbol{q}) = I_i \left(\frac{r_0}{R_0}\right)^2 |F(\boldsymbol{q})|^2 S_{N_1}(\boldsymbol{q}\cdot\boldsymbol{a}) S_{N_2}(\boldsymbol{q}\cdot\boldsymbol{b}) S_{N_3}(\boldsymbol{q}\cdot\boldsymbol{c}) \qquad \textbf{(2.26)}$$

When the following conditions are met simultaneously, the so-called Laue conditions for diffraction, equation ***(2.25)*** displays maxima:

$$\begin{aligned} \boldsymbol{q}\cdot\boldsymbol{a} &= 2\pi h \\ \boldsymbol{q}\cdot\boldsymbol{b} &= 2\pi k \\ \boldsymbol{q}\cdot\boldsymbol{c} &= 2\pi l \end{aligned} \qquad \textbf{(2.27)}$$

Where the *Miller indices h, k* and *l* take integer values. The Laue conditions are simultaneously satisfied by the vector:

$$\boldsymbol{q} = h\boldsymbol{a}^* + k\boldsymbol{b}^* + l\boldsymbol{c}^* \qquad \textbf{(2.28)}$$

Where **a***, **b*** and **c*** are related to the real space vectors by:

$$\boldsymbol{a}^* = 2\pi \frac{\boldsymbol{b}\times\boldsymbol{c}}{\boldsymbol{a}\cdot(\boldsymbol{b}\times\boldsymbol{c})}, \boldsymbol{b}^* = 2\pi \frac{\boldsymbol{c}\times\boldsymbol{a}}{\boldsymbol{a}\cdot(\boldsymbol{b}\times\boldsymbol{c})} \; and \; \boldsymbol{c}^* = 2\pi \frac{\boldsymbol{a}\times\boldsymbol{b}}{\boldsymbol{a}\cdot(\boldsymbol{b}\times\boldsymbol{c})} \qquad \textbf{(2.29)}$$

A 3D lattice of **q** values that satisfy the Laue conditions can be formed by substituting arbitrary integer values of *h*, *k* and *l* into equation (***2.28***). This lattice is known as the *reciprocal lattice* and is defined by the *reciprocal lattice vectors* from equation (***2.29***). In a diffraction experiment the points on the reciprocal lattice are labelled by the (*h,k,l*) values of the crystal planes from which they are scattered and reveal the position of the Bragg peaks (maximum scattered intensity). The reciprocal lattice vector $\boldsymbol{G}(hkl) = h\boldsymbol{a}^* + k\boldsymbol{b}^* + l\boldsymbol{c}^*$ is normal to the plane defined by *h, k* and *l*. As the real space vectors have units of angstroms (Å), the reciprocal lattice vectors have units of $Å^{-1}$. Outside of discrete values of **q** that lie on the reciprocal lattice, the diffracted intensity from a large 3D crystal is zero. Consequently, the scattered intensity in a diffraction experiment is measured as a function of the momentum transfer from which it is possible to infer a unit cells real space structure. The intensity at a position is reciprocal space is thus:

$$I_{hkl} = I_i \left(\frac{r_0}{R_0}\right)^2 |F(h\boldsymbol{a}^* + k\boldsymbol{b}^* + l\boldsymbol{c}^*)|^2 N_1^2 N_2^2 N_3^2 \quad \textbf{(2.30)}$$

2.3.3 Surface X-ray Diffraction

Scattering from a 2D monolayer and Crystal Truncation Rods

Up to this point, only the general case of diffraction from a large 3D crystal has been considered. The model can then be progressed to consider the case of diffraction from a surface or a buried interface. First the case of a 2D monolayer can be considered as shown in Figure 2.8(a *left*). This is corresponding to setting N_3 in equation **(*2.25*)** to 1, where the **c** vector is along the surface normal and the vectors **a** and **b** are in the plane of the surface. The diffraction in this case is independent of the momentum transfer in the surface normal direction (**q** · **c**). Therefore, for integer values of *h* and *k*, there is an intensity observed for all values of *l* when in the plane of the surface the Laue conditions are met. Figure 2.8(a *right*) shows the resultant diffraction where the scattering is sharp in directions parallel to the surface however, in the direction normal to the crystal surface is completely diffuse. Figure 2.8 (b *right*) shows the 'rods' of scattering superimposed onto the scattering from the 3D crystal passing through the bulk reflections. Figure 2.8 (c *right*) shows the diffracted intensity pattern in the case of a real surface, created by slicing the crystal along a particular orientation, the intensity is streaked between the Bragg peaks along the *l* direction forming *Crystal Truncation Rods* or CTR's. The intensity profile of the CTR can be understood via consideration of equation **(*2.25*)** for the case of a crystal extended in the directions defined by the **a** and **b** vectors (N_1, $N_2 \rightarrow \infty$), and a finite thickness of $\boldsymbol{N_3 c}$. The $sin^2(N_3 \boldsymbol{q} \cdot \boldsymbol{c})$ term is a rapidly varying function of **q** for large $\boldsymbol{N_3}$ and is taken to be its average value of ½. Replacing this into equation **(*2.25*)** the scattered intensity as a function of the surface normal momentum transfer when the Laue conditions are met is given by:

$$I_{CTR} = I_0 \left(\frac{r_0}{R_0}\right)^2 |F(\boldsymbol{q})|^2 N_1^2 N_2^2 \frac{1}{2sin^2(\boldsymbol{q} \cdot \boldsymbol{c}/2)} \quad \textbf{(2.31)}$$

The expression generates sharp peaks in intensity i.e. Bragg peaks at values of $\boldsymbol{q} \cdot \boldsymbol{c} = 2\pi l$ where *l* is an integer. In between the Bragg peaks the intensity is 'smeared' along the surface normal direction as shown by the solid black line in Figure 2.9.

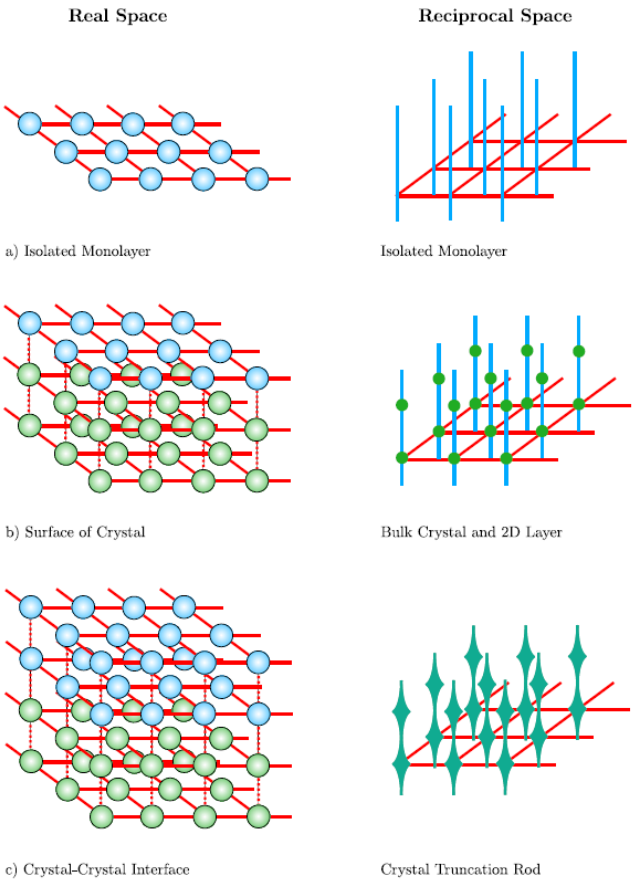

Figure 2.8:Real space (left) and reciprocal space diffraction (right) for (a) a two-dimensional monolayer, (b) the surface of a crystal and (c) a crystal-crystal interface.

2.3.4 Modelling Surface Structure

So far, the derivation of the scattered intensity along the CTR's has assumed a single crystal that is defect-free and perfectly terminated. However, surface properties such as surface relaxation, roughness and relative occupation affect the CTR profile and thus need to be considered to accurately model the scattered intensity. The effect these surface properties have on the CTR profile is illustrated in Figure 2.9. The general form of the CTR profile for a perfectly terminated crystal surface is represented by the solid black line. The Bragg conditions are satisfied and a maximum in the intensity is observed when l is an integer.

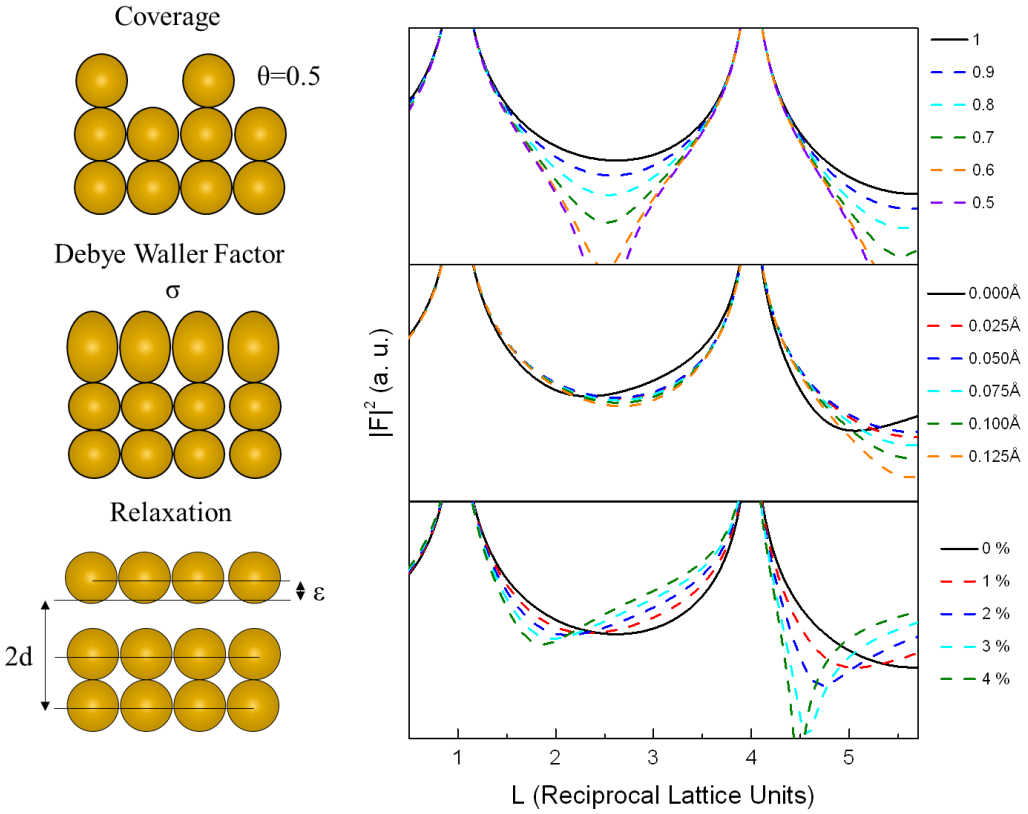

Figure 2.9:Demonstration of the effect of the various parameters on the CTR profile compared to a perfectly terminated crystal surface (solid black line). The illustrations on the left highlight the physical definitions of each parameter. Each line shows how a [1 0 L] CTR for an Au(111) crystal would change if the value of the parameter highlighted in the illustrations were change to that of the values shown in the legend. Coverage is given as a fraction of the total coverage, the Debye-Waller factor is terms of root mean squared displacement given in Å and relaxation is given in units of percentage expansion from the bulk lattice spacing.

When *l* has half integer values the scattering is at a minimum, known as 'anti-Bragg' positions. At these minima, the scattering is comparable to that of the scattering from a single monolayer, due to the cancelling out of scattering from the bulk crystal. A decrease in the relative occupation or an increased roughness of the topmost atomic layer causes the intensity between the Bragg peaks to fall off sharply, whereas changes in relaxation causes asymmetry around the Bragg peaks. The *specular* CTR is when the CTR is dependent only on the surface normal component of the momentum transfer. Measurement of the (0, 0, *l*) CTR is sensitive only to the atomic planes stacked in the direction of the surface normal. *Non-specular* CTRs have an additional in-plane component of the momentum transfer for integer values of *h* and *k* satisfying the Laue diffraction conditions. CTR measurements at these fixed (*h, k*) positions are sensitive to the registry of surface and bulk layers. If the surface layer has periodicity that

differs from that of the bulk, e.g. the Au(111) surface can reconstruct to form a (23 x √3) structure, then the scattering from the surface is able to be observed separately from the bulk CTR in reciprocal space. A detailed three-dimensional model for the surface structure can be formed through measurement and modelling of the specular and non-specular CTRs'.

2.3.5 Reciprocal Lattice for the Low-Index fcc Metal Surfaces

It is desirable during surface x-ray scattering experiments to define the Miller indices such that l is in the direction of the surface normal, and h and k lie in the plane of the surface. Therefore, the specular CTR will lie in the surface normal direction. In this thesis the results discussed pertain to [111], [110] and [100] oriented, face centred cubic (fcc) metals. As such, a description of the real-space parameters, the resultant reciprocal space lattices and the surface parameters used in the subsequent modelling will now be provided.

The fcc(111) surface

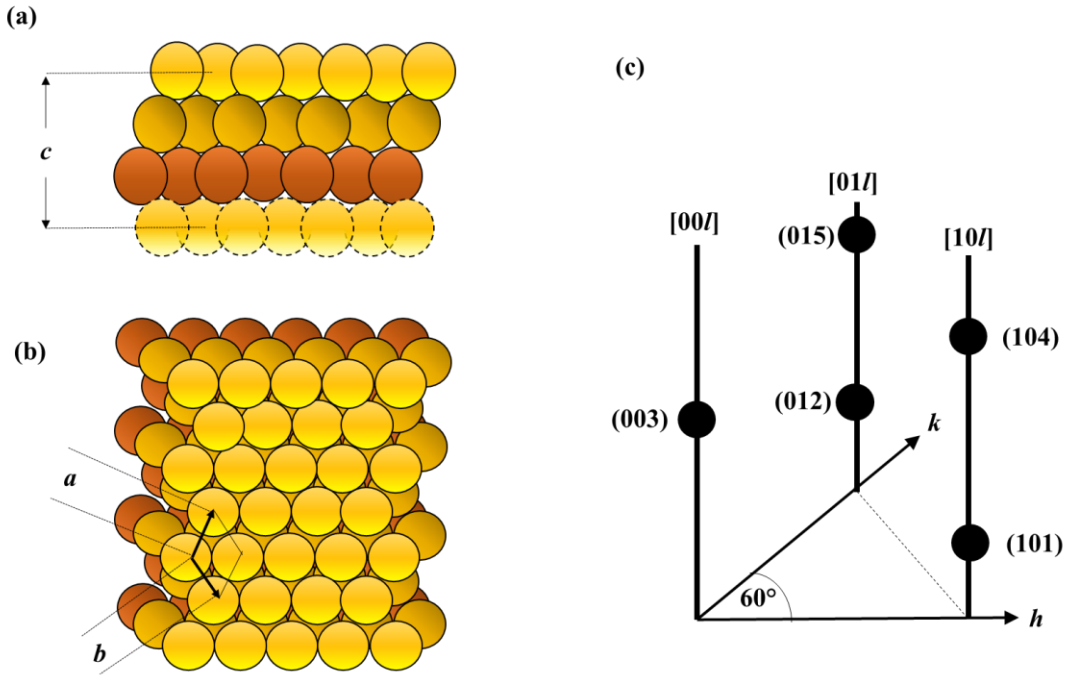

Figure 2.10:Fcc(111) real space surface structure: (a) 'side' view and (b) 'top' view. (c) corresponding reciprocal space lattice.

The (111) surface is the most densely packed of the three low index faces. This surface defined such that the surface normal direction is along the $(0, 0, l)_{hex}$ direction and the $(h, 0, 0)_{hex}$ and $(0, k, 0)$ directions lie in the surface plane and subtend 60°. This is performed by defining a hexagonal surface unit cell such that the **a** and **b** vectors are equal to the nearest neighbour spacing, a_{NN}, and subtend an angle of 120°. Figure 2.10(b) shows the hexagonally close packed (*hcp*) surface structure. The unit cell comprises of three atomic layers defining the **c**

parameters brought about by ABC stacking in the [111] direction as shown in Figure 2.10(a). The units of *h*, *k* and *l* are defined as:

$$a^* = b^* = \frac{4\pi}{\sqrt{3}a_{NN}} \qquad and \qquad c^* = \frac{2\pi}{\sqrt{6}a_{NN}} \tag{2.32}$$

In Figure 2.10(c) the Bragg peaks are represented as circles and are separated by three units of *l* due to the three atomic layer repetition in the [111] direction in the unit cell. The fcc unit cell notation can be related to the hexagonal unit cell notation via the following transforms:

$$\begin{aligned} h_c &= \frac{2}{3}h_s - \frac{2}{3}k_s + \frac{1}{3}l_s \\ k_c &= \frac{2}{3}h_s + \frac{4}{3}k_s + \frac{1}{3}l_s \\ l_c &= -\frac{4}{3}h_s + \frac{2}{3}k_s + \frac{1}{3}l_s \end{aligned} \tag{2.33}$$

Such that (003) in surface notation represents the (111) Bragg peak.

The bulk structure factor, F_{Bulk}, is initially considered to evaluate the CTR scattering profile from this surface. F_{Bulk} for an unrelaxed, unmodified crystal is given by:

$$\begin{aligned} F_{Bulk} &= f\ DW_{Bulk} \sum_{n=0}^{\infty} e^{in[2\pi\left(\frac{h}{3}-\frac{k}{3}-\frac{l}{3}\right)]} \\ &= \frac{f\ DW_{Bulk}}{1 - e^{2\pi i\left(\frac{h}{3}-\frac{k}{3}-\frac{l}{3}\right)}} \end{aligned} \tag{2.34}$$

where f is the **q** dependent atomic form factor. DW_{Bulk} is the term representing the Debye-Waller factor, which accounts for thermal disorder, that has the overall effect of decreasing the diffracted intensity. The bulk Debye-Waller factor is derived from the Debye temperature which has been calculated for all elements[23]. This term is dependent on the root-mean-square (rms) displacement about their average position (σ) of the atoms for which the relationship between DW_{Bulk} and σ is shown in equation (***2.36***).

$$DW_{Bulk} = e^{-\frac{1}{2}(\boldsymbol{q}\sigma)^2} \tag{2.35}$$

Scattering from the surface layers is considered as the continuation of the bulk structure in addition to the bulk structure factor. In the case of a metal crystal, where the bonds are not strongly directional, modelling the CTR data considering the relaxations in the three outermost surface layers is suitable.

$$F_{Surf} = f\theta_n DW_n e^{2\pi i[n\left(-\frac{h}{3}+\frac{k}{3}+l\left|\frac{1}{3}+\varepsilon_n\right|\right)]} \qquad for\ n = 1,2,3 \quad \textbf{(2.36)}$$

As in the near surface region, there is a difference in the interatomic bond strengths compared to the bulk. The Debye-Waller factor is therefore considered for each layer individually (DW_n). The relative occupation of the surface layer is controlled by the θ_n term. This is simply a multiplicative fraction from 0 to 1ML that controls the density of the individual layers. The surface normal displacement of each layer, either expansion or relaxation, is controlled by the ε_n. Section 2.3.4 and Figure 2.9 show the induced asymmetry either side of the Bragg peak, compared to a perfectly terminated crystal surface brought about by this term. The change in the scattering is due to interference effects between x-rays scattered from solely the modified surface layer and those scattered from the bulk crystal. The total scattered intensity is given by:

$$I_{Tot} = |F_{Tot}|^2 = \left|F_{Bulk} + F_{Surf}\right|^2 \qquad \textbf{(2.37)}$$

The fcc(110) surface

Of the three low-index fcc structures, the (110) surface, depicted in Figure *2.11*, is the most open. Here a rectangular unit cell is defined such that *h* and *k* are along the $[1\bar{1}0]$ and [010] directions respectively. *l* is defined in the [110] direction which has ABAB stacking. As such the Bragg peaks are spaced out in the *l* direction in units of 2. The units of *h*, *k* and *l* are defined as:

$$a^* = c^* = \frac{2\pi}{a_{NN}} \qquad and \qquad b^* = \frac{4\pi}{\sqrt{2}a_{NN}} \quad \textbf{(2.38)}$$

The surface notation can be converted to bulk units via the following transformations:

$$\begin{aligned} h_c &= h_s + l_s \\ k_c &= -h_s + l_s \\ l_c &= k_s \end{aligned} \qquad \textbf{(2.39)}$$

The CTR's for this surface can then be described by:

$$F_{Bulk} = \frac{f\ DW_{Bulk}}{1 - e^{2\pi i\left(\frac{h}{2}+\frac{k}{2}+\frac{l}{2}\right)}} \qquad \textbf{(2.40)}$$

With the scattering factors from the outermost three layers given by:

$$F_{Surf} = f\theta_n DW_n e^{2\pi i[n\left(\frac{h}{2}+\frac{k}{2}+l\left|\frac{1}{2}+\varepsilon_n\right|\right)]} \qquad for\ n = 1,2,3 \quad \textbf{(2.41)}$$

Where the symbols have the same meaning as for the (111) crystal. The total scattering is

then given by equation (2.37).

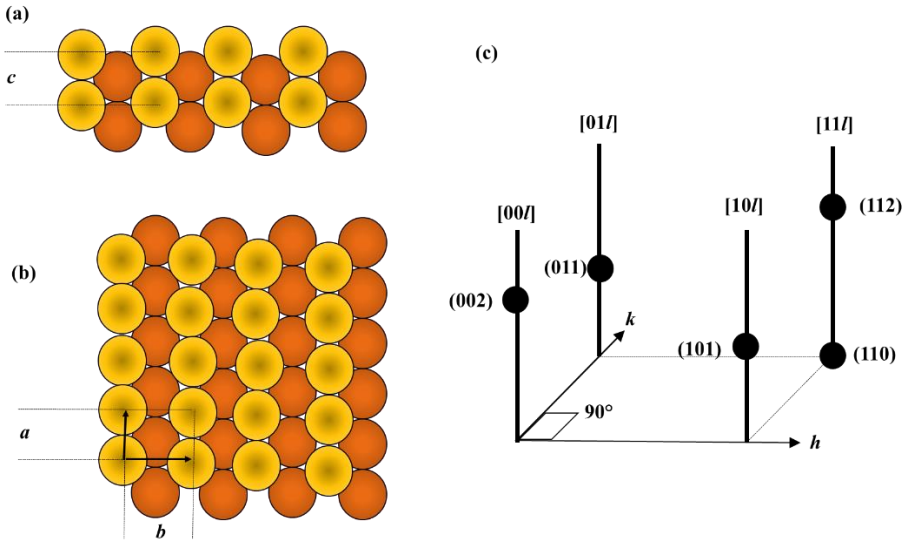

Figure 2.11Fcc(110) real space surface structure: (a) 'side' view and (b) 'top' view. (c) corresponding reciprocal space lattice.

The fcc(100) surface

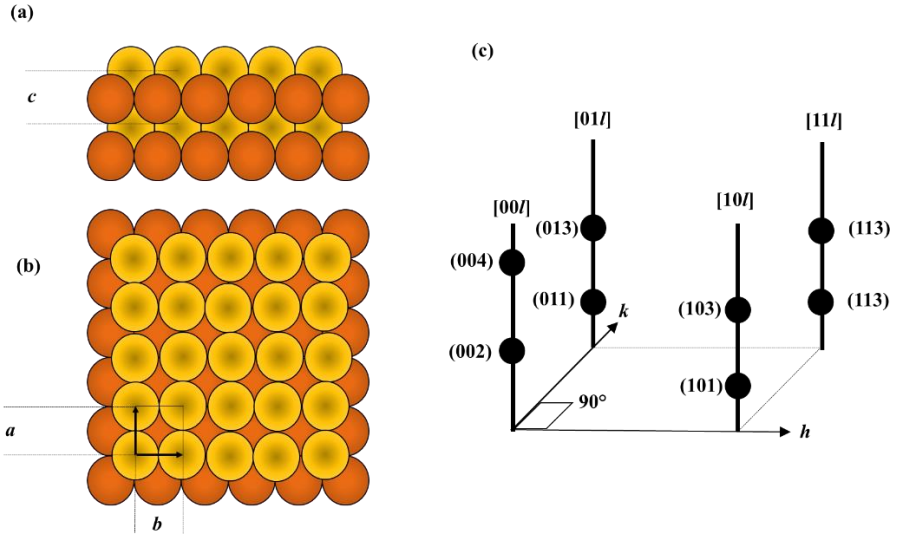

Figure 2.12: Fcc(100) real space surface structure: (a) 'side' view and (b) 'top' view. (c) Corresponding reciprocal space lattice.

Figure 2.12 displays the surface unit cell for the (100) surface utilised in the x-ray diffraction experiments along with the corresponding reciprocal space map. The units of h, k and l for this surface are given by:

$$a^* = b^* = \frac{2\pi}{a_{NN}} \qquad and \qquad c^* = \frac{4\pi}{\sqrt{2}a_{NN}} \tag{2.42}$$

The bulk cubic unit cell is related to the surface tetragonal unit cell that is shown here via the following transformations.

$$\begin{aligned} h_c &= h_s + k_s \\ k_c &= h_s - k_s \\ l_c &= l_s \end{aligned} \tag{2.43}$$

In the same way as the case for the (111) surface the CTR's for this surface can be described via the consideration of the contributions from the surface layers and the bulk separately. The bulk structure factor is given by:

$$F_{Bulk} = \frac{f\ DW_{Bulk}}{1 - e^{2\pi i\left(\frac{h}{2}+\frac{k}{2}+\frac{l}{2}\right)}} \tag{2.44}$$

And the scattering from the outermost three layers is:

$$F_{Surf} = f\theta_n DW_n e^{2\pi i[n\left(\frac{h}{2}+\frac{k}{2}+l\left|\frac{1}{2}+\varepsilon_n\right|\right)]} \qquad for\ n = 1,2,3 \tag{2.45}$$

Where the terms have the same meaning as for the (111) crystal. The total scattering is then given by equation (2.37).

2.3.6 Additional contributions to the scattered intensity

The calculation for the scattered intensity can be modified by one of several schemes to account for additional factors such as pronounced roughness, and the contribution to the scattering brought about by the electrolyte.

The β Factor

While multiple methods exist to modify equation ***(2.31)*** to account for pronounce surface roughness, the simplest approach was proposed by Robinson [25]. This model has a similar form to that commonly used to explain the scattering from systems with partial stacking disorder. It assumes an exponential distribution of heights where the first layer is fully occupied, followed by a second layer with a fraction of β occupied sites, then another layer with β^2 sites occupied and so on. This modifies the scattered intensity to:

$$I_{Rough} = I_{CTR}\frac{(1-\beta)^2}{1+\beta^2-2\beta\cos(\boldsymbol{q}\cdot a_3)} \qquad \textbf{(2.46)}$$

Electrolyte Contribution

CTRs can be affected by ordering in the electrolyte and thus the contributions from the electrolyte need to be included in the structure factor. In plane ordering would only be expected in the case where the electrolyte species are strongly adsorbed. The more common case is considered here, where planes of concentrated electron density are parallel to the crystal surface. Such vertical ordering is expected in electrochemical systems, but some ordering may also be expected where any smooth hard wall meets a liquid [26–28]. A structure solely ordered perpendicular to the surface plane will only affect the specular CTR (00L), as in such a measurement there is no in plane momentum transfer. Also known as extended reflectivity, measurements of the specular CTR are a direct probe of the scattering along the surface normal. To account for this, additional structure factor needs to be added to equation (2.46).

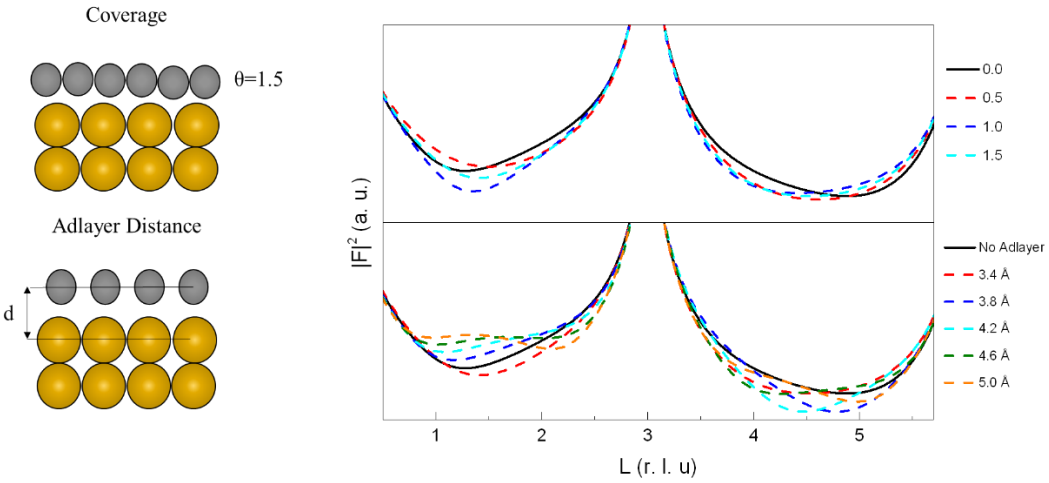

Figure 2.13: Demonstration of how the various structural parameters for a layer of adsorbed adatoms can affect the form of a specular CTR. The illustrations on the left side represent the physical meaning of the parameters being varied. The coloured lines demonstrate how a perfectly terminated Au(111) crystal is modified by changes in the adlayer. The black line shows the perfect termination of the bulk crystal with no adlayer. Unless indicated, the adlayer has a coverage θ=1, distance 3 Å from the crystal surface and a rms roughness of 0.2 Å.

The simplest case is that of the adlayer, a single atomic layer above the surface at height H_{ad} with structure factor:

$$F_{adlayer} = \theta_{ad} f_{adlayer} e^{-\frac{1}{2}(qu_{ad})^2} e^{2\pi i(H_{ad}l)} \qquad \textbf{(2.47)}$$

where θ_{ad} is the fractional coverage of the layer to the metal surface, $f_{adlayer}$ the scattering factor for the atoms in the layer, the $e^{-\frac{1}{2}\langle qu_{ad}\rangle^2}$ term accounts for disorder and $e^{2\pi i(H_{ad}l)}$ is the structure factor where the k=0 and h=0 since this is for the specular CTR only. The height is also in terms of the bulk unit cell. A comparison of how various coverages of carbon, as used in Chapter 6, affect the specular CTR is shown in Figure 2.13. Also depicted in Figure 2.13 is how the distance of such layers from the crystal affect the CTR. Changes in the layer height affect the CTR in a different manner to changes in coverage and roughness, due to its effect on the path difference of the interfering waves.

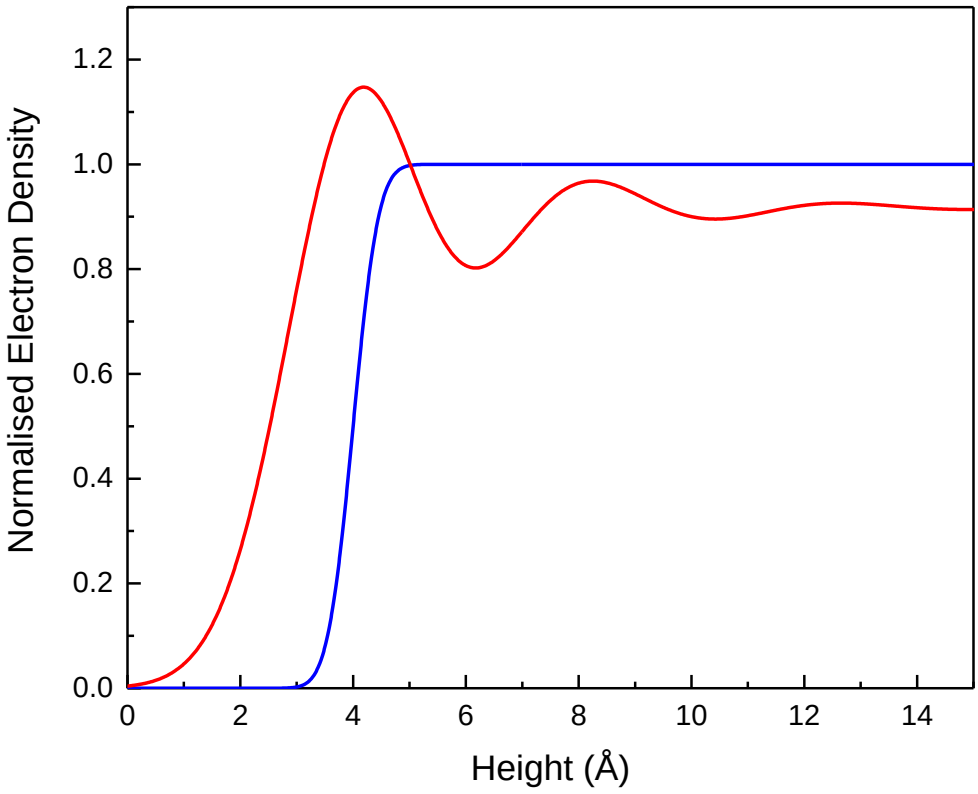

Figure 2.14: Graph showing the difference between a liquid above the surface modelled with an error function (blue line) and a liquid modelled with layers that broadens as the layers move further away from the surface (red line). The metal surface is located at height 0 Å and is not shown here. The error function is modelled with σ_0=0.5 Å, situated at a height of 4 Å. The liquid layer model has parameters σ_0=0.7 Å, σ_{bar}=0.5 Å, d=3.5 Å at a height of 4 Å.

A further matter to consider is that the discontinuity where the electron density in the electrolyte transitions towards the bulk electrolyte density affects the CTR. Figure 2.14

illustrates two ways the liquid structure at the interface can be modelled as vertical electron density plots. An error function is the most basic model shown, a smooth varying function that plateaus at the bulk liquid density. The structure factor of this function is as follows:

$$F = if\ (A_{uc}\rho)\frac{e^{-\frac{1}{2}(Q\sigma_0)^2}}{Q}e^{2\pi i(lH)} \tag{2.48}$$

Where f is the scattering factor of the liquid, ρ(=0.033Å^{-3} for water) is the density of the bulk liquid, A_{UC} is the area of the liquid unit cell, σ_0 is width of the error function and H is the height above the surface in unit cell coordinates.

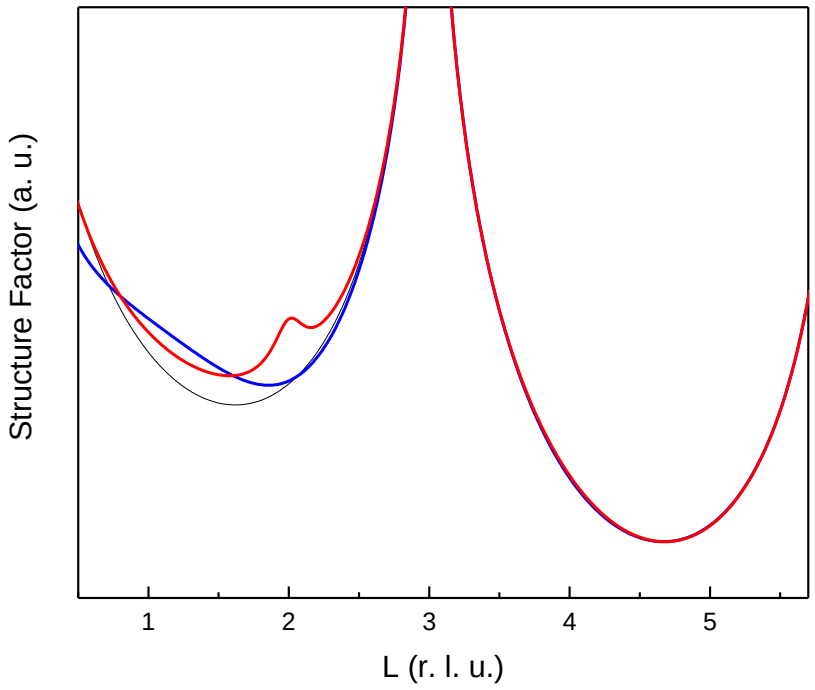

Figure 2.15: Comparison of how the various liquid models after the shape of a specular CTR compared to a perfectly terminated bulk Au(111) crystal (black line). The error function (blue line) and the layered model (red line) are modelled using the same parameters as those used in Figure 2.14

An alternative approach is for a layered water profile where the where each successive layer is broadened away from the surface following the form:

$$\sigma_j = \sqrt{\sigma_0^2 + j\sigma_{bar}^2} \tag{2.49}$$

The structure factor is thus:

$$F = if\ (A_{uc}\rho)\frac{e^{-\frac{1}{2}(Q\sigma_0)^2}}{1 - e^{-\frac{1}{2}(Q\sigma_{bar})^2}e^{iQd}}e^{2\pi i(lH)} \qquad \textbf{(2.50)}$$

Where d in this equation is the spacing between layers, σ_{bar} is the broadening term from equation (2.49). The structure factor of an error function is recovered in the case where σ_{bar} tends to 0. Figure 2.15 demonstrates how the form of a CTR is affected by these liquid components within each model. At low q the error function alters the CTR, but its contribution drops off rapidly, whereas the layered liquid model has a quasi-Bragg peak at Q=(2π/d) brought about by the layering of the liquid near the surface. For water at charged mineral surface the layered model has been found to work well[29] . However, for electrochemical interfaces with either a significant diffuse region or adsorbed species the layered model may not be appropriate. A detailed discussion of the error function and layered model along with their relative merits can be found in[30].

2.4 X-ray Voltammetry

X-ray Voltammetry (XRV) combines both cyclic voltammetry and x-ray diffraction measurements. It was shown earlier via Figure 2.9 that the diffracted CTR intensity is sensitive to certain structural properties of the electrode surface. Therefore, it is possible to form an understanding of the structural effects occurring, as well as the stable potential range of any modified surface structures. This is achieved by measurement of the reflected intensity at a fixed (*hkl*) value that is sensitive to surface relaxation or an adsorption process, for example, as a function of potential. XRV measurements are typically used to highlight interesting structural changes that are then characterised by potentiostatic CTR measurements. Macroscopic electrochemical measurements can be linked to atomic scale structural changes through comparing the XRV data with CV measurements. In experiments where structural changes such as an ordered adsorbate layer or a reconstructed surface layer with an altered symmetry compared to the bulk lattice, XRV measurement are particularly useful. In these situations, it is possible to monitor the potential window of stability of the structure in a case where the scattering can be completely isolated from the scattering of the bulk of the crystal. XRV is a key tool employed in the studies in this thesis and multiple examples will be presented in chapters 4-6.

3 Experimental Techniques

The use of electrochemistry in conjunction with *in-situ* x-ray diffraction is an established method for investigation of the electrode/electrolyte interface. Using these methods, investigations are carried out and the collected data are processed and analysed to gain information on the structure of the interface. First, section one gives details of sample preparation methods and the equipment that is utilised to carry out *in-situ* surface x-ray diffraction investigations of single crystal surfaces. Secondly, section two describes the physical process of measuring the structural changes in the electrode/electrolyte interface and the data processing and analysis methods.

3.1 Sample Preparation

Reliable and reproducible preparation of the single crystal surface is a vital stage of experimental setup as small changes in a metal electrode can impact the electrochemical behaviour of a system . The samples used in the experiments detailed in this thesis are metallic fcc single-crystals (Au), oriented to either the [111], [100] or [110] crystallographic direction. Typically, they are 10.0 mm or 6.0 mm in diameter and have a depth of 3.0 mm, with a central groove for easy mounting in the UHV environment. The Au single crystals used in this work were purchased from Matek, where they had been grown, oriented to the specific crystallographic orientation with an accuracy of at least 0.2° and polished.

The single crystal samples were initially prepared in Ultra High Vacuum (UHV) in a series of argon ion sputter and thermal annealing cycles to produce a clean surface. Argon ion sputter cycles remove impurities from the sample's surface via the bombardment of Ar ions. During anneal cycles, the sample is heated to temperatures below the surface melting temperature to recover long range ordering in the surface layers. Samples are subjected to anneal cycles either by passing current through a filament in thermal contact with the sample or, for higher temperatures, using an e^-beam heater. An e^-beam heater works by heating through electron bombardment i.e., accelerating high energy electrons into a grounded sample. Low energy electron diffraction (LEED) and x-ray photoemission spectroscopy (XPS) are used between 'sputter and anneal' cycles to assess the quality of the surface. LEED is a surface sensitive diffraction technique that entails the firing of a beam of electrons at the surface and collecting the scattered electrons on a photo-fluorescent screen. The scattered electrons produce a diffraction pattern caused by the interference of electrons on the screen. The strongly

interacting nature of electrons, which do not penetrate far into the sample, give rise to the surface sensitivity. A well-ordered surface is indicated by sharp spots on a LEED pattern. In the case of Au (111), which can reconstruct, any sharp satellite spots on the LEED pattern is a further sign of a well-ordered surface. XPS works by irradiating a sample with an x-ray beam and measuring the kinetic energy of the electrons ejected from the sample. The electron's kinetic energy (E_k) can be converted to binding energy (E_b) through the relationship:

$$E_b = E_p - (E_k + \phi)$$

where E_p is the photon energy (known in advance) and ϕ is the work function of the electron analyser. By plotting binding energy against the number of counts, several peaks are observed. These peaks correspond to the atomic (or molecular) energy levels of the sample being investigated. XPS can be used in the preparation of samples for electrochemistry to verify there are no surface contaminates.

Preparing a sample via UHV before every measurement can be impractical to do prior to every measurement, therefore other simple techniques known to give reproducible surfaces were preferred in this work. The choice of technique depends on the sample to be measured. The primary technique selected for the measurements detailed here was 'flame annealing' [31]. Flame annealing gold with a butane torch produces large flat terraces and a reconstruction that survives transfer into an electrochemical cell[6]. The gold surface is heated until it reaches a bright red colour, while being careful to not cause any melting, by constantly moving the flame on and off the sample. The sample is then cooled in an inert atmosphere, typically nitrogen or argon, and then covered with a droplet of ultra-pure water. However, if the droplet is added too soon, it will quench the sample. This is known to lead to a poor surface and gradually, the thermal shock will damage the bulk of the crystal.

3.2 Electrochemistry

In Chapter 2 the standard three electrode cell was described. However, to make in-situ X-ray measurements the design requires significant modifications. A schematic of an X-ray thin layer cell is shown in Figure 3.1comparable to that described in [32, 33]. Given the nature of the contents of the cell, a material that is inert is required. For this reason, Kel-F or Polychlorotrifluoroethylene (PCTFE) is used as it is both inert and has good machinability. The fittings used are made of similar materials such as Teflon or PEEK. The counter electrode is typically a polycrystalline wire consisting of the same material as the working electrode. For most aqueous systems Ag/AgCl reference electrodes (WPI- Leak-Free reference electrode, catalogue no. 69-0023 [LF – 2]) appear to function adequately. As mentioned in

Chapter 2 the working electrode is the single crystal sample being used in the study. This sits in a collet that tightens around the crystal as the collet is screwed into the cell. The contact for the working electrode is formed with a polycrystalline wire, coiled into a spring and passed through the base of the collet. The cell also has fittings to allow for in and out electrolyte tubing, this enables the addition/removal of electrolyte from the cell, controlled by opening taps to either an electrolyte reservoir (in) or a syringe (out). Covering the top of the cell is a polypropylene film that is transparent to x-rays and secured with an O-ring, preferably made of an inert material. The film can be 'raised/lowered' (inflated/deflated) by controlling the amount of electrolyte in the cell. The whole cell is then surrounded by an outer Kapton hood and has an overpressure of inert gas such as Nitrogen or Argon.

An alternative X-ray electrochemical cell used in this work is the droplet cell shown in Figure 3.2(a), comparable to that seen in references [34–39]. The base of the cell holding the working electrode is typically made of the same materials used in the X-ray thin layer cell mentioned previously. Rather than containing the electrolyte inside the cell with a polypropylene film, the electrolyte is fed through a crosspiece into a capillary tube that is held above the working electrode. This allows for a droplet of electrolyte to be held between the end of the capillary and the working electrode. The capillary tube and crosspiece are made of glass, quartz, polytetrafluoroethylene (PTFE) or similar materials. However, any problems in the cell, for example an air bubble inside the capillary or the crosspiece, cannot be identified while in situ if the crosspiece is made of PTFE or similar opaque materials. Therefore, care must be taken during the piecing together of the crosspiece and capillaries. The crosspiece is held in place by the aluminium top piece of the Kapton hood as shown in the Figure 3.2(b). On either side of the crosspiece is an inlet to maintain the droplet on the surface of the working electrode. The electrolyte tubing has a comparable setup to the thin layer cell, except for the addition of a Hamilton syringe with a PTFE Luer lock attached to the inlet tubing, which can be depressed to 'top up' the droplet if required. The counter electrolyte, as in the thin layer setup, is a polycrystalline wire usually comprising of the same material as the working electrode. The counter electrode is fed down to the droplet through a small hole in the top of the Kapton hood and forms a ring above the working electrode that sits inside the droplet and helps to stabilise it. The reference is slightly different compared to the thin layer setup as it has to be fed from the top of the crosspiece and down through the capillary tube. Therefore, a 'flexi-reference' is used (World Precision instruments FLEXREF-Flexible Dri-Ref Reference Electrode) to give the added length required and providing the added benefit of lowering the RC of the circuit. Thus, allowing for the measuring of current transients of the system in situ. The fittings for the crosspiece are made of Ethylene tetrafluoroethylene (ETFE).

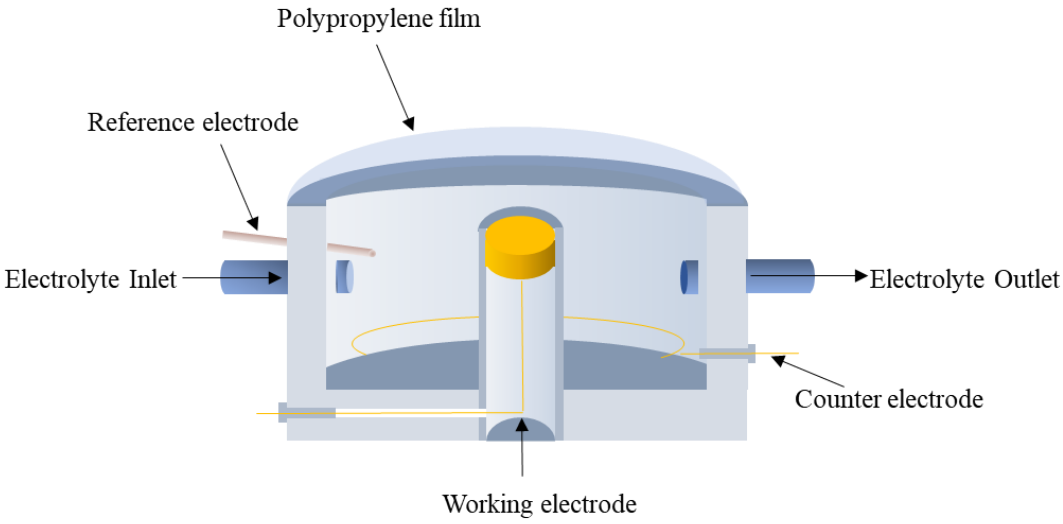

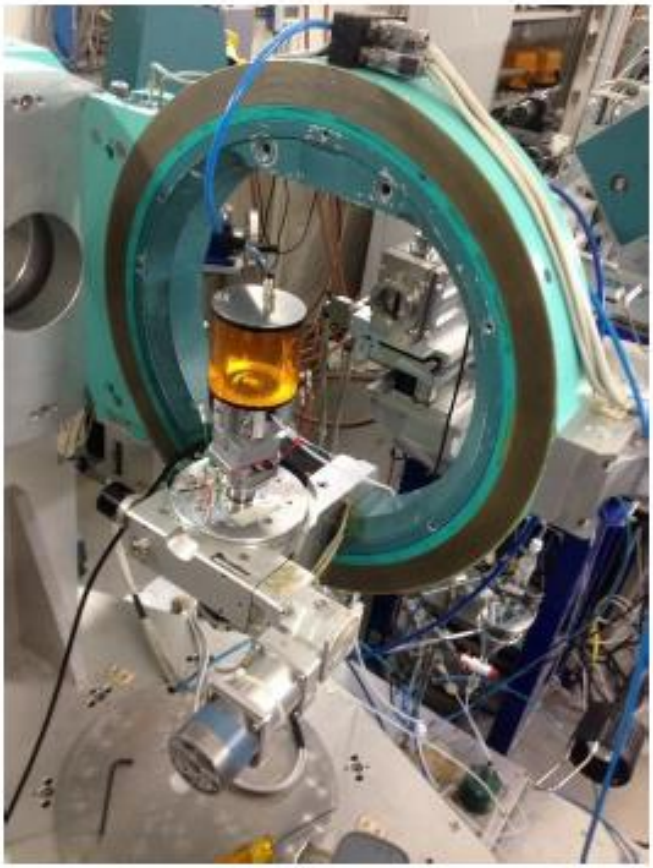

Figure 3.1(a) Illustration of the thin layer *in situ* electrochemical cell, around the cell a 'Kapton' hood is also placed. (b) Photograph of the thin layer cell on a diffractometer, around the cell is the Kapton hood that allows for the atmosphere around the electrochemical cell to be controlled.

Tubing, cell, fittings and any required glassware are soaked overnight in a 50:50 mixture of concentrated H_2SO_4 and HNO_3. They are then rinsed several times in ultrapure water (Milli-Q), with a resistivity of 18.2 MΩ·cm that has undergone several filtering and deionizing steps. Following this rinsing the parts are then boiled in fresh ultrapure water and rinsed a further 10 times. Depending on the material being used, gold in the case of the experiments in this work, any polycrystalline wires are also dipped in acid and rinsed in ultrapure water. The wires are then flame annealed, allowed to cool and then rinsed once more in ultrapure water. The polypropylene film is rinsed several times in ultrapure water, then boiled and rinsed 3 times. The single crystal working electrode is prepared following the methodology outline in the previous section and then transferred into the cell via the collet as it is covered in a droplet of ultrapure water. Once the collet has been secured the cell is topped up with electrolyte and the polypropylene film secured. After this, any trapped air in the cell is removed and the electrolyte is exchanged for fresh deaerated electrolyte. The hood is then fastened over the cell and the full setup is transferred to the beamline and fitted on a diffractometer. The thin layer setup can limit diffusion and therefore voltammetry should be carried out with the film raised to reduce these effects. Nevertheless, for the conducting of x-ray measurements the thin-film should be deflated (the thickness when deflated is ~10μm) to reduce absorption of the x-ray beam.

In the case of the droplet cell the preparation methodology is the same as the thin layer setup with the following exceptions. Once the components of the cell have been acid cleaned, rinsed and boiled, the crosspiece, capillary, reference electrode and electrolyte inlet are pieced together. The crosspiece and capillary are then filled with electrolyte and any bubbles are removed. The working electrode is mounted in the base of the cell is mounted in the methodology outlined above. The crosspiece is then mounted onto the hood and the counter electrode is fed through the top of the hood and down so that a loop of the wire sits just below the capillary. The electrolyte is then exchanged for fresh deaerated electrolyte and the hood is placed over the base of the cell so that the capillary and counter electrode sit above the working electrode. The droplet is then formed by depressing the Hamilton syringe attached to the electrolyte inlet gently. The hood is then fastened in place and the full setup is transferred to the beamline and mounted on the diffractometer.

(a)

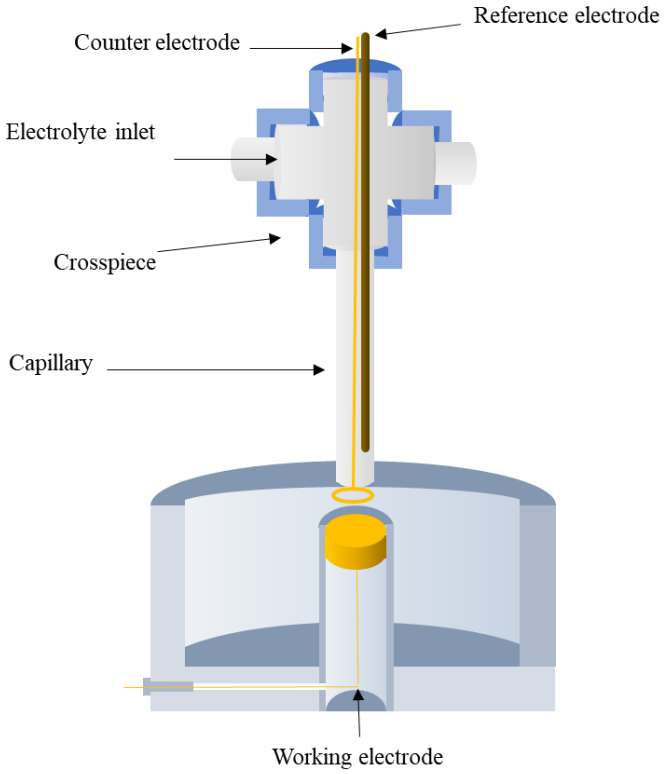

(b)

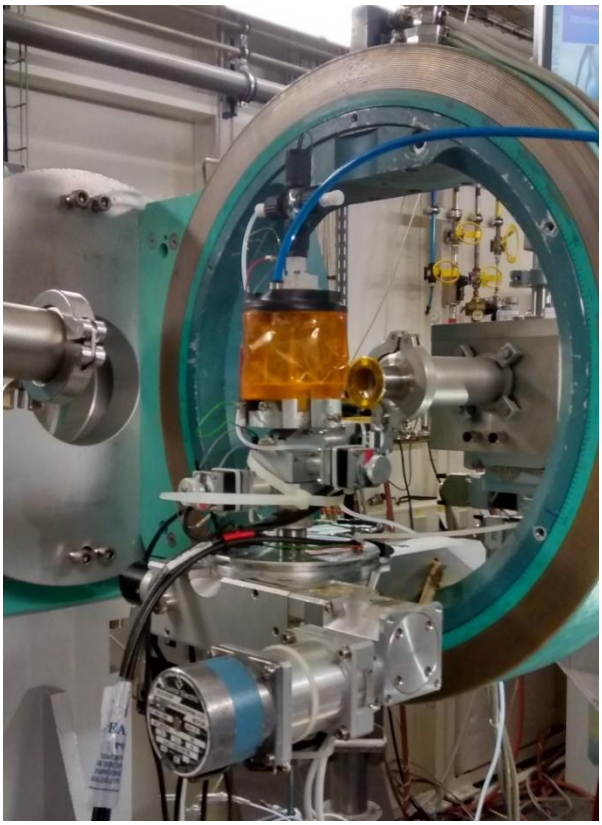

Figure 3.2(a): Illustration of the droplet in situ electrochemical cell, around the cell a 'Kapton' hood is placed that holds the crosspiece in place. (b) Photograph of the droplet cell on a diffractometer, around the cell is the Kapton hood that allows for the atmosphere around the electrochemical cell to be controlled.

3.3 Synchrotrons and Beamlines

Scattering along a crystal truncation rod is approximately 10^5 times less intense than that of the scattering from Bragg peaks. In combination with the nature of the electrochemical set up; i.e. a liquid layer on top of the working electrode sample surface, an extremely high photon flux is required. Whilst laboratory based rotating anode sources are improving, the availability of the fluxes high enough for in-situ experiments is still relatively low. Synchrotrons are a much better source of x-rays and have the added benefit of being a tuneable energy source of x-rays.

The emission of synchrotron radiation is generated by the acceleration of charged particles on a curved path through a magnetic field. The use of synchrotrons began parasitically, when scientists realised the synchrotron radiation particle physicists viewed as 'wasteful energy' could be put to good use, these were known as 1st generation synchrotrons. 2nd generation synchrotrons used bending magnets and were solely dedicated to the production of synchrotron radiation. 3rd generation synchrotrons brought about the inclusion of arrays of magnets called insertion devices, allowing for more intense and tuneable beams of light. A typical 3rd generation light source arrangement is shown in Figure 3.3.An electron beam is initially produced, in like manner to a television cathode ray tube, and then accelerated in a linear accelerator (LINAC). After this it is passed around a booster synchrotron to achieve the required energy, the electrons are then transferred into the storage ring. The storage ring consists of several straight sections and large electromagnets ("bending magnets") that curve the electron beam as it travels between straight sections. Radio frequency (RF) cavities are used to prevent the loss of energy from the electrons as the electron beam moves through the various components of the storage ring. Around the storage ring several beamlines are situated, located at either a bending magnet where synchrotron radiation is already produced or adjacent to a straight section where, to cause the electron beam to move and generate x-rays, a separate device is needed. This device is known as an insertion device and consists of two main types; undulators and wigglers. A wiggler brings about the emission of synchrotron radiation via periodic deflection of the electron beam by a series of magnets. As a result, the intensity from the wiggler is greater than that of a bending magnet as the contribution of all the magnets is additive. In contrast, an undulator provides a further enhancement in brightness by using a periodic arrangement of magnets that oscillate the beam by a small deviation such that the radiation emitted constructively interferes with subsequent oscillations.

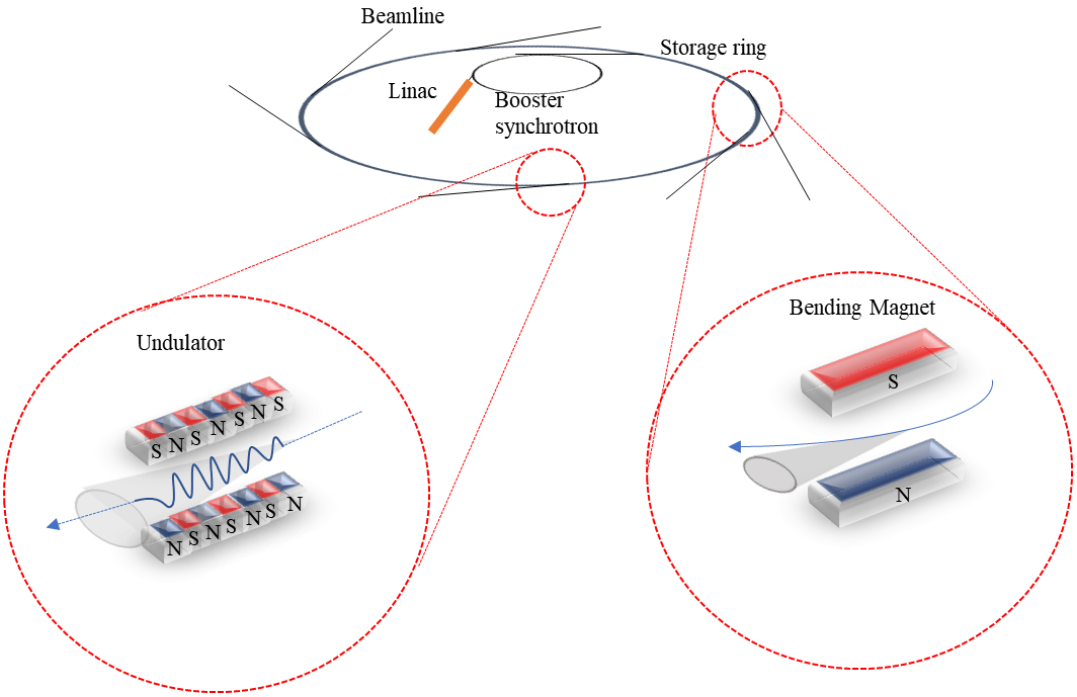

Figure 3.3: A simplified schematic of a 3rd generation synchrotron. Also shown are simplified diagrams of an undulator and a bending magnet.

The generated cone of synchrotron x-rays then enters a beamline, a typical layout can be seen in Figure 3.4. Generally, a diffraction beamline consists of three ‘hutches’: an optics hutch, an experimental hutch and a control hutch, from which the beamline is operated. For most experiments it is desirable to either select or be able to control the wavelength from the ‘white beam’ of the produced synchrotron radiation. This can be done via the use of a monochromator in the path of the beam. The monochromator needs to be a high-quality single crystal which allows for the selecting of the desired wavelength by varying the incident angle in accordance with Bragg’s law. Silicon is often the material of choice for this purpose, due to its relatively cheap cost, to produce a good defect free crystal. After passing through the monochromator, focussing lenses and mirrors are used to focus the beam towards the centre of the diffractometer in the experimental hutch. Various issues need to be considered regarding the desired properties of the incident beam before the beam reaches the diffractometer. If the feature being observed is so intense that it may damage the detector, e.g. a Bragg peak or the ‘straight through beam’, the beam can be attenuated via the use of various filters consisting of metal foils (e.g. Molybdenum, Aluminium) of varying thicknesses. As a point of reference for the measured signal, the x-ray beam passes through a ‘monitor’ to measure the number of counts in the incident beam. This monitor can take the form of either an ion chamber that the beam is transmitted through or a mylar scatter form that deflects a fraction of the beam into the monitor detector. Before incidence on the sample, adjustable slits are used to define the beam in vertical and horizontal width. For diffraction the sample is mounted at the centre of

rotation of a diffractometer allowing its movement in the beam. The diffracted beam is subsequently measured by a detector, before which further attenuators, monitors and detectors slits, can also be in place on the detector arm in order to enhance the signal to noise ratio or adjust the spectrometer resolution. Detectors can take several forms; 2D arrays such as charge coupled devices (CCDs) or a scintillation/photomultiplier tube combination. Also becoming popular are single-count solid state 2D detectors like the PILATUS range, developed at the Swiss Light Source[40] .

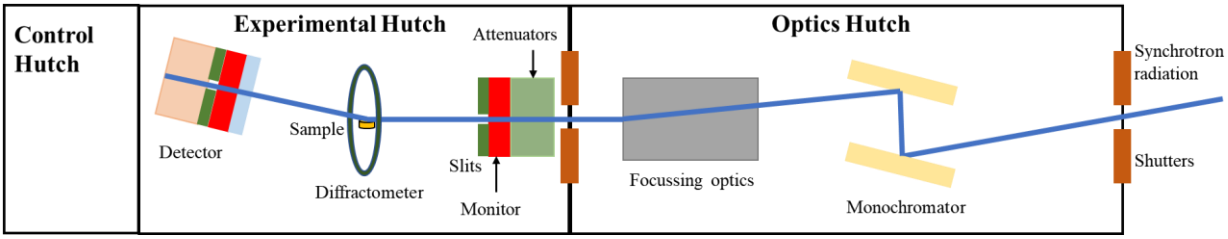

Figure 3.4: An illustration of a typical synchrotron beamline layout consisting of 3 hutches. The control hutch contains the user and computers to control operation, the sample and detector is housed inside the experimental hutch and the optics hutch is where the incident x-ray beam is prepared. The x-ray beam is shown as the blue line.

3.4 Diffractometers

For the purposes of orienting a sample to meet the Bragg condition, in principle only four degrees of freedom are needed. However, extra degrees of freedom are needed in practice to keep certain angles constant or to overcome limitations brought on by experimental apparatus blocking areas of reciprocal space. For surface diffraction there are many types of diffractometers available, some of the common diffractometers are: 4 circle[41], 2+2 circle[42], z-axis[43], 2+3 circle[44, p. 3] and 6 circle[45]. The results discussed in chapter 4 were taken at the ESRF on the ID-3 beamline using a 2+3 circle diffractometer and on the UK CRG beamline, XMaS using a 6-circle diffractometer in 4 -circle mode. Chapter 5 contains results also obtained from the XMaS beamline in 4-circle mode. The results in chapter 6 consist of data taken from I07 at Diamond Light Source (UK) and MS - X04SA: Materials Science surface diffraction at the Swiss Light Source, both of which were using a 2+3 diffractometer. Figure 3.5(a) illustrates a schematic of a 4-circle diffractometer with the various angles indicated and Figure 3.5(b) similarly displays the schematic for the 2+3 circle diffractometer and its various angles. The methodology for successful completion of synchrotron x-ray diffraction experiments follows a well-established routine. Diffractometers today are computer controlled and at all facilities specialist software for diffractometry is available. The ESRF and SLS use a UNIX based software called SPEC to drive the motors along with other parts of the beamline (slit size, energy, attenuation, electrode potential etc.)

as well as being the tool for data acquisition. On the XMaS beamline the 'fourc' version of spec can be used to operate the standard diffractometer in the four-circle geometry. DLS uses a Jython based program called the Generic Data Acquisition system (GDA) for their motor control and data acquisition. As mentioned earlier diffractometers today are controlled via computer, meaning a user can simply enter a coordinate in reciprocal space and the computer will convert this into the corresponding diffractometer angles for the respective sample and wavelength. To calculate this an orientation matrix, known as a UB matrix, is required. The description for a 4-circle diffractometer is found in[41]. This orientation matrix gives the sample orientation with respect to the diffractometer angles and can thus be used to calculate for a scattering vector Q the angles required. The U matrix is a rotation matrix that rotates the frame of reference (FOR) of the sample into the diffractometer's FOR. B transforms a reciprocal space coordinate into a real-space coordinate in the sample's FOR. Two or more reciprocal space positions (typically Bragg peaks) are required to first calculate the diffractometer angles, the procedure for which will now be described for a four-circle diffractometer.

First, it must be verified that the beam passes through the diffractometer's centre of rotation. This is achieved by placing a pin in the sample goniometer and focussing an optical telescope on the head of the pin. The φ and χ circles are each rotated 180° and the goniometer adjusted until the pin-head does not move as the circles rotate (i.e. it is in the centre). Next, burn paper is placed in the path of the beam, after which the diffractometer is translated so that the pin is in the centre of the burn mark. The χ, 2θ and θ motors should be checked to make sure they are correctly zeroed (φ is arbitrary), the sample can then be mounted on the goniometer. A laser beam is then reflected from the sample onto the wall to ensure the sample is as flat as possible. The goniometer tilts are then adjusted so that the reflected laser beam does not change position with the rotation of the φ motor. Following this the sample is then adjusted in height by scanning the z-axis motor through the incident beam and then setting the motor value to a point at which the intensity is that of half the 'straight through' beam. This ensures that the sample is in the centre of rotation of the diffractometer (at which point the x-ray beam is focussed) and that the sample is horizontal with respect to the beam. The next step is to locate two Bragg peaks to calculate a UB matrix. Locating a specular peak first can be useful due to having no dependence on φ therefore θ and χ can be optimised without the need to consider the φ position; making finding a non-specular position afterward easier. Optimisation of the motor positions is an iterative procedure where the diffractometer is rotated while measuring intensity, the diffractometer is then moved to the maximum peak intensity and then the next angle rotated and optimised. This process is then repeated until an overall maximum is reached. Once a specular position is located the computer can then make an improved calculation of the location of an off-specular Bragg peak for all rotations except for φ. As such,

to locate the Bragg peak, the φ circle must first be rotated. Once a Bragg peak has been found it can then be optimised using the procedure outlined for the specular position with the inclusion of the φ motor and then this position used for calculation of the UB matrix. This should then be repeated for another reflection. However, care should be taken when labelling Bragg peaks so that the sense of the φ rotation is correct, i.e. φ rotates in the correct direction from one reflection to another. If this is not the case, the reflection should be labelled as a symmetry equivalent.

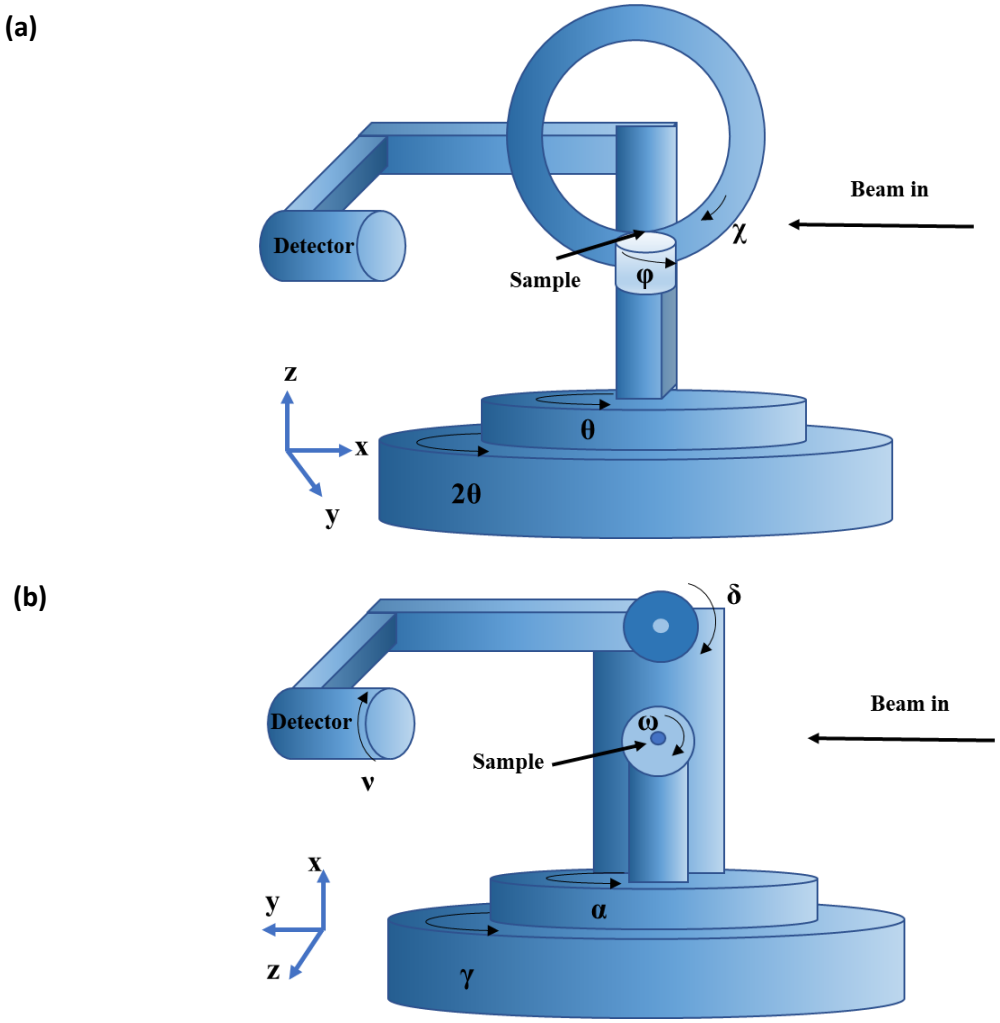

Figure 3.5 (a): Diagram of a 4-circle diffractometer used to orient samples to meet various diffractions conditions. Indicated are the laboratory frame of reference and sense of rotations. A full description can be found in reference[41]. (b): Diagram of a 2+3 circle diffractometer in vertical mode. Indicated are the laboratory frame of reference and sense of rotations. A full description can be found in reference[44].

3.5 Data Acquisition and Extraction

Several types of scan can be carried out to take crystal truncation rod measurements or fractional rod measurements (brought about by surface reconstruction). Those used in this work are detailed below:

3.5.1 Rocking Scans

Rocking scans are one of the most common x-ray measurements used. This type of scan is carried out by initially setting the sample and detector to a reciprocal space position along a CTR, meeting the Bragg condition in 2 of the 3 directions. One of the motors is then moved to rotate the sample and the scattered intensity is measured with the detector position fixed in place. Adjusting the position along the rod and repeating this measurement allows for the CTR profile to be obtained via the integrated area. A rocking scan's width is a convolution of the instrumental resolution and an intrinsic width of the crystal, brought about by defects such as sample mosaicity and dislocations. Significant mosaic spread would give rise to a broader peak due to the Bragg condition being met for a range of angles. To enable good determination of the background signal, the crystal needs to be rocked over a sufficient angle.

The integrated intensity, i.e. the area under the peak, is directly proportional to the structure factor. The integrated area can be calculated in several ways. In general, this is accomplished by fitting a line-shape and analytically calculating the area. The typical line-shape to use is a Lorentzian. An example rocking scan is shown in Figure 3.6 with a Lorentzian line-shape fitted to it with an additional straight-line background. There is an associated counting error, $\sqrt{n}$ (where n is the signal and $\sqrt{n}$ is the error according to Poisson statistics), with every data point and this is combined with the counting error on the monitor. Defining a Lorentzian function as:

$$L(x) = \frac{hw^2}{w^2 + 4(x-c)^2}$$

where h is the height, w is the full width half maximum (FWHM) and c the peak centre, then the area under the peak simply will be $\frac{1}{2}\pi hw$. An alternative approach is to numerically integrate the area under the peak, using a numerical procedure such as the Simpson's rule. If the peak is non-standard, this approach would give a more accurate determination of the area however meaningful determination of the errors is difficult. The integrated intensities typically have a counting error around 1-3%. Nevertheless, there is a systematic error, determined from comparing symmetry equivalent reflections, that must also be included of around 5-10%.

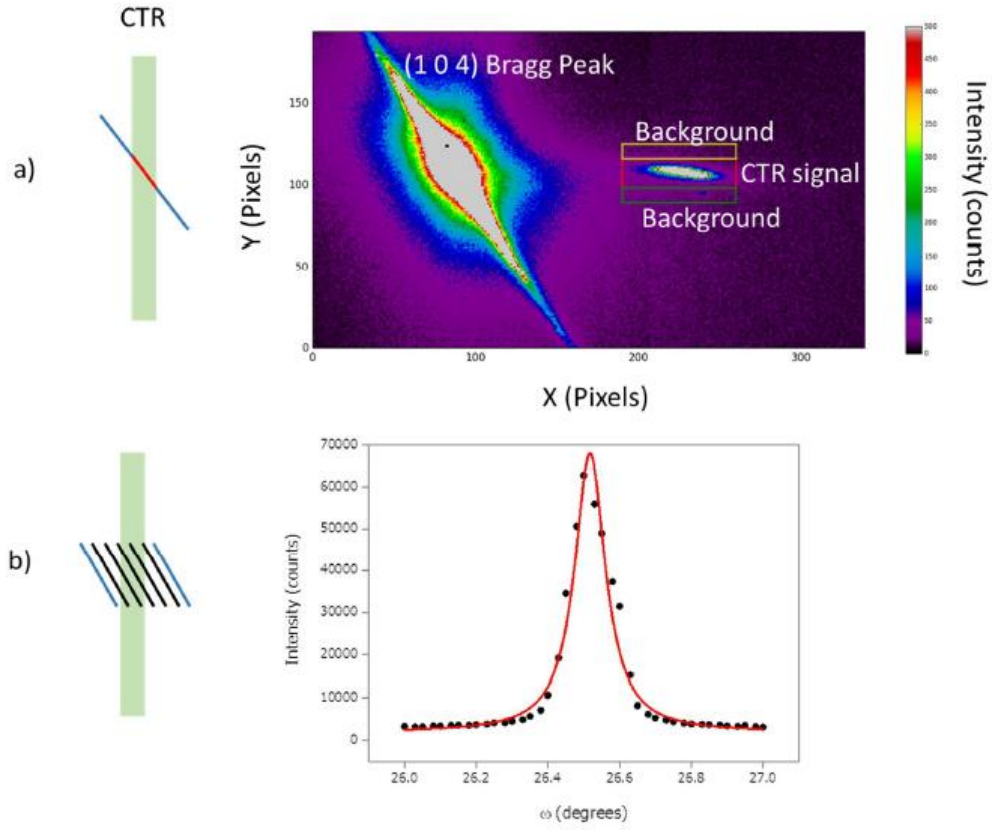

Figure 3.6: Demonstration of the difference between a 2D stationary scan and a rocking scan reproduced with permission from[46] . Both measurements were made on the same system at (1 0 3.7), a position close to the Bragg peak. More information can be found in [47]. (a) 2D detector image measured through the (1 0 L) CTR. The sum of the intensity in the 'CTR signal' ROI minus the sum of the intensity in the two background regions is proportional to the structure factor. The (1 0 4) Bragg peak is also visible. (b) Rocking scan for which the sample is rotated around an angle, ω, therefore scanning the detector resolution function over the CTR. The area of the peak is proportional to the structure factor. Each point has an error √n.

3.5.2 Stationary Scans

Stationary scans offer an alternative to angular rocking scans by using an area detector to integrate the entire width of the CTR at once, an example of this measurement is shown in Figure 3.6(a) reproduced with permission from [46]. There are several advantages in this approach; decreased collection time, increased counting statistics and improved background detection. Peak asymmetries and unwanted contributions to the signal are also easier to recognise.

The most straightforward way of extracting the intensity of the CTR is by choosing a region of interest (ROI) that contains the signal and sums the counts in each pixel. A region representative of the background is chosen and then subtracted from the signal. However, this

method is not without its difficulties, if for example the sample has a significant mosaicity the integrated intensity in this scanning mode will not reflect this, whereas a rocking scan would. Furthermore, this method comes with an increased complexity of data analysis, even when using ROIs. In addition, fitting a 2D Lorentzian would possibly be more appropriate as the use of ROIs alone may not be the most accurate method of extracting intensities. Each pixel on the detector technically has a different reciprocal space coordinate that should be accounted for.

3.5.3 Reciprocal Space Scan

In a reciprocal space scan, the diffractometer scans along a plane in reciprocal space, normally at a fixed Q_Z or *l value* in *hkl* reciprocal space. With this type of scan structures with a different periodicity can be investigated, e.g. surface reconstruction. This type of scan is used throughout chapter 4.

3.6 Data Analysis

3.6.1 Correction Factors

Depending on the diffractometer angles, there are several factors relating to the beam and the sample that affect the measured integrated intensities. For an x-ray beam of incidence β_{in} and the diffracted beam exiting the sample at angle β_{out}, the correction factors for both the 4-circle (Figure 3.5 (a)) and 2+3 circle (Figure 3.5 (b)) geometries, using their associated motor angles, are given below:

The Lorentz Factor

This factor corrects for the fact that rocking scan intensity is integrated not in reciprocal space but in angular space. For a 4-circle diffractometer it is simply:

$$\boldsymbol{L = \frac{1}{\sin 2\theta}}$$

L for a 2+3 circle diffractometer is given by:

$$\boldsymbol{L = \frac{1}{\sin \theta \cos \gamma}}$$

Rod Interception

The angle that the detector makes with the rod is accounted for by rod interception. The area of interception of a plane cutting a rod at 90° will be that of a circle, at any other angle it will be that of an ellipse. The correction factor for both geometries will be:

$$\boldsymbol{R = \cos \beta_{out}}$$

Active Area Correction

This accounts for the overlap of both the beam footprint and the detector footprint on the sample. This correction depends on beam defining slits, detector slits and sample geometry, it is best calculated numerically as in [48]. Ignoring the footprint and sample size, the active sample area for a 2+3 diffractometer is:

$$\boldsymbol{A = \frac{\cos \beta_{out}}{\sin \delta}}$$

The integrated intensities are converted to structure factors via division by these factors.

3.6.2 Non-Linear Least Squares Fitting

Having obtained structure factors, the model outlined in chapter 2 is fit to the data using a non-linear least squares method in which structural parameters such as the surface atomic layer expansion (ε), relative surface occupations (θ) and the surface roughness (σ) can be used as variables. The parameters defining the model are varied to minimise a χ^2 value given by:

$$\boldsymbol{\chi^2 = \sum \frac{(M - T)^2}{\sigma^2}}$$

Where M and T are the measured and theoretical values respectively and σ^2 is the variance of the data. The reduced χ^2 is calculated by division of the number of degrees of freedom i.e. the number of values – number of parameters -1.

4 The Au(*hkl*) Surface Reconstructions and the Effect of CO on the Surface/Electrolyte interface

4.1 Introduction

Gold surfaces represent key model systems for the understanding of general surface processes such as surface reconstruction, adsorption and electrocatalytic reactions. At room temperature, the low index surfaces of Au single crystals all exhibit a reconstruction of the surface layer, adopting a different symmetry to the underlying bulk crystal. As the surface atoms are exposed to a different environment to that of the bulk, surface reconstruction occurs in an effort to minimise the surface energy. In recent decades, the discovery of the enhanced catalytic activity towards the oxidation of carbon monoxide of gold nanoparticles on oxide supports reported by Haruta and co-workers[7, 49] has stimulated renewed interest into the surfaces of Au for both heterogeneous catalysis and electrocatalysis applications. Considerable attention has been directed towards the surface reconstructions of Au in the electrochemical environment due to the ability to control the surface atomic structure via the applied electrode potential. Recently work by Rodriguez, Koper and co-workers has revealed a rather surprising promoting effect of adsorbed carbon monoxide on the electrooxidation of alcohols by gold catalysis. In a series of papers describing the enhanced electrocatalytic properties[8, 50–53], it was shown that the enhancement effect only occurs on the Au surfaces that exhibit hexagonal reconstruction, i.e., Au(111) and Au(100).

The experiments outlined in this chapter were part of a detailed SXS study[54][1]of the structural changes that occur at the interface between the Au(111) Au(100), and Au(110) electrodes and 0.1 M KOH electrolyte. The aim of the experiments was to explore the dependence of the Au surface reconstructions on the applied electrode potential, in particular at the high negative potentials achievable due to the high pH in alkaline solutions. In addition, the effect of the presence of CO in solution on the potential dependent behaviour of the low index surface reconstructions is explored.

[1] J. J. Fogg's contributions to the work are as follows. Measurement and analysis of the data taken at ID-03 on the Au(111) crystal, measurement and 50% analysis of the data measured at the Xmas beamline on the Au(100) crystal. Measurement of the data taken on the Au(110) crystal at I-07.

4.1.1 The Au(*hkl*) Surface Reconstructions

The clean, low index surfaces of gold have been shown to reconstruct under certain conditions of sample temperature and surface preparation in the UHV environment. For the Au(111) and Au(001) surfaces this leads to the formation of a surface layer with a higher density than the underlying bulk crystal. In contrast the Au(110) surface reconstruction has a density of the order of 50% less than the underlying bulk crystal. These reconstructions all survive the transfer into the electrolyte and the nature of the surface layer, be it reconstructed or unreconstructed, can then be controlled by applying electrical potential across the electrode/electrolyte interface. The right side of Figure 4.1 illustrates the bulk terminated (1 x1) surface structures for the three low index surface orientations. The left side shows a simplified schematic representation of the reconstructed surfaces.

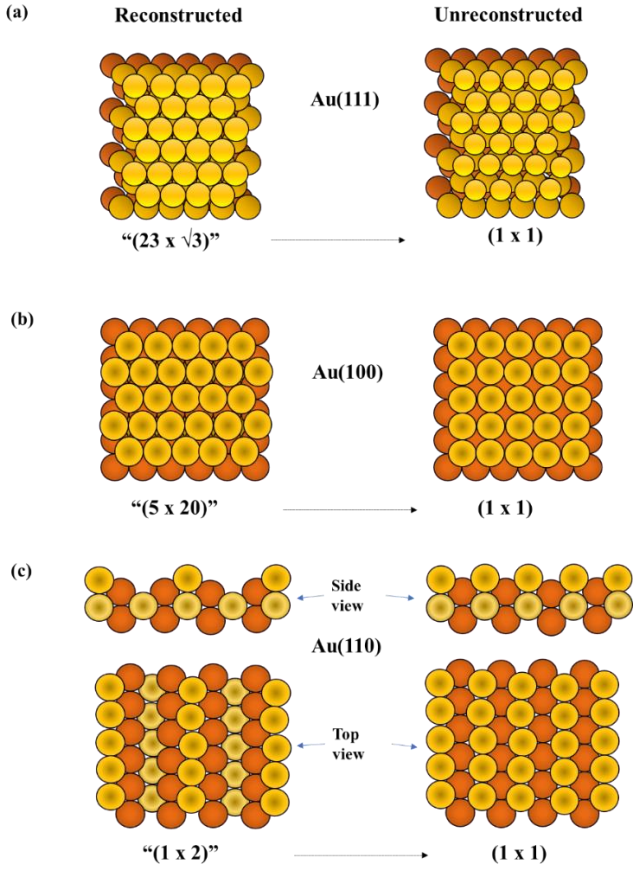

Figure 4.1: Simplified real space models for left: reconstructed; right: the bulk terminated low-index surfaces of gold. (a) Au(111)- (23 x√ 3)↔ Au(111)-(1 x 1); (b) Au(100)-(5x20) ↔Au(100)-(1 x 1) and (c) Au(110)-(1 x 2) ↔Au(110)-(1 x 1).

Au(111)-(p x √3) Surface Reconstruction

The Au(111) reconstructed surface has been intensively studied in UHV[55–57], SXS[58, 59] as well as in the electrochemical environment[60, 61]. When reconstructed, the Au(111) surface undergoes a distortion in the surface stacking from an ABC to an ABA stacking

sequence in the centre of the unit cell leading to stripes that can be seen using techniques such as STM and thus is often called the 'striped' phase or 'herringbone' reconstruction. This distortion leads to an increase in surface density that corresponds with a uniaxial compression where p+1 surface atoms sit in place of p, a compression of (p+1)/p-1=1/p (~4.5%for p=22). This (p x √3) reconstruction produces a well-defined diffraction pattern that is characterised by a hexagon of additional diffraction spots, in the surface plane of reciprocal space, around the scattering that occurs for the bulk Au(111) crystal [58, 60]. Figure 4.2 (a) shows an illustration of the in-plane diffraction pattern from the reconstructed Au(111) surface, the solid circles represent the diffraction from the underlying hexagonal lattice with the surrounding symbols originating from the (p x √3) reconstructed phase. Figure 4.2 (b) shows a 'zoomed in' map of the scattering that occurs in reciprocal space around (0, 1, *l*) plane.

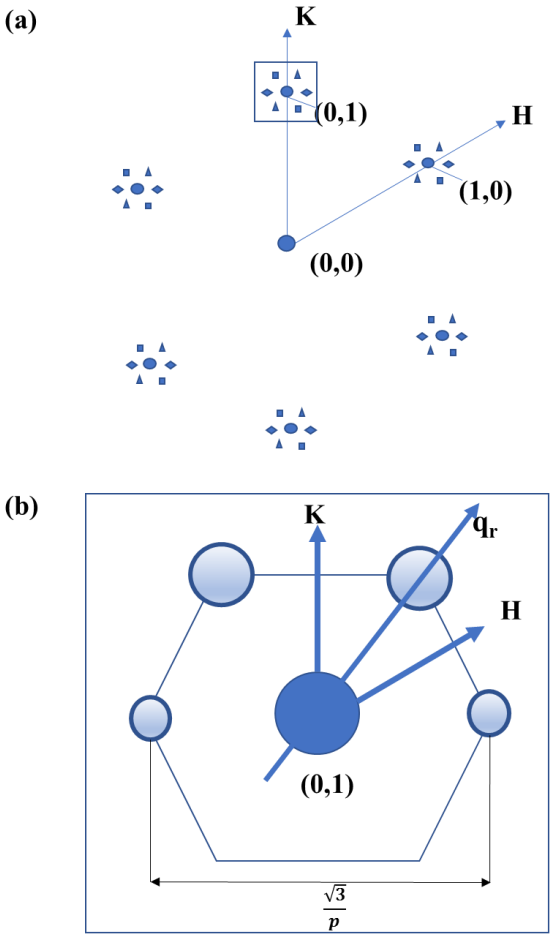

Figure 4.2 (a): In plane diffraction pattern from the Au(111) surface. Solid circles represent diffraction from the underlying hexagonal lattice. The symbols surrounding it originate from the (p x √3) reconstructed phase with three equivalent rotated domains (squares, triangles and rhombus'). (b) : 'Zoomed in' Schematic of the scattering in the surface plane around the (0,1, *l*) CTR (solid blue circle) , around the CTR are the peaks that arise due to the (p x √3) reconstruction (faded blue symbols) and the direction q_r of the example scan made in of Figure 4.7.

Au(100)-(5 x 20) Surface Reconstruction

The Au(100) surface also exhibits a hexagonal reconstruction despite its underlying cubic symmetry. Often referred to as either a (5 x 20) or 'hex' reconstruction, the surface layer is buckled and slightly distorted and the hexagonal structure is aligned close to the [110] bulk direction[55, 62]. The 'hex' surface has an atomic density that is ≳ 20% of the bulk terminated (1 x 1) surface. The Au(100)-hex reconstruction forms two symmetry-equivalent domains that are rotated by 90° with respect to each other, closely aligned to the underlying bulk lattice. The principle diffraction peak for one of these domains is observed at the (1+δ, 1+δ, 0) in-plane position, where δ~0.2. This defines the in-plane lattice constant of the hexagonal overlayer and corresponds to the layer's incommensurability[63]. The reconstructed Au(100) surface structure has been extensively studied in UHV[63–65], STM[66–69], by electrochemical methods[61, 70] and in-situ SXS[60, 71]. Figure 4.3 shows the corresponding diffraction pattern due to the reconstructed hex phase in terms of the bulk fcc unit cell notation. The solid black circles and lines represent the scattering from the Au(100) bulk lattice, with the hex domains being represented by the blue squares and lines.

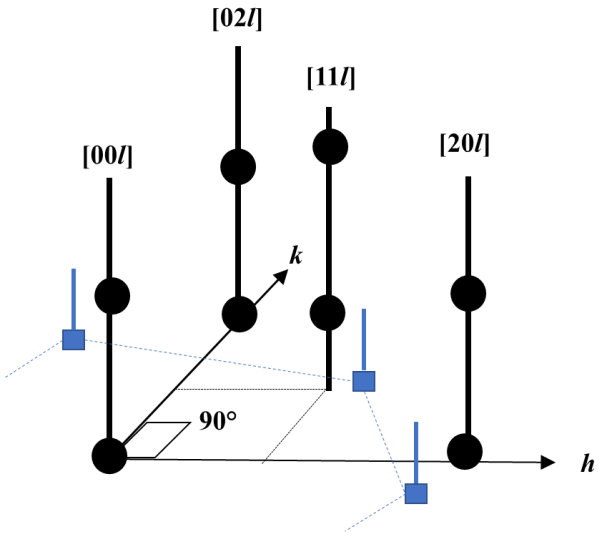

Figure 4.3: Schematic representation of the x-ray scattering from the '*hex*' surface. Solid circles represent the position of the Bragg peaks along the bulk CTR's. Blue squares and lines represent the positions of the 'surface rods' due to the (hex) phase.

Au(110)-(1 x p) Surface Reconstruction

The Au(110) surface in the electrochemical environment undergoes a potential dependant transition from the unreconstructed (1 x 1) surface structure to what is known as the 'missing row' (1 x 2) or (1 x 3) reconstruction in the negative potential region[72, 73]. UHV studies[74, 75] have shown that the missing row reconstruction, named as such due to alternate rows of gold atoms being absent, can consist of higher order (1 x *n*) domains. Figure 4.4 shows the

'side' and 'top' views for the basic models of (a) the (1 x 1) phase, (b) the (1 x 2) surface reconstruction and (c) the (1 x 3) surface reconstruction. The lower sections of the figures show the corresponding diffraction patterns in terms of the surface cell unit notation (**a** = **c** = 4.078 Å, **b** = 2.884 Å and $\alpha = \beta = \gamma = 90°$).

The Au(110) surface reconstruction has been extensively studied by a combination of electrochemistry and surface science techniques, including STM[73, 76, 77]and *in-situ* SXS[72]. In the electrochemical environment, the nature of the dominating reconstructed domains is dependent upon the composition of the supporting electrolyte. Furthermore, the Au(110) crystal surface is intrinsically complex due to the inhomogeneous nature of the missing row reconstruction. Indeed, in-situ STM studies[67] showed that in acidic solution the surface can be inherently stepped. This is due to reconstructed (1 x *n*) domains, of which n can equal 2,3 or higher, are able to coexist on the surface. Via in-situ SXS measurements[72] it was revealed that, in salt solution, only (1 x 3) domains of the Au(110) surface reconstruction can exist. Conversely in acidic media, a poorly correlated intermediate phase between the (1 x 2) and (1 x 3) reconstruction was observed.

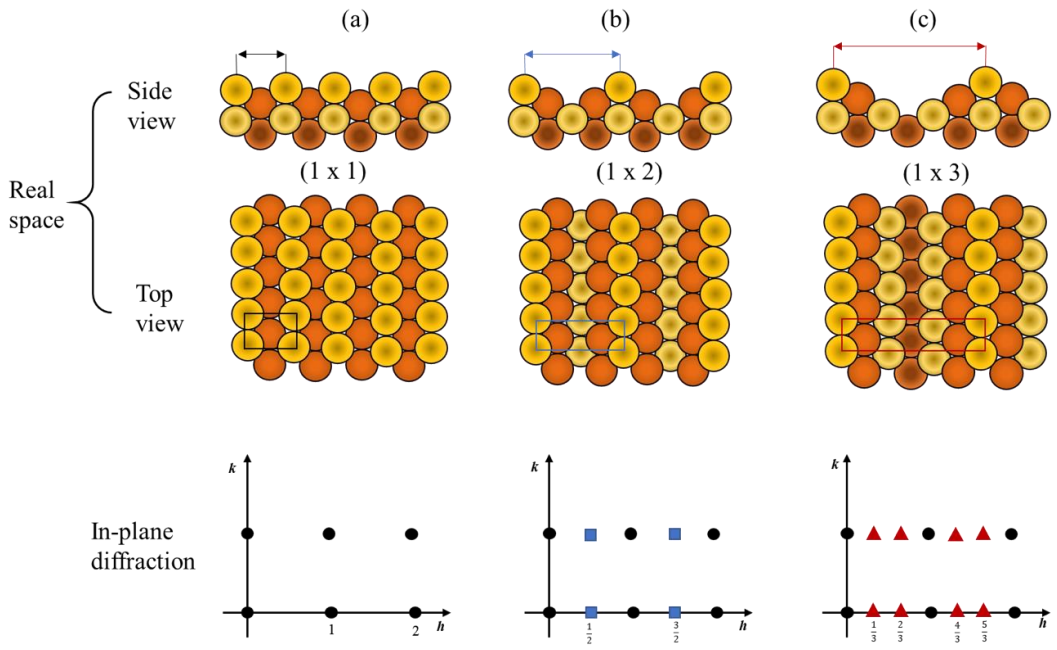

Figure 4.4: Illustrations of the 'side' and 'top' views with the corresponding in-plane scattering geometry for (a) the (1 x 1) surface of Au(110); (b) the (1 x 2) 'missing row' surface reconstruction and (c) the (1 x 3) reconstruction. The filled circles on the in-plane diffraction correspond to scattering from the substrate structure. The solid squares and triangles correspond to the scattering from the reconstructed surface. For example, the appearance of a diffraction peak at (5/3, 0, 0.6).

4.2 Experimental

The experimental procedure that follows is outlined in chapter 3 and other studies such as references[34–39]. The electrolyte used for these experiments was 0.1M KOH (99.995% purity) solution, the counter electrode consisted of 0.5mm polycrystalline gold wire (99.999% purity). For the experiments conducted on the Au(111) surface, the droplet cell was used. The reference electrode was Ag/AgCl (World Precision instruments FLEXREF-Flexible Dri-Ref Reference Electrode). X-ray measurements were performed on the beam line ID-03 at the ESRF, Grenoble using focussed incident X-rays at an energy of 25keV. During the experiment and the experiments carried out on the Au(100) and Au(110) electrode surface, the 'hood' of the x-ray cell was constantly purged with nitrogen to protect the surfaces from oxygen.

X-ray measurements conducted on the Au(100) surface were carried out using the thin layer x-ray cell at BM28 (XMaS), the UK-CRG beamline at the ESRF, Grenoble using focussed incident x-rays at an energy of 11.8 keV. The reference electrode used was Ag/AgCl (WPI-Leak-Free reference electrode, catalogue no. 69-0023 [LF – 2]). For the CO studies the electrolyte was saturated with CO and the CO saturated electrolyte was pulled through the electrochemical cell with the potential held at -1 V for the experiments on CO adsorption. The electrolytes investigated were 0.1 M KOH solution, and 0.01 M KH_2PO_4 + 0.01 M K_2HPO_4solution. For both the Au(111) and Au(100) systems, prior to each experiment the potential was cycled between -1.0 V and -0.1V (at 50mV/s) for 30-60 minutes and then held at -1.0 V. This was to ensure reproducible surface preparation ('surface conditioning') in each case[59].

X-ray measurements on the Au(110) crystal surface were carried out at the I-07 beamline at the Diamond Light Source, Didcot, UK using focussed energy of 18 keV. The Au(110) crystal was prepared in UHV via sputtering and annealing cycles as described in 3.2. The crystal surface was then observed in LEED to be reconstructed in the (1 x 2) domain as shown in Figure 4.5. The crystal was then transferred into the thin layer x-ray cell.

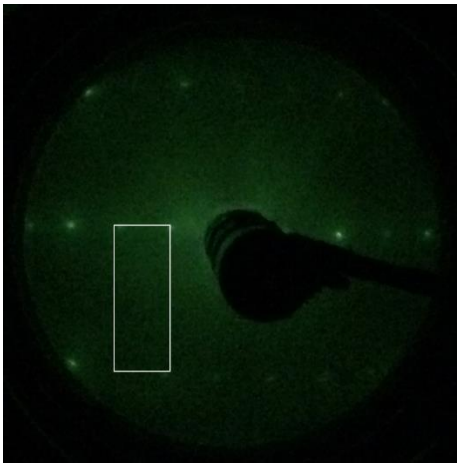

Figure 4.5: LEED measurement of the Au(110) electrode surface at an electron beam energy of 150 eV. The white rectangle highlights the (1 x 2) reconstructed phase of the Au(110) surface following sputter-anneal cycles in the UHV environment.

4.3 0.1M KOH

4.3.1 Au(111)

The Au(111) surface was first investigated in 0.1 M KOH solution. Utilising the Maxipix 2D detectors, a series of continuous acquisition theta scans along the *l*=0.5 plane around the (0, 1, L) CTR were measured at a range of potentials starting from -0.7 V stepping positively to 0.05 V. The measured scans were then binned using the BINoculars software[78] and then combined to form an image of the reconstruction with pixels coordinated to the corresponding (*h, k*) value. Following the processing of the scans in BINoculars, the binned images had to undergo an extra layer of processing as BINoculars software places the (*h, k*) axes orthogonal to each other. By using an image shear transformation, the (*h, k*) axes were adjusted to have 60° separation, the resulting output is shown in Figure 4.6(a). The central reflection is the resulting scattering from the (0 1 0.3) reflection, the surrounding reflections highlighted by a white circle arise from the scattering due to the three rotated domains of the reconstructed surface layer like that shown in the schematic of the reconstruction in Figure 4.2(b).The information was then extracted from each image by measuring a series of regions of interest (ROI's) along a set path, as displayed by the solid white rectangle in Figure 4.6 (b), and integrating the intensity of each ROI. The resulting output is akin to that of a reciprocal space scan. The extracted profiles were then fit to a double Lorentzian lineshape, shown in Figure 4.7, thus, enabling both the values of the correlation length, ζ, and the stripe separation, p, for each point of the reconstruction to be obtained. The Lorentzian line shape originates from a 1D real space atomic model where ζ decays exponentially with a length $\zeta=a/(2\pi\sigma)$, where σ is the full width half maximum (FWHM) of the peak in units of H. The correlation length measures the distance that the atoms in the reconstructed surface layer are positionally

correlated. *p* is given by p=1/(2ΔH) in these units, where ΔH is the separation from the CTR position to the position of the peak due to the reconstruction, projected along the H reciprocal space direction [58]. Thus, p is the stripe separation in terms of the lattice constant a, where the real space distance is thus L=pa. It is worth noting however, that the line shape can be affected by mosaic effects on the substrate that have both a Gaussian component and an asymmetry brought about by a distribution of domains with a range of p values. The Lorentzian model does not account for these effects, nevertheless, from the analysis the essential structural information can be obtained.

It is worth commenting here on the apparent stepped background visible on the images in Figure 4.6 (a) and (b). This became apparent after the processing of the images using BINoculars and arises from a slight overlap in the continuous acquisition scans. As can be seen in the figure, several of the reflections brought about by the Au(111) surface reconstruction lie on these overlaps. Nevertheless, the essential information of the peaks could be extracted by subtracting the background from the most positive scan and thus removing the stepped background. However, despite the reconstruction still being visible on the in-plane images, it was impossible to distinguish the reflections from the background at potentials positive of -0.2 V.

Figure 4.6 (c)-(f) shows the intensities and p-value as a function of the applied potential for each of the rotated domains from the reconstruction. Comparing the intensities, the reflections at points 1 and 2; 3 and 4 respectively follow similar trends. The lower intensity at the symmetry equivalent reflections, 1 and 2, is also visible just from inspection of the contour map in Figure 4.6 (a). For each domain an almost identical potential dependent compression of the surface is shown with p varying between 27 and 22.5. This corresponds to a change in the near neighbour spacing, a_{NN}, between 2.78 Å and 2.76 Å in the p direction of the reconstruction as the reconstruction is uniaxially incommensurate. Discrepancies in the values obtained for each domain may have arisen from systematic errors introduced in the processing of the acquisition scans and the extraction of the data from the images to create the linescans.

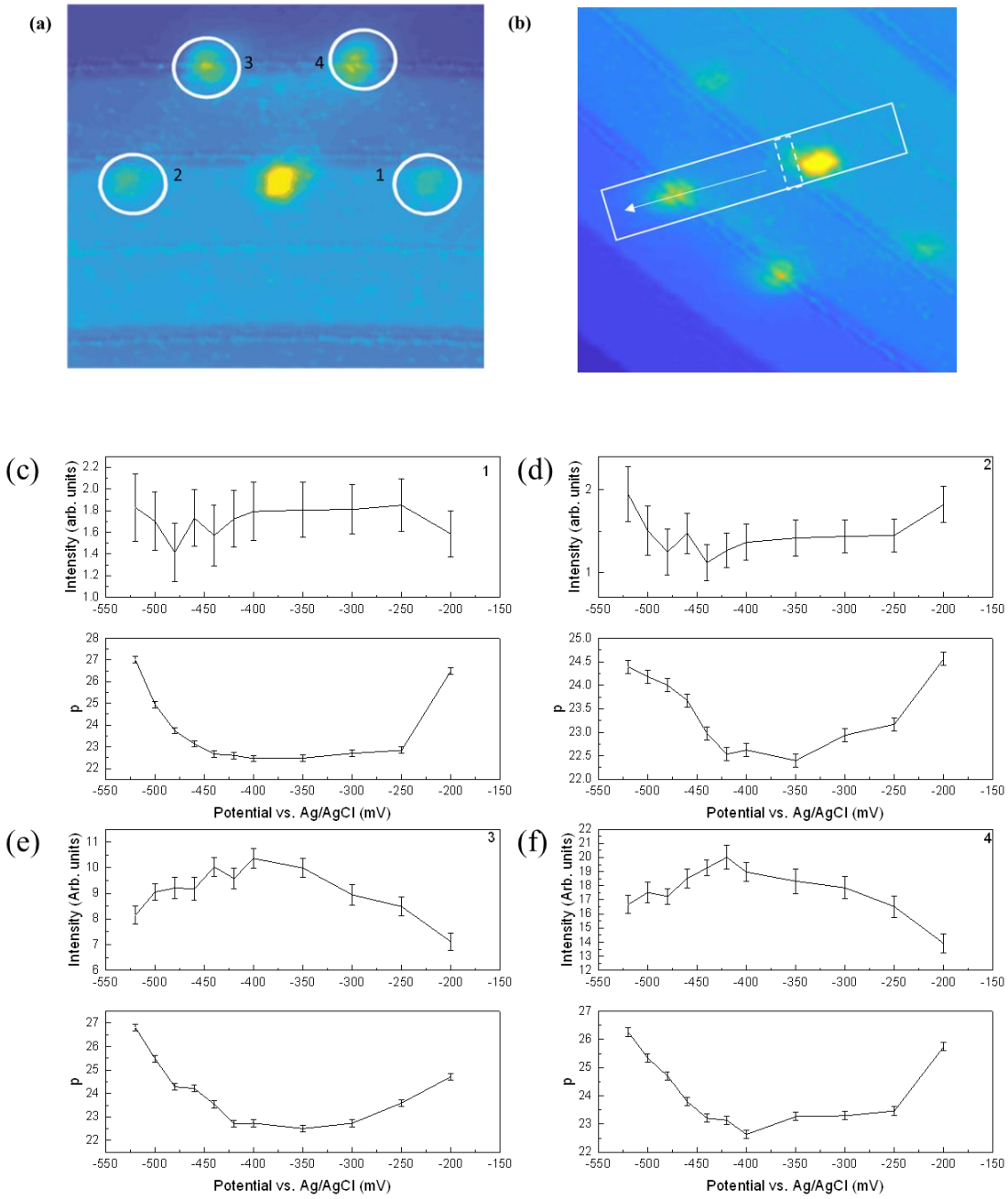

Figure 4.6: (a)BINoculars processed image of the measured x-ray intensity in the l=0.5 plane around the (0, 1, *l*) CTR. Each of the reflections brought about by the reconstruction are outlined by a white circle and correspond to reflections from the 3 rotated domains of the reconstruction. The numbers next to each reflection is to allow for ease of reference. (b) BINoculars processed image of the measured x-ray intensity in the *l*=0.5 plane around the (0,1,*l*) CTR. The white rectangle with solid lines represents an example of the area over which the block integrals were measured. The dotted white rectangle represents an example ROI used in the extraction of the line-shape. (c) Integrated intensity(top) and p-value (bottom) versus potential for the reflection labelled as "1". (d) Integrated intensity(top) and p-value (bottom) versus potential for the reflection labelled as "2". (e) Integrated intensity(top) and p-value (bottom) versus potential for the reflection labelled as "3". (f) Integrated intensity(top) and p-value (bottom) versus potential for the reflection labelled as "4".

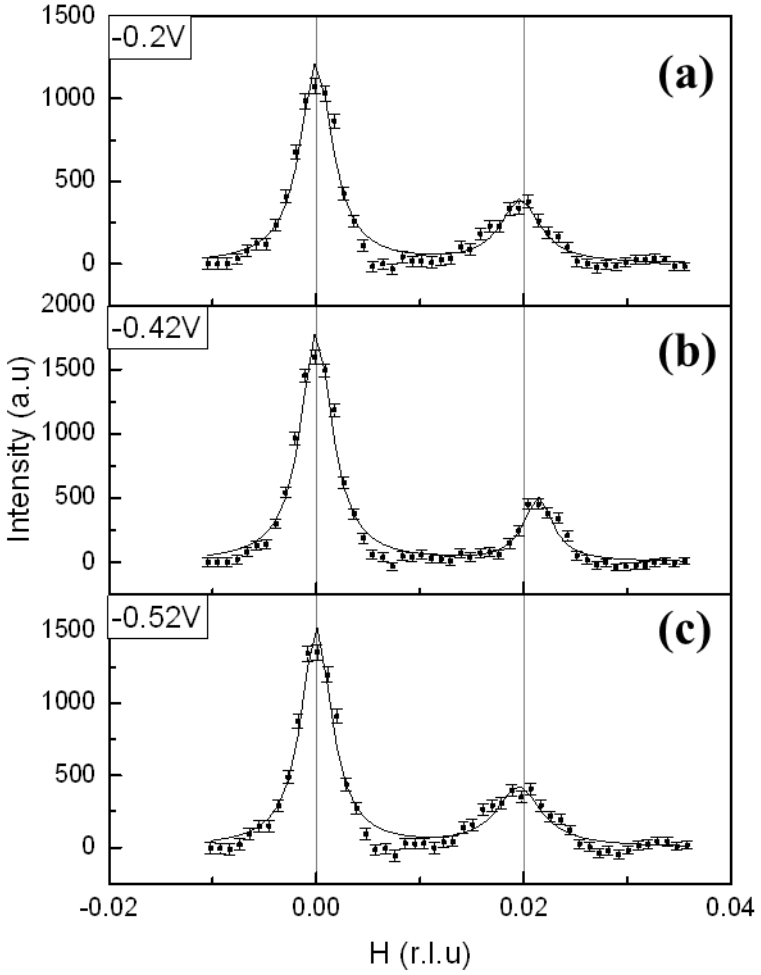

Figure 4.7: Extracted line-profiles of the in-plane diffraction from the reconstructed Au(111) electrode surface in 0.1M KOH, measured along the [0, 1, 0] direction through the (0, 1, 0.3) CTR position at (a) -0.2 V (b) -0.42 V (c) -0.52 V (vs. Ag/AgCl). The data is fitted with a double Lorentzian lineshape (solid line). The solid vertical lines indicate the peak positions for the CTR and the reflection brought about by the reconstruction. It is worth noting here that the stepped background visible in Figure 4.6(a) has been removed manually prior to the fitting of the double Lorentzian profiles.

The potential dependent in-plane compression of the Au(111) reconstructed surface layer can be seen in the in-plane x-ray diffraction through the (0, 1, 0.3) CTR position and the reflection labelled as 'point 3' in Figure 4.6 at (a) -0.2 V, (b) -0.42 V and (c) -0.52 V. A movie depicting the in-plane surface compression can also be found in the supplementary materials of [54]. The results detailed here can be compared to results obtained from a previous experiment measured by Yvonne Gründer shown in Figure 4.8. These results were obtained at beamline 7-2 at SSRL, Stanford. Following the same surface conditioning outlined here, a series of reciprocal space scans in the [1, 0, 0] direction, the q_r direction shown in Figure 4.2(b), through

the (0, 1, 0.3) reciprocal lattice point at varied electrode potentials. Comparing a_{NN}, shown in Figure 4.8(b) to the results obtained at ID-03, over the same potential range i.e. -0.54 V to -0.2 V, there is a very similar variation in near neighbour spacing between ~2.78 Å and ~2.76 Å. Furthermore, the variation in the integrated intensity shown by the black symbols in Figure 4.8(a) a comparable trend is observed with that of the integrated intensities for the reflections at points 3 and 4 highlighting the reproducibility of the results and the potential dependent in-plane surface compression. The red triangles in Figure 4.8(a) represent the integrated intensity from the (0, 1, 0.3) CTR reflection, the sharp increase in intensity beginning at ~0.2 V correlates with the lifting of the surface reconstruction.

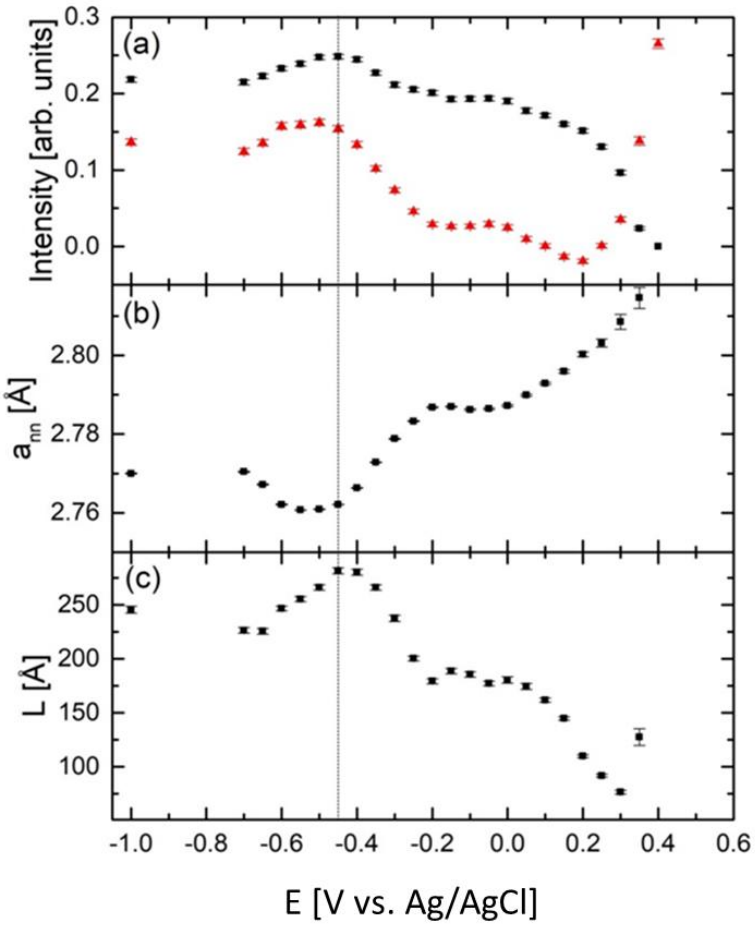

Figure 4.8: (a) Integrated intensity of the reconstruction peak shown in Figure 2 as a function of the applied electrode potential. The red symbols (triangles) correspond to the integrated intensity measured at the CTR position, (0, 1, 0.3). (b) Near neighbour, in-plane lattice constant, a_{NN}, of the Au(111)-(p x √3) reconstruction derived from fits to the data such as that shown in Figure 2. (c) Domain size of the (p x √3) reconstruction. The black dotted vertical line acts as a guide for the eye indicating the pzc. Measurements conducted at the 7-2 beamline at the SSRL by Yvonne Gründer

4.3.2 Au (100)

A series of measurements analogous to those carried out on the Au(111) surface were performed on the Au(100) electrode surface. X-ray voltammetry measurements were taken at the (1.206, 1.206, 0.3) reciprocal lattice position over the potential range -0.9 V to -0.45 V at 1 mV/s. This is a position is where one of the domains of the '*hex*' reconstructed surface layer is situated. This measurement was repeated at the (1, 1, 0.3) CTR position. Both XRV's are shown in Figure 4.9 (a) and (b) for the (1, 1, 0.3) CTR position and the (1.206, 1.206, 0.3) reflection respectively, the arrows displayed on each figure represent the direction of the potential sweep. Following the XRV measurements, a series of reciprocal space scans measured along [1, 1, 0] direction through the (1, 1, 0.3) CTR position and the reconstruction peak at ~ (1.2, 1.2, 0.3) in steps of 25 mV over the potential range -0.9 V to -0.45 V. These measurements were repeated for the [1, $\overline{1}$, 0] direction through the (1, $\overline{1}$, 0.3) CTR position and the reconstruction peak at ~ (1.2, $\overline{1.2}$, 0.3). The peaks were then fitted to a double Gaussian lineshape, an example of which is shown by the solid line in Figure 4.10. Similar to the scans through the Au(111) reconstruction peaks, fitting the data enable the extraction of the near neighbour spacing, coherence length.

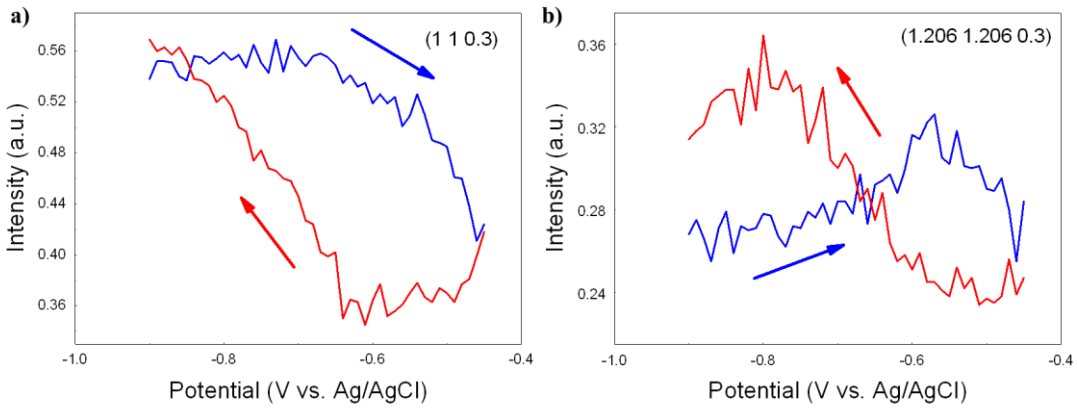

Figure 4.9: X-ray voltammetry measurements of the Au(100) electrode surface in 0.1 M KOH between -0.9 V and -0.45 V at a sweep rate of 1 mV/s at (a) the (1, 1, 0.3) CTR position (b) (1.206, 1.206, 0.3) reciprocal lattice position. The blue and red lines represent the cathodic and anodic sweeps respectively.

The nearest neighbour, in plane lattice constant, a_{NN}, can be derived from the fits to the data via:

$$a_{nn} = \frac{\sqrt{2}a_0}{\sqrt{3}h}$$

Where a_0= 4.078 is the bulk lattice constant of Au and h is the reciprocal lattice co-ordinate of the surface rod from the (hex) reconstruction. In this case, the equation only really depends

on the *h* reciprocal lattice co-ordinate due to scanning along either the [1, $\overline{1}$, 0] or the [1 1 0] direction and thus, the position in *h* will be of equal magnitude to the position in *k* at any point along either direction. Figure 4.11 shows the potential dependence of the integrated intensity of the (hex) reconstructed peak and the near neighbour, in-plane lattice spacing. The red and blue arrows indicate the scan direction. In both data sets, there is a notable transition in the reconstruction evidenced by a change in both intensity and the near neighbour spacing, occurring around -0.7 V. The intensity for both positions appears to begin to increase upon reaching -0.7 V before decreasing as the potential for the lifting of the reconstruction is approached. During the cathodic sweep, the intensity then increases as the potential approaches -0.6 V before reaching its original value at the start of the scan.

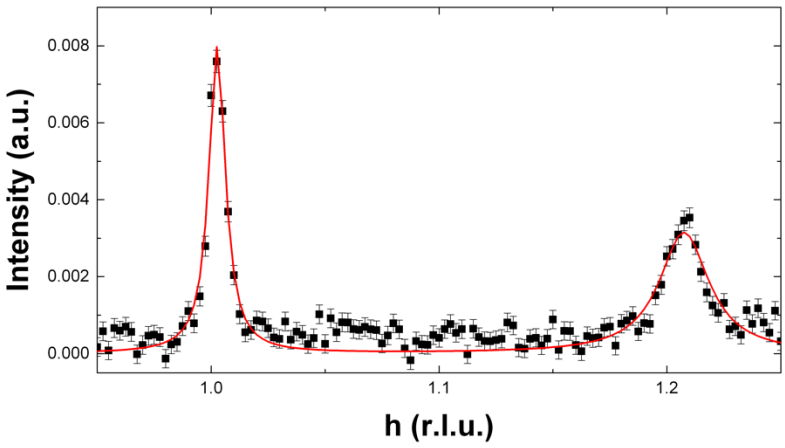

Figure 4.10:In plane x-ray diffraction from the reconstructed Au(100) electrode surface in 0.1 M KOH electrolyte, measured along the [1, 1, 0] direction through the(1, 1, 0.3) CTR and the reconstruction peak at ~(1.2, 1.2, 0.3) (solid shapes) measured at an electrode potential of -0.9 V (vs. Ag/AgCl). The data is fitted with a double Gaussian lineshape (solid line).

As the potential is shifted anodically, a decrease in the near neighbour spacing, a_{NN} is observed. In the [1, $\overline{1}$, 0] direction, the transition where a_{NN} decreases between -0.7 V and -0.55 V from a stable value of 2.763 ± 0.001 Å to 2.756 ± 0.001 Å is more noticeable in comparison to a gentler decrease from 2.768 ± 0.001 Å and 2.760 ± 0.001 Å over the same potential range in the [1, 1, 0] direction. When the (hex) reconstruction is in a high compression state, it would be expected that the lattice constant measured at both rotated domains would be the same however, there appears to be a discrepancy of around 0.005 Å. This could be attributed to a systematic error in the scale of the measurement due to crystal alignment. Nevertheless, it is worth noting the reproducibility between the two rotated domains of the (hex) reconstructed surface layer indicating that the change in the near neighbour spacing is isotropic.

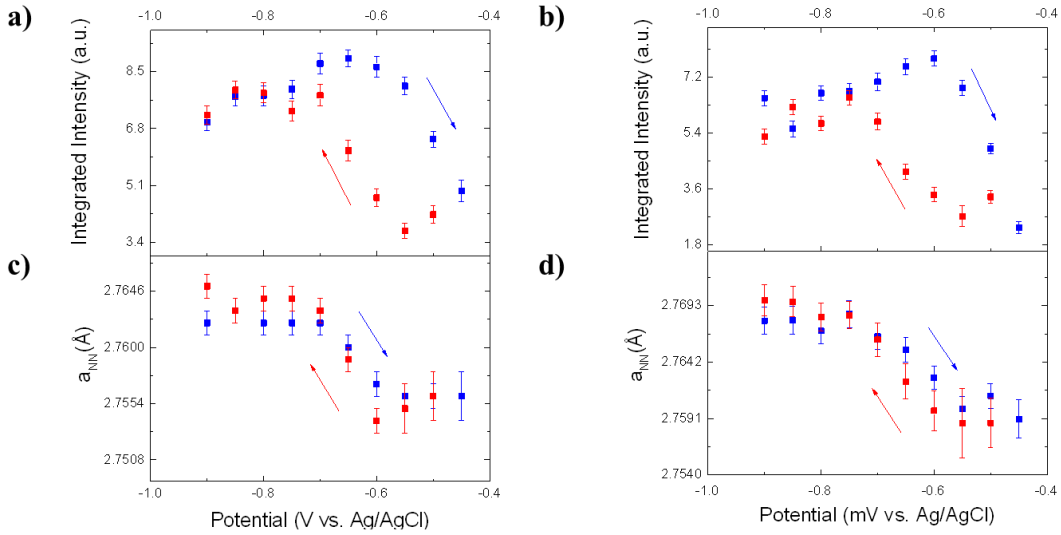

Figure 4.11: (a) Integrated intensity of the Au(100)-(hex) reconstruction peak at ~ (1.2, $\overline{1.2}$, 0.3) shown in Figure 4.10as a function of the applied electrode potential. (b) Integrated intensity of the reconstruction peak at ~(1.2, 1.2, 0.3) (c) Near-neighbour, in-plane lattice constant, a_{NN}, of the Au(100)-hex reconstruction derived from fits to the data taken at ~(1.2, $\overline{1.2}$, 0.3) (d) Near-neighbour, in-plane lattice constant, a_{NN}, of the Au(100)-hex reconstruction derived from fits to the data taken at ~(1.2, 1.2, 0.3). The blue and red points represent the anodic and cathodic sweeps respectively.

A series of reciprocal space scans along the [1, 1, 0] direction analogous to the previous measurements was carried out over a wider potential range of -0.9 V and 0 V. The extracted intensities are plotted as a function of potential in Figure 4.12(a). The intensities follow a similar trend with that shown in Figure 4.11(a) over the same potential range in the anodic direction before falling to zero at -0.2 V, when the (hex) phase has been lifted and no scattering due to the reconstruction is observed. When the potential is stepped in the cathodic direction (red markers) no scattering from to the (hex) reconstruction is observed until -0.68 V. The in-plane lattice constant is plotted against potential in Figure 4.12(b). In the anodic direction, a change in a_{NN} comparable to that from the previous measurement in Figure 4.11(b) is observed starting at -0.6 V and stabilising again at -0.4 V where a_{NN} reaches a maximum value for surface compression. The observation of the in-plane surface compression and the agreement of these results with the previous measurement highlight the reproducibility of the measurements.

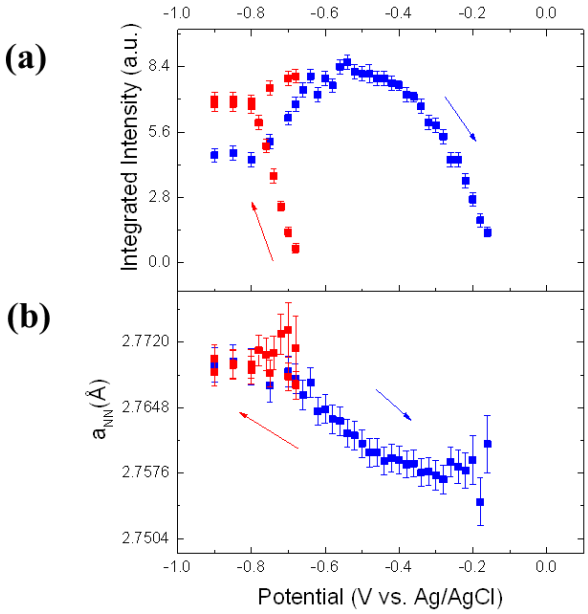

Figure 4.12 : (a) Integrated intensity of the Au(100)-(hex) reconstruction peak at ~ (1.2, 1.2, 0.3) shown in Figure 4.10as a function of the applied electrode potential. (b) Near-neighbour, in-plane lattice constant, a_{NN}, of the Au(100)-hex reconstruction derived from fits to the data taken at ~ (1.2, 1, 0.3). The blue and red points represent the anodic and cathodic sweeps respectively.

4.3.3 Au(110)

Following alignment of the Au(110) electrode surface on the diffractometer, a reciprocal space scan in the [0 1 0] direction (Figure 4.13(a)) was measured to detect if the (1 x 2) reconstructed domain shown via LEED in Figure 4.5 survived the transition into the x-ray thin layer cell. As can be seen from Figure 4.13(a), no evidence of the (1 x *n*) reconstructed domains are present. The potential was then contacted at -0.3 V and a series of potential scans between 0.1 V and -0.7 V were conducted and the reciprocal space scan was repeated following each potential cycle. Figure 4.13 (b) shows the integrated intensity of one of the potential cycles measured at the (0, 1, 0.6) CTR position. As the potential is swept in the positive direction, there is a general decrease in the intensity which increases and returns to its original point as the potential is scanned in the negative direction. Over the course of the measurements, a peak was observed at (0 1.667, 0.6) via reciprocal space scans(Figure 4.13(c) black line), this peak continued to grow in intensity over further potential scans as evidenced by the red and blue lines in Figure 4.13(c). The peak at (0, 1.667, 0.6) corresponds to the Au(110) electrode surface being reconstructed in a (1 x 3) phase. Following the series of potential cycles and reciprocal space scans, the potential was held at -0.7 V and a rocking scan of the peak measured at (0, 1.667, 0.6) was taken. Unfortunately, from the rocking scan shown in Figure 4.13(d) it became apparent that the observed peak was not brought about by the (1 x 3) domain of the 'missing row' reconstruction but a powder line that had grown over time, this is further

confirmed by Figure 4.13(e) that is an in-plane image captured using the 2D detector during the rocking scan measurement. This prevented measurements similar to those taken on both the Au(111) and Au(100) electrode surfaces from being measured.

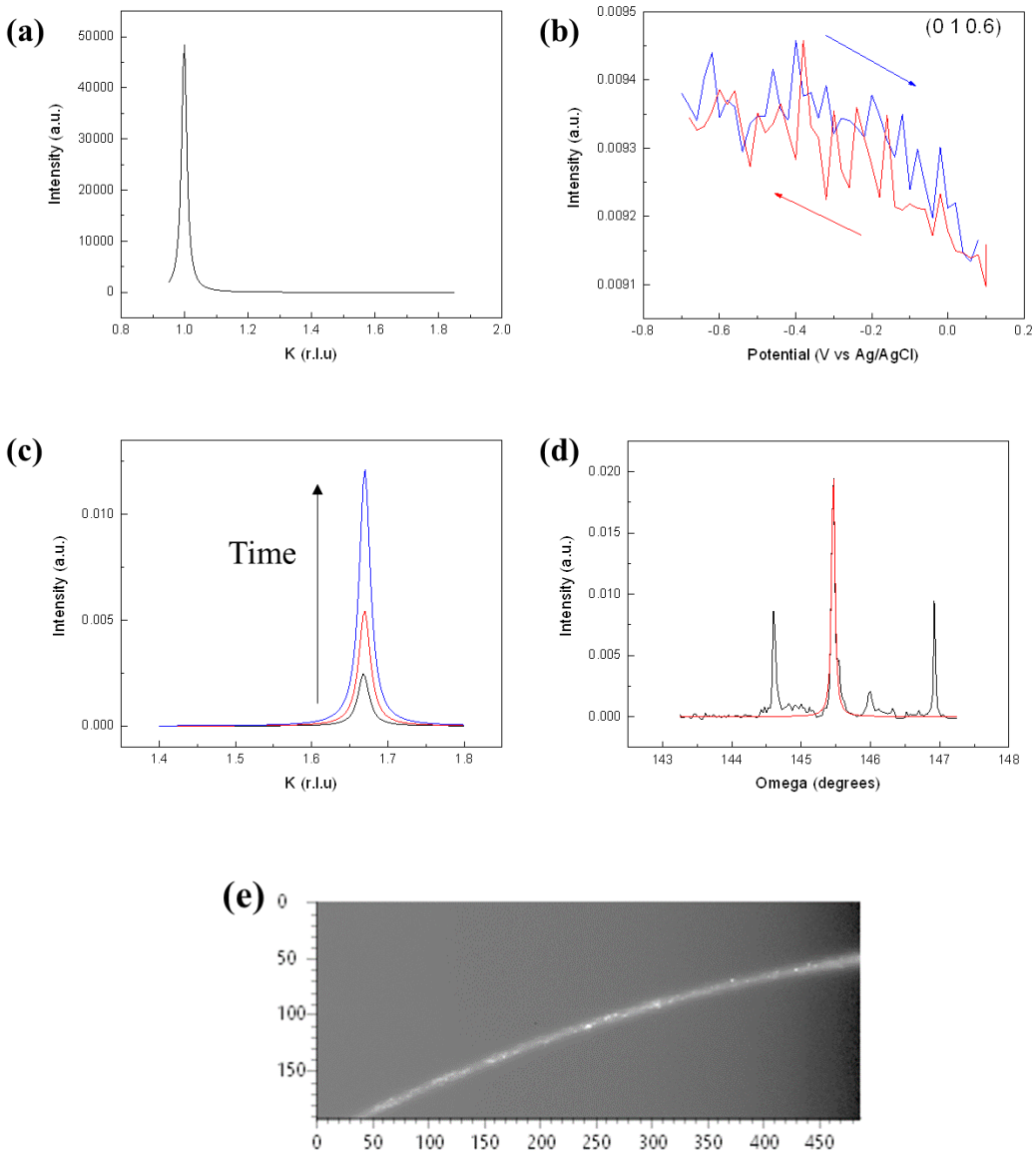

Figure 4.13: (a) Reciprocal space scan of the Au(110) surface in 0.1 M KOH along the [0 1 0] direction through the (0 1 0.6) CTR position. (b) Scattered intensity measured as a function of applied electrode potential at the (0 1 0.6) CTR position between -0.7 V and 0.1 V (vs. Ag/AgCl) at a scan rate of 4 mV/s.(c) Reciprocal space scans along the [0 1 0] direction through a peak found at (0, 1.667, 0.6) thought to be brought about by the (1 x 3) reconstructed domain of the Au(110) surface. The arrow indicates the growth of the peak with time through subsequent potential scans. (d) Rocking scan measurement of the peak found at (0 1.667, 0.6), the blackline shows the background subtracted measurement, the red line represents the fitted Lorentzian line shape to the peak. (e) In-plane image taken during the rocking scan measurement at (0, 1.667, 0.6), the curved white line is characteristic of a powder line.

4.3.4 Au(111) and Au(100) in 0.1 M KOH

It is now worth discussing the results of the measurements taken on both the Au(100) and Au(111) electrode surfaces in terms of two potential regions determined by the electrochemistry[79, 80]. The onset of adsorption of hydroxide species correlates to a potential of -0.45 V. There is no specific adsorption onto the Au for potentials <-0.45 V. Based on differential capacitance measurements[81] on Au(111) it has been suggested that -0.45 V corresponds to the local potential of zero charge (*pzc*). As has been shown, in the potential range of -1.0 V and -0.45 V, both the Au(111) and Au(100) surface display similar behaviour i.e. an in-plane surface compression. The observed increase of the in-plane Au-Au spacing can be understood as a pure charging effect. Excess surface charge, in the absence of specific adsorption, determines the Au-Au surface interaction independent of the underlying Au substrate. Halide anion adlayers with hexagonal geometry adsorbed onto noble metal surfaces have displayed similar electrocompresibility[82–84]. The 2D isothermal compressibility of the reconstructed monolayer is:

$$\kappa_{2D} = \frac{1}{N_{ion}e}\left(\frac{dA}{dE}\right)$$

Where $\left(\frac{dA}{dE}\right)$ is the change in area A per adsorbate atom with the applied potential E and N_{ion} is the ionic charge of the surface atom. The exact charge of the surface atom is unknown. Assuming a 2D free electron gas model, the electrocompressibility is given by:

$$\kappa_{\tau} = \frac{m_e A^2}{\pi\hbar(Z - N_{ion})^2}$$

Where $(Z - N_{ion})$ denotes the number of electrons contributing to the free electron gas, m_e is the electron mass, $\hbar$ is the Planck's constant $\hbar = h/(2\pi)$. In the case of gold, Z=1 for the 6s electron and N_{ion} gives the modification through the additional charge of the surface atom. Obtaining $\left(\frac{dA}{dE}\right)$ and the surface area, A, per atom from the experimental value for the nearest neighbour distance, a_{NN}, the charge of the surface gold atoms, N_{ion}, can be obtained by assuming a 2D isothermal compressibility for the electrocompressibility ($\kappa_{2D} = \kappa_{\tau}$). This is shown in Figure 4.14 as a function of the applied potential. From these values an electrocompressibility of the order 1 Å^2/eV is obtained which is of the same order as the values found for electrochemically deposited metal monolayers [85–87]. Although the assumed model is based on the free electron model and neglects any possible influence of the 5d electrons, it shows that the change in electrocompressibility observed can be explained through a change in the charge of the surface atoms. The minimal nearest neighbour distance corresponds in this case to the point where the charge on the surface atom changes signs.

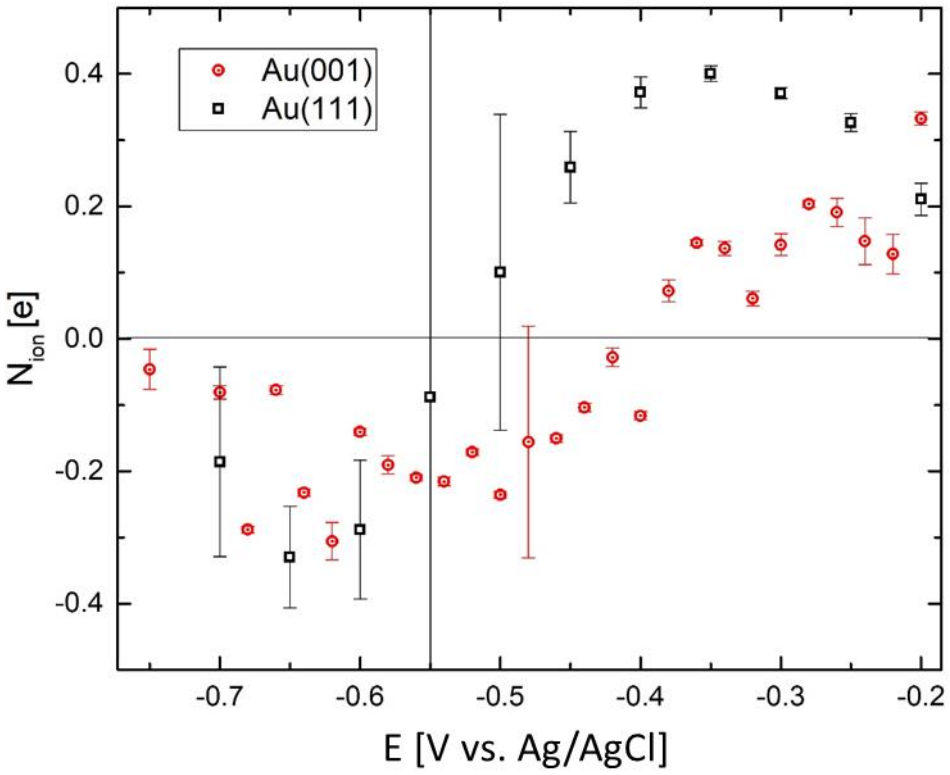

Figure 4.14: Potential dependent surface charge per atom obtained for the reconstructed Au(001) and Au(111) surfaces by comparing the experimental electrocompressibility to the compressibility for a 2D layer in the free electron model.

Both the Au(111) and Au(100) surfaces exhibit reconstructions closest to the phases observed in UHV at -0.45 V. As previously stated, this potential marks the onset of hydroxide adsorption onto the Au surfaces and leads to the lifting of the surface reconstructions. However, for the Au(111) surface, a stable intermediate phase forms during the initial stages of lifting between -0.2 V and 0 V before the complete lifting of the reconstruction. Similar intermediate phases prior to the lifting of the reconstruction have also been observed in acidic electrolyte solution by STM[88]. Vaz-Domínguez and co-workers found that in both 0.1 M H_2SO_4 and 0.1 M $HClO_4$ + 1 mM KCl solutions in the potential region coinciding with the peak potential of the peak attributed to the lifting of the reconstruction (0.36-0.37 V vs Ag/AgCl), a network of dislocation lines arranged in domains rotated 120° were observed. Some of which having merged and forming geometrical figures such as triangles and chevrons, all maintaining the trigonal geometry of the surface. These domains were observed to grow with potential until around 0.49 V where the reconstruction was observed to be completely lifted. Chen and Lipkowski[80] proposed in their study of hydroxide adsorption onto Au(111), that the OH^- forms a polar bond at negative potential. At positive charge the polarity of this bond decreases due to strong screening of the anion charge by either significant charge transfer from OH^- to Au or by the charge on the metal. Recent studies into the effect

of halide adsorption onto Cu(001) electrode surfaces have explicitly shown that the sub-surface metal layers play a key role in the bonding mechanism[88, 89]. By a change in the in-plane compression, or p value, it is clear that the Au(111) surface is able to accommodate significant OH^- adsorption. Density functional theory (DFT) calculations have recently shown that for the formation of these reconstructed phases, there are only small energy differences. In contrast to the Au(111) reconstruction, beyond -0.45 V the Au(100)-(hex) surface reconstruction immediately begins to lift and there is no change in the Au-Au surface compression. In this case the adsorption of hydroxide species appears to drive the lifting of the reconstruction[90, 91].

4.4 Au(*hkl*): the CO effect

Whilst the observed potential-dependent changes in the Au surface are interesting from a fundamental perspective, an additional point to consider is whether the changes in the structure are connected to electrocatalytic behaviour. Following the measurements in 0.1M KOH on Au(100), the electrolyte was exchanged to a CO saturated 0.1M KOH electrolyte in order to gain insight into the mechanism behind the promotion of electrocatalytic reactivity by the adsorption of CO. Figure 4.15 shows the XRVs on the (hex) reconstruction peak, at ~ (1.2, 1.2, 0.3), and at the (1, 1, 0.3) CTR position between -0.9 V and -0.45 V at a sweep rate of 1 mV/s. In contrast to the XRV measurements in CO free electrolyte, there is no significant change in the intensities of either the reconstruction or the CTR. This would appear to agree with previous SXS studies where the adsorbed CO was observed to have a stabilising effect on the reconstructed surface layer allowing the reconstructed phase to exist over a much larger potential range[79]. A series of measurements analogous to those taken earlier on the CO free system between -0.9 V and -0.45 V in the [1, 1, 0] direction was taken.

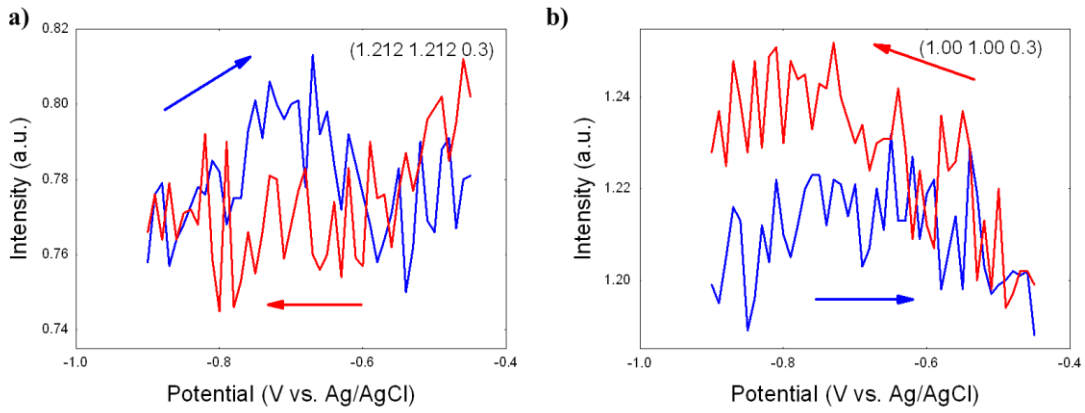

Figure 4.15: X-ray Voltammetry measurements of the Au(100) electrode surface in CO saturated 0.1 M KOH between -0.9 V and -0.45 V (vs. Ag/AgCl) at a sweep rate of 1 mV/s at (a) the Au(100)-(hex)

reconstruction peak at (1.212, 1.212, 0.3) (b) the (1, 1, 0.3) CTR position. The blue and red lines represent the anodic and cathodic scans respectively.

Figure 4.16 (a) shows the extracted integrated intensities vs. potential for the (1.2, 1.2 ,0.3) reflection of the (hex) reconstruction. Contrary to the measurements shown in Figure 4.11 and 4.13, no significant change in intensity is observed. Comparing the calculated near neighbour spacing, a_{NN}, in Figure 4.16(b) no specific trend is observed. In fact, the results show no evidence of the in-plane surface compression that is observed in the non-CO saturated KOH electrolyte in Figure 4.11 and 4.13. This can visually be seen in the location of the peak positions shown in Figure 4.17(a) of the (1.2, 1.2, 0.3) reflection in CO saturated 0.1 M KOH solution at -1.0 V and -0.5 V respectively. As can be seen the peak position stays at a constant, this corresponds to a value for the in-plane lattice constant to be near to the maximum surface compression, i.e. a_{NN} ~2.76 Å.

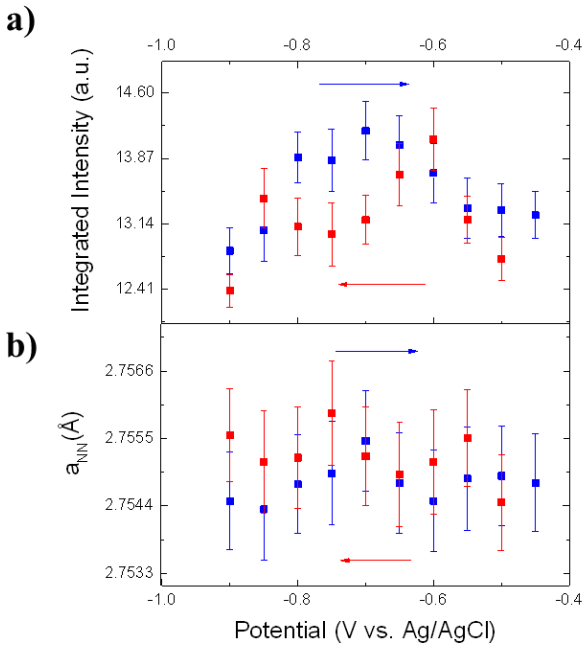

Figure 4.16: Measurements of the Au(100) electrode surface in CO saturated 0.1M KOH (a) Integrated intensity of the Au(100)-(hex) reconstruction peak at ~ (1.2, 1.2, 0.3) as a function of the applied electrode potential (b) Near-neighbour, in-plane lattice constant, a_{NN}, of the Au(100)-hex reconstruction derived from fits to the data taken at ~(1.2, 1.2, 0.3). The blue and red points represent the anodic and cathodic sweeps respectively.

These results will now be compared to measurements taken on the Au(111) (p x √3) in CO-saturated 0.1M electrolyte. The left side of Figure 4.17 shows a comparison of the peaks obtained from reciprocal space scans through the Au(100)-(hex) reconstruction, measured in the [1, 1, 0] direction in CO saturated 0.1 M KOH at -1.0 V and -0.5 V. The right side of

Figure 4.17 shows a comparison of the peaks obtained from the the Au(111) (0, 1, 0.3) CTR position and the peak due to the (p x √3) reconstruction at (0.019, 1.019, 0.3) -1.0 V and -0.5 V in CO saturated solution (right). As can be seen for the measurements made on the Au(111) (p x √3) reconstruction in CO saturated solution, the CO appears to have a stabilising effect as it did with the Au(100) '*hex*' reconstruction, effectively locking the (p x √3) reconstruction at a value of p~23.6 or a_{NN} ~ 2.76. It has previously been shown that on the Au(100) surface, adsorbed CO stabilises the Au(100) over a much larger potential range. This is demonstrated in Figure 4.18 which shows a comparison of two XRVs measured at the (0, 0, 1.02) 'anti-Bragg' position on the specular CTR in CO free and CO saturated 0.1 M KOH solution. This position is sensitive to changes in the atomic density of the Au surface atomic layer and thus shows large changes when the surface reconstruction is formed and lifted. As can be seen, the Au(100) surface reconstruction is preserved in the presence of CO right up to the onset of oxide formation at positive potentials. In fact, the lifting of the Au(111) and Au(100) surface reconstructions occur at similar potentials in CO-saturated electrolyte, i.e. after or concurrent with the oxidation of adsorbed CO.

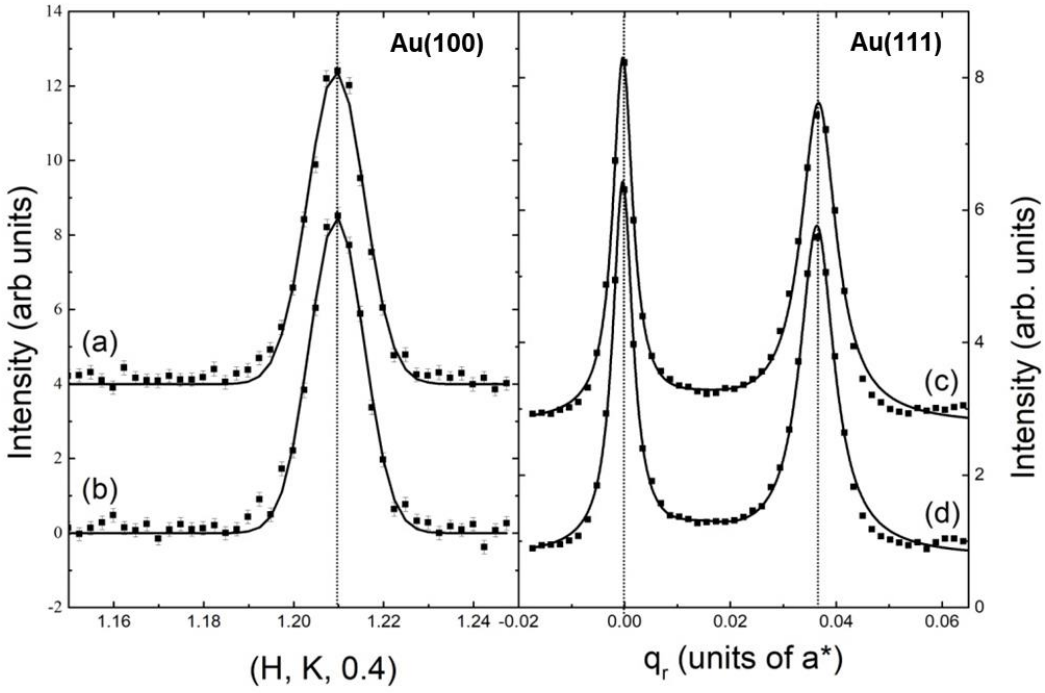

Figure 4.17: (left) In-plane x-ray diffraction from the Au(100)-(hex) reconstructed electrode surface in CO saturated 0.1 M KOH electrolyte, measured along the [1, 1, 0] direction at an electrode potential (a) -1.0 V (b) -0.5 V (vs. Ag/AgCl). (right) In plane X-ray diffraction from the (p x √3) reconstructed Au(111) electrode surface in CO saturated 0.1 M KOH electrolyte, measured along the [1, 1, 0] direction through the (0, 1, 0.3) CTR position and the reconstruction peak at electrode potential (c) -1.0 V (d) -0.5 V. The dashed vertical lines are guides for the eye.

Both the reconstructed phases of the Au(111) and Au(100) surfaces appear to be stabilised at a lattice constant close to that of the maximum surface compression, a_{NN} ~ 2.76 Å, when CO is adsorbed onto the surface, it is thus apparent that the adsorbed CO suppresses the potential-induced changes in the Au near neighbour spacing. No electrocompression is observed and thus the simple model of a 2D electron gas fails as a description, possibly due to a modification of the electron density of the surface atoms through a bonding to the CO. It is therefore likely that the adsorbed CO molecule acts as a tuneable dipole, accommodating the changes in the surface charge rather than the Au surface atoms. Indeed, combined Fourier transform infrared reflection−absorption spectroscopy (FTIRRAS) studies and DFT calculations[52] have found that on the Au(111) electrode surface, CO adsorbed on: hollow, bridge and top sites undergoes a potential-dependent shift in the CO stretching frequency. This shift corresponds to a Stark tuning rate, i.e. the change in the C–O stretching frequency with applied potential, of 40 – 20 cm^{-1} V^{-1}. This could be the origin of the observed enhanced electrocatalytic activity as the reactions no longer require a through-gold interaction and take place in the outer layer of the double layer structure at the interface. This is consistent with the model of CO-promoted OH^- adsorption as the mechanism for the enhanced electrooxidation of alcohols on the hexagonal Au surfaces unique to the Au(111) and Au(100) single crystals.

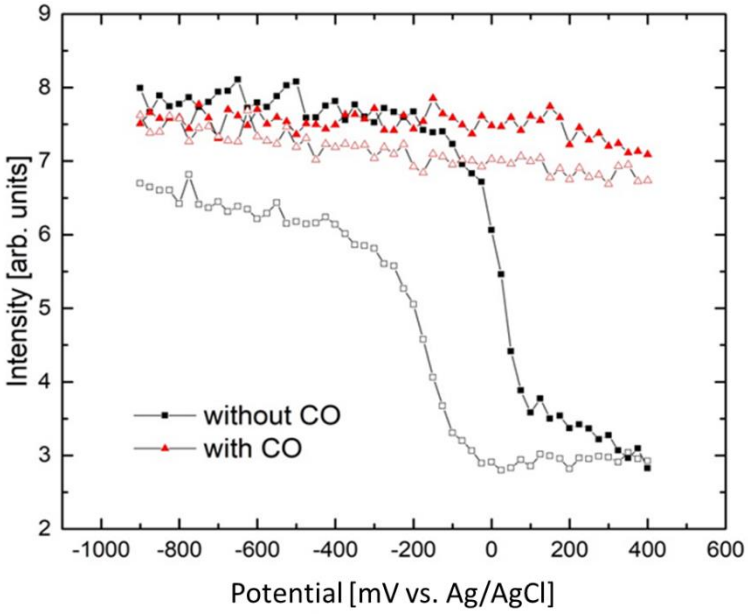

Figure 4.18: Scattered intensity measured as a function of potential at (0, 0, 1.02) an 'anti-Bragg' position on the specular CTR. The potential was swept at a sweep rate of 2 mV/s. The black symbols show the results obtained in 0.1 M KOH and the red symbols show the scattered intensity following the saturation of the electrolyte with CO.

To give a complete picture of the effects of CO adsorption on the low index surfaces of gold, the effects of CO adsorption on Au(110) electrode surfaces are reproduced here from the scientific literature. On Au(110) crystals, in 0.1 M KOH solution the 'missing row' reconstruction in a mixed phase bringing about a highly defected (1 x 3) surface with numerous stacking faults and steps. A comparison of the rocking scans in CO-free 0.1M KOH solution and CO-saturated solution measured at (1.7, 0, 0.1) shifted from the expected position for the reconstructed (1 x 3) domain of (1.667, 0 0.1) is shown in Figure 4.19(b') taken from [79]. The sharp increase in intensity in CO-saturated solution was suggested to be indicative of significant enhancement of the reconstruction in the presence of CO in solution. Figure 4.19 (b) and (c)show XRV measurements on the reconstruction position at (1.7, 0, 0.1) and the (0, 0, 1.7) position on the specular rod respectively in CO- free (dashed lines) and CO saturated solution (solid lines). In N_2 purged 0.1 M KOH solution, the lifting of the 'missing row' surface reconstruction is evidenced by the decrease in intensity on the positive potential sweep of the XRV shown by the black line in Figure 4.19 (b) measured at the (1.7, 0, 0.1) position. This decrease in intensity on the reconstruction position coincides with OH^- adsorption in like behaviour to both Au(100) 'hex' and Au(111) (p x $\sqrt{3}$) surface reconstructions. The lifting of the 'missing row' reconstruction also corresponds to an increase in intensity at the (0, 0, 1.7) position shown in Figure 4.19 (c). In CO saturated solution the onset of CO oxidation coincides with OH^- adsorption. In addition, the presence of CO in solution acts to stabilise the Au(110) surface reconstruction up to potentials as positive at 1.2 V (vs. RHE), a similar effect that is observed on Au(111) and Au(100). Recent FTIRRAS[52] measurements of CO adsorption on Au(110) have found that in contrast to Au(111) and Au(100) electrodes, where the CO adsorbs on top, bridge and hollow sites, CO only adsorbs on top sites. Furthermore, no evidence of the potential dependent change in the CO stretching frequency was observed. It was concluded from these studies that this potential dependent change seems to only occur on surfaces with hexagonal orientations.

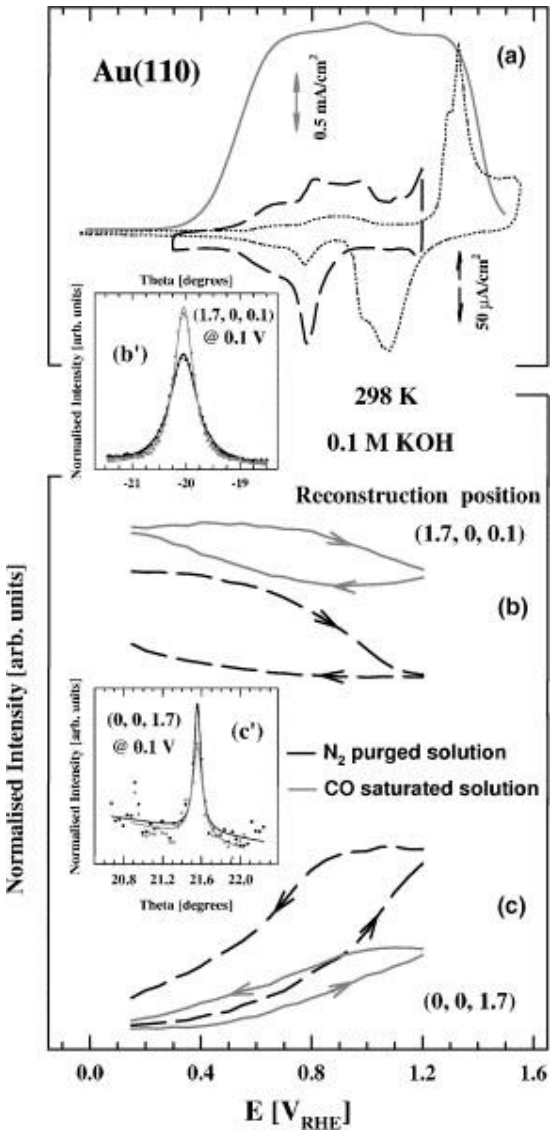

Figure 4.19: Reproduced with permission from [79]. (a) Cyclic voltammetry of the Au(110) electrode surface in 0.1 M KOH along with the polarisation curve for CO oxidation in CO-saturated 0.1 M KOH solution at a sweep rate of 50mV/s. (b')Rocking scans measured through the (1.7, 0, 0.1) position in both CO-free (black line) and CO-saturated (grey line) solution. (b) XRV measurements at the (1.7, 0, 0.1) reconstruction position in CO-free (dashed line) and CO saturated (solid line) solution. (c) XRV measurements at the specular position (0, 0, 1.7) that is sensitive to the surface reconstruction in both CO free and CO saturated solution. (c') Rocking scan measurements at the specular CTR position in CO-free and CO-saturated solution at a potential of (0.1 V vs. RHE) where the Au(110) surface is reconstructed. For all XRV data the scan rate was 5 mV/s.

4.5 Au(100): the effect of pH on the 'hex' reconstruction

Another series of measurements were conducted on the Au(100) electrode in a pH 7 electrolyte. Following repreparation the electrolyte was changed to a 0.01 M KH_2PO_4 + 0.01 M K_2HPO_4 (neutral) solution. Figure 4.20 shows an XRV measured at the (1, 1, 0.6) CTR

reflection over the potential range -0.5 V to 0.5 V at a sweep rate of 1 mV/s. The changes in intensity correlate with the lifting and reformation of the (hex) reconstructed phase for the anodic and cathodic sweeps respectively. On the anodic sweep, the sharp increase in intensity starting ~ -0.1V implies that the (hex) reconstruction is lifted positive of this potential. Indeed, looking at the extracted intensity curves versus potential, for a series of reciprocal space scans measured in the [1, 1, 0] direction, no evidence of scattering due to the reconstructed peak is observed beyond -0.2 V in the cathodic direction.

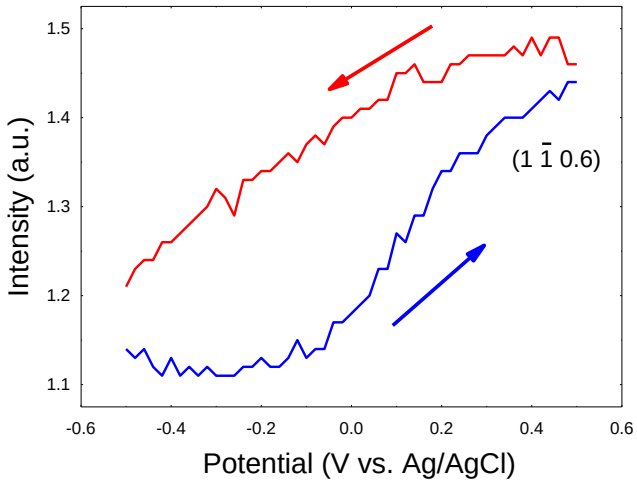

Figure 4.20: X-ray voltammetry measurement of the Au(100) electrode surface in 0.01 M KH_2PO_4 + 0.01 M K_2HPO_4 electrolyte over the potential range -0.5 V to 0.5 V (vs. Ag/AgCl) at a sweep rate of 1 mV/s at the (1, 1, 0.6) CTR reflection. The blue and red lines represent the anodic and cathodic sweeps respectively.

When the potential is stepped back from 0.5 V cathodically, the reconstruction is not observed to reform until 0 V where the peak intensity goes on to increase back to its position at the start of the measurement. Looking at the in-plane lattice spacing versus potential for the (hex) reconstruction the in-plane surface compression observed in the previous measurements is apparent during the anodic scans, albeit over a larger potential range. The near neighbour spacing, a_{NN}, begins to decrease from -0.45 V and then stabilises at a maximum compression of 2.752 ± 0.001 Å. During the cathodic measurements, once the (hex) reconstruction reforms at 0 V, a_{NN} is shown to remain constant at a value of 2.765 ± 0.001 Å. The presence of this in-plane surface compression in pH 7 solution suggests that this potential dependent change in the surface density is a charging effect on the electrode surface which occurs irrespective of pH.

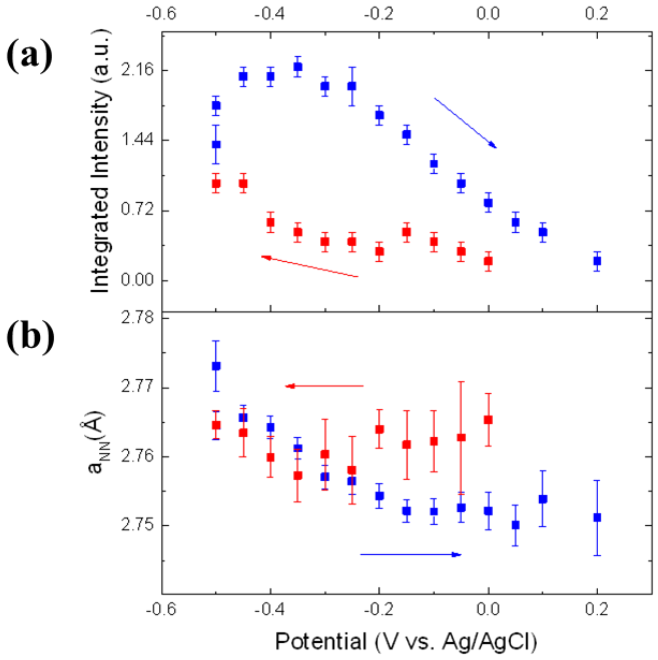

Figure 4.21: In-plane X-ray diffraction the (hex) reconstructed Au(100) electrode surface in 0.01 M KH_2PO_4 + 0.01 M K_2HPO_4 electrolyte over the potential range -0.5 V to 0.5 V (vs. Ag/AgCl), measured in the [1, 1, 0] direction. (a) Integrated intensity of the Au(100)-'hex' reconstruction peak at ~ (1.2, 1.2, 0.6) as a function of the applied electrode potential. (b) Near-neighbour, in-plane lattice constant, a_{NN}, of the Au(100)-hex reconstruction derived from fits to the data taken at ~ (1.2, 1.2, 0.6). The blue and red points represent the anodic and cathodic sweeps respectively.

4.6 Conclusions

In the electrochemical environment, the hexagonal reconstructions that occur on the Au(111) and Au(100) surfaces both exhibit a potential dependent compressibility in alkaline solution. The origin of the compressibility is explained as a pure charging effect at potentials negative of -0.45 V with the highest Au compression observed at -0.45 V. Analysis of the data within a free electron model suggests that the compression is driven by the charge on the Au atoms which reaches a minimum at -0.45 V. This potential marks the onset of OH^- adsorption which leads to a reduction in the surface compression on Au(111) and on Au(100) which marks the onset of the lifting of the (hex) reconstructed phase. Measurements of the Au(100) surface in pH 7 electrolyte suggest the compressibility being a charging effect on the electrode surface irrespective of pH. Attempts to investigate the same type of potential dependent compressibility on Au(110) were unsuccessful due to the formation of a powder line at a position in reciprocal space correlating with the where the (1 x n) missing row reconstruction is expected to be observed. In CO-saturated electrolyte, where CO is adsorbed onto the surface

at a potential of -1.0V, the previously observed surface compressibility is suppressed and both the Au(111) and Au(100) surfaces are locked into the highly compressed phases observed at -0.45 V in CO-free electrolyte. From this it is suggested that adsorbed CO can act as a tuneable dipole and accommodate the excess surface charge induced by the applied potential. Therefore, this is the mechanism that underpins the previously observed enhancement in both electrocatalytic reactivity and the increased stability on the reconstructed surfaces over a larger potential range. Measurements from the scientific literature of the effect of CO adsorption on the Au(110) surface reconstruction were also discussed. It was shown that CO stabilises the missing row reconstruction over a larger potential range in a similar manner to that observed on the surface reconstructions of Au(111) and Au(100). Nevertheless, the potential dependent change in the CO stretching frequency observed on the Au(111) and Au(100) surface reconstructions is not observed on Au(110) suggesting that this behaviour only occurs on surfaces with hexagonal reconstructions.

5 Formation of a Au/Pb Surface Alloy in the Au(111)/Pb UPD system

5.1 Introduction

The development of new functional materials is transforming many technological fields from electronics and catalysis to detection and bio-sensing. Pivotal to these advancements is surface alloying and self-organisation phenomena, driven by surface stress and elastic interactions in metals. In general, alloying between two surfaces is driven by the negative enthalpy of mixing and lowering of surface free energy. Nevertheless, alloying can be observed even in systems where it does not occur in the bulk phase when confined to a few surface layers. Theoretical models[93] have shown that in general elements with a large lattice mismatch, so called immiscible systems, form surface alloys at intermediate coverage regimes during the deposition processes in an effort to reduce surface strain and thus the total surface energy for the system.

The Au(111)/Pb UPD system has been extensively studied via electrochemical techniques[93–101], UV-vis reflectance studies[99], STM[102–107], AFM[108, 109], SXS[33, 110, 111] and SHG[113]. As Pb atoms are approximately 20% larger than Au atoms they favour the formation of incommensurate adlayers during the UPD process. Indeed, surface X-ray diffraction studies have found that the Pb atoms form a hexagonally close packed (*hcp*) incommensurate adlayer that is rotated between 0° and 2.5° depending on the applied potential,[111]. This coincides with a change in the Pb-Au vertical separation over the same potential region[112]. In the last two decades there has been debate as to whether a surface alloy is formed during the Pb UPD process on the Au(111) electrode surface[9]. In some studies, no alloy formation was observed[107, 108] whereas others reported a significant roughening of the gold surface following the stripping of the Pb UPD layer, indicative of a surface alloy[106]. Surface stress studies of the UPD process have noted what they call a 'hump' in the surface stress versus potential curve between a coverage of θ_{Pb}=0.41 and θ_{Pb}=0.83 when the potential was scanned in the cathodic direction at θ_{Pb}=0.43 and θ_{Pb}=0.83 in the anodic direction[114].

Figure 5.1 shows the characteristic CV overlaid with the observed surface stress curve taken from Shin *et al.*[115]. The stress for the initial scan is set arbitrarily to zero. As the potential is scanned cathodically, the stress is observed to change in a positive, or tensile, direction. This is identical, in the initial potential region, to that of Au(111) in Pb^{2+} free solution

represented by the dotted line in the figure. The surface stress changes in a compressive direction around -0.43V (vs. sulphated silver electrode, SSE, this is equal to 0.22 V vs. Ag/AgCl) due to the formation of Au-Pb bonds, reducing the tensile surface stress inherent to the clean Au surface. This compression continues until stress relaxation in a tensile direction is observed over a narrow potential region between -0.635 to -0.670 V (-0.035 V to -0.07 V vs. Ag/AgCl). As the deposition continues, the stress once again shifts in a compressive direction as further Pb atoms are incorporated into the adlayer, bringing about contraction of the interatomic spacings and eventual rotation of the monolayer. This compressive-tensile-compressive transition is termed the *stress relaxation hump*[115]. As the potential is swept anodically, the surface stress exhibits reversible behaviour. After the hump, larger hysteresis is observed with the anodic sweep appearing to be more compressive than the cathodic direction. As the potential reaches 0 V, the surface stress returns to its initial value indicating that all the Pb atoms have been stripped from the Au surface.

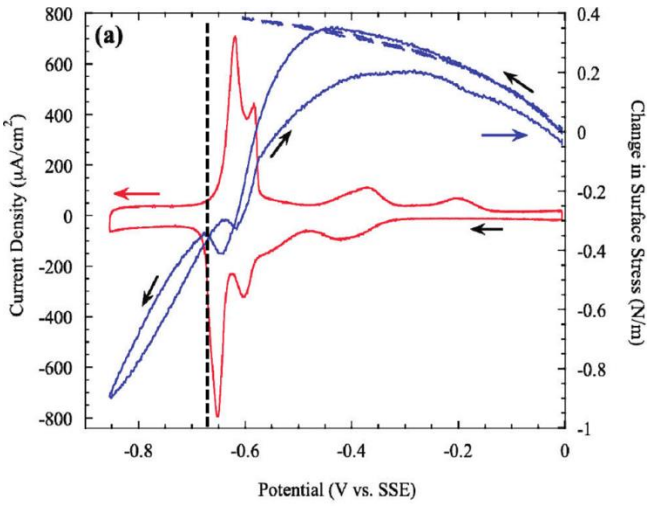

Figure 5.1: Surface stress potential curve for Pb UPD on Au(111). The red lines represent the CV and the solid blue line represents the surface stress curve. The dotted blue line represents the expected surface stress change for clean Au(111). The black dotted line acts as a guide for the eye to mark the potential location of 0.19 V vs. Pb/Pb^{+2} Reprinted with permission from [115]. Copyright 2010 American Chemical Society.

Seo and Yamazaki[114] suggested that this so called surface relaxation hump coincides with the rotation of the hexagonal incommensurate Pb adlayer from 0° to 2.5°. However, Stafford and Bertocci[116] surmise that the rotation found via x-ray diffraction studies occurred in the potential range of full monolayer coverage. Furthermore, the rotation of the adlayer causes no corresponding change in the nearest neighbour spacing of the adlayer. They therefore suggest that this 'hump' is brought about by Pb island coalescence during the deposition process. They

rationalise the stress change during the stripping process by pointing out that the stress moves in the tensile direction as Pb atoms are removed from the adlayer and relieve the compressive elastic strain. Toney *et al.*[111], note a point at around 0.19 V (vs. Pb/Pb^{2+}, -0.01 V vs. Ag/AgCl) at which the near-neighbour distance exceeds the 0.35 nm value for that of bulk Pb. This suggests that the strain can become slightly positive. Green *et al.*[106] showed via STM studies that the stripping of the Pb layer initially occurs at the step edges. The stripping is then followed by pit formation in the adlayer terrace plane, leaving isolated islands on the surface. As the monolayer is broken up, tensile stress in the isolated islands relaxes and thus produces the compressive hump in the stress vs potential curve.

Shin *et al.* [115] attributed most of the stress response and the stress relaxation hump to kinetically controlled surface alloying occurring solely at low coverages of Pb. Whilst at high coverages, a Pb monolayer is formed and the surface alloy is removed. Thus, the stress hump would appear to be caused by the formation and removal of the surface alloy. Nutariya *et al.*[10] in a series of surface stress, in-situ STM and extended polarisation measurements, found evidence of significant mass transport and removal/displacement of Au surface atoms during the Pb UPD process. This can be attributed to the incorporation of Pb and surface mixing during the early stages of deposition and subsequent de-alloying at higher Pb coverage. STM images taken of the Pb-free Au(111) surface following repeated CV cycles showed clear indication of surface alloying during the Pb UPD process, in particular the presence of new Au ad-islands formed during Pb dissolution brought about by expulsion of Au atoms from the top surface layer. This is driven by the Pb overlayer transitioning to a Pb-Au surface alloy as the Pb coverage decreases. However, at this time the surface alloying transformation and the nature of the surface alloy in-situ has not yet been fully investigated.

In the case of the underpotential deposition of Pb on Au(100) electrode surfaces, three types of structures have been observed: c(2 x 2)[116, 117], c($3\sqrt{2}$ x 2)R30°[118] and an incommensurate hexagonal layer similar to that observed during Pb UPD on Au(111). However, the x-ray study carried out by K. M. Robinson *et al.* [117]claim to have observed via CTR analysis an alloying effect as the potential was scanned in the cathodic direction. It is suggested that initially a (1x1) structure of around 60% coverage adsorbs weakly onto the (5 x 20) reconstructed surface and then as the potential is shifted the reconstruction is lifted and during this process the Pb atoms form a substitutional alloy with the gold surface.

The experiments outlined in this chapter endeavour to elucidate the nature of the surface alloy via the use of *in-situ* surface x-ray diffraction measurements on the Au(111) surface. In addition, *in-situ* surface x-ray diffraction studies exploring the nature of the Au(100)/Pb interface will also be discussed.

5.2 Experimental

Measurements were conducted at BM28 (XMaS), the UK-CRG beamline at the ESRF, Grenoble using focussed x-rays at energies of 11.5 keV and 12.835 keV. The Au(111) and Au(100) crystals were prepared and transferred into the x-ray thin layer electrochemical cell using the methodology outlined in section 3.1, the sample was then transferred into the thin layer x-ray electrochemical cell and mounted on the diffractometer. For the measurements on the Au(111) electrode surface, the electrolyte comprised of 0.1 M $HClO_4$ + 10 mM $PbCO_3$ solution, the counter electrode was Au polycrystalline wire and the reference electrode was Ag/AgCl ((WPI- Leak-Free reference electrode, catalogue no. 69-0023 [LF – 2])). Measurements on the Au(100) electrode were conducted as part of an investigation of the oxygen reduction reaction in alkaline solution, as such the electrolyte used in the measurements described here was 0.1 M KOH + 1 mM $PbCO_3$ solution.

5.2 Characterisation of the Pb/Au(111) UPD system

Initially the Au(111) surface was characterised at 0.75 V, a potential where no deposition of Pb is observed. The potential was then stepped to -0.05 V and a radial scan of the double peak brought about by contributions from the two Pb domains of the rotated Pb UPD overlayer at (0, 0.8167, 0.4) can be seen in Figure 5.2(a). The Pb overlayer was found to be rotated 2.2° from the Au [010] direction, in the range of 0-2.5° found in x-ray diffraction studies[33, 110]. A reciprocal space map of the scattering brought about by the rotated incommensurate *hcp* Pb overlayer is shown in Figure 5.2(b). In the Au [010] direction the peaks arising from the Pb overlayer are found at a position (0, 2δ) where 2δ is a measure of the incommensurability of the Pb structure [119]. The coverage of the Pb overlayer can be calculated by $\theta_{Pb} = a_{au}/a_{Pb}$, where a_{au} and a_{Pb} are the near neighbour spacings of Au (2.885 Å) and Pb respectively. The near neighbour spacing of Pb can be calculated by $a_{Au}/2\delta$ = 3.489 Å, in line with the values calculated by Toney *et al.*[111]. The coverage it therefore directly equal to 2δ and thus θ_{Pb} = 0.8267. Specular CTR data measured via the use of rocking scans in intervals of *l* is shown in Figure 5.3 for (a) 0.75 V, (b) 0.35 V and (c) -0.05 V. The solid black line represents the best fit obtained for each potential. The best fit parameters and their associated errors obtained from the output of the linear least squares fitting program obtained for the CTR data at each potential is shown in Table 5.1.

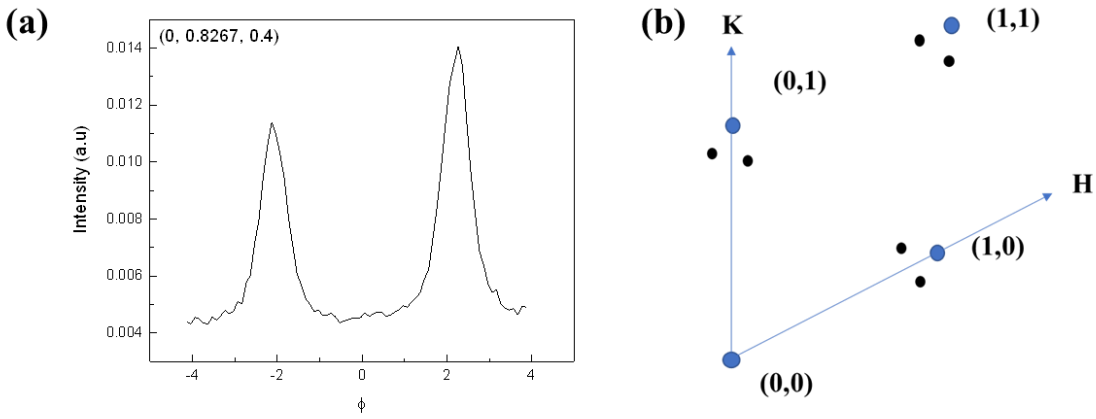

Figure 5.2: (a) Radial scan of the two Pb domains plotted relative to the Au [010] direction at (0, 0.8267, 0.4). (b) reciprocal space map of the scattering brought about by the formation of the rotated incommensurate *hcp* Pb overlayer relative to the scattering from Au(111) electrode surface.

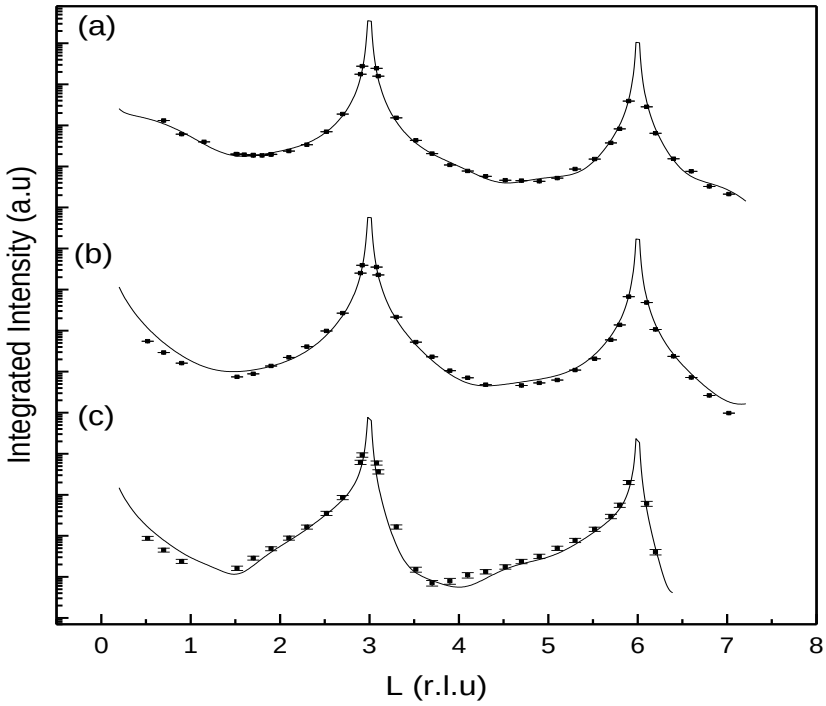

Figure 5.3: Fits to the specular crystal truncation rods measured at (a) 0.75 V, (b) 0.35 V (c) -0.05 V. The parameters for the model are given in Table 5.1 . The solid black lines represent the best fit obtained for the data at each potential.

From the best fit parameters outlined in Table 5.1, the results at -0.05 V show a coverage of the Pb adlayer of 0.77 ±0.06, within error of the calculated coverage based on the radial scan of the rotated Pb domains. Contrary to the studies conducted by Chabala *et al.*[112] that find

the Pb-Au planar spacing of 2.3 Å, the best fit to the CTR data finds a Pb-Au planar spacing of 2.87 ± 0.05 Å. A simplified illustration of the structural model measured at -0.05 V is displayed in Figure 5.4. Contrary to previous SXS studies[111] a significant outward relaxation of the Au surface layer of an 0.27 ± 0.04 Å is observed. This could be indicative of a Pb/Au dealloying process occurring prior to the completion of the Pb adlayer. Furthermore, when the potential is swept up to -0.35 V there is evidence of significant roughening on the Au surface (β ~ 0.25). This would correlate with STM studies[106] that have reported significant roughening of the Au surface observed following the stripping of the Pb layer. At this potential the majority of the Pb adatoms have been stripped from the Au(111) electrode surface with only ~10% remaining. The remaining Pb adatoms are found at a vertical separation of 2.82 ± 0.13 Å from the Au(111) surface.

	Parameter	0.75 V	0.35 V	-0.05 V
Metal Layers	ε_{34} (Å)	0	0	0
	ε_{23} (Å)	0.008 ± 0.004	0	0.08 ± 0.02
	ε_{12} (Å)	-0.008 ± 0.003	0.021 ± 0.008	0.27 ± 0.04
	σ_2 (Å)	0.07 ± 0.01	0	0
	σ_1 (Å)	0.10 ± 0.01	0	0
	θ_1	0.95 ± 0.02	1	1
	B	0	0.24 ± 0.02	0.05 ± 0.01
Pb adlayer	Θ	0	0.09 ± 0.03	0.77 ±0.07
	d (Å)	0	2.82 ± 0.13	2.87 ± 0.05
	σ (Å)	0	0.2	0.35 ± 0.02
Error Function	d (Å)	5.75 ± 0.48	0	0
	σ (Å)	1.27 ± 0.23	0	0
	χ2 red	1.89	2.13	3.7

Table 5.1:Best fit parameters and their associated errors obtained via linear least squares fitting techniques for the CTR data measured at 0.75 V, 0.35 V and -0.05 V. The definitions and physical meanings of these parameters can be found in 2.3.4.

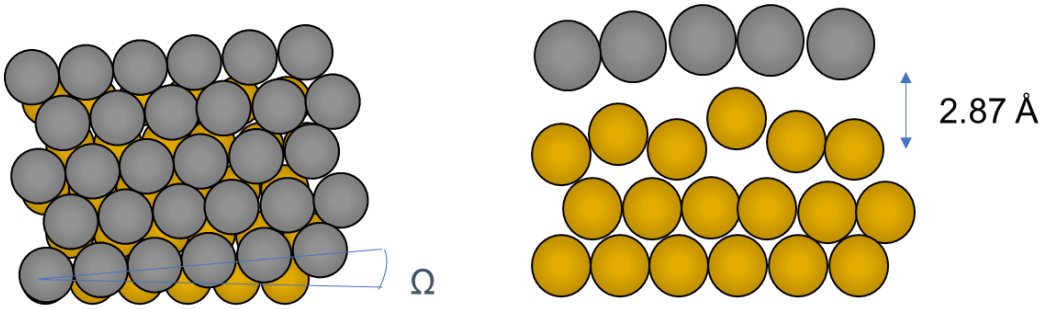

Figure 5.4: Illustration of the structural model obtained from the CTR data measured at -0.05 V. The left side represent the 'top' view of the model showing the incommensurate hcp Pb adlayer (grey circles) rotated at an angle Ω from the underlying Au surface (yellow circles). The right side displays the 'side' view of the surface with the roughened Au surface layer and the Pb adlayer at a distance of 3.48 Å from the Au surface.

5.4 Formation of an Au/Pb surface alloy

As CTR measurements yield electron density profiles, Au and Pb can be hard to discern as they have comparable electron densities. By measuring the changes in intensity at a position in reciprocal space as a function of the incident x-ray energy through the adsorption edge on an atom in the sample, it is possible to differentiate between elements of similar electron densities. The atomic form factor of the element being probed must be adjusted for the dispersion corrections:

$$f(Q,E) = f(Q) + f'(E) + if''(E)$$

where *f(Q,E)* is the corrected form factor, comprising of 3 components; the atomic form factor *f(Q)* and the real and imaginary parts of the dispersion corrections *f'(E) and if''(E)*. In terms of physical measurements *f''* is directly related to the absorption spectrum and can be obtained by measuring the fluorescent signal from the element being probed[120]. By using a Multi-Channel Analyser (MCA), both the elastic and fluorescent signals can be separated simultaneously during the same measurement. To carry out the energy measurements, the detector was switched from a photo diode to Vortec detector. The signal is then passed through an MCA, allowing for the exclusion of fluorescence from the measurements. The energy of the incident x-rays was increased to 12.835 keV close to the lead L(III) edge (13.035 keV). These measurements were employed in conjunction with CTR measurements to identify the Au/Pb alloy in-situ.

The potential was stepped to -0.15 V and in a series of x-ray voltammetry (XRV) measurements at the (0, 0, 1.52) position, the potential was swept up to 0.3 V, in stages (A-F) at a sweep rate of 2.5 mV/s, shown in Figure 5.5. From -0.15 V to 0.0 V (points A to C) the stripping of the Pb overlayer is evidenced by the decrease in intensity. This followed by slow

stripping of the incommensurate UPD layer evidenced by the increase in the intensity as a function of applied potential (D to F). The insets (a-e) of Figure 5.5 represent rocking 'check' scans of the (0, 0, 1.52) CTR position measured before (black line) and after (red line) the XRV sweeps: (a) B-C, (b) C-D, (d) D-E and (e) E-F. These rocking scans were used to monitor for any changes in the background during the XRV measurement to ensure that the observed change is real via background subtraction.

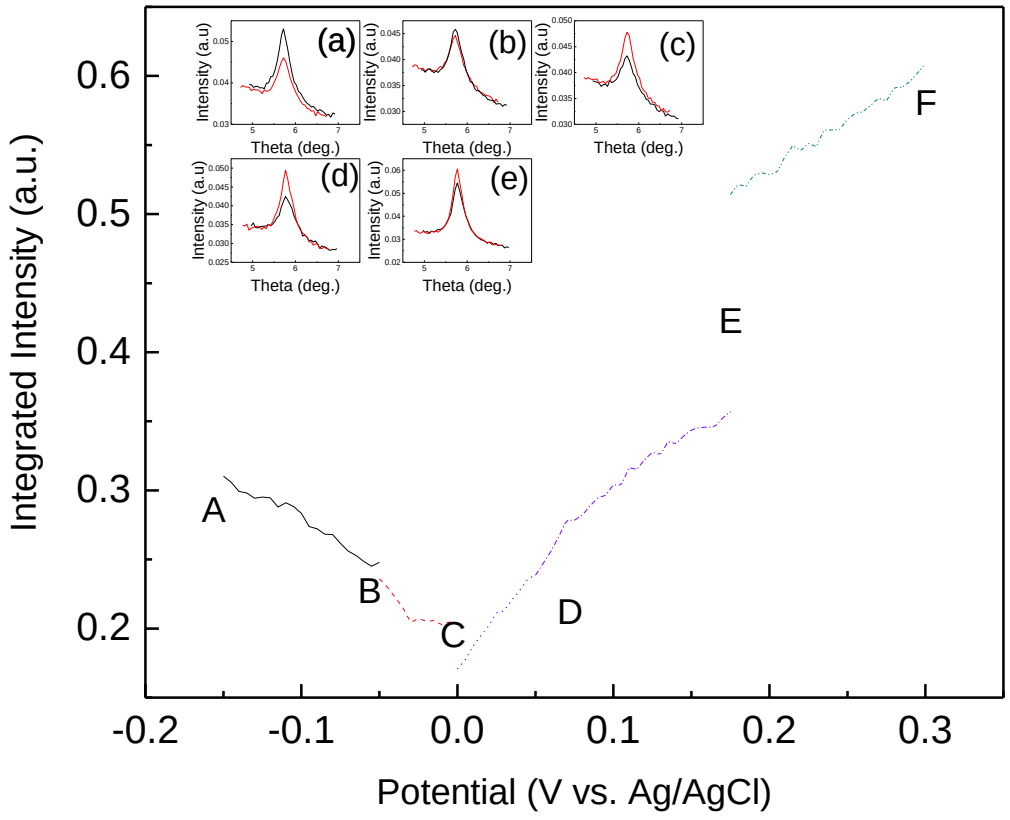

Figure 5.5: Linear XRV sweeps taken from -0.15 V to 0.3 V at (0 0 1.52) at a rate of 2.5mV/s. The insets show the rocking scans measured at (0 0 1.52) prior to and following the XRV measurements (a) -0.15 V to -0.05 V, (b) -0.05 V to 0.05 V, (c) 0.05 V to 0.175 V and (d) 0.175 V to 0.3 V. The black and red lines represent the rocking scans measured prior to and following the XRV measurement respectively.

CTR measurements were then taken at 0.05 V, 0.175 V and 0.3 V (Points D, E and F in Figure 5.5 respectively) to attempt to identify the presence of an Au/Pb surface alloy at intermediate potentials between the clean surface and the surface upon which the rotated hcp Pb layer is observed. These measurements were taken at 12.835 keV with energy scans through the lead L(III) edge taken at each potential as well as at -0.05 V (point B on the potential scale in Figure 5.5). The energy scans were measured at the specular anti-Bragg position (0, 0, 1.52) and were

run in a 'fixed Q' mode, this enabled automated corrections of the diffractometer angles to allow for the position in reciprocal space to remain constant as the wavelength changes. Using the models obtained from the specular CTR profiles, the structure factor at (0 0 1.52) was calculated as a function of energy and then convoluted with a gaussian function representing the energy resolution of the monochromator. A comparison of the model against the energy scans for the data taken at -0.05 V is shown in Figure 5.6.

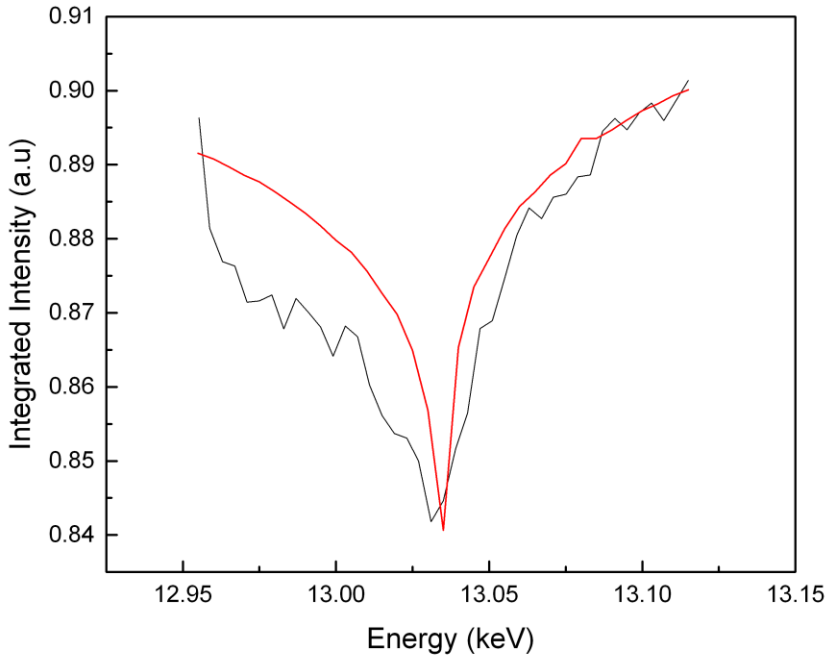

Figure 5.6: Energy scan measured at (0 0 1.52) a so called 'anti Bragg' position at -0.05 V vs Ag/AgCl between 12.985 keV and 13.125 keV. The red line represents the approximation of the scan based on the model for the CTR measured at the same potential.

The next CTR and energy measurements were taken at 0.05 V, the energy data along with the fit to the model is shown in Figure 5.7 (right). The inversion of the 'peak' as it passes through the absorption edge suggests a change in phase, possibly brought about by a variance in the surface layer expansions the lead atoms are present in. Given the significant change in the line shape of the scattered intensity as the energy was increased through the Pb L(III) edge, it was suspected that the surface alloy had formed at this potential. The alloy was modelled as a substitutional alloy of the top Au surface layer with a coverage of Pb equal to *1- θ_{Au}*. The Pb atoms were assigned an expansion parameter separate to the Au surface layer to allow for the buckling of the top layer brought about by the surface alloy formation. The best fit to the measured CTR data at this potential utilising this model is displayed on the left side of Figure

5.7. The parameters for the models obtained at this potential along with the successive measurements at 0.175 V and 0.3 V are shown in Table 5.2. The results show a substitutional surface alloy in the Au:Pb coverage ratio of 0.85:0.15 ± 0.02 with the top Au layer outwardly relaxed by 0.1 Å and the Pb atoms inwardly relaxed by 0.20 Å. This in combination with the large rms of the layer (σ~0.28 Å) implies a buckling of the surface layer. Pb islands are at a distance of 2.84 ± 0.25 Å from the Au(111) electrode surface, closer than that measured at -0.05 V, which implies that the Pb atoms are strongly bonded to the surface, possibly using the substitutional Pb atoms as a nucleation point for the growth of the Pb adlayer. An illustration of the surface structure based on this model is shown in Figure 5.8. Given the nature of the alloy, it is likely that a portion of the Au atoms removed from the surface are intermixed with the Pb adlayer. Indeed, recent STM studies[10] have shown the presence of such Au ad-islands on the Au(111) surface during the UPD process.

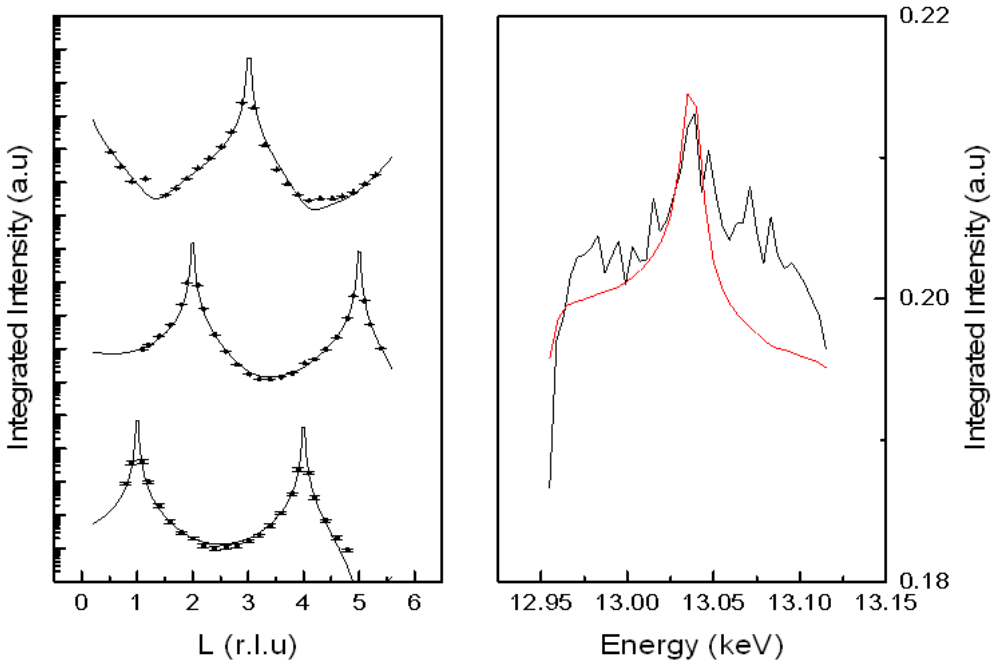

Figure 5.7 left: CTR data of the specular [00L] and non-specular rods [01L] [10L], from top to bottom respectively, measured at 0.05 V. The solid lines represent the best fit found using the outlined substitutional alloy model displayed in Figure 5.8. The CTR data were fit simultaneously. Right: energy scan measured at 0.05 V vs. Ag/AgCl measured at (0 0 1.52). The red line represents the calculated line shape based on the model.

	Parameter	0.05 V	0.175 V	0.3 V
Metal Layers	ε_{34} (Å)	0	0	0
	ε_{23} (Å)	0	0	0
	ε_{12} (Å)	0.1 ± 0.15	0.016 ± 0.006	0.004 ± 0.005
	$\varepsilon_{12\,(Pb)}$ (Å)	-0.39 ± 0.15	0	0
	σ_2 (Å)	0.10± 0.01	0.08 ± 0.02	0.08 ± 0.02
	σ_1 (Å)	0.28 ±0.05	0.22 ± 0.01	0.20 ± 0.01
	$\theta_{1(Au)}$	0.85 ± 0.02	1	1
	$\theta_{1(Pb)}$	0.15 ± 0.02	0	0
Pb adlayer	θ	0.47 ± 0.02	0.33 ± 0.02	0.29 ± 0.03
	d (Å)	2.84 ± 0.25	2.85 ± 0.05	2.88± 0.06
	σ (Å)	0.5 ± 0.3	0.1	0.1
'O' adlayer	θ	0	0.51 ± 0.21	0.34 ± 0.22
	d (Å)	0	5.76 ± 0.23	5.55± 0.40
	σ (Å)	0	0.2	0.2
Error Function	d (Å)	0	0	0
	σ (Å)	0	0	0
	χ2 red	4.22	3.09	2.71

Table 5.2: Best fit parameters and their associated errors for the CTR data measured at 0.05 V, 0.175 V and 0.3 V.

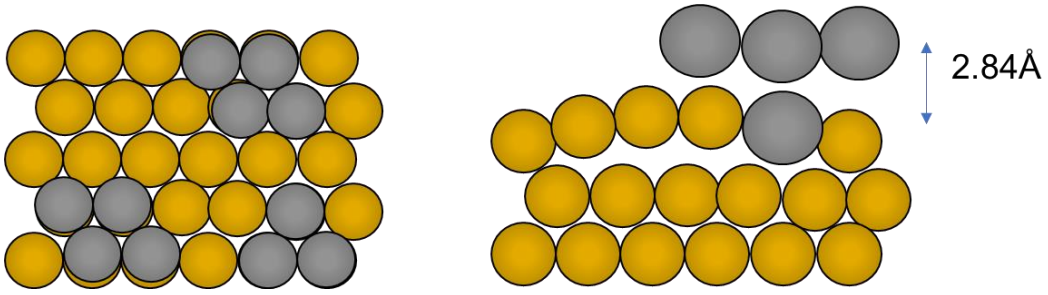

Figure 5.8: Illustrations showing the 'top' and 'side' views of the substitutional surface alloy model used for the data measured at 0.05 V. Pb atoms and Au atoms are displayed as the grey and yellow circles respectively.

CTR data and energy scans were measured at 0.175 V following potential sweep D to E. The best fit to the CTR data and the resultant fit to the model vs. the measured energy scan data is shown in Figure 5.9. No evidence of the substitutional alloy found at 0.05 V is observed at this potential, instead the coverage of the Pb adlayer remains constant at a coverage of

approximately 0.3 and a negligible change in the layer spacing from 2.84 ±0.38 Å to 2.85 ± 0.05 Å. Comparing these values, along with the final set of CTR and energy measurements taken at 0.3 V that is shown in Figure 5.10 and the best fit parameters are shown in Table 5.2, is perhaps of more value as the parameters for the data taken at 0.175 V and 0.3 V are almost identical. This would appear to suggest that, once the surface has de-alloyed the remaining Pb islands are relatively stable until the final stripping peak around 0.4 V. To achieve the best possible fit for the specular CTRs, the introduction of an oxygen adlayer was required. The 'oxygen' layer was used to approximate the adsorption of hydroxide molecules. The presence of OH^- at potentials positive of the main UPD peaks correlate with the measurements taken in AFM[109] and results on Pt(111) electrodes[120, 121].

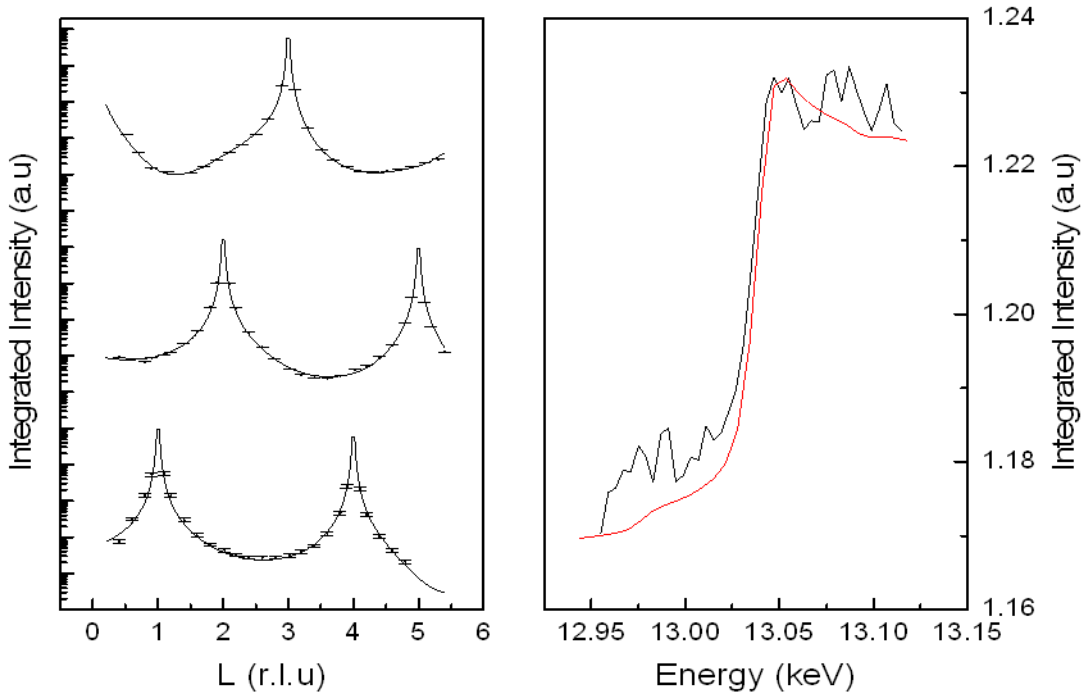

Figure 5.9 left CTR data of the specular [00L] and non-specular rods [01L] [10L], from top to bottom respectively, measured at 0.175 V. The solid lines represent the fit to the data using the model in Figure 5.11 Right: Energy scan measured at 0.175 V vs. Ag/AgCl measured at (0 0 1.52). The red line represents the calculated line shape based on the model.

.

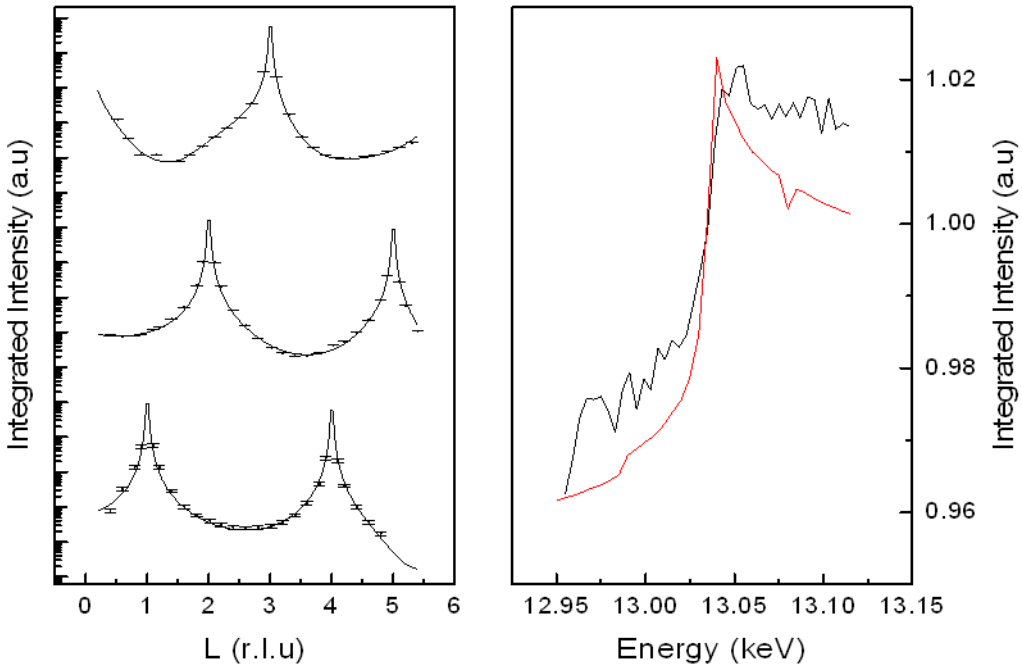

Figure 5.10 left: CTR data of the specular [00L] and non-specular rods [01L] [10L], from top to bottom respectively, measured at 0.3 V. The solid lines represent the fit to the data using the model in Figure 5.11. Right: Energy scan measured at 0.3 V vs. Ag/AgCl measured at (0 0 1.52). The red line represents the calculated line shape based on the model.

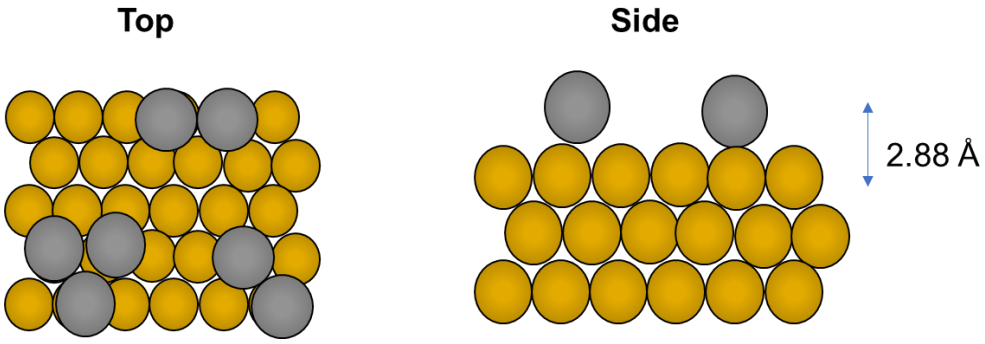

Figure 5.11: Illustrations of the 'top' and 'side' views for the model obtained from the best fits to the data measured at 0.175 V and 0.3 V.

From the results reported here the following process is suggested. As the Pb hcp overlayer is stripped from the surface brought about by the potential being scanned anodically, a substitutional Pb/Au surface alloy forms in an effort to reduce the total surface energy of the system[93]. As the potential continues to be scanned anodically and Pb adatoms continue to be stripped from the Au electrode surface it is likely more energetically favourable for the

electrode surface to de-alloy prior to the complete stripping of Pb adatoms from the Au surface. As a result, the coverage of the deposited Pb adlayer remains fairly constant up to the final anodic stripping peak at 0.4 V. It can therefore be inferred that there is a threshold of deposited Pb on the Au(111) electrode of coverage ~0.33, prior to which the deposited Pb is stable without surface alloying occurring. It is possible that the adsorption of hydroxide species at these potentials stabilises the Pb islands at these coverages.

Studies of Pb UPD on Pt(111) systems share similarities with the processes observed on Au(111). Indeed, the voltammetric profile for gold and platinum electrodes in the presence of lead cations in solution changes slightly in the oxide region[94, 101, 120, 121].This suggests the presence of residual lead on the electrode surface brought about by an irreversible adsorption process. Furthermore, as already mentioned at potentials positive of the main UPD peaks, AFM studies[109] indicate the presence of hydroxide species based on the adlayer height being larger than that of metallic lead. The presence of partially charged lead species at these potentials has also been indicated by electroreflectance studies[99], which would appear to agree with the results found here. Lead has also been found to alloy with Pt(111) electrodes in the presence of bromide[123]. Contrary to the apparent alloy formation reported here, the Pt_3Pb alloy consists of a p(2 x 2) structure that forms when the potential is held at ~0 V (vs. Ag/AgCl) over a period of ca. 2 h. This structure is not present in bromide-free solutions however, suggesting that bromide in solution ‘catalyses’ the kinetics of alloy formation.

5.5 Au(100) in 0.1 M KOH +1 mM $PbCO_3$

Although analysis of the Au(100)/Pb UPD system is as yet incomplete, the data shows some interesting features that are worthy of discussion. Figure 5.12 displays XRV measurements taken between 0.05 V and -0.7 V at a scan rate of 5 mV/s. Figure 5.12(a) shows the XRV measurement taken at (1, 1, 0.2), a position near to the ‘anti-Bragg’ position sensitive to ordering commensurate to the Au surface. As the potential is scanned in the cathodic direction, the intensity remains constant until approximately -0.55 V where the intensity sharply decreases. On the anodic sweep, the intensity continues to decrease until around -0.65 V where the intensity then gradually increases back to its original value at the anodic limit. This change in intensity is also observed (Figure 5.12(b)) at (0, 0 ,3.02) and ‘anti-Bragg’ position on the specular CTR. This could imply that the decrease in intensity is indicative of the formation of the incommensurate hcp overlayer prior to bulk deposition beginning to occur around -0.6 V.

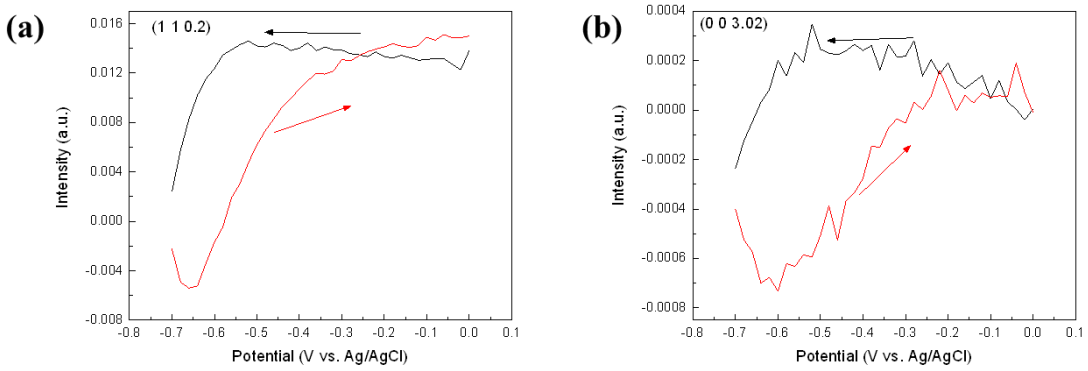

Figure 5.12: scattered intensity as a function of applied electrode potential between 0.05 V and -0.7 V at a scan rate of 5 mv/s at (a) the (1, 1, 0.2) CTR position; (b) (0, 0, 3.02) an 'anti-Bragg' position on the specular CTR and The arrows indicate the direction of the scanned potential for the red and black lines respectively.

Figure 5.13(a) shows specular and non-specular CTR measurements taken at 0.05 V (black), -0.4 V(red) and -0.6 V(blue). From inspection of the CTRs, at 0.05 V and -0.4 V there appears to be slight oscillation along the L direction. The oscillation is not present in the data measured at -0.6 V which is possibly due to a structural change of the deposited Pb at his potential. This oscillation is more prominent in the CTR measurements shown in Figure 5.13(b). These measurements were taken following repreparation of the Au(100) electrode surface by repeated potential cycles in Pb-free electrolyte to ensure no lead was deposited on the surface and then flame annealed as outlined in 3.1. Following alignment of the crystal, the potential was contacted at 0.05 V and specular and non-specular CTR data were measured at 0.05 V (black), -0.4 V (red) and -0.55 V (blue). From inspection of Figure 5.13(b) the oscillation observed in Figure 5.13(a) at 0.05 V and -0.4 V is significantly more pronounced and is present at all measured potentials following repreparation. The increase in the size of the oscillation the measurements conducted at -0.55 V show evidence of the structure observed at 0.05 and -0.04 V although with a significantly reduced intensity, this correlates with the reduction in intensities observed on the XRV measurements and is likely indicative of a change in the Pb structure, possibly the formation of an incommensurate hcp overlayer. The presence of this structure following re-preparation is indicative of either spontaneous formation of a Pb structure on the Au(100) surface or an irreversible change having occurred to the Au(100) electrode. Further experiments have since been conducted using the same Au(100) crystal and no evidence of an irreversible change brought about by the measurements outlined here has been observed. This is evidenced by the measurements of the Au(100) 'hex' reconstruction discussed in Chapter 4. Therefore, it can be concluded that the observed changes to the CTR profiles are brought about by a spontaneous formation of a deposited Pb structure on the

Au(100) surface. This type of behaviour has not been reported in the literature before, however previous investigations into the Au(100)/Pb interface have been conducted in acid solution implying that the observed changes here could be an effect brought about by the measurements being conducted in alkaline solution.

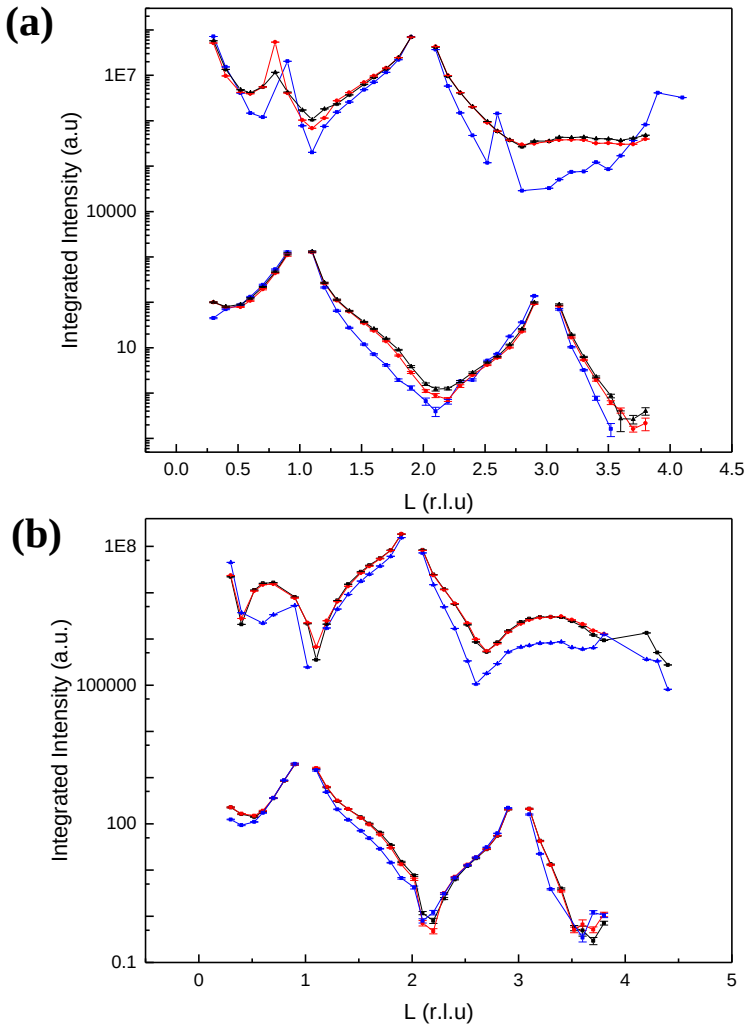

Figure 5.13: Specular(top) and non-specular(bottom) crystal truncation rod data measured on the Au(100) electrode surface in the presence of 0.1 M KOH +1 mM $PbCO_3$ (a) 0.05 V (black), -0.4 V(red) and -0.6 V(blue). (b) CTR measurements conducted following the repreparation of the Au(100) electrode surface at 0.05 V (black), -0.4 V (red) and -0.55 V(blue).

Current attempts to analyse the CTR data have focussed on the data measured at 0.05 V following the repreparation of the Au(100) electrode as this has the most prominent oscillation along the L direction. Attempts to fit the data using the structures reported in the literature (c(2 x 2) and c(3√2 x 2)R30°)[116, 117] have so far been unsuccessful. The current best approximation of a fit to the data is shown in Figure 5.14. The values for the parameters for the best fit to the data are shown in Table 5.3. The model was calculated by varying the layers of

Au. The bottom gold layer (layer 3 in the table) is assumed to be the Au surface with the two layers above it approximating the Pb structure. The model positioned the second layer on the bridge site (1/2, 0) of Au(100) surface with the layer above being located at a position (3/2, 3/2) relative to the assumed top gold layer. Both layers have an occupancy of approximately 0.5. With this information it appears to suggest that the Pb structure that has formed is a (2 x 1) bilayer structure, nevertheless, attempts to fit this using a (2 x 1) structure have been as yet unsuccessful.

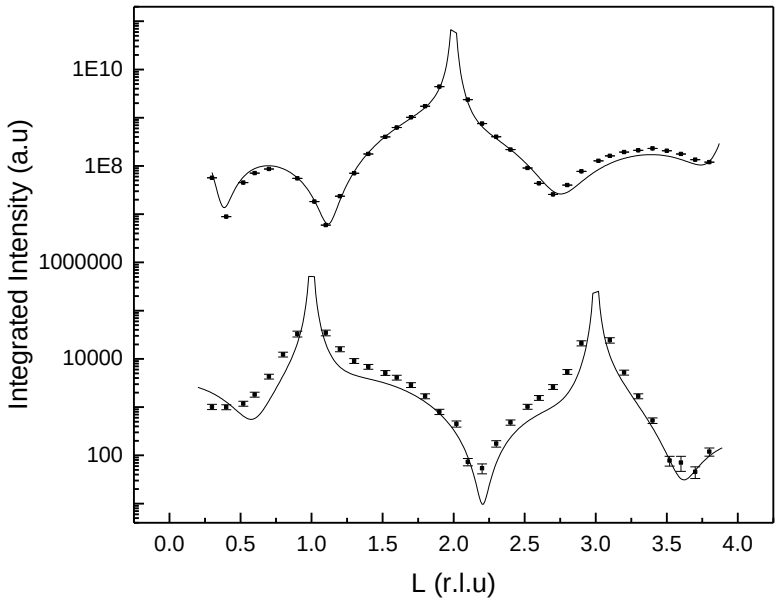

Figure 5.14: Specular (top) and non-specular (bottom) CTR data measured at 0.05 V following repreparation of the Au(100) electrode surface. The solid line represents the current best approximation of a fit to the data.

	Parameter	0.05 V
Metal Layers	**ε_{34} (Å)**	0
	ε_{23} (Å)	0.70 ± 0.03
	ε_{12} (Å)	0.33 ± 0.03
	σ_3 (Å)	0.01
	σ_2 (Å)	0.05
	σ_1 (Å)	0.05
	θ_3	1
	θ_2	0.47 ± 0.01
	θ_1	0.44 ± 0.02
	χ2 red	9.7

Table 5.3: Parameters and their associated errors obtained from linear least squares fitting methods for the best fit to the CTR data measured at 0.05 V. The model consists of three layers of Au with the top two layers being used to approximate the Pb structure. The second gold layer is located on the bridge

sites of the layer beneath and the third layer of gold.

5.6 Conclusions and Summary

Using *in-situ* x-ray scattering studies, a substitutional Au/Pb surface alloy in the ratio of ~ 4:1 has been identified at partial coverages of Pb which had formed during the stripping process of Pb from the Au(111) electrode surface. It is proposed that the alloy forms to reduce the surface strain and as a result the total surface energy as has been suggested by theoretical models of surface alloy formation on immiscible systems. As the potential is scanned anodically, it is shown that the surface has de-alloyed prior to the complete removal of the deposited Pb adatoms from the Au surface. It is suggested that at Pb coverages below 0.33 surface alloying does not occur. Measurements on the Au(100) electrode surface show an apparent spontaneous formation of a (2 x 1) Pb bilayer structure. This is observed to occur irrespective of potential or surface preparations. A series of exploratory reciprocal space scans and x-ray voltammetry measurements would yield insight into the nature of the Pb structure forming on the Au(100) surface and enable accurate fitting of the CTR data.

6 The Adsorption of Acetonitrile at the Au(111)/Electrolyte Interface

6.1 Introduction

An important aspect of surface electrochemistry and the development of new catalysts is understanding the effect of adsorbed species on electrode surfaces. This is because adsorbed molecules can strongly affect electrode reactions. The study of the adsorption of small organic molecules and their influence on electrode surfaces can help to resolve the following key questions remaining before a fundamental understanding of interfacial phenomena at a molecular level can be achieved: the influence of water on electrocatalytic reactions and its structure, the role of anions in the electrochemical double layer and the nature of bonding between metals and organic species. Acetonitrile (CH3CN) is one of the most widely used polar aprotic solvents in electrochemistry since it is miscible in aqueous solutions, has a high dielectric constant and a wide potential window [124]. In addition, acetonitrile (AcN) is a mildly dissociative organic solvent comprised of polar, covalent bonds and functions primarily as a weak Lewis base and can bond with charge-withdrawing sites such as transition metal centres[125].

AcN adsorption from aqueous solutions has been extensively studied on Pt(111)[125, 126], polycrystalline platinum Pt(poly)[1, 4] and platinised platinum Pt/Pt[128–130] via cyclic voltammetry and various spectrometry techniques. Some references[11, 125, 126] report that chemisorbed AcN undergoes reduction/oxidation quasi-reversibly during potential cycling. Cyanide ions have been detected in Raman spectroscopy studies[132] at potentials around 0.1 V (vs. Ag/AgCl) on polycrystalline platinum electrodes as well as copper[133] and silver foils[134]. A combination of CV and mass spectrometry measurements on porous Pt electrodes in aqueous solution 0.005 M H_2SO_4 + 0.05 M AcN have shown that at higher potentials (> 0.5 V) adsorbed acetonitrile may undergo oxidation to CO_2 and NO_x and reduction to ethane and ammonia at potentials below -0.1 V. There has also been discussion based upon high-resolution vibrational spectroscopy (HREELS), Auger electron spectroscopy (AES) and LEED measurements, of AcN being partially converted to acetamide CH_3CONH_2, a product of AcN hydration. However, it has been shown that cyclic voltammetry measurements [127] in sulphuric acid solutions containing acetamide differ from those obtained in the presence of acetonitrile. Radioactive-tracer techniques[130] have established that the adsorption of AcN occurs around 0.8 V (vs. Ag/AgCl) after partial desorption of oxygen. In the same study it was suggested that the kinetics of AcN adsorption on Pt electrodes

is slow. More recent studies of AcN adsorption on Pt electrodes in sulphuric acid have confirmed that above 0.8 V there is no electrochemical conversion of AcN whilst at higher potentials on polycrystalline Pt electrodes, the oxidation of AcN proceeds simultaneously with the desorption of its products[12]. AcN has also been shown to block adsorption sites for H^+ and OH^- ions[128].

Similar studies on Au electrodes have been carried out however, to a lesser extent. On polycrystalline gold in perchloric acid solutions it was shown, via *in-situ* vibrational spectroscopy[135], that two types of bonding of AcN molecules existed at the interface. One of which being a chemisorbed AcN molecule with its dipole vector perpendicular to the interface with its negative end bonded to the surface. The other being AcN molecules hydrogen bonded to chemisorbed water molecules which results in AcN being situated further away from the electrode surface. Studies on both polycrystalline gold in perchloric acid and Au(111) in sulphuric acid have shown that the effect of AcN adsorption is much weaker on those systems in comparison to that of polycrystalline Pt and Pt(111) electrodes respectively[4, 11]. Figure 6.1 shows a series of CV measurements taken from [12] of the Au(111) electrode surface in 0.5 M H_2SO_4 and increasing concentrations of AcN. In sulphuric acid the presence of the "disordered (bi)sulphate -(√3 x √7)R19.1°" structure found on Au(111) electrodes[136] is still present around 0.8 V (~1 V vs SHE in Figure 6.1) and almost independent of the AcN concentration. In perchloric acid, the inhibiting effects of AcN on the kinetics of the oxygen reduction reaction on polycrystalline gold are shown to be very pronounced[128].

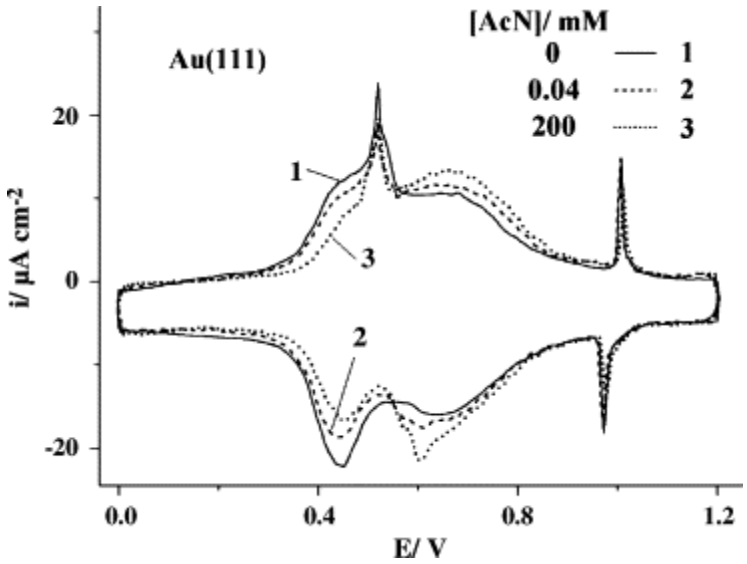

Figure 6.1: Cyclic voltammetry measurements (vs. Standard Hydrogen electrode) of Au(111) in 0.5 M H_2SO_4 with the addition of AcN at 0.1 V/s . AcN concentration, mM: (1) 0; (2) 0.04; (3) 200. Reprinted from[12]. Copyright 2009, with permission from Elsevier.

The underpotential deposition of copper onto transition metal single crystals in AcN free solutions has been extensively studied in the past using many of the techniques available to investigate the behaviour of these systems, ranging from electrochemical methods[136–139], *in-situ* STM[140–143], AFM[144, 145], X-ray techniques[146–148] and *ex-situ* UHV techniques such as LEED[149–151]. These studies have provided detailed knowledge of these systems particularly Cu UPD on Au(111) electrodes in sulphuric media. Initial structural studies of the copper adlayer were carried out in the UHV environment via RHEED and LEED measurements[149–151]. The results yielded two different structures at two stages of deposition; a (√3 x √3)R30° honeycomb structure at a coverage θ_{Cu} = 0.67 and a (1 x 1) structure at coverage θ_{Cu} = 1. There was some controversy as to the nature of the honeycomb structure, initial STM[19, 21, 31–33] and AFM[145] measurements yielded a (√3x√3)R30° structure, taking the highest points on the surface to be Cu adatoms implying a coverage of copper for this structure to be θ_{Cu} = 0.33. These contradicted results found via electrochemical quartz crystal microbalance (EQCM)[155–159] and chronocoulometry[155, 156] measurements that indicated a coverage of copper for this initial stage in the deposition process to be θ_{Cu} = 0.67 with (bi)sulphate anions deposited with a coverage θ_{anions} = 0.33. These results were reconciled via in-situ surface x-ray scattering studies carried out by Toney *et al*.[148] which found that the Cu adlayer at intermediate coverages has a honeycomb (√3x√3)R30° structure. In this structure θ_{Cu} = 0.67 with copper atoms occupying 3-fold hollow sites of the Au(111) surface and (bi)sulphate anions occupying the centres of the honeycombs with θ_{anions} = 0.33, in agreement with EQCM and chronocoulometry measurements. Therefore, what had previously been interpreted as Cu atoms in STM and AFM measurements were the (bi)sulphate anions protruding well above the Cu plane occupying the centres of the honeycomb. At the second stage of the UPD process, copper atoms fill the honeycomb structure to form a pseudomorphic (1 x 1) structure with (bi)sulphate adsorbed on top of the copper adlayer. The nature of this (bi)sulphate layer had been under some debate, thermodynamic and coulometry studies by Shi *et al*.[140] revealed that the (bi)sulphate anions form a (√3 x √7)R19.1° structure on top of the Cu UPD monolayer, the same structure observed on both bulk Au(111) and Cu(111). In contrast to this in-situ x-ray scattering studies[161] and EQCM[162] measurements showed that the sulphate structure actually formed a (√3x√3)R30° structure. Recent STM studies by Madry *et al*.[144] found that at monolayer coverage of copper the (bi)sulphate anions form a (√3 x √7)R19.1° structure and as the copper coverage increases to θ_{Cu} = 1.67 the honeycomb (√3x√3)R30° structure that is found at coverage θ_{Cu} = 0.67 is formed on top of the (1 x 1) copper monolayer. Figure 6.2 displays a characteristic CV in the Cu UPD region taken from [143] of the Au(111)/ Cu UPD system in sulphuric acid. On the cathodic sweep the first sharp peak at 0.2 V represents the formation of the honeycomb (√3x√3)R30° structure at copper coverage 0.67, the second sharp

peak represents the formation of the pseudomorphic (1 x 1) layer at copper coverage 1. Figure 6.3(a) and (b) show illustrations of the (√3 x √7)R19.1° (bi)sulphate structure and the copper honeycomb (√3x√3)R30° structure respectively.

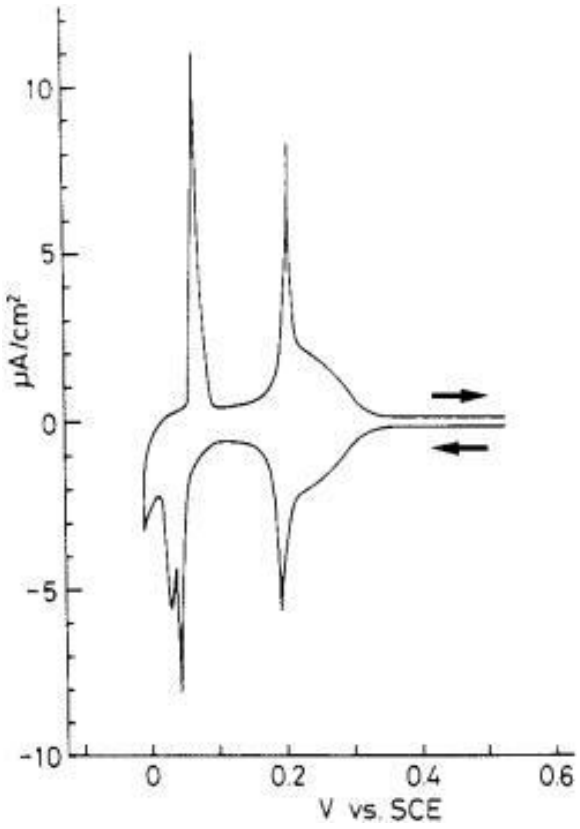

Figure 6.2: CV profile of the Au(111) electrode in 0.05 M H_2SO_4 +1 mM $CuSO_4$. Scan rate 1 mV/s. Reprinted from[143]. Copyright 1991, with permission from Elsevier.

Studies into the effect acetonitrile has on Cu UPD on gold electrodes are limited[162, 163]. In the presence of AcN Cu^+ ions can be stabilised by forming a $[Cu(C_2H_3N)_4]^+$ complex[165], whereas in aqueous solutions copper cations are rapidly reduced from Cu(II) to Cu(0). As such it has been suggested that the $[Cu(C_2H_3N)_4]^+$ ion may interact directly with the electrode surface via much weaker electrostatic forces and as such have a much smaller distance between the $[Cu(C_2H_3N)_4]^+$ ion and the electrode surface compared to Cu deposited in AcN free solutions[164]. Furthermore, due to the formation of this complex, in sulphuric acid solutions the formation of the characteristic copper honeycomb (√3x√3)R30° structure would be hindered. The effect of AcN on Cu deposition on Pt electrodes in sulphuric acid has also been studied[166] and found that AcN competes with Cu atoms for adsorption sites at step edges.

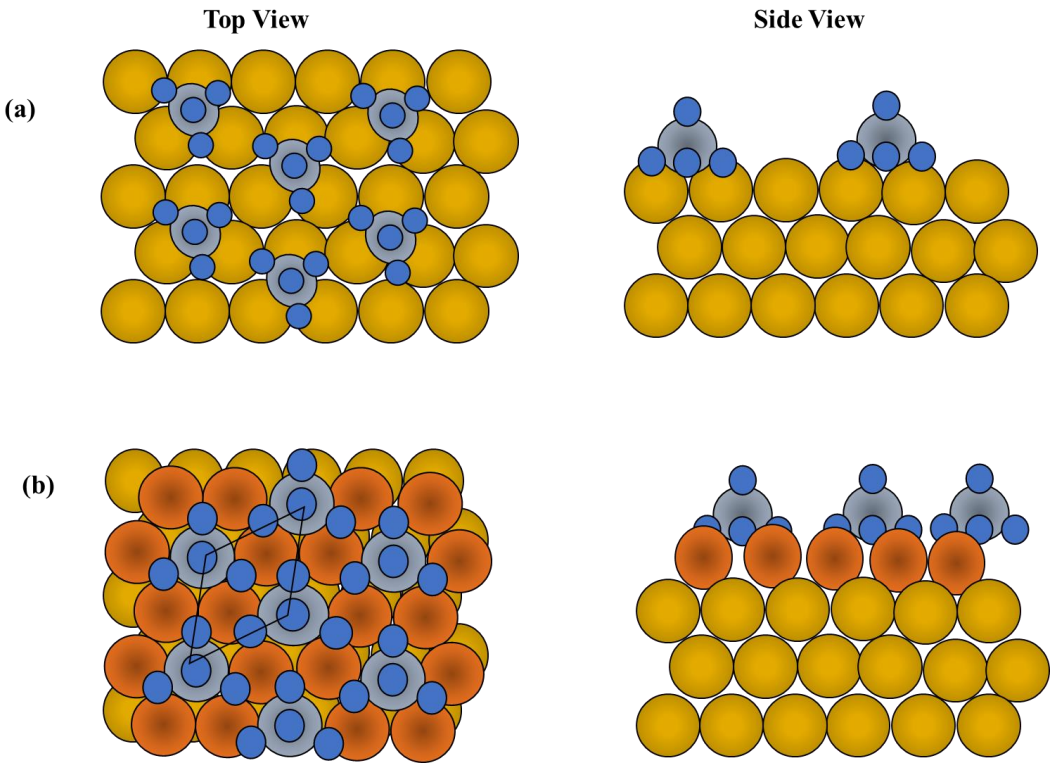

Figure 6.3:Illustrations showing the 'top' and 'side' views for (a) the (bi)sulphate(√3 x √7)R19.1° structure on the bulk Au(111) electrode surface and (b) the (√3x√3)R30°copper honeycomb structure. The gold atoms are represented by the yellow circles, copper atoms are represented by the brown circles. Sulphur atoms and oxygen atoms are represented by the grey circles and blue circles respectively.

In this chapter *in-situ* scattering is used to probe the adsorption of AcN on the Au(111) electrode surface in sulphuric acid solution at various concentrations of AcN. The interaction between Cu and AcN and its effect on the Au(111)/Cu UPD process in sulphuric acid solution is also explored.

6.2 Experimental

Measurements were conducted at MS - X04SA: Materials Science surface diffraction beamline at the Swiss Light Source in Villigen, Switzerland, using focussed x-rays at an energy of 11.8 keV. The Au(111) crystal was prepared and transferred into the x-ray electrochemical cell using the methodology outlined in chapter 3.1, the sample was then transferred into the thin layer x-ray electrochemical cell and mounted on the diffractometer. The electrolyte consisted of 0.1 M H_2SO_4 solution, for the Cu UPD measurements, 1 mM of $CuSO_4$ was added to the electrolyte solution. For the measurements with 10 mM and 1 M acetonitrile, the potential was disconnected, and the electrolyte was exchanged. The counter electrode was Au polycrystalline wire and the reference electrode was Ag/AgCl (WPI- Leak-Free reference electrode, catalogue no. 69-0023 [LF – 2]). Prior to x-ray measurements the

potential was cycled between 0.8 V and -0.2 V at a sweep rate of 50 mV/s to improve the surface ordering as was similarly carried out in Chapter 4.

6.3 Au(111) in H2SO4

To provide a comparison for the effect of AcN on the Au(111) electrode in sulphuric acid media, the system was first characterised in clean 0.1 M H_2SO_4. Figure 6.4 (a) shows an XRV measured at the (0.0185 1.0185 0.52) reciprocal lattice position, sensitive to the formation and lifting of the Au(111) (p x $\sqrt{3}$) surface reconstruction, between -0.2 V and 0.8 V at a sweep rate of 5 mV/s. The sharp decrease in intensity on the anodic sweep at ~0.3 V at this position is characteristic of the lifting of the (p x $\sqrt{3}$) surface reconstruction on the Au(111) electrode surface. On the cathodic sweep the intensity remains constant until ~0.1 V where the intensity starts to gradually increase however, does not reach the intensity observed at the beginning on the scan showing the reconstruction reforms very slowly. Figure 6.4(b) shows reciprocal space scans measured in the [0, 1, 0] direction through the (0, 1, 0.52) CTR position and the reconstruction peak at ~(0.02, 1.02, 0.52) .The black line represents the scan measured prior to the XRV scan and the other lines represent repeated measurements taken after the XRV at 0.55 V. The reconstruction peak that is present in the initial scan is absent in following scans in accordance with the XRV measurement and does not recover on subsequent scans. This is expected as 0.55 V is too positive for the formation of the surface reconstruction to begin. Figure 6.4 (e) shows a comparison of XRV measurements at (0 1 3.2) over the potential range of 0.55 V to 1 V and 0.55 V and 0.9 V for the AcN free solution (black line) and 10 mM AcN (red line) electrolytes respectively, both measurements were taken at a sweep rate of 5 mV/s. As can be seen from the comparison, the addition of 10 mM AcN to the electrolyte appears to have no effect on the metal layer ordering when compared to AcN free solution.

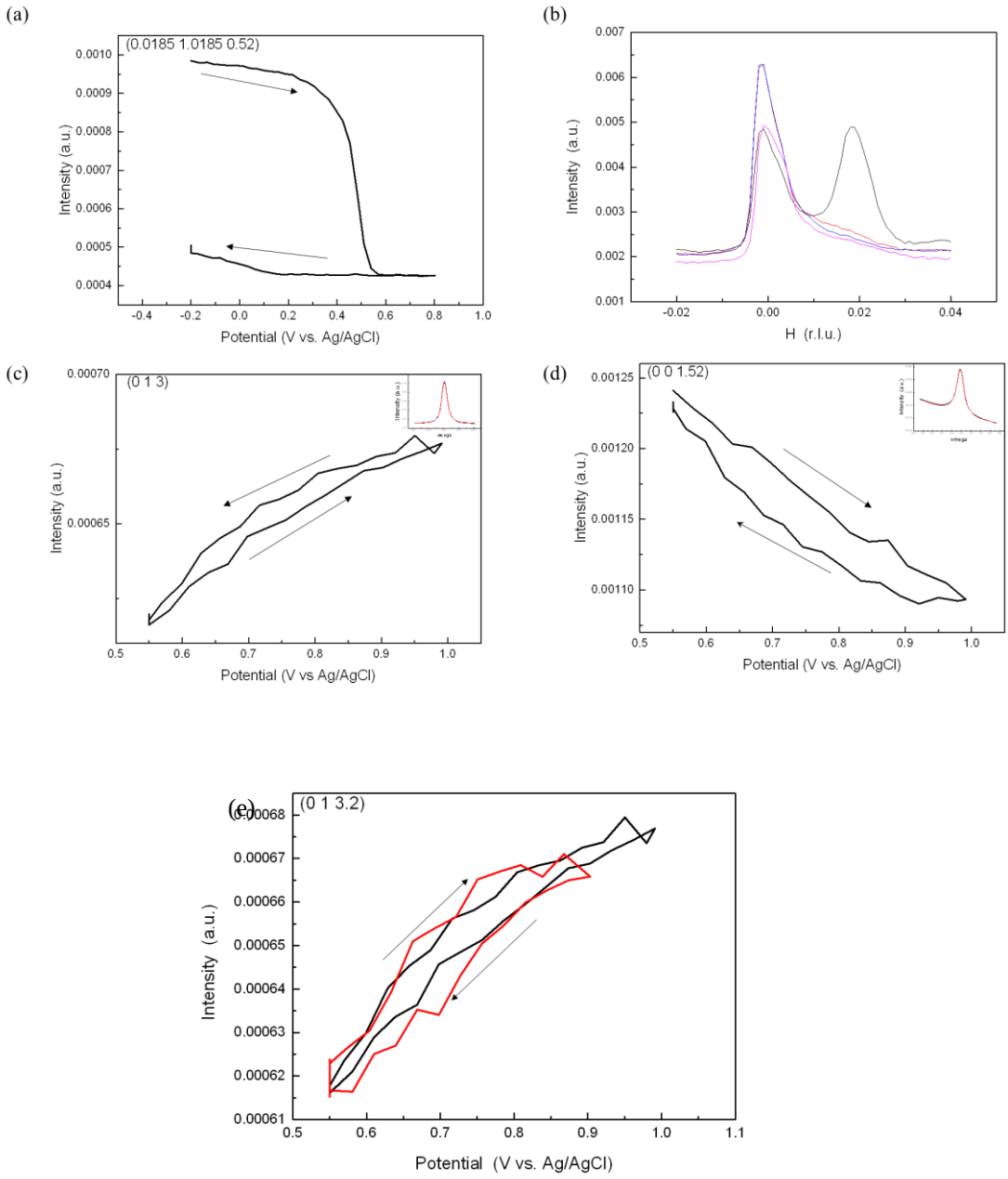

Figure 6.4(a)Scattered intensity as a function of the applied potential for the Au(111) electrode surface in 0.1 M H_2SO_4 measured at (0.0185, 1.0185, 0.52) a position sensitive to the (23 x √3) surface reconstruction between -0.2 V and 0.8 V. (b) reciprocal space scans taken in the [1 1 0] direction at a potential of -0.2 V through the peak at the (0, 1, 0.52) CTR position and the peak at ~(0.02, 1.02 0.52) arising from the surface reconstruction. The black line indicates the initial reciprocal space scans with the other coloured lines representing subsequent scans measures at 0.55 V. (c) X-ray voltammetry measurements between 0.55 V and 1.0 V at (0, 1, 3) . (d) XRV measurement between 0.55 V and 1.0 V at (0, 0, 1.52) an 'anti-Bragg' position on the specular CTR. (e) Comparison of XRV measurements between 0.55 V and 1.0 V in AcN free (black) and 10 mM AcN solution (red) at the (0, 1, 3.2) CTR position.

CTR data were measured at potentials of 0.7 V, 0.8 V and 1.15 V in AcN free and 10 mM AcN solutions. The model used to fit the CTR data in this chapter and account for adsorbates and the scattering from the bulk electrolyte is detailed in Chapter 2. An illustration of the model used is shown in Figure 6.5 Sulphate molecules for the data in this chapter have been modelled as single scattering centres, instead of the individual elements and corresponding bonds. The AcN molecule has been modelled by using the atomic form factor for carbon as nitrogen and carbon have similar atomic numbers. For each adsorbate layer the rms roughness was fixed slightly above the rms of Au at 0.15 Å. To account for scattering from the bulk electrolyte the model included an error function representing the bulk electrolyte of width 0.5 Å and a maximum density equal to that of the bulk density of water at a height determined by the best fit to the data. The number of adlayers chosen and thus the complexity of the model was determined by whether there was any reduction in the reduced χ^2 between the data and the model. Figure 6.6 shows the CTR data measured in AcN free (black) and 10 mM AcN (red) solutions overlaid to show a comparison of the data. The models for the best fit to the data for the measurements in AcN free solution and 10 mM AcN solution are also shown as the solid lines. Table 6.1 displays the best fit parameters for the models. From inspection of the CTR data in Figure 6.6(a-c) it can be seen that there are negligible changes between the AcN free data and the data measured in 10 mM AcN solution except for the [00L] 'specular' CTRs. Indeed, the parameters in Table 6.1 show changes of <0.01 Å in terms of metal layer relaxation and small changes in the rms disorder.

Specular CTR data or extended reflectivity are only sensitive to ordering along the surface normal and are therefore a measure of the vertical electron density profile. Figure 6.5(b) shows how a vertical electron density profile relates to the model for AcN adsorption used here. Figure 6.7 shows the vertical electron density profiles normalised to the bulk density of water for the data measured in 10 mM AcN solution at 0.8 V (blue) and 0.7 V (red). Each profile includes a resolution broadening where the electron density is plotted as a Gaussian distribution that has an effective vibrational amplitude (u_{eff}) corresponding to the vibrational amplitude of the atom (σ) and a resolution determined width (u_{res}) added in quadrature, or $u_{eff} = \sqrt{{u_{res}}^2 + \sigma^2}^2$ where $u_{res} = 1.1/Q_{max}$ and Q_{max} is the maximum momentum transfer of the measurement. The choice of u_{res} is determined by consideration of a Patterson function and is discussed in more detail in Ref. [167]. The effective electron density is then:

$$\rho_{eff}(z) = \frac{\tau\theta Z}{(2\pi)^2 u_{eff} e^{\frac{1}{2}\left(\frac{z-z_0}{u_{eff}}\right)^2}}$$

where z_0 is the position above the surface of an atom with charge Z, θ is the coverage and τ is the inverse unit cell area.

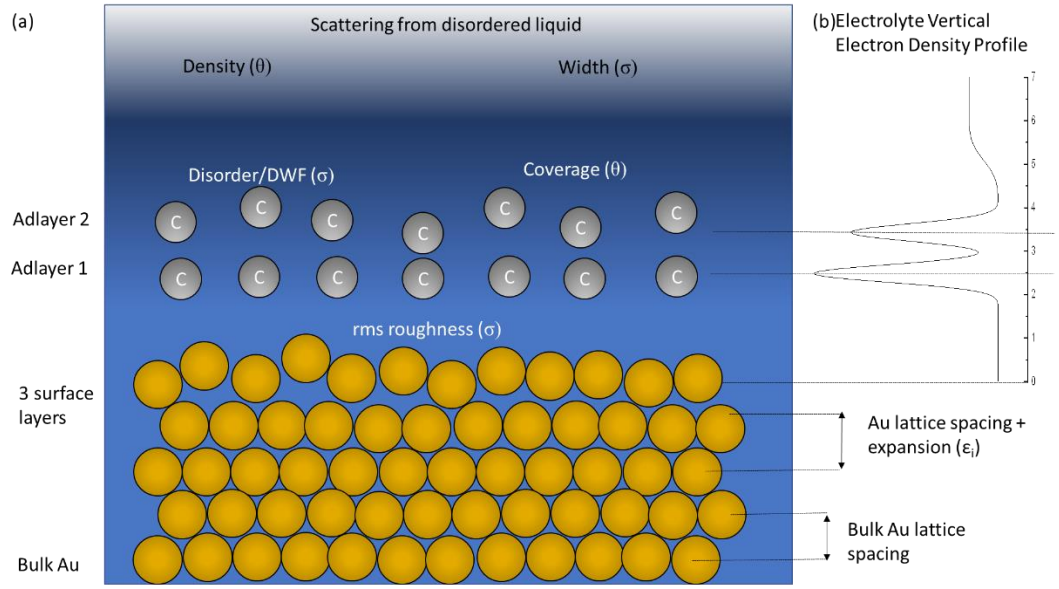

Figure 6.5: (a) illustration of the model used to fit the data. The model comprises of bulk metal layers and surface layers. Above the metal layers, several adlayers are included, modelled with the form factor for carbon. Above that is an error function to account for scattering from the bulk electrolyte. (b) The graph shows how a vertical electron density map corresponds to various components in the model.

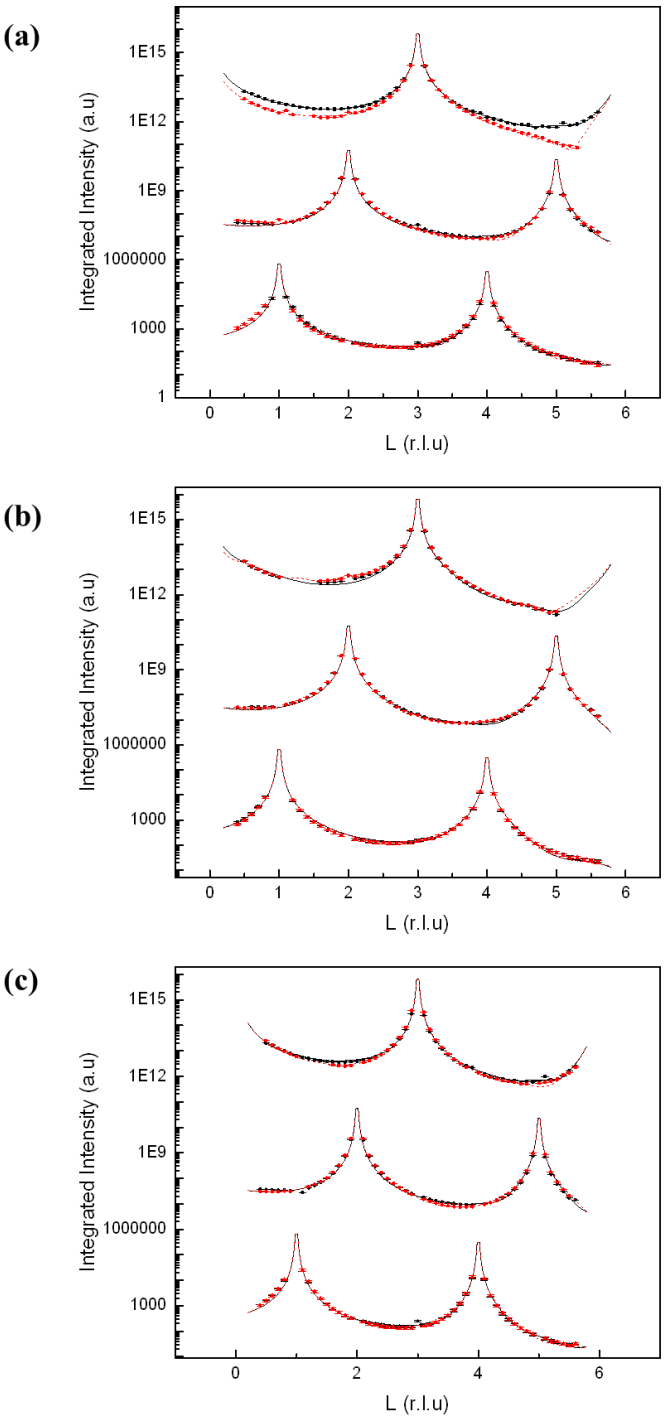

Figure 6.6: Fits to, from top to bottom, the specular and non-specular crystal truncation rods for the Au(111) electrode surface in 0.1 M H_2SO_4 AcN free(black symbols) and 10 mM AcN (red symbols) solutions measured at (a) 1.15 V; (b) 0.8 V and (c) 0.7 V. Measured data is shown as squares with error bars and corresponds to the background subtracted intensity normalised to the monitor and corrected for the diffraction geometry. A systematic error of 10% is assumed. The soli lines represent the best fits obtained to the data.

	Parameter	0.7 V		0.8 V		1.15 V	
			10 mM AcN		10 mM AcN		10 mM AcN
Metal layers	ε_{23} (Å)	0	0.008 ± 0.002	0	0	0	-0.004 ± 0.003
	ε_{12} (Å)	0.014 ± 0.003	0.014 ± 0.004	-0.007 ± 0.003	-0.004 ± 0.002	-0.020 ± 0.003	-0.028 ± 0.003
	σ_2 (Å)	0.100 ± 0.004	0.085 ± 0.006	0.100 ± 0.004	0.082 ± 0.005	0.100 ± 0.004	0.100 ± 0.004
	σ_1 (Å)	0.140 ± 0.002	0.150 ± 0.05	0.157 ± 0.007	0.150 ± 0.008	0.140 ± 0.002	0.150 ± 0.004
	$\theta_{1(Au)}$	1	1	1	1	1	1
Sulphate	θ	0	0	0.24 ± 0.08	0.27 ± 0.08	0	0
	d (Å)	0	0	2.984 ± 0.39	3.084 ± 0.4	0	0
	σ (Å)	0	0	0.05	0.05	0	0
Adlayer 1	Layer	n/a	C	O	C	O	O
	θ	0	1.44 ± 0.25	0.48 ± 0.12	0.22 ± 0.14	0.21 ± 0.07	1.63 ± 0.37
	d (Å)	0	2.29 ± 0.04	2.40 ± 0.10	2.33 ± 0.45	2.48 ± 0.17	2.43 ± 0.08
	σ (Å)	0	0.15	0.05	0.15	0.05	0.2
Adlayer 2	Layer	n/a	C	n/a	C	n/a	n/a
	θ	0	0.89 ± 0.17	0	0.91 ± 0.09	0	0
	d (Å)	0	4.72 ± 0.05	0	3.89 ± 0.08	0	0
	σ (Å)	0	0.15	0	0.15	0	0
Error Function	d (Å)	0	5.70 ± 0.42	3.55 ± 2.16	5.20 ± 0.19	0	3.17 ± 0.25
	σ (Å)	0	0.5	2.25 ± 0.94	0.5	0	0.5
	χ2 red	1.96	3.06	2.78	2.39	2.02	3.7

Table 6.1: Parameters obtained for the best fit to the crystal truncation rod data for the Au(111) electrode in 0.1 M H_2SO_4 AcN free and 10 mM AcN solution displayed in Figure 6.6. The parameters and their associated errors were obtained via a least-squares fit to the CTR data. Numbers without error represent parameters that were fixed during the fitting procedure.

The data measured at 0.7 V and 0.8 V in the presence of AcN were modelled, by including two adlayers and an error function thereby producing the best possible fit. While the electron density profiles displayed in Figure 6.7, show that the heights above the electrode surface appear to be constant, the model used here assumes the electrode surface terminates at the height of commensurately adsorbed adlayers. Therefore, at 0.8 V, 0 in the electron density

profile is at the height of the adsorbed sulphate layer. Thus, the AcN molecule is located at a height closer to 5 Å in relation to the Au(111) electrode surface. Furthermore, at 0.8 V, the contribution from AcN is significantly smaller than that measured at 0.7 V. In fact, from Table 6.1 there is a correlation between the coverage of carbon in the adlayer and the occupancy of the (bi)sulphate layer. It can therefore be inferred that at this potential, AcN is possibly enhancing the adsorption of (bi)sulphate molecules. At 0.7 V, when the ($\sqrt{3}$ x$\sqrt{7}$)sulphate has been lifted, the occupancy of adsorbed AcN increases revealing that AcN molecules compete with sulphate for adsorption sites as previously suggested from voltammetry measurements [12]. Nevertheless, the bond lengths observed here are greater than molecular bonds in AcN and therefore could be an indication of the molecule having dissociated into a cyanide and methyl group. This has been observed on platinum, copper and silver surfaces[131–133] although at more negative potentials than were measured here.

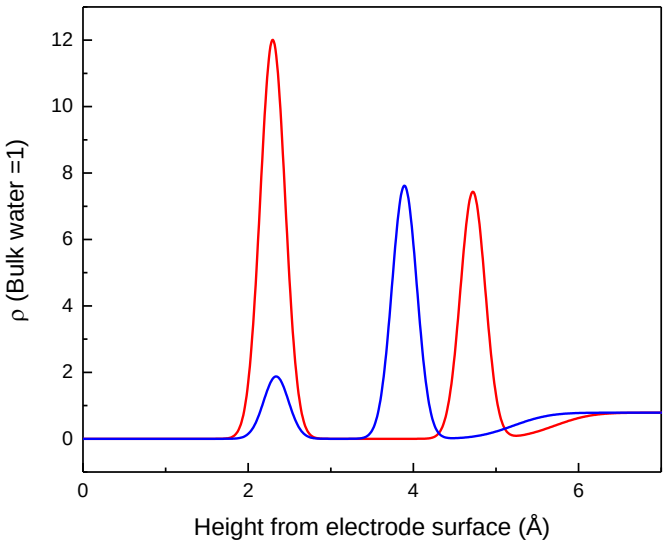

Figure 6.7: Vertical electron density profiles, normalised to the bulk density of water, of the best fit to the CTR data obtained at 0.8 V (blue) and 0.7 V (red) in the presence of 10 mM AcN. The metal layers and adsorbed sulphate molecules have been neglected.

A further set of measurements was taken in solution where the concentration of AcN was increased to 1 M. Figure 6.8 (a) and (b) show XRV measurements taken between 0 V and 1.15 V on the (0 1 0.52) and the (0 0 1.9) positions respectively. From inspection of the XRV measured at (0 1 0.52) an 'anti-Bragg' position sensitive to changes in the ordering of adsorbates commensurate with the Au electrode, significant hysteresis is observed. The intensity plateaus in the anodic direction up until ~0.65 V after which the intensity decreases at a steady rate. After reaching 1.15 V, as the potential is swept in the cathodic direction the

intensity continues to decrease until it reaches 0.75 V after which there is a sharp increase in intensity before reaching a plateau. Figure 6.8 (c) shows a comparison of a reciprocal space scan of the reconstruction measured in AcN free electrolyte (black) and in 1 M AcN solution (red) at -0.2 V. No evidence of the formation of the (p x √3) reconstruction is observed in this solution. Attempts to extract CTR data from this system following the x-ray voltammetry measurements proved unsuccessful due to evidence, via the comparison of repeated rocking scans of the (0, 1, 0.52) 'anti-Bragg' CTR position as shown in Figure 6.8 (d), of significant roughening of the electrode surface.

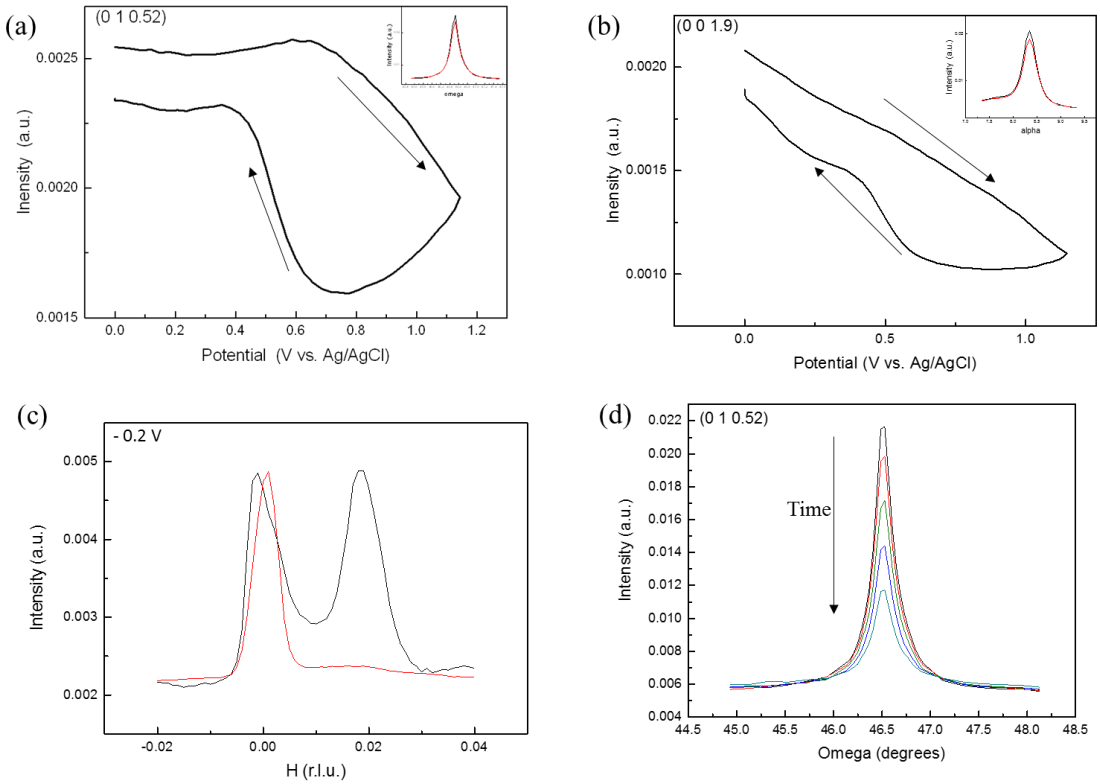

Figure 6.8:Scattered intensity as a function of the applied electrode potential for the Au(111) electrode surface in 0.1 M H_2SO_4 + 1 M AcN between 0 V and 1.15 V at (a) the (0, 1, 0.52) 'anti-Bragg' position and (b) (0, 0, 1.9) 'specular' CTR position. The insets represent rocking scans measured at the respective reciprocal space position before (black) and after (red) the XRV measurements to monitor any changes in background noise (c) Reciprocal space scans measured in the [1 1 0] direction through the (0, 1, 0.52) CTR position and the peak arising from the Au(111) (23 x √3) surface reconstruction at (0.02, 1.02, 0.52). The black line represents the reciprocal space scan measured in AcN free 0.1 M H_2SO_4 solution and the red line represents the scan measured in 1 M AcN solution -0.2 V. (d) Rocking scan measurements of the (0, 1, 0.52) CTR 'anti-Bragg' position used as 'check scans' during the measurement of the CTR data at 0.8 V. The black line displays the intensity measured at the beginning of the measurement, the red, green purple and blue lines represent the scans taken over the course of the measurement.

6.4 Cu UPD on Au(111) in H_2SO_4

To investigate the effect of AcN on the Cu UPD system on the Au(111) electrode surface in sulphuric acid solution, a combination of XRV and CTR measurements was carried out. Figure 6.9 displays x-ray voltammetry measurements of the Au(111) electrode surface in 0.1 M H_2SO_4 + 1 mM $CuSO_4$ solution between 0.58 V and 0.05 V at a scan rate of 5 mV/s. Figure 6.9 (a) shows the XRV measurement at the (2/3, -1/3, 1.2) reciprocal lattice position that is sensitive to the (√3 x √3) R30° structure. As the potential is swept in the cathodic direction, the intensity can be seen to be stable at potentials above 0.2 V at which it increases sharply and begins to level off near the cathodic limit. In the anodic direction the intensity follows a similar pattern, decreasing sharply as the potential approaches 0.2 V and then remaining constant. This sharp change in the intensity is indicative of the lifting/formation of the (√3 x √3)R30° structure at 0.2 V. It is interesting to note the intensity continues to evolve following the formation of (√3 x √3)R30° as the potential approaches the completion of the pseudomorphic (1 x 1) Cu layer, a similar change was reported by Nakamura *et al.*[161] . The XRV measured at (0, 0, 1.8) a position on the specular CTR (Figure 6.9 (c)) shows a similar transition at 0.2 V where in the cathodic direction the intensity increases up to 0.2 V before sharply decreasing. Figure 6.9 (b) shows the XRV measured at (1, 0, 3.6), a position sensitive to the adsorption of ordered layers commensurate to the Au electrode surface. In a similar trend, the intensity appears to increase slightly as the potential is swept negatively before 0.2 V and then decreases. In addition, the XRV measured at (0, 0, 3.3), a position on the specular CTR, a significant increase in the intensity as the potential is swept below 0.2 V. This coincides with the formation of the (√3 x √3)R30° structure.

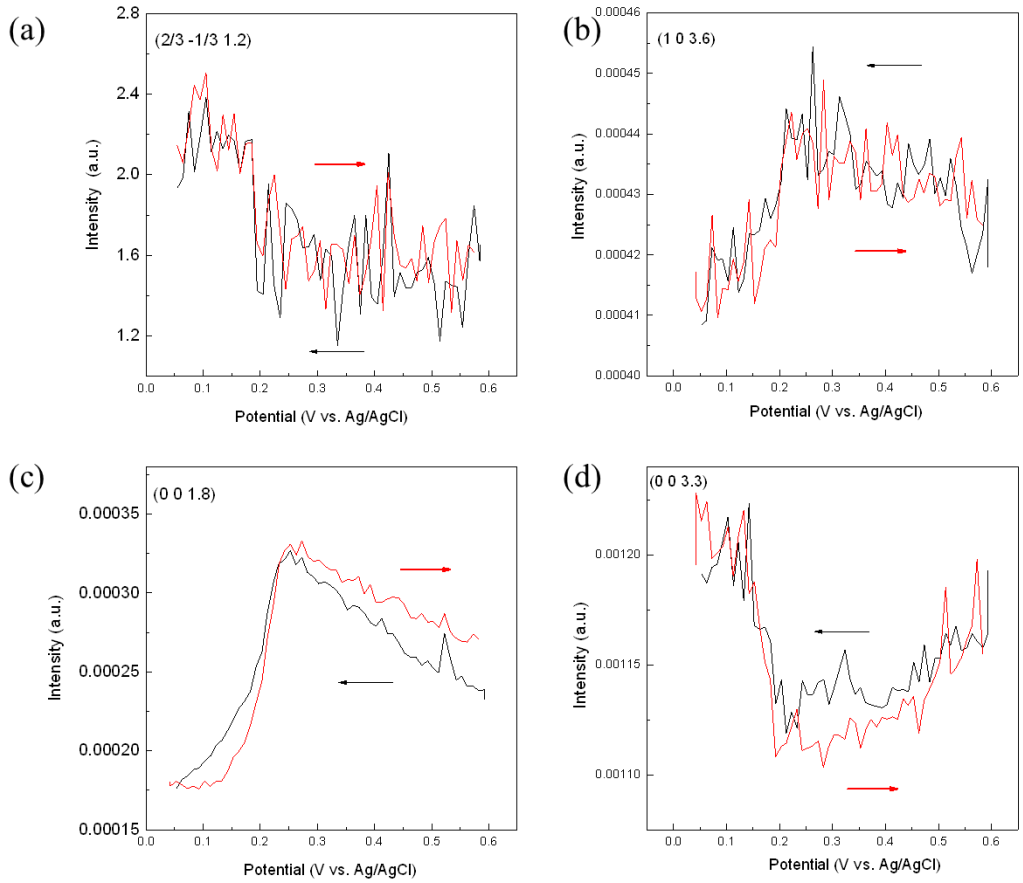

Figure 6.9: Scattered intensity as a function of the applied electrode potential for the Au(111) in 0.1 M H_2SO_4 + 1 mM $CuSO_4$ solution measured between 0.58 V and 0.05 V at a sweep rate of 5 mV/s at (a) The (2/3, -1/3, 1.2) reciprocal lattice position sensitive to the (√3x√3)R30° structure;(b) the (1, 0, 3.6) CTR position; (c) (0, 0, 1.8) a position on the 'specular' CTR and (d) the (0, 0, 3.3) specular CTR position.

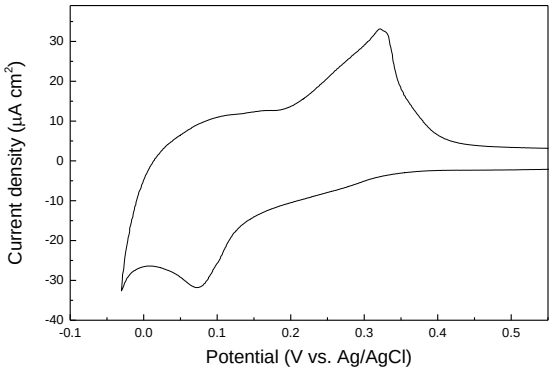

Figure 6.10 displays x-ray voltammetry measurements of the Au(111) electrode surface when the electrolyte has been substituted to 0.1 M H_2SO_4 + 1 mM $CuSO_4$ + 10 mM ACN solution.

In contrast to the XRVs measured in AcN free solution, the x-ray voltammetry measured at

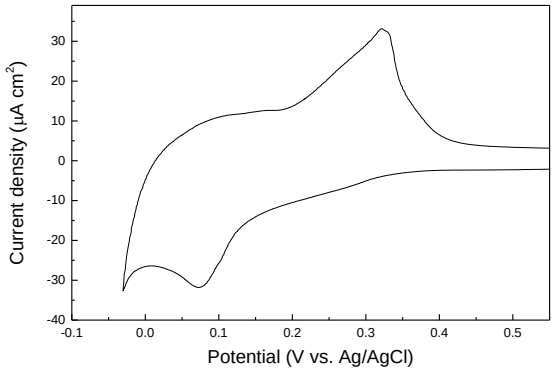

(2/3, -1/3, 1.2) displayed in

Figure 6.10 (a) shows no changes in intensity thus presenting no evidence of the formation of the (√3 x √3)R30° structure. This is likely due to the formation of a $[Cu(C_2H_3N)_4]^+$ complex hindering the honeycomb structure as suggested by Pekmez *et al.*[164]. Furthermore, the XRVs measured at (0, 0, 2.7) and (0, 0, 1.8) shown in

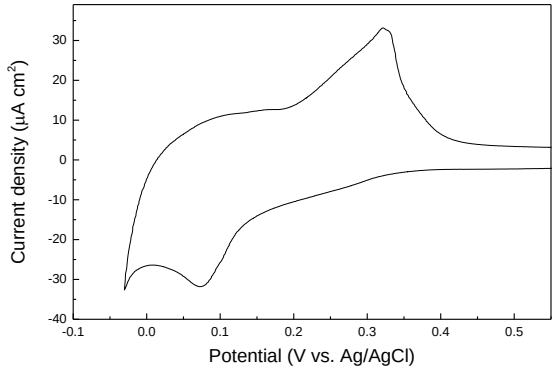

Figure 6.10(b) and (c) respectively show minimal changes in intensity, gradually decreasing as the potential is scanned negatively which increases back to its original state for the (0, 0, 1.8) position. This change in intensity is indicative of some ordering on the surface, i.e. copper deposition. However, it should be noted that for the XRV measured at (0, 0, 2.7) the intensity does not return to its original value on the positive sweep, possibly indicating an irreversible change on the surface.

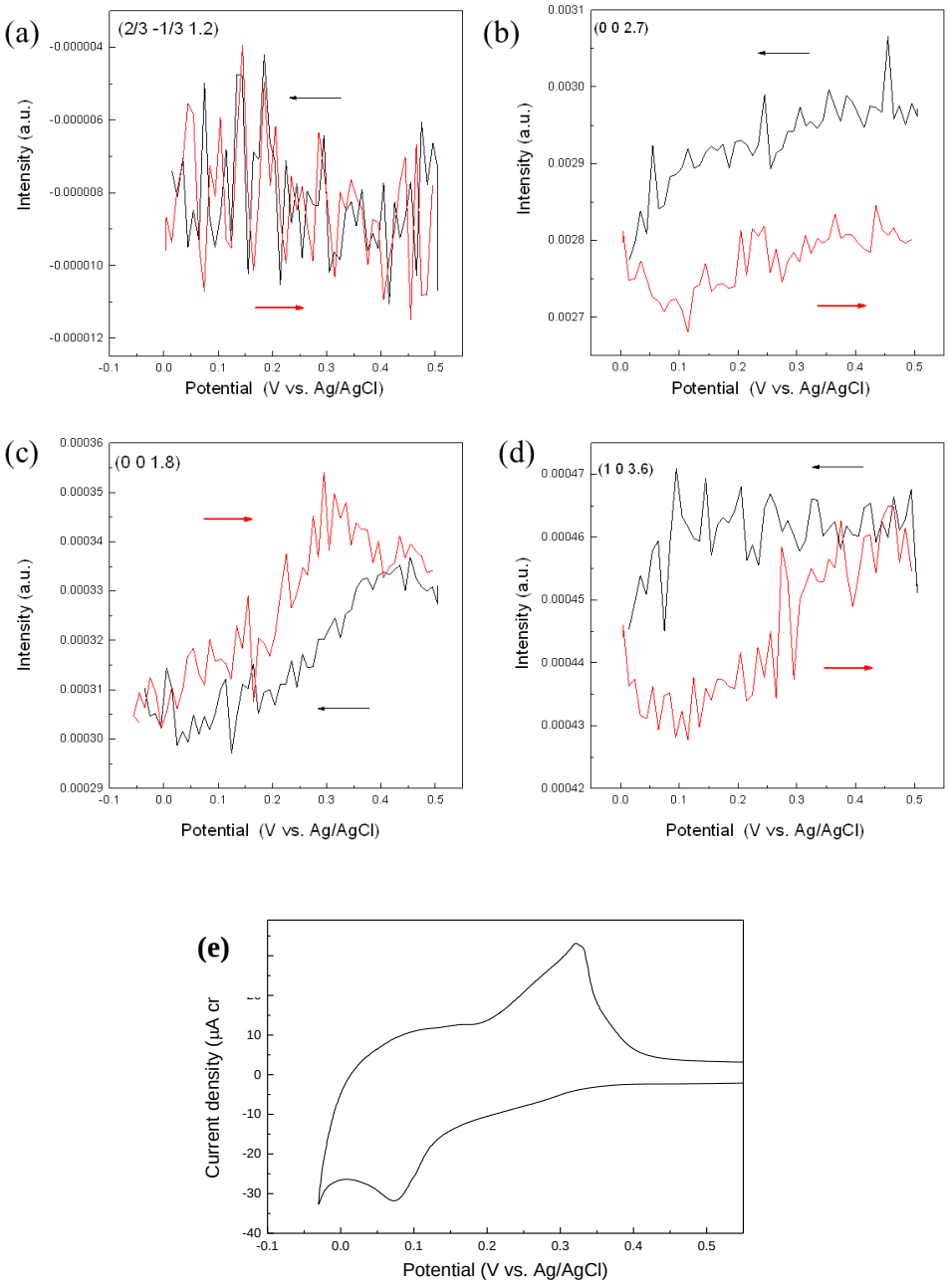

Figure 6.10: Scattered intensity as a function of the applied electrode potential for the Au(111) in 0.1 M H_2SO_4 + 1 mM $CuSO_4$ + 10 mM AcN solution measured between 0.58 V and 0.05 V at a sweep rate of 5 mV/s at (a) The (2/3, -1/3, 1.2) reciprocal lattice position sensitive to the (√3x√3)R30° structure;(b) the (0, 0, 2.7) specular CTR position; (c) (0, 0, 1.8) a position on the 'specular' CTR and (d) the (1, 0, 3.6) CTR position.(e) Cyclic voltammogram of the Au(111) electrode surface in 0.1 M H_2SO_4 + 1 mM $CuSO_4$ + 10 mM AcN solution at a scan rate of 5 mV/s by Nikolaos Antonatos.

Comparing the XRV measured in Figure 6.9(b) to

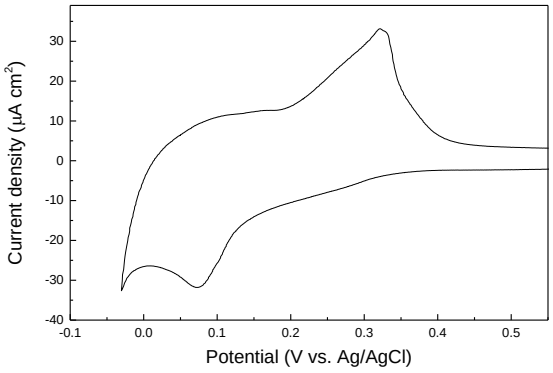

Figure 6.10 (d) at (1, 0 3.6), a much larger change in the intensity is observed correlating to the adsorption of Cu. Significant hysteresis is also observed, with the intensity returning to its original position at 0.58 V at a much more gradual rate. Figure 6.10 (e) displays a cyclic voltammogram of the Au(111)/Cu UPD system in 0.1 M H_2SO_4 + 10 mM ACN solution measured off-site by Nikolaos Antonatos. What is interesting to note is the absence of the characteristic double peak that is present in Figure 6.2. Thus it can be inferred that the Cu UPD process in the presence of ACN occurs in one distinct stage as opposed to the two stage process observed in ACN free solution.

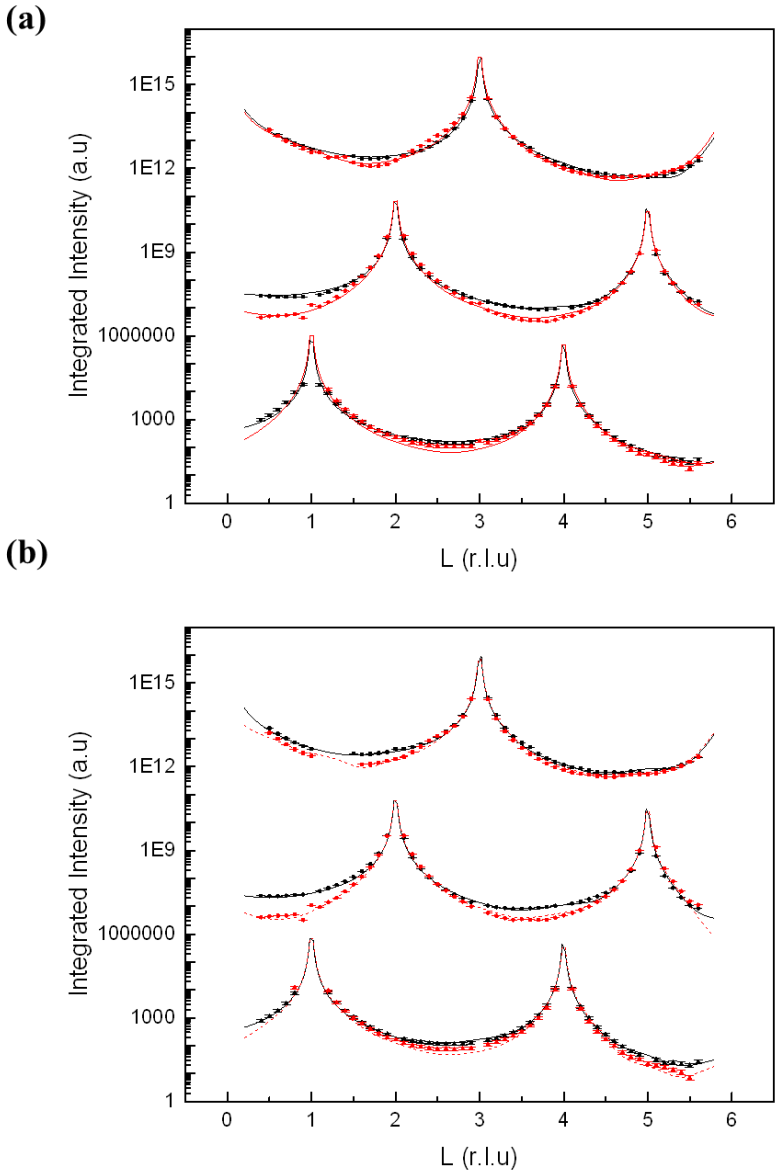

Figure 6.11: Fits to, from top to bottom, the specular and non-specular crystal truncation rods for the Au(111) electrode surface in 0.1 M H_2SO_4 + 1mM $CuSO_4$ AcN free(black symbols) and 10 mM AcN(red symbols) solutions measured at (a) 0.9 V; (b) 0.3 V. Measured data is shown as squares with error bars and corresponds to the background subtracted intensity normalised to the monitor and corrected for the diffraction geometry. A systematic error of 10% is assumed. The solid lines represent the best fits obtained to the data.

CTR data measured at MS - X04SA at 0.9 V and 0.3 V in AcN free (black) and in 10 mM AcN solutions is shown in Figure 6.11. Table 6.2 shows the parameters for the best fits to the CTR data. The data measured at 0.3V shows an occupancy of deposited copper of only approximately 10%. At 0.9 V no evidence of the (√3 x √7)R19.1° sulphate structure is observed. Comparing this with the data measured in 10 mM AcN solution there is a significant

increase in the amount of copper deposited on the Au(111) electrode surface at 0.3 V of approximately 30 %. Also, interesting to note is the decrease in the Au-Cu spacing of approximately 20% (from 2.43 Å to 1.93 Å). This result implies that while in the early stages of Cu UPD, the $[Cu(C_2H_3N)_4]^+$ complex is interacting weakly via electrostatic forces with the underlying Au(111) electrode surface allowing for a much smaller distance between the $[Cu(C_2H_3N)_4]^+$ ions and the electrode surface as suggested by Pekmez *et al.* [164]. This is further evidence by the negligible changes in the surface relaxations of the top Au layers. The model that yielded the best fit to the data measured at 0.3 V in the presence of AcN required two adlayers and an error function.

Crystal truncation rod measurements taken at the I-07 beamline at potentials of 0.58 V and 0.2 V in AcN free solution are displayed as the black points in Figure 6.12. The parameters for the best fits obtained for the AcN free data are displayed in Table 6.3. At 0.58 V the model shows some slight relaxation in the Au(111) surface layers compared to the data measured at 0.9 V The model obtained for the data at 0.2 V finds the (√3 x √3)R30° honeycomb structure with an occupancy of 0.67 ± 0.20, a value within error of that found by Toney *et al.*[148] of 0.85± 0.15. The value for the occupancy found in the model here correlates to a copper coverage of 0.45 ± 0.13 and a sulphate coverage of 0.22 ± 0.07. The model also shows an Au-Cu plane spacing of 2.46 ± 0.36 Å and a Cu-S plane spacing of 0.88 ± 0.3 Å, values close to those reported by Nakamura *et al.* [161].

	Parameter	**0.3V**		**0.9 V**	
			10 mM AcN		10 mM AcN
Metal layers	**ε_{23} (Å)**	-0.007 ± 0.002	0.009 ± 0.004	0	0
	ε_{12} (Å)	0.015 ± 0.006	0.015 ± 0.007	-0.011 ± 0.003	-0.01 ± 0.02

	σ_2 (Å)	0.100 ± 0.004	0.11 ± 0.01	0.100 ± 0.004	0.08 ± 0.01
	σ_1 (Å)	0.130 ± 0.006	0.22 ± 0.01	0.154 ± 0.004	0.08 ± 0.03
	$\theta_{1(Au)}$	1	1	1	1
Copper layer	**θ**	0.13 ± 0.01	0.40 ± 0.02	0	0
	d (Å)	2.43 ± 0.01	1.93 ± 0.05	0	0
	σ (Å)	0.05	0.2	0	0
adlayer 1	**Layer**	O	C	O	O
	θ	0.21 ± 0.08	1.62 ± 0.34	0.63 ± 0.07	0.6 ± 0.2
	d (Å)	2.21 ± 0.12	3.34 ± 0.15	2.22 ± 0.04	0.94 ± 0.37
	σ (Å)	0.2	0.2	0.05	0.05
adlayer 2	**Layer**	n/a	C	n/a	O
	θ	0	1.99 ± 0.41	0	0
	d (Å)	0	3.92 ± 0.12	0	0
	σ (Å)	0	0.15	0	0
Error Function	**d (Å)**	0	3.49 ± 0.09	0	5.39 ± 0.43
	σ (Å)	0	0.5	0	1.31 ± 0.31
	χ2 red	1.6	5.52	2.15	4.85

Table 6.2: Parameters obtained for the best fit to the crystal truncation rod data for the Au(111) electrode in 0.1 M H_2SO_4 + 1mM $CuSO_4$ AcN free and 10 mM AcN solution displayed in Figure 6.11. The parameters and their associated errors were obtained via a least-squares fit to the CTR data. Numbers without error represent parameters that were fixed during the fitting procedure.

The CTR data measured in 10 mM AcN solution at 0.58 V and 0.2 V is displayed as the red points in Figure 6.12. The best fits to the models obtained here required two adlayers and an error function. At 0.58 V, the presence of AcN in solution appears to cause a reduction in the inward relaxation of the topmost Au surface layer compared to the model obtained in AcN free solution. As with the measurements taken at MS - X04SA, there is a significant increase in the amount of copper deposited on the Au(111) electrode surface at 0.2 V with the addition of 10 mM AcN to the electrolyte. First, the presence of 10 mM AcN in solution prevents the formation of the characteristic (√3 x √3)R30° honeycomb structure. Measurements on Pt(111) electrodes suggested that the AcN molecules compete with sulphate molecules for adsorption sites[166]. In the case of Cu UPD on Au(111), this would prevent the formation of the (√3 x √3)R30° honeycomb structure as this is a co-adsorption process between copper and (bi)sulphate ions[148]. However, copper and AcN ions forming a $[Cu(C_2H_3N)_4]^+$ complex could also explain this result. The presence of AcN in solution appears to enhance the deposition of Cu on the Au(111) surface. At 0.2 V, the best fit to the data finds an initial layer of copper deposited with an occupancy of 0.8 with an additional layer beginning to form of occupancy 0.13. In contrast to the data measured at 0.3 V where there were negligible changes in the Au surface relaxations, the presence on AcN induces a change in the surface relaxation

at 0.2 V from an inward relaxation of -0.021 ± 0.002 Å in AcN free solution to an outward relaxation of 0.014 ± 0.002 Å correlating with the increased coverages of copper observed.

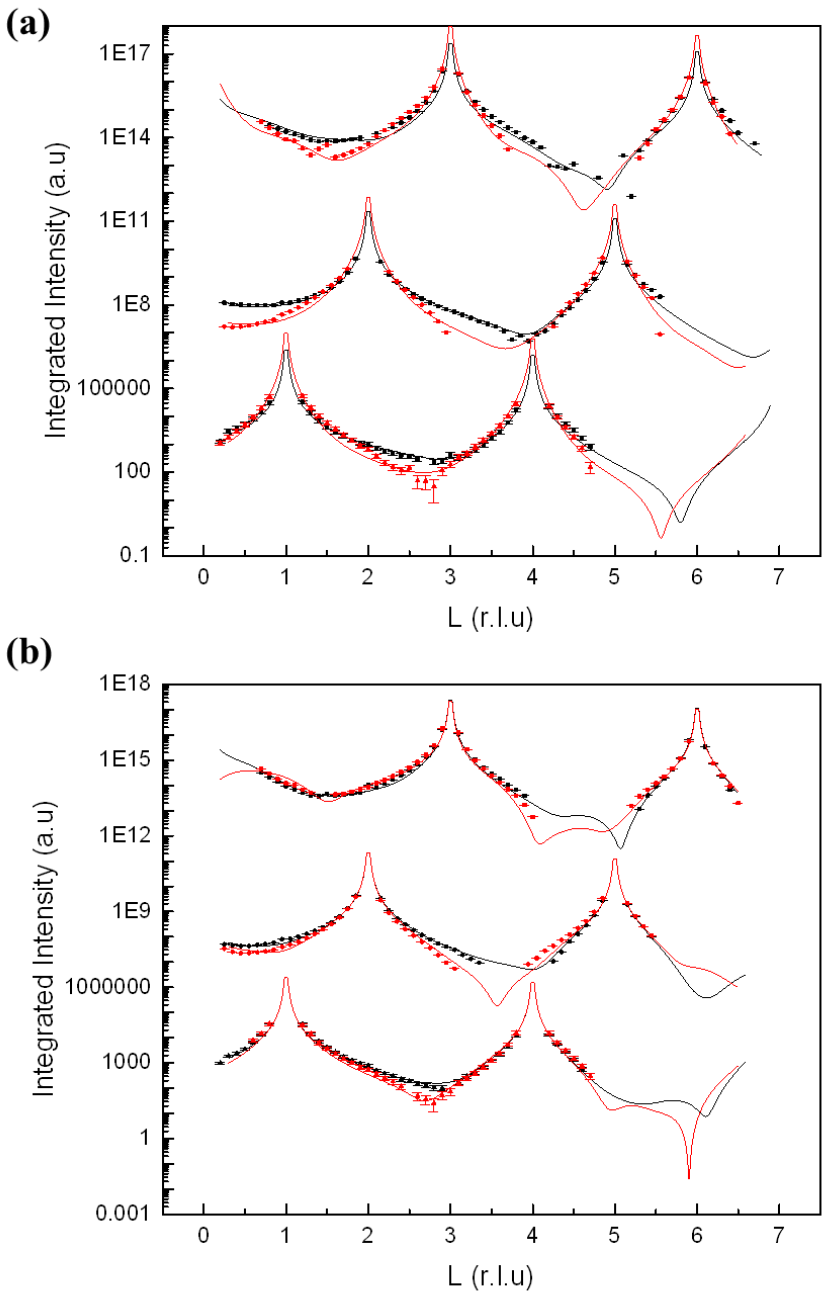

Figure 6.12: Fits to, from top to bottom, the specular and non-specular crystal truncation rods for the Au(111) electrode surface in 0.1 M H_2SO_4 + 1mM $CuSO_4$ AcN free(black symbols) and 10 mM AcN (red symbols) solutions measured at (a) 0.58 V; (b) 0.2 V. Measured data is shown as squares with error bars and corresponds to the background subtracted intensity normalised to the monitor and corrected

for the diffraction geometry. A systematic error of 10% is assumed. The solid lines represent the best fits obtained to the data.

	Parameter	0.2 V	0.58 V
Metal layers	**ε_{23} (Å)**	0.017 ± 0.002	0.010 ± 0.006
	ε_{12} (Å)	-0.021 ± 0.002	-0.047 ± 0.009
	σ_2 (Å)	0.10 ± 0.01	0.07 ± 0.01
	σ_1 (Å)	0.19 ± 0.01	0.21 ± 0.01
	$\theta_{1(Au)}$	1	1
($\sqrt{3}$ x $\sqrt{3}$)R30°	**θ**	0.67 ± 0.20	0
	d (Å)	2.46 ± 0.32	0
	d (Å)	0.883 ± 0.2	
	σ (Å)	0.05	0
	σ (Å)	0.05	0
Adlayer 1	**Layer**	O	O
	θ	0.54 ± 037	0.68 ± 0.35
	d (Å)	5.19 ± 0.37	5.67 ± 0.19
	σ (Å)	0.34 ± 0.07	0.1
Adlayer 2	**Layer**	n/a	n/a
	θ	0	0
	d (Å)	0	0
	σ (Å)	0	0
Error Function	**d (Å)**	6.03 ± 1.50	6.68 ± 0.35
	σ (Å)	1.04 ± 2.07	0.47 ± 0.56
	χ2 red	3.98	3.49

Table 6.3: Parameters obtained for the best fit to the crystal truncation rod data for the Au(111) electrode in 0.1 M H_2SO_4 + 1mM $CuSO_4$ solution displayed in Figure 6.12. The parameters and their associated errors were obtained via a least-squares fit to the CTR data. Numbers without error represent parameters that were fixed during the fitting procedure.

	Parameter	0.2 V	0.58 V
		+ 10 mM AcN	
Metal layers	ε_{23} (Å)	0	0.02 ± 0.01
	ε_{12} (Å)	0.014 ± 0.002	-0.01 ± 0.01
	σ_2 (Å)	0.1	0.07 ± 0.03
	σ_1 (Å)	0.22 ± 0.02	0.25 ± 0.02
	$\theta_{1(Au)}$	1	1
Copper Layer	Θ	0.82 ± 0.02	0
	d (Å)	2.516 ± 0.07	0
	σ (Å)	0.21 ± 0.11	0
Copper Layer 2	Θ	0.13 ± 0.07	0
	d (Å)	3.07 ± 0.27	0
	σ (Å)	0.1	0
Adlayer 1	Layer	C	C
	Θ	1.78 ± 2.33	1.05 ± 1.75
	d (Å)	2.99 ± 0.7	1.09 ± 0.42
	σ (Å)	0.15	0.15
Adlayer 2	Layer	C	C
	Θ	1.99 ± 2.17	1.99 ± 1.33
	d (Å)	3.59 ± 0.5	3.22 ± 4.98
	σ (Å)	0.15	0.15
Error Function	d (Å)	5.53 ± 0.35	0.07 ± 0.32
	σ (Å)	0.5	0.5
	χ2 red	5.11	3.73

Table 6.4: Parameters obtained for the best fit to the crystal truncation rod data for the Au(111) electrode in 0.1 M H_2SO_4 + 1mM $CuSO_4$ + 10 mM AcN solution displayed in Figure 6.12. The parameters and their associated errors were obtained via a least-squares fit to the CTR data. Numbers without error represent parameters that were fixed during the fitting procedure.

It is now worth discussing the model obtained for the data measured in 10 mM solution in terms of vertical electron density profiles. The profiles for the data measured at 0.2 V (black), 0.3 V (red) and 0.58 V (blue) are displayed in Figure 6.13. 0.9 V is a potential where AcN has desorbed from the surface and as such the data measured at this potential is not significant to this discussion. At 0.58 V, there is evidence of adsorbed AcN at the Au(111) electrode surface. At 0.3V there is a marked increase in the amount of AcN close to the Au surface. This increase coincides with the early stages of Cu deposition. The large coverages of AcN at this

potential can be attributed to the presence of a $[Cu(C_2H_3N)_4]^+$ complex. As the potential decreases, the quantity of AcN remains fairly constant, however as can be seen from Figure 6.13, there is a shift in the distance from the electrode. This implies a possible change in orientation of the AcN molecule. However, this shift closer to the electrode coincides with the large increase in deposited copper on the surface. The model used here follows the same process as that used for Au(111) in Cu-free sulphuric acid, where 0 in Figure 6.13 is the height at which commensurately deposited layers lie with respect to the Au(111) electrode surface. Thus, this change in height of the adlayers is likely due to the increase in coverage and stability of the deposited Cu layers.

From the coverages of shown Cu for the data measured at 0.2 V in 10 mM AcN containing solution shown in Table 6.4, it is suggested that the growth mode of the Cu deposited layers is not layer by layer. If the growth mode were layer by layer it would be expected the coverage of copper to reach 1 before the second layer begins to grow. From the results found the following process is suggested: in the potential region positive of the onset of Cu deposition but negative of AcN desorption, AcN molecules are weakly adsorbed on the surface. Then as the potential is swept negatively, copper in the form of $[Cu(C_2H_3N)_4]^+$ begins to weakly interact with the Au(111) electrode surface and replace the adsorbed AcN molecules, hence the large reduction in the Au-Cu spacing. As the coverage of copper approaches monolayer coverage, it becomes more energetically favourable for Cu to lose its solvation shell and form a stable overlayer and thus allow for the formation of a second monolayer of copper prior to completion of the first monolayer. Therefore, the copper adatoms in the first monolayer would begin to dissociate with the AcN ions to allow the second layer of copper adatoms to begin to deposit albeit still in the form of the $[Cu(C_2H_3N)_4]^+$ complex. In this way the suggested process could explain the large coverages in the adsorbate layers that have been obtained for the best fits to the model. Nevertheless, it cannot be ruled out that an alternative model would yield a better fit to the data. Indeed, to truly understand the nature of the $[Cu(C_2H_3N)_4]^+$ complex and its interactions with the Au(111) electrode surface, the simplified approach to modelling AcN is likely not sufficient, as evidenced by the high coverages in the adlayers of the model required for the best fits to the data.

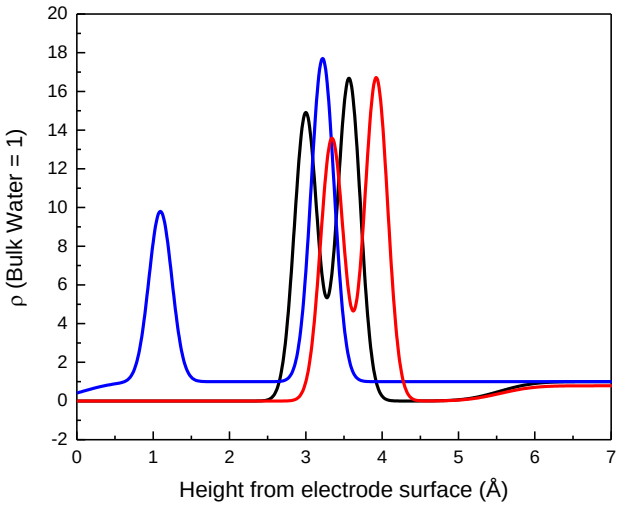

Figure 6.13: Vertical electron density profiles, normalised to the bulk density of water, of the best fit to the CTR data obtained at 0.2 V (black), 0.3 V (red) and 0.58 V (blue) in the presence of 10 mM AcN. The metal layers and deposited copper atoms have been neglected to highlight features above the electrode surface.

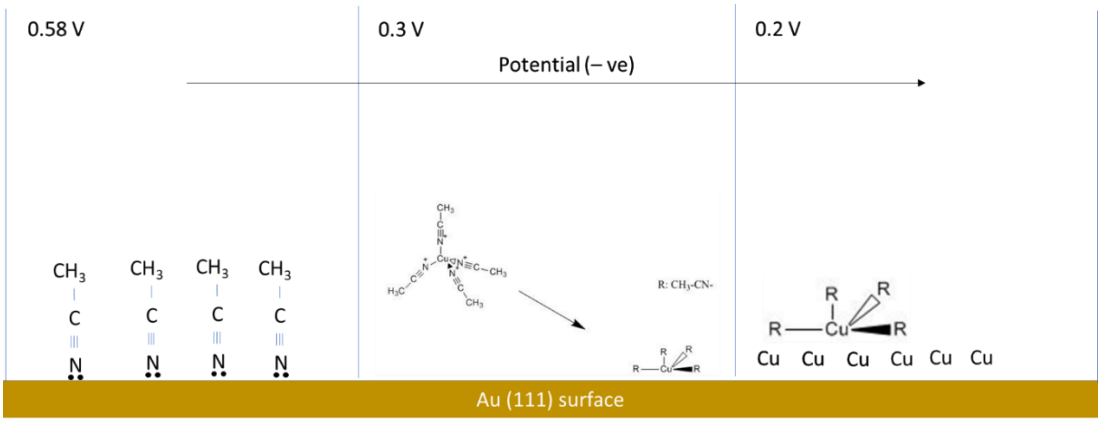

Figure 6.14:Simplified illustration of the interaction of copper and Acetonitrile on the Au(111) electrode surface with the change of potential based on the model for the current best fits to the data.

6.5 Conclusions and summary

In this chapter the effect of Acetonitrile adsorption on Au(111) surfaces in sulphuric acid media has been explored via CTR and x-ray voltammetry measurements. In accordance with previous measurements on the system, AcN is shown to weakly interact with the Au(111) electrode surface. An interesting correlation is observed between the coverage of the approximated AcN adlayers and the coverage of sulphate in the (√3 x √7)R19.1° structure. The effect of AcN on the Cu UPD process in sulphuric acid media was also explored. The results show that AcN greatly enhances the Cu deposition, inducing greater amounts of Cu

deposited on the Au(111) than that found at similar potentials in AcN free sulphuric acid solution. The substantial coverages for the approximated AcN layers can be explained by the copper forming a $[Cu(C_2H_3N)_4]^+$ complex with AcN. Based on models of the best fits to the data the process of Cu deposition on the Au(111) electrode surface is suggested. It is expected that investigations into the Cu UPD processes using solutions where Cu and AcN are known to be in the form of $[Cu(C_2H_3N)_4]^+$, for example using tetrakisacetonitrile copper(i) triflate as part of the electrolyte solution, would provide a good comparison to the measurements detailed here.

7 Conclusion and Future Outlook

For this work, *in-situ* surface x-ray diffraction has been used to probe the atomic structure at the Au single crystal electrode/electrolyte interface. This technique has the advantage of allowing simultaneous characterisation of electrode/adlayer structures at the atomic scale as well as directly monitoring changes to the surface under reaction conditions. Gold was selected as the primary metal surface as it represents the key model system for investigating general surface processes. It was observed that the hexagonal reconstructions of Au(111) and Au(100) in alkaline solutions undergo a charge driven potential dependent in plane surface compressibility. Adsorption of carbon monoxide on gold electrodes was shown to 'lock' the surface reconstructions at highly compressed phases observed in CO-free solution. CO acts as a tuneable dipole, accommodating excess surface charge brought about by the applied potential. It can therefore be inferred that this mechanism underpins the enhancement of both the electrocatalytic reactivity and the increased stability of the reconstructed surfaces over a larger potential range than has been previously observed[7].

Thereafter a study to answer the debate [10] on the presence of alloy formation during the UPD process was carried out. This work has revealed that Pb forms a substitutional Au/Pb surface alloy during the stripping of the deposited incommensurate Pb adlayer from the Au(111) electrode surface and that the surface de-alloys prior to the complete removal of Pb adatoms from the Au(111) surface. This has been attributed to the surface alloying/de-alloying process that occurs in order to reduce the total surface energy of the system.

An *in-situ* investigation into the structure of the electrochemical double layer of Au(111) in various concentrations of Acetonitrile (AcN) was performed to explore the adsorption of AcN on Au(111) in H_2SO_4. It was shown that the adsorption of AcN weakly interacts with the Au(111) surface evidenced by marginal changes in the surface relaxations of the Au substrate. Additionally, an investigation was carried out to determine the effect of AcN on the Au(111)/$CuSO_4$ UPD process. Considering that this phenomenon is not widely understood, the interactions of copper and AcN on the Au(111) surface interestingly showed that AcN enhances the deposition of copper onto the Au surface. From modelling of the vertical electron density profiles, it can be inferred that copper and AcN form a $[Cu(C_2H_3N)_4]^+$ complex thus hindering the formation of the characteristic honeycomb $(\sqrt{3} \times \sqrt{3})R30°$ structure observed in AcN free sulphuric acid solution.

The analysis of the Au(100)/Pb interface as discussed in chapter 5 could yield some interesting insights into the behaviour of the interactions between Pb and Au surfaces. It is currently unclear as to the driving mechanism behind the apparent spontaneous formation of the as yet unknown Pb structure in alkaline solution. Further x-ray measurements could reveal the structure. Conventional SXRD studies can be very time consuming (of the order of 10 hours for a quantitative data set) and with the use of point or small 2D detectors, unexpected structures can be easily missed. New techniques such as high energy surface x-ray diffraction could allow for the rapid acquisition of CTR's, providing greater temporal resolution as has been demonstrated by Gustafson *et al.* [168]. By using this technique, a large volume of reciprocal space can be mapped over a comparably shorter period of time, thereby overcoming limitations of conventional SXRD. Measurements exploring this technique were conducted at the ID-15 beamline at the ESRF, Grenoble on the well understood Au(100)/Cu/Br system[169] at energies of 70 keV. Analysis of this data is ongoing.

8 References

[1] S. Trasatti, 'Surface science and electrochemistry: concepts and problems', *Surf. Sci.*, vol. 335, pp. 1–9, Jul. 1995.

[2] H. E. Hoster and H. A. Gasteiger, 'Ex-situ surface preparation and analysis: transfer between UHV and electrochemical Cell', in *Handbook of Fuel Cells*, American Cancer Society, 2010.

[3] M. El-Jawad, J.-L. Chemin, B. Gilles, and F. Maillard, 'A portable transfer chamber for electrochemical measurements on electrodes prepared in ultra-high vacuum', *Rev. Sci. Instrum.*, vol. 84, no. 6, p. 064101, Jun. 2013.

[4] P. M. Kolb, D. L. Rath, R. Wille, and W. N. Hansen, 'An ESCA Study on the Electrochemical Double Layer of Emersed Electrodes', *Berichte Bunsenges. Für Phys. Chem.*, vol. 87, no. 12, pp. 1108–1113, Dec. 1983.

[5] E. R. Kötz, H. Neff, and K. Müller, 'A UPS, XPS and work function study of emersed silver, platinum and gold electrodes', *J. Electroanal. Chem. Interfacial Electrochem.*, vol. 215, no. 1, pp. 331–344, Dec. 1986.

[6] D. M. Kolb, 'An atomistic view of electrochemistry', *Surf. Sci.*, vol. 500, pp. 722–740, Mar. 2002.

[7] M. Haruta, 'Catalysis: Gold rush', *Nature*, vol. 437, no. 7062, pp. 1098–1099, Oct. 2005.

[8] P. Rodriguez, Y. Kwon, and M. T. M. Koper, 'The promoting effect of adsorbed carbon monoxide on the oxidation of alcohols on a gold catalyst', *Nat. Chem.*, vol. 4, no. 3, pp. 177–182, Mar. 2012.

[9] E. Herrero, L. J. Buller, and H. D. Abruña, 'Underpotential Deposition at Single Crystal Surfaces of Au, Pt, Ag and Other Materials', *Chem. Rev.*, vol. 101, no. 7, pp. 1897–1930, Jul. 2001.

[10] J. Nutariya, J. Velleuer, W. Schwarzacher, and N. Vasiljevic, 'Surface Alloying/Dealloying in Pb/Au(111) System', *ECS Trans.*, vol. 28, no. 25, pp. 15–25, Oct. 2010.

[11] H. Angerstein-Kozlowska, B. Macdougall, and B. E. Conway, 'Electrochemisorption and reactivity of nitriles at platinum electrodes and the anodic H desorption effect', *J. Electroanal. Chem. Interfacial Electrochem.*, vol. 39, no. 2, pp. 287–313, Oct. 1972.

[12] A. V. Rudnev, E. B. Molodkina, A. I. Danilov, Y. M. Polukarov, A. Berna, and J. M. Feliu, 'Adsorption behavior of acetonitrile on platinum and gold electrodes of various structures in solution of 0.5M H2SO4', *Electrochimica Acta*, vol. 54, no. 14, pp. 3692–3699, May 2009.

[13] D. Pletcher, R. Greff, R. Peat, L. M. Peter, and J. Robinson, '1 - Introduction to the fundamental concepts of electrochemistry', in *Instrumental Methods in Electrochemistry*, D. Pletcher, R. Greff, R. Peat, L. M. Peter, and J. Robinson, Eds. Woodhead Publishing, 2010, pp. 15–41.

[14] A. C. Fisher, *Electrode Dynamics*. Oxford Chemistry Primers 34, 1996.

[15] O. Stern, 'The theory of the electrolytic double-layer', *Z Elektrochem*, vol. 30, no. 508, pp. 1014–1020, 1924.

[16] D. C. Grahame, 'The Electrical Double Layer and the Theory of Electrocapillarity.', *Chem. Rev.*, vol. 41, no. 3, pp. 441–501, Dec. 1947.

[17] I. K. Robinson and D. J. Tweet, 'Surface X-ray diffraction', *Rep. Prog. Phys.*, vol. 55, no. 5, p. 599, May 1992.

[18] J. Als-Nielsen and D. McMorrow, *Elements of modern X-ray physics*. New York: Wiley, 2001.

[19] C. A. Lucas and N. M. Marković, 'Structure Relationships in Electrochemical Reactions', in *Encyclopedia of Electrochemistry*, Wiley-VCH Verlag GmbH & Co. KGaA, 2007.
[20] C. Kittel, *Introduction to Solid State Physics, 8th Edition*. Wiley, 2004.
[21] R. Feidenhans'l, 'Surface structure determination by X-ray diffraction', *Surf. Sci. Rep.*, vol. 10, no. 3, pp. 105–188, May 1989.
[22] P. H. Fuoss and S. Brennan, 'Surface Sensitive X-Ray Scattering', *Annu. Rev. Mater. Sci.*, vol. 20, no. 1, pp. 365–390, 1990.
[23] E. Prince, Ed., *International Tables for Crystallography: Mathematical, physical and chemical tables*, 1st ed., vol. C. Chester, England: International Union of Crystallography, 2006.
[24] S. Brennan and P. L. Cowan, 'A suite of programs for calculating x-ray absorption, reflection, and diffraction performance for a variety of materials at arbitrary wavelengths', *Rev. Sci. Instrum.*, vol. 63, no. 1, pp. 850–853, Jan. 1992.
[25] I. K. Robinson, 'Crystal truncation rods and surface roughness', *Phys. Rev. B*, vol. 33, no. 6, pp. 3830–3836, Mar. 1986.
[26] F. Spaepen, 'A structural model for the solid-liquid interface in monatomic systems', *Acta Metall.*, vol. 23, no. 6, pp. 729–743, Jun. 1975.
[27] W. A. Curtin, 'Density-functional theory of the solid-liquid interface', *Phys. Rev. Lett.*, vol. 59, no. 11, pp. 1228–1231, Sep. 1987.
[28] F. F. Abraham, 'The interfacial density profile of a Lennard-Jones fluid in contact with a (100) Lennard-Jones wall and its relationship to idealized fluid/wall systems: A Monte Carlo simulation', *J. Chem. Phys.*, vol. 68, no. 8, pp. 3713–3716, Apr. 1978.
[29] P. Fenter and N. C. Sturchio, 'Calcite (1 0 4)–water interface structure, revisited', *Geochim. Cosmochim. Acta*, vol. 97, pp. 58–69, Nov. 2012.
[30] P. Fenter and N. Sturchio, 'Mineral–water interfacial structures revealed by synchrotron X-ray scattering', *Prog. Surf. Sci.*, vol. 77, pp. 171–258, Dec. 2004.
[31] L. A. Kibler, 'Preparation and Characterization of Noble Metal Single Crystal Electrode Surfaces', p. 56.
[32] M. G. Samant, M. F. Toney, G. L. Borges, L. Blum, and O. R. Melroy, 'In-situ grazing incidence X-ray diffraction study of electrochemically deposited Pb monolayers on Ag(111)', *Surf. Sci.*, vol. 193, no. 1, pp. L29–L36, Jan. 1988.
[33] M. G. Samant, M. F. Toney, G. L. Borges, L. Blum, and O. R. Melroy, 'Grazing incidence x-ray diffraction of lead monolayers at a silver (111) and gold (111) electrode/electrolyte interface', *J. Phys. Chem.*, vol. 92, no. 1, pp. 220–225, Jan. 1988.
[34] K. Tamura, B. M. Ocko, J. X. Wang, and R. R. Adžić, 'Structure of Active Adlayers on Bimetallic Surfaces: Oxygen Reduction on Au(111) with Bi Adlayers', *J. Phys. Chem. B*, vol. 106, no. 15, pp. 3896–3901, Apr. 2002.
[35] Z. Nagy and H. You, 'Applications of surface X-ray scattering to electrochemistry problems', *Electrochimica Acta*, vol. 47, no. 19, pp. 3037–3055, 2002.
[36] K. Krug, D. Kaminski, F. Golks, J. Stettner, and O. M. Magnussen, 'Real-Time Surface X-ray Scattering Study of Au(111) Electrochemical Dissolution', *J. Phys. Chem. C*, vol. 114, no. 43, pp. 18634–18644, Nov. 2010.
[37] F. Golks, K. Krug, Y. Gründer, J. Zegenhagen, J. Stettner, and O. M. Magnussen, 'High-Speed in situ Surface X-ray Diffraction Studies of the Electrochemical Dissolution of Au(001)', *J. Am. Chem. Soc.*, vol. 133, no. 11, pp. 3772–3775, Mar. 2011.
[38] M. Nakamura, H. Kaminaga, O. Endo, H. Tajiri, O. Sakata, and N. Hoshi, 'Structural Dynamics of the Electrical Double Layer during Capacitive Charging/Discharging Processes', *J. Phys. Chem. C*, vol. 118, no. 38, pp. 22136–22140, Sep. 2014.

[39] M. Nakamura *et al.*, 'Real–time observation of interfacial ions during electrocrystallization', *Sci. Rep.*, vol. 7, no. 1, p. 914, Apr. 2017.
[40] C. Broennimann *et al.*, 'The PILATUS 1M detector', *J. Synchrotron Radiat.*, vol. 13, no. 2, pp. 120–130, Mar. 2006.
[41] W. R. Busing and H. A. Levy, 'Angle calculations for 3- and 4-circle X-ray and neutron diffractometers', *Acta Crystallogr.*, vol. 22, no. 4, pp. 457–464, Apr. 1967.
[42] K. W. Evans-Lutterodt and M. T. Tang, 'Angle Calculations for a `2+2' Surface X-ray Diffractometer', *J. Appl. Crystallogr.*, vol. 28, no. 3, pp. 318–326, Jun. 1995.
[43] J. M. Bloch, 'Angle and index calculations for `z-axis' X-ray diffractometer', *J. Appl. Crystallogr.*, vol. 18, no. 1, pp. 33–36, Feb. 1985.
[44] E. Vlieg, 'A (2+3)-Type Surface Diffractometer: Mergence of the z-Axis and (2+2)-Type Geometries', *J. Appl. Crystallogr.*, vol. 31, no. 2, pp. 198–203, Apr. 1998.
[45] M. Lohmeier and E. Vlieg, 'Angle calculations for a six-circle surface X-ray diffractometer', *J. Appl. Crystallogr.*, vol. 26, no. 5, pp. 706–716, Oct. 1993.
[46] G. S. Harlow, 'Surface X-ray Diffraction Studies of the Electrochemical Interface', p. 147.
[47] 'On the use of CCD area detectors for high-resolution specular X-ray reflectivity - Fenter - 2006 - Journal of Synchrotron Radiation - Wiley Online Library'. [Online]. Available: https://onlinelibrary.wiley.com/doi/abs/10.1107/S0909049506018000. [Accessed: 10-Jul-2018].
[48] E. Vlieg, 'Integrated Intensities Using a Six-Circle Surface X-ray Diffractometer', *J. Appl. Crystallogr.*, vol. 30, no. 5–1, pp. 532–543, Oct. 1997.
[49] M. Haruta, T. Kobayashi, H. Sano, and N. Yamada, 'Novel Gold Catalysts for the Oxidation of Carbon Monoxide at a Temperature far Below 0 °C', *Chem. Lett.*, vol. 16, no. 2, pp. 405–408, Feb. 1987.
[50] P. Rodriguez, J. M. Feliu, and M. T. M. Koper, 'Unusual adsorption state of carbon monoxide on single-crystalline gold electrodes in alkaline media', *Electrochem. Commun.*, vol. 11, no. 6, pp. 1105–1108, Jun. 2009.
[51] P. Rodríguez, A. A. Koverga, and M. T. M. Koper, 'Carbon Monoxide as a Promoter for its own Oxidation on a Gold Electrode', *Angew. Chem. Int. Ed.*, vol. 49, no. 7, pp. 1241–1243, Jan. 2010.
[52] P. Rodriguez, N. Garcia-Araez, A. Koverga, S. Frank, and M. T. M. Koper, 'CO Electroxidation on Gold in Alkaline Media: A Combined Electrochemical, Spectroscopic, and DFT Study', *Langmuir*, vol. 26, no. 14, pp. 12425–12432, Jul. 2010.
[53] P. Rodriguez, N. Garcia-Araez, and M. T. M. Koper, 'Self-promotion mechanism for CO electrooxidation on gold', *Phys. Chem. Chem. Phys.*, vol. 12, no. 32, pp. 9373–9380, Aug. 2010.
[54] Y. Grunder, G. S. Harlow, E. Cocklin, J. Fogg, J. W. Beane, and C. A. Lucas, 'Potential-dependent Surface Compression of Gold and its Link to Electrocatalytic Reactivity', *Surf. Sci.*, vol. 680, pp. 113-118 Feb. 2019.
[55] A. R. Sandy, S. G. J. Mochrie, D. M. Zehner, K. G. Huang, and D. Gibbs, 'Structure and phases of the Au(111) surface: X-ray-scattering measurements', *Phys. Rev. B*, vol. 43, no. 6, pp. 4667–4687, Feb. 1991.
[56] J. V. Barth, H. Brune, G. Ertl, and R. J. Behm, 'Scanning tunneling microscopy observations on the reconstructed Au(111) surface: Atomic structure, long-range superstructure, rotational domains, and surface defects', *Phys. Rev. B*, vol. 42, no. 15, pp. 9307–9318, Nov. 1990.
[57] K. Takayanagi, Y. Tanishiro, K. Yagi, K. Kobayashi, and G. Honjo, 'UHV-TEM study on the reconstructed surface of Au(111): Metastable p″ × p″ and stable p × 1 surface structure', *Surf. Sci.*, vol. 205, no. 3, pp. 637–651, Nov. 1988.

[58] J. Wang, A. J. Davenport, H. S. Isaacs, and B. M. Ocko, 'Surface Charge-Induced Ordering of the Au(111) Surface', *Science*, vol. 255, no. 5050, pp. 1416–1418, 1992.

[59] J. Wang, B. Ocko, A. Davenport, and H. Isaacs, 'In situ x-ray-diffraction and - reflectivity studies of the Au(111)/electrolyte interface: Reconstruction and anion adsorption', *Phys. Rev. B*, vol. 46, no. 16, pp. 10321–10338, Oct. 1992.

[60] I. M. Tidswell, N. M. Marković, and P. N. Ross, 'Potential dependent structure of single crystal gold interfaces in alkaline electrolyte: an in situ X-ray scattering study', *Surf. Sci.*, vol. 317, no. 1–2, pp. 241–252, Sep. 1994.

[61] D. M. Kolb and J. Schneider, 'Surface reconstruction in electrochemistry: Au(100-(5 × 20), Au(111)-(1 × 23) and Au(110)-(1 × 2)', *Electrochimica Acta*, vol. 31, no. 8, pp. 929–936, Aug. 1986.

[62] D. L. Abernathy *et al.*, 'Reconstruction of the (111) and (001) surfaces of Au and Pt: thermal behavior', *Surf. Sci.*, vol. 283, no. 1, pp. 260–276, Mar. 1993.

[63] D. Gibbs, B. M. Ocko, D. M. Zehner, and S. G. J. Mochrie, 'Structure and phases of the Au(001) surface: In-plane structure', *Phys. Rev. B*, vol. 42, no. 12, pp. 7330–7344, Oct. 1990.

[64] M. A. V. Hove *et al.*, 'The surface reconstructions of the (100) crystal faces of iridium, platinum and gold. II. Structural determination by LEED intensity analysis', *Surf. Sci.*, vol. 103, no. 1, pp. 218–238, Feb. 1981.

[65] O. K. Binnig, H. Rohrer, C. Gerber, and E. Stoll, 'Real-space observation of the reconstruction of Au(100)', *Surf. Sci.*, vol. 144, no. 2, pp. 321–335, Sep. 1984.

[66] G. J. Edens, X. Gao, M. J. Weaver, N. M. Markovic, and P. N. Ross, 'Influence of adsorbed hydroxyl and carbon monoxide on potential-induced reconstruction of Au(100) as examined by scanning tunneling microscopy', *Surf. Sci.*, vol. 302, no. 1, pp. L275–L282, Jan. 1994.

[67] X. Gao, A. Hamelin, and M. J. Weaver, 'Elucidating complex surface reconstructions with atomic-resolution scanning tunneling microscopy: Au(100)-aqueous electrochemical interface', *Phys. Rev. B*, vol. 46, no. 11, pp. 7096–7102, Sep. 1992.

[68] R. J. Nichols, O. M. Magnussen, J. Hotlos, T. Twomey, R. J. Behm, and D. M. Kolb, 'An in-situ STM study of potential-induced changes in the surface topography of Au(100) electrodes', *J. Electroanal. Chem. Interfacial Electrochem.*, vol. 290, no. 1, pp. 21–31, Sep. 1990.

[69] B. B. Blizanac, C. A. Lucas, M. E. Gallagher, P. N. Ross, and N. M. Marković, 'Surface Structures and Phase Transitions at the Au(100)−Br Interface: pH and CO Effects', *J. Phys. Chem. B*, vol. 108, no. 17, pp. 5304–5313, Apr. 2004.

[70] A. Hamelin, 'The crystallographic orientation of gold surfaces at the gold-aqueous solution interphases', *J. Electroanal. Chem. Interfacial Electrochem.*, vol. 142, no. 1, pp. 299–316, Dec. 1982.

[71] B. M. Ocko, J. Wang, A. Davenport, and H. Isaacs, 'In situ x-ray reflectivity and diffraction studies of the Au(001) reconstruction in an electrochemical cell', *Phys. Rev. Lett.*, vol. 65, no. 12, pp. 1466–1469, Sep. 1990.

[72] B. M. Ocko, G. Helgesen, B. Schardt, J. Wang, and A. Hamelin, 'Charge induced (1×3) reconstruction of the Au(110) surface: An x-ray scattering study', *Phys. Rev. Lett.*, vol. 69, no. 23, pp. 3350–3353, Dec. 1992.

[73] 'In situ scanning tunneling microscopy observations of the potential-dependent (1 × 2) reconstruction on Au(110) in acidic electrolytes', *Surf. Sci.*, vol. 289, no. 1–2, pp. 139–151, May 1993.

[74] E. Vlieg, I. K. Robinson, and K. Kern, 'Relaxations in the missing-row structure of the (1 × 2) reconstructed surfaces of Au(110) and Pt(110)', *Surf. Sci.*, vol. 233, no. 3, pp. 248–254, Jul. 1990.

[75] W. Moritz and D. Wolf, 'Structure determination of the reconstructed Au(110) surface', *Surf. Sci.*, vol. 88, no. 2, pp. L29–L34, Oct. 1979.
[76] X. Gao, A. Hamelin, and M. J. Weaver, 'Reconstruction at ordered Au(110)-aqueous interfaces as probed by atomic-resolution scanning tunneling microscopy', *Phys. Rev. B*, vol. 44, no. 19, pp. 10983–10986, Nov. 1991.
[77] X. Gao and M. J. Weaver, 'Charge-induced (1 × 3) reconstruction of Au(110): mechanistic insights from potentiodynamic scanning tunneling microscopy in alkali iodide electrolytes', *Surf. Sci.*, vol. 313, no. 1, pp. L775–L782, Jun. 1994.
[78] S. Roobol, W. Onderwaater, J. Drnec, R. Felici, and J. Frenken, 'BINoculars: data reduction and analysis software for two-dimensional detectors in surface X-ray diffraction', *J. Appl. Crystallogr.*, vol. 48, no. 4, pp. 1324–1329, Aug. 2015.
[79] M. E. Gallagher, B. B. Blizanac, C. A. Lucas, P. N. Ross, and N. M. Marković, 'Structure sensitivity of CO oxidation on gold single crystal surfaces in alkaline solution: Surface X-ray scattering and rotating disk measurements', *Surf. Sci.*, vol. 582, no. 1, pp. 215–226, May 2005.
[80] A. Chen and J. Lipkowski, 'Electrochemical and Spectroscopic Studies of Hydroxide Adsorption at the Au(111) Electrode', *J. Phys. Chem. B*, vol. 103, no. 4, pp. 682–691, Jan. 1999.
[81] S. B. Aoun, Z. Dursun, T. Koga, G. S. Bang, T. Sotomura, and I. Taniguchi, 'Effect of metal ad-layers on Au(111) electrodes on electrocatalytic oxidation of glucose in an alkaline solution', *J. Electroanal. Chem.*, vol. 567, no. 2, pp. 175–183, Jun. 2004.
[82] C. A. Lucas, N. M. Markovic-acute, and P. N. Ross, 'Adsorption of halide anions at the Pt(111)-solution interfacestudied by in situ surface x-ray scattering', *Phys. Rev. B*, vol. 55, no. 12, pp. 7964–7971, Mar. 1997.
[83] O. M. Magnussen, 'Ordered Anion Adlayers on Metal Electrode Surfaces', *Chem. Rev.*, vol. 102, no. 3, pp. 679–726, Mar. 2002.
[84] B. M. Ocko, O. M. Magnussen, J. X. Wang, R. R. Adić, and T. Wandlowski, 'The structure and phase behavior of electrodeposited halides on single-crystal metal surfaces', *Phys. B Condens. Matter*, vol. 221, no. 1, pp. 238–244, Apr. 1996.
[85] O. R. Melroy *et al.*, 'An in-situ grazing incidence X-ray scattering study of the initial stages of electrochemical growth of lead on silver (111)', *J. Electroanal. Chem. Interfacial Electrochem.*, vol. 258, no. 2, pp. 403–414, Jan. 1989.
[86] M. F. Toney *et al.*, 'Underpotentially deposited thallium on silver (111) by in situ surface x-ray scattering', *Phys. Rev. B*, vol. 45, no. 16, pp. 9362–9374, Apr. 1992.
[87] O. R. Melroy *et al.*, 'Two-dimensional compressibility of electrochemically adsorbed lead on silver (111)', *Phys. Rev. B*, vol. 38, no. 15, pp. 10962–10965, Nov. 1988.
[88] C. Vaz-Domínguez, A. Aranzábal, and A. Cuesta, 'In Situ STM Observation of Stable Dislocation Networks during the Initial Stages of the Lifting of the Reconstruction on Au(111) Electrodes', *J. Phys. Chem. Lett.*, vol. 1, no. 14, pp. 2059–2062, Jul. 2010.
[89] Y. Gründer and C. A. Lucas, 'Probing the charge distribution at the electrochemical interface', *Phys. Chem. Chem. Phys.*, vol. 19, no. 12, pp. 8416–8422, Mar. 2017.
[90] Y. Joly *et al.*, 'Simulation of Surface Resonant X-ray Diffraction', *J. Chem. THEORY Comput.*, vol. 14, pp. 973–980, Feb. 2018.
[91] K. P. Bohnen and D. M. Kolb, 'Charge- versus adsorbate-induced lifting of the Au(100)-(hex) reconstruction in an electrochemical environment', *Surf. Sci.*, vol. 407, no. 1, pp. L629–L632, Jun. 1998.
[92] S. Venkatachalam, P. Kaghazchi, L. A. Kibler, D. M. Kolb, and T. Jacob, 'First principles studies of the potential-induced lifting of the Au(100) surface reconstruction', *Chem. Phys. Lett.*, vol. 455, no. 1–3, pp. 47–51, Mar. 2008.
[93] J. Tersoff, 'Surface-Confined Alloy Formation in Immiscible Systems', *Phys. Rev. Lett.*, vol. 74, no. 3, pp. 434–437, Jan. 1995.

[94] J. W. Schultze and D. Dickertmann, 'Potentiodynamic desorption spectra of metallic monolayers of Cu, Bi, Pb, Tl, and Sb adsorbed at (111), (100), and (110) planes of gold electrodes', *Surf. Sci.*, vol. 54, no. 2, pp. 489–505, 1976.
[95] A. Hamelin, 'Lead adsorption on gold single crystal stepped surfaces', *J. Electroanal. Chem. Interfacial Electrochem.*, vol. 101, no. 2, pp. 285–290, Aug. 1979.
[96] A. Hamelin and A. Katayama, 'Lead underpotential deposition on gold single-crystal surfaces: The (100) face and its vicinal faces', *J. Electroanal. Chem. Interfacial Electrochem.*, vol. 117, no. 2, pp. 221–232, Jan. 1981.
[97] A. Hamelin, 'Underpotential deposition of lead on single crystal faces of gold. Part I. The influence of crystallographic orientation of the substrate', *J. Electroanal. Chem.*, vol. 165, no. 1–2, pp. 167–180, 1984.
[98] A. Hamelin and J. Lipkowski, 'Underpotential deposition of lead on gold single crystal faces: Part II. General discussion', *J. Electroanal. Chem. Interfacial Electrochem.*, vol. 171, no. 1–2, pp. 317–330, Aug. 1984.
[99] R. Adzic, E. Yeager, and B. D. Cahan, 'Optical and Electrochemical Studies of Underpotential Deposition of Lead on Gold Evaporated and Single-Crystal Electrodes', *J. Electrochem. Soc.*, vol. 121, no. 4, pp. 474–484, Apr. 1974.
[100] K. Engelsmann, W. J. Lorenz, and E. Schmidt, 'Underpotential deposition of lead on polycrystalline and single-crystal gold surfaces: Part I. Thermodynamics', *J. Electroanal. Chem. Interfacial Electrochem.*, vol. 114, no. 1, pp. 1–10, Nov. 1980.
[101] K. Engelsmann, W. J. Lorenz, and E. Schmidt, 'Underpotential deposition of lead on polycrystalline and single-crystal gold surfaces: Part II. Kinetics', *J. Electroanal. Chem. Interfacial Electrochem.*, vol. 114, no. 1, pp. 11–24, Nov. 1980.
[102] D. L. Rath, 'Studies of electrode resistance in the electrochemical cell', *J. Electroanal. Chem. Interfacial Electrochem.*, vol. 150, no. 1, pp. 521–534, Jul. 1983.
[103] M. P. Green *et al.*, 'In-situ STM studies of electrochemical underpotential deposition of Pb on Au(111)', *J. Microsc.*, vol. 152, no. 3, pp. 823–829, Dec. 1988.
[104] M. P. Green *et al.*, 'In situ scanning tunneling microscopy studies of the underpotential deposition of lead on gold (111)', *J. Phys. Chem.*, vol. 93, no. 6, pp. 2181–2184, Mar. 1989.
[105] M. P. Green, K. J. Hanson, R. Carr, and I. Lindau, 'STM Observations of the Underpotential Deposition and Stripping of Pb on Au(111) under Potential Sweep Conditions', *J. Electrochem. Soc.*, vol. 137, no. 11, pp. 3493–3498, Nov. 1990.
[106] M. P. Green and K. J. Hanson, 'Alloy formation in an electrodeposited monolayer', *Surf. Sci.*, vol. 259, no. 3, pp. L743–L749, 1991.
[107] M. Binggeli, D. Carnal, R. Nyffenegger, H. Siegenthaler, R. Christoph, and H. Rohrer, 'Electrolytic scanning tunneling microscopy and point contact studies at electrochemically polished Au(111) substrates with and without Pb adsorbates', *J. Vac. Sci. Technol. B*, vol. 9, no. 4, pp. 1985–1992, Jul. 1991.
[108] N. J. Tao, J. Pan, Y. Li, P. I. Oden, J. A. DeRose, and S. M. Lindsay, 'Initial stage of underpotential deposition of Pb on reconstructed and unreconstructed Au(111)', *Surf. Sci.*, vol. 271, no. 1, pp. L338–L344, Jan. 1992.
[109] C. H. Chen, N. Washburn, and A. A. Gewirth, 'In situ atomic force microscope study of lead underpotential deposition on gold (111): structural properties of the catalytically active phase', *J. Phys. Chem.*, vol. 97, no. 38, pp. 9754–9760, Sep. 1993.
[110] T. A. Brunt, T. Rayment, S. J. O'Shea, and M. E. Welland, 'Measuring the Surface Stresses in an Electrochemically Deposited Metal Monolayer: Pb on Au(111)', *Langmuir*, vol. 12, no. 24, pp. 5942–5946, Jan. 1996.
[111] M. F. Toney *et al.*, 'In-Situ Atomic Structure of Underpotentially Deposited Monolayers of Pb and Tl on Au(111) and Ag(111): A Surface X-ray Scattering Study', *J. Phys. Chem.*, vol. 99, no. 13, pp. 4733–4744, Mar. 1995.

[112] E. D. Chabala, B. H. Harji, T. Rayment, and M. D. Archer, 'In-situ x-ray diffraction study of underpotential deposition at the gold(111) surface', *Langmuir*, vol. 8, no. 8, pp. 2028–2033, Aug. 1992.

[113] D. A. Koos and G. L. Richmond, 'Structure and stability of underpotentially deposited layers on gold(111) studied by optical second harmonic generation', *J. Phys. Chem.*, vol. 96, no. 9, pp. 3770–3775, Apr. 1992.

[114] M. Seo and M. Yamazaki, 'Changes in Surface Stress of Gold Electrode during Underpotential Deposition of Pb', *J. Electrochem. Soc.*, vol. 151, no. 8, pp. E276–E281, Aug. 2004.

[115] J. W. Shin, U. Bertocci, and G. R. Stafford, 'Underpotential Deposition of Tl on (111)-Textured Au: In Situ Stress and Nanogravimetric Measurements', *J. Phys. Chem. C*, vol. 114, no. 41, pp. 17621–17628, Oct. 2010.

[116] G. R. Stafford and U. Bertocci, 'In Situ Stress and Nanogravimetric Measurements During Underpotential Deposition of Pb on (111)-Textured Au', *J. Phys. Chem. C*, vol. 111, no. 47, pp. 17580–17586, Nov. 2007.

[117] K. M. Robinson and W. E. O'Grady, 'X-ray surface diffraction studies of the restructuring and electrodeposition of Pb monolayers on Au(100) single crystals', *Faraday Discuss.*, vol. 95, no. 0, pp. 55–64, Jan. 1993.

[118] U. Schmidt, S. Vinzelberg, and G. Staikov, 'Pb UPD on Ag(100) and Au(100) — 2D phase formation studied by in situ STM', *Surf. Sci.*, vol. 348, no. 3, pp. 261–279, Mar. 1996.

[119] B. M. Ocko and J. Wang, 'Surface Structure at the Au(111) Electrode', in *Synchrotron Techniques in Interfacial Electrochemistry*, C. A. Melendres and A. Tadjeddine, Eds. Dordrecht: Springer Netherlands, 1994, pp. 127–155.

[120] A. Menzel *et al.*, 'Resonance anomalous surface X-ray scattering', *Radiat. Phys. Chem.*, vol. 75, no. 11, pp. 1651–1660, Nov. 2006.

[121] J. Clavilier, J. M. Orts, J. M. Feliu, and A. Aldaz, 'Study of the conditions for irreversible adsorption of lead at Pt(h,k,l) electrodes', *J. Electroanal. Chem. Interfacial Electrochem.*, vol. 293, no. 1, pp. 197–208, Oct. 1990.

[122] J. M. Feliu, A. Fernandez-Vega, J. M. Orts, and A. Aldaz, 'The behaviour of lead and bismuth adatoms on well-defined platinum surfaces', *J. Chim. Phys.*, vol. 88, pp. 1493–1518, 1991.

[123] N. M. Marković, B. N. Grgur, C. A. Lucas, and P. N. Ross, 'Underpotential deposition of lead on Pt(111) in the presence of bromide: RRDPt(111)E and X-ray scattering studies1Dedicated to Professor Aleksandar Despić in honour of his 70th birthday.1', *J. Electroanal. Chem.*, vol. 448, no. 2, pp. 183–188, May 1998.

[124] S. Pons, 'The use of fourier transform infrared spectroscopy for in situ recording of species in the electrode-electrolyte solution interphase', *J. Electroanal. Chem. Interfacial Electrochem.*, vol. 150, no. 1, pp. 495–504, Jul. 1983.

[125] N. S. Marinković, M. Hecht, J. S. Loring, and W. R. Fawcett, 'A sniftirs study of the diffuse double layer at single crystal platinum electrodes in acetonitrile', *Electrochimica Acta*, vol. 41, no. 5, pp. 641–651, Apr. 1996.

[126] S. Morin, H. Dumont, and B. E. Conway, 'Evaluation of the effect of two-dimensional geometry of pt single-crystal faces on the kinetics of upd of h using impedance spectroscopy', *J. Electroanal. Chem.*, vol. 412, no. 1, pp. 39–52, Aug. 1996.

[127] S. Morin, B. E. Conway, G. J. Edens, and M. J. Weaver, 'The reactive chemisorption of acetonitrile on Pt(111) and Pt(100) electrodes as examined by in situ infrared spectroscopy', *J. Electroanal. Chem.*, vol. 421, no. 1, pp. 213–220, Jan. 1997.

[128] I. Srejić, M. Smiljanić, Z. Rakočević, and S. Štrbac, 'Oxygen Reduction on Polycrystalline Pt and Au Electrodes in Perchloric Acid Solution in the Presence of Acetonitrile', *Int J Electrochem Sci*, vol. 6, p. 11, 2011.

[129] G. Horányi and E. M. Rizmayer, 'Formation of ethane during the electroreduction of acetonitrile at a platinized platinum electrode: A special feature in diluted aqueous solutions', *J. Electroanal. Chem. Interfacial Electrochem.*, vol. 113, no. 2, pp. 305–309, Oct. 1980.
[130] M. Szklarczyk and J. Sobkowski, 'The behaviour of high polar organic solvents at platinum electrode — II. Adsorption and electrode reactions of acetonitrile', *Electrochimica Acta*, vol. 25, no. 12, pp. 1597–1601, Dec. 1980.
[131] S. Wasmus and W. Vielstich, 'Electro-oxidation and electroreduction of acetonitrile in aqueous acid solution: A DEMS study', *J. Electroanal. Chem.*, vol. 345, no. 1, pp. 323–335, Feb. 1993.
[132] R. A. Gu, P. G. Cao, Y. H. Sun, and Z. Q. Tian, 'Surface-enhanced Raman spectroscopy studies of platinum surfaces in acetonitrile solutions', *J. Electroanal. Chem.*, vol. 528, no. 1, pp. 121–126, Jun. 2002.
[133] T. P. Mernagh and R. P. Cooney, 'Raman evidence for the photochemical formation of cyanide from acetonitrile on copper electrodes', *J. Electroanal. Chem. Interfacial Electrochem.*, vol. 177, no. 1, pp. 139–148, Oct. 1984.
[134] A. T. Hubbard, E. Y. Cao, and D. A. Stern, 'Surface analysis of electrodes by ultra-high vacuum techniques: acetonitrile solvent chemisorption at Pt(111)', *Electrochimica Acta*, vol. 39, no. 8, pp. 1007–1014, Jun. 1994.
[135] P. W. Faguy, W. R. Fawcett, G. Liu, and A. J. Motheo, 'A study of the adsorption of acetonitrile on a gold electrode from aqueous solutions using in situ vibrational spectroscopy', *J. Electroanal. Chem.*, vol. 339, no. 1, pp. 339–353, Nov. 1992.
[136] A. I. Danilov, 'Scanning tunnelling and atomic force microscopy in the electrochemistry of surfaces', *Russ. Chem. Rev.*, vol. 64, no. 8, p. 767, 1995.
[137] S. Szabó, 'Underpotential deposition of metals on foreign metal substrates', *Int. Rev. Phys. Chem.*, vol. 10, no. 2, pp. 207–248, Apr. 1991.
[138] M. H. Hölzle, U. Retter, and D. M. Kolb, 'The kinetics of structural changes in Cu adlayers on Au(111)', *J. Electroanal. Chem.*, vol. 371, no. 1, pp. 101–109, Jun. 1994.
[139] M. H. Hölzle, V. Zwing, and D. M. Kolb, 'The influence of steps on the deposition of Cu onto Au(111)', *Electrochimica Acta*, vol. 40, no. 10, pp. 1237–1247, Jul. 1995.
[140] Z. Shi, S. Wu, and J. Lipkowski, 'Investigations of Cl− adsorption at the Au(111) electrode in the presence of underpotentially deposited copper atoms', *J. Electroanal. Chem.*, vol. 384, no. 1–2, pp. 171–177, Mar. 1995.
[141] O. M. Magnussen, J. Hotlos, R. J. Nichols, D. M. Kolb, and R. J. Behm, 'Atomic structure of Cu adlayers on Au(100) and Au(111) electrodes observed by in situ scanning tunneling microscopy', *Phys. Rev. Lett.*, vol. 64, no. 24, pp. 2929–2932, Jun. 1990.
[142] R. J. Nichols, D. M. Kolb, and R. J. Behm, 'STM observations of the initial stages of copper deposition on gold single-crystal electrodes', *J. Electroanal. Chem. Interfacial Electrochem.*, vol. 313, no. 1, pp. 109–119, Sep. 1991.
[143] T. Hachiya, H. Honbo, and K. Itaya, 'Detailed underpotential deposition of copper on gold(III) in aqueous solutions', *J. Electroanal. Chem. Interfacial Electrochem.*, vol. 315, no. 1, pp. 275–291, Oct. 1991.
[144] B. Madry, K. Wandelt, and M. Nowicki, 'Deposition of copper and sulfate on Au(111): New insights', *Appl. Surf. Sci.*, vol. 388, no. Part B, pp. 678–683, Dec. 2016.
[145] S. Manne, P. K. Hansma, J. Massie, V. B. Elings, and A. A. Gewirth, 'Atomic-Resolution Electrochemistry with the Atomic Force Microscope: Copper Deposition on Gold', *Science*, vol. 251, no. 4990, pp. 183–186, Jan. 1991.
[146] N. Podgaynyy, S. Wezisla, C. Molls, S. Iqbal, and H. Baltruschat, 'Stick–slip behaviour on Au(111) with adsorption of copper and sulfate', *Beilstein J. Nanotechnol.*, vol. 6, no. 1, pp. 820–830, Mar. 2015.

[147] S. Wu, J. Lipkowski, T. Tyliszczak, and A. P. Hitchcock, 'Effect of anion adsorption on early stages of copper electrocrystallization at Au(111) surface', *Prog. Surf. Sci.*, vol. 50, no. 1–4, pp. 227–236, Sep. 1995.
[148] M. F. Toney *et al.*, 'Electrochemical deposition of copper on a gold electrode in sulfuric acid: Resolution of the interfacial structure', *Phys. Rev. Lett.*, vol. 75, no. 24, pp. 4472–4475, 1995.
[149] J. R. I. Lee, R. L. O'Malley, T. J. O'Connell, A. Vollmer, and T. Rayment, 'X-ray Absorption Spectroscopy Characterization of Cu Underpotential Deposition on Au(111) and Organothiol-Self-Assembled-Monolayer-Modified Au(111) Electrodes from Sulfate Supporting Electrolyte', *J. Phys. Chem. C*, vol. 113, no. 28, pp. 12260–12271, Jul. 2009.
[150] Y. Nakai, M. S. Zei, D. M. Kolb, and G. Lehmpfuhl, 'A LEED and RHEED Investigation of Cu on Au(111) in the Underpotential Region', *Berichte Bunsenges. Für Phys. Chem.*, vol. 88, no. 4, pp. 340–345, Apr. 1984.
[151] D. M. Kolb, 'UHV Techniques in the Study of Electrode Surfaces', *Z. Für Phys. Chem.*, vol. 154, no. 1–2, pp. 179–199, 1987.
[152] M. S. Zei, G. Qiao, G. Lehmpfuhl, and D. M. Kolb, 'The influence of anions on the structure of underpotentially deposited Cu on Au(111): A LEED, RHEED and AES study', *Berichte Bunsenges. Für Phys. Chem.*, vol. 91, no. 4, pp. 349–353, Apr. 1987.
[153] O. M. Magnussen, J. Hotlos, G. Beitel, D. M. Kolb, and R. J. Behm, 'Atomic structure of ordered copper adlayers on single-crystalline gold electrodes', *J. Vac. Sci. Technol. B Microelectron. Nanometer Struct. Process. Meas. Phenom.*, vol. 9, no. 2, pp. 969–975, Mar. 1991.
[154] N. Batina, T. Will, and D. M. Kolb, 'Study of the initial stages of copper deposition by in situ scanning tunnelling microscopy', *Faraday Discuss.*, vol. 94, no. 0, pp. 93–106, Jan. 1992.
[155] M. P. Green and K. J. Hanson, 'Copper adlayer formation on Au(111) from sulfuric acid electrolyte', *J. Vac. Sci. Technol. A*, vol. 10, no. 5, pp. 3012–3018, Sep. 1992.
[156] Z. Shi and J. Lipkowski, 'Investigations of SO42− adsorption at the Au(111) electrode in the presence of underpotentially deposited copper adatoms', *J. Electroanal. Chem.*, vol. 364, no. 1, pp. 289–294, Jan. 1994.
[157] Z. Shi and J. Lipkowski, 'Coadsorption of Cu2+ and SO42− at the Au(111) electrode', *J. Electroanal. Chem.*, vol. 365, no. 1, pp. 303–309, Feb. 1994.
[158] Z. Shi, S. Wu, and J. Lipkowski, 'Coadsorption of metal atoms and anions: Cu upd in the presence of SO42−, Cl− and Br−', *Electrochimica Acta*, vol. 40, no. 1, pp. 9–15, Jan. 1995.
[159] J. G. Gordon, O. R. Melroy, and M. F. Toney, 'Structure of metal-electrolyte interfaces: Copper on gold(111), water on silver(111)', *Electrochimica Acta*, vol. 40, no. 1, pp. 3–8, Jan. 1995.
[160] G. L. Borges, K. K. Kanazawa, J. G. Gordon II, K. Ashley, and J. Richer, 'An in-situ electrochemical quartz crystal microbalance study of the underpotential deposition of copper on Au(111) electrodes', *J. Electroanal. Chem.*, vol. 364, no. 1–2, pp. 281–284, Jan. 1994.
[161] M. Nakamura, O. Endo, T. Ohta, M. Ito, and Y. Yoda, 'Surface X-ray diffraction study of Cu UPD on Au(111) electrode in 0.5 M H2SO4 solution: the coadsorption structure of UPD copper, hydration water molecule and bisulfate anion on Au(111)', *Surf. Sci.*, vol. 514, no. 1, pp. 227–233, Aug. 2002.
[162] M. Watanabe, H. Uchida, M. Miura, and N. Ikeda, 'Electrochemical quartz crystal microbalance study of copper ad-atoms on highly ordered Au(111) electrodes in sulfuric acid', *J. Electroanal. Chem.*, vol. 384, no. 1, pp. 191–195, Mar. 1995.

[163] A. Vaskevich and I. Rubinstein, 'Underpotential deposition of copper in acetonitrile', *J. Electroanal. Chem.*, vol. 491, no. 1, pp. 87–94, Sep. 2000.

[164] K. Pekmez, E. Avci, H. G. Baumgärtel, and C. Donner, 'The Under Potential Deposition of Cu on Au (111) in Nonaqueous Acetonitrile', *Z. Für Phys. Chem.*, vol. 226, no. 9–10, pp. 953–963, Oct. 2012.

[165] H.-C. Liang, E. Kim, C. D. Incarvito, A. L. Rheingold, and K. D. Karlin, 'A Bis-Acetonitrile Two-Coordinate Copper(I) Complex: Synthesis and Characterization of Highly Soluble B(C6F5)4- Salts of [Cu(MeCN)2]+ and [Cu(MeCN)4]+', *Inorg. Chem.*, vol. 41, no. 8, pp. 2209–2212, Apr. 2002.

[166] A. V. Rudnev, E. B. Molodkina, A. I. Danilov, Y. M. Polukarov, and J. M. Feliu, 'Kinetics of copper UPD on stepped platinum single crystals in the presence of acetonitrile', *Electrochem. Commun.*, vol. 10, no. 4, pp. 502–505, Apr. 2008.

[167] P. Fenter, M. T. McBride, G. Srajer, N. C. Sturchio, and D. Bosbach, 'Structure of Barite (001)− and (210)−Water Interfaces', *J. Phys. Chem. B*, vol. 105, no. 34, pp. 8112–8119, Aug. 2001.

[168] J. Gustafson *et al.*, 'High-Energy Surface X-Ray Diffraction for Fast Surface Structure Determination', *Science*, p. 1246834, Jan. 2014.

[169] Y. Gründer, P. Thompson, A. Brownrigg, M. Darlington, and C. A. Lucas, 'Probing the Halide–Metal Interaction by Monolayer Metal Deposition at the Electrochemical Interface', *J. Phys. Chem. C*, vol. 116, no. 10, pp. 6283–6288, Mar. 2012.

Appendices

Linear least squares code for the analysis of CTR data

```
#!/usr/bin/python
#SPECULAR CTR FIT

#The least-sqaures algothrim has been replaced by
#the more versatile lmfit-py library to allow easy paramerisation of
#varibles and the calculation of confidence intervals

#2016-04(YG) The programme has been modified:
# single functions in files to avoid copy+Paste errors
# plotting counts rod automatically

# ! when using programme please make sure you load:
# *the right model (111), (001) or (110)
# * the right f_atoms for the wavelength used
# *the right corrections for the setup used (xmascorr, diamondcorr,
slscorr)
# * the right residual (either 'residual' for single dataset or
'residualdouble' for the ratio fit)
#Please check this for all sub-functions....
# and
# modify the parameter file
# give the right path to the parameter file
# the folder 'fit' for output files exists in the folder specified

import lmfit as lf
import numpy as np
import sys
import scipy
import os
import time
from scipy.integrate import quad
from scipy.special import erf
from scipy.special import erfc
from TF import TF
from read_data import read_data
from f_atom_1127A import f_atom
from read_parameters import read_parameters
from residual import residual
from  xmascorr import corr_factors
from  model001 import model
from time import gmtime, strftime
global expEy, expAy, amcorr1, fthick,  specular, constants

import datetime
print datetime.datetime.now()
params,fmethod,tol, specularrod, atoms, constants, file1, syserror =
read_parameters('para.py')

#file1=filea
data = read_data(file1)
data = np.asarray(data)
data = data.astype(np.float64)

#put cols in seperate numpy lists
```

```
h = abs(data[:,0])#,decimals=2)
k = abs(data[:,1])#,decimals=2)
l =data[:,2]#,decimals=2)
expA = data[:,3]
expE =
data[:,4]#np.sqrt(data[:,4])#,decimals=2)**2)#+1*(abs((np.around(dat
a[:,3],decimals=2)-np.around(data[:,5],decimals=2))))**2+
(syserror*expA)**2)
expAa = data[:,3]#,decimals=2)
expEa =
data[:,4]#np.sqrt(data[:,4])#,decimals=2)**2)#+1*(abs((np.around(dat
a[:,9],decimals=2)-np.around(data[:,7],decimals=2))))**2+
(syserror*expA)**2)
#print expA, expE
for i in range(len(expE)):
        if h[i]==0 and k[i]==0:
                expA[i] = expAa[i]
                expE[i] = np.sqrt(expEa[i]**2)+(syserror*expA[i])
        else:
                expA[i] = expAa[i]
                expE[i] = np.sqrt(expEa[i]**2)+(syserror*expA[i])

#perform the fit
result = lf.Minimizer(residual, params,
fcn_args=(h,k,l,expA,expE,specularrod,atoms,constants))

result.prepare_fit()

if fmethod == "leastsq":
        result.leastsq(xtol = tol[0], ftol = tol[1], maxfev =
tol[2])
if fmethod == "lbfgsb":
        result.lbfgsb(maxfun = tol[2])
if fmethod == "nelder":
        result.fmin(xtol = tol[0], ftol = tol[1], maxfun = tol[2])
#calculate chi squared
final = np.zeros(len(l))
final1 = np.zeros(len(l))
expAx = np.zeros(len(l))
expEx= np.zeros(len(l))
chisq = 0
for i in range(len(l)):
        final1[i] = model(h[i],k[i],l[i],expA[i],expE[i],params,
atoms,constants)

expAx[i]=expA[i]/corr_factors(h[i],k[i],l[i],params,constants)

expEx[i]=expE[i]/corr_factors(h[i],k[i],l[i],params,constants)
        #print expA[i],expE[i],final1[i],h[i],k[i],l[i]
        if specularrod == 0:
           if h[i] == 1 or k[i] ==1:
                chisq = chisq + ((expA[i] - final1[i])/expE[i])**2
        else:
          chisq = chisq + ((expA[i] - final1[i])/expE[i])**2
#print chisq
# write error report
lf.report_fit(params)

# plot results!
#convert y to log scale and seperate the different rods
kcount=1
```

```
ichange=0
hnew=np.array([])
knew=np.array([])
hnew=abs(h[0])
knew=abs(k[0])
if isinstance(hnew, float) :
        hnew=np.asarray([hnew])
        hnew=hnew.astype(np.float64)
        knew=np.asarray([knew])
        knew=knew.astype(np.float64)

for i in range(len(l)):

        if i>0:
              if (h[i]!=h[i-1]) or (k[i]!=k[i-1]):
                    hnew=np.append(hnew,abs(h[i]))
                    knew=np.append(knew,abs(k[i]))


for i in range(len(hnew)):
        local_namespace=locals()
        name='ytheory'+str(hnew[i])[0]+str(knew[i])[0]

local_namespace['ytheory'+str(hnew[i])[0]+str(knew[i])[0]]=[]
        local_namespace['yexp'+str(hnew[i])[0]+str(knew[i])[0]]=[]
        local_namespace['yerr'+str(hnew[i])[0]+str(knew[i])[0]]=[]
        local_namespace['l'+str(hnew[i])[0]+str(knew[i])[0]]=[]

local_namespace['l'+str(hnew[i])[0]+str(knew[i])[0]+'theo']=[]
#ytheory00 = []
#ytheory01 = []
#ytheory10 = []

ltheo = []
h1 = []
h2 = []
h3 = []
k1 = []
k2 = []
k3 = []
l1 = []
l2 = []
l3 = []
steps=(max(l))*100
#for i in range(len(hnew))
h1=np.ones(steps)*hnew[0]
k1=np.ones(steps)*knew[0]
l1=np.arange(0.2,max(l)+0.1,.01)
#print len(hnew)
if len(hnew)>1:
        h2=np.ones(steps)*hnew[1]
        k2=np.ones(steps)*knew[1]
        l2=np.arange(0.2,max(l)+0.2,.01)

if len(hnew)>2:
        h3=np.ones(steps)*hnew[2]
        k3=np.ones(steps)*knew[2]
        l3=np.arange(0.2,max(l)+0.2,.01)

if len(hnew)>3:
        h4=np.ones(steps)*hnew[3]
```

```
        k4=np.ones(steps)*knew[3]
        l4=np.arange(0.2,max(l)+0.2,.01)
llayer=np.arange(0.05,7,.01)

ltheo=np.concatenate([l1, l2,l3])#,l4])
htheo=np.concatenate([h1, h2,h3])#,h4])
ktheo=np.concatenate([k1, k2,k3])#,k4])
finaltheo = np.zeros(len(ltheo))
#print ltheo
for i in range(len(ltheo)):
        finaltheo[i] =
model(htheo[i],ktheo[i],ltheo[i],ltheo[i],ltheo[i],params,
atoms,constants)/corr_factors(htheo[i],ktheo[i],ltheo[i],params,cons
tants)
        #finaltheo[i]=amcorr1
ftot1=0
temp=0

 #oxygen layers
shift = 0

for i in range(1,4):
       #if (params
                        cov = params['Ocoverage'+str(i)].value
                        shift = params['Oeps'+str(i)].value
                        flayer = (6)*np.exp(-
(llayer**2*params['Odwf'+str(i)].value**2)/2)
*cov#*np.exp(1j*llayer)
                        ftot1 +=
flayer*np.exp(2*np.pi/7.063*1j*params['Oeps'+str(i)].value*llayer)
        #layered water structure

if(params['Lcoverage'].value > 0):
                        #print "LAYERED MODEL INCLUDED!"
                        temp = np.exp(-
(llayer**2*params['Lsigmabar'].value**2)/2)*np.exp(1j*llayer*params[
'Lcw'].value)
                        flayer1 = params['Lcoverage'].value*np.exp(-
(llayer**2*params['Lsigma0'].value**2)/2)*np.exp(2*np.pi/7.063*1j*(p
arams['Ldist'].value-params['Lcw'].value)*llayer)

                        ftot1 += flayer1/(1-temp)
if(params['Lcoverage1'].value > 0):
                        #print "LAYERED MODEL INCLUDED!"
                        temp = np.exp(-
(llayer**2*params['Lsigmabar1'].value**2)/2)*np.exp(1j*llayer*params
['Lcw1'].value)
                        flayer1 =
params['Lcoverage1'].value*np.exp(-
(llayer**2*params['Lsigma01'].value**2)/2)*np.exp(2*np.pi/7.063*1j*(
params['Ldist'].value-params['Lcw'].value)*llayer)

                        ftot1 += flayer1/(1-temp)
        #error function
if(params['Ecoverage'].value > 0):
                       # print "ERROR FUNCTION INCLUDED!"
                        flayer1 =
1j*(params['Ecoverage'].value)*np.exp(-
((llayer*params['Esigma'].value)**2/2))/llayer*np.exp(2*np.pi/7.063*
1j*params['Edist'].value*llayer)
                        ftot1 = ftot1 +flayer1
```

```
        #calculate complex conjugate

amp1 = np.log10(abs(ftot1*np.conjugate(ftot1)))



for i in range(len(ltheo)):
  for j in range(len(hnew)):
        if htheo[i] == hnew[j] and ktheo[i] == knew[j]:

local_namespace['l'+str(hnew[j])[0]+str(knew[j])[0]+'theo'].append(l
theo[i])

local_namespace['ytheory'+str(hnew[j])[0]+str(knew[j])[0]].append(np
.log10(finaltheo[i]))


for i in range(len(l)):
  for j in range(len(hnew)):
        if h[i] == hnew[j] and k[i] == knew[j]:

local_namespace['l'+str(hnew[j])[0]+str(knew[j])[0]].append(l[i])

local_namespace['yexp'+str(hnew[j])[0]+str(knew[j])[0]].append(np.lo
g10(expAx[i]))

local_namespace['yerr'+str(hnew[j])[0]+str(knew[j])[0]].append(0.434
*(expEx[i]/expAx[i]))


xlayer=[]
ylayer=[]
xlayer=np.arange(-3,50,.01)
yerrlayer=(1+erf((xlayer-
params['Edist'].value)/params['Esigma'].value))/2*params['Ecoverage'
].value
ylayerlayer1=0
ylayerlayer2=0
ylayerlayer=0

for i in range(1,30):
     ylayerlayer1 +=    np.exp(-(xlayer-(i)*params['Lcw'].value-
(params['Ldist'].value-
params['Lcw'].value))**2/(2*(params['Lsigma0'].value+(i)*params['Lsi
gmabar'].value)**2))/(2*(params['Lsigma0'].value+(i)*params['Lsigmab
ar'].value)/np.sqrt(2*np.pi))*params['Lcoverage'].value
     ylayerlayer += np.exp(-(xlayer-(i)*params['Lcw'].value-
(params['Ldist'].value-
params['Lcw'].value))**2/(2*(params['Lsigma0'].value+(i)*params['Lsi
gmabar'].value)**2))/(2*(params['Lsigma0'].value+(i)*params['Lsigmab
ar'].value)/np.sqrt(2*np.pi))*params['Lcoverage'].value
     ylayerlayer2 += np.exp(-(xlayer-(i)*params['Lcw1'].value-
(params['Ldist1'].value-
params['Lcw1'].value))**2/(2*(params['Lsigma01'].value+(i)*params['L
sigmabar1'].value)**2))/(2*(params['Lsigma01'].value+(i)*params['Lsi
gmabar1'].value)/np.sqrt(2*np.pi))*params['Lcoverage1'].value

     ylayerlayer += np.exp(-(xlayer-(i)*params['Lcw1'].value-
(params['Ldist1'].value-
params['Lcw1'].value))**2/(2*(params['Lsigma01'].value+(i)*params['L
```

```
sigmabar1'].value)**2))/(2*(params['Lsigma01'].value+(i)*params['Lsi
gmabar1'].value)/np.sqrt(2*np.pi))*params['Lcoverage1'].value
oxlayer=0
for i in range(1,3):
     oxlayer += np.exp(-(xlayer-
params['Oeps'+str(i)].value)**2/(2*(params['Odwf'+str(i)].value)**2)
)/(2*(params['Odwf'+str(i)].value)/np.sqrt(2*np.pi))*params['Ocovera
ge'+str(i)].value


ylayer=yerrlayer+ylayerlayer+oxlayer
print
print "Fit Succeeded"
print file1
print "--------------------"
print   "Chi Squared:", chisq
if fmethod == "leastsq":
                print   "Degrees of Freedom:", result.nfree
                print   "Reduced Chi Squared:", chisq/result.nfree

import pylab
from matplotlib.ticker import NullFormatter,MultipleLocator,
FormatStrFormatter

myxlim= [min(l00)-0.1,max(l00)+0.2]

for j in range(len(hnew)):
       local_namespace['myylim'+str(hnew[j])[0]+str(knew[j])[0]]=
[min(local_namespace['yexp'+str(hnew[j])[0]+str(knew[j])[0]])-
0.2,max(local_namespace['yexp'+str(hnew[j])[0]+str(knew[j])[0]])+0.2
]
myylimwater=[min(ylayer)-0.2,max(ylayer)+0.2]
myxlimwater=[min(xlayer)-0.2,max(xlayer)+0.2]
pylab.figure(num=None, figsize=(10, 8),facecolor='white')
#subplots_adjust(hspace=0.000)
number_of_subplots=len(hnew)+2

for i,v in enumerate(xrange(len(hnew))):
    v = v+1
    ax1 = pylab.subplot(number_of_subplots,1,v)

    pylab.plot(local_namespace['l'+str(hnew[i])[0]+str(knew[i])[0]],
local_namespace['yexp'+str(hnew[i])[0]+str(knew[i])[0]], "ro",
label='Experiment', markersize=2)

pylab.errorbar(local_namespace['l'+str(hnew[i])[0]+str(knew[i])[0]],
local_namespace['yexp'+str(hnew[i])[0]+str(knew[i])[0]],
local_namespace['yerr'+str(hnew[i])[0]+str(knew[i])[0]],fmt="none",)

pylab.plot(local_namespace['l'+str(hnew[i])[0]+str(knew[i])[0]+'theo
'], local_namespace['ytheory'+str(hnew[i])[0]+str(knew[i])[0]], "r-
", label='Theory')
    pylab.xlim(myxlim)

pylab.ylim(local_namespace['myylim'+str(hnew[i])[0]+str(knew[i])[0]]
)
    pylab.ylabel(str(hnew[i])[0]+str(knew[i])[0]+"L")
    ax1.yaxis.set_label_position("right")
    pylab.minorticks_off()

    ax1.xaxis.set_major_formatter( NullFormatter() )
```

```
pylab.title(file1  + '\n Reduced-Chi^2:
'+str(chisq/result.nfree),fontdict={'fontsize':12})
ax4 = pylab.subplot(len(hnew)+2,1,len(hnew)+1)
pylab.plot(llayer, amp1, "b-", label='Theory')
myyliml= [min(amp1)-0.2,max(amp1)+0.2]
pylab.xlim(myxlim)
#pylab.xlim(3)
pylab.ylim(myylimwater)
ax4.xaxis.set_major_formatter( NullFormatter() )


ax5 = pylab.subplot(len(hnew)+2,1,len(hnew)+2)
pylab.plot(xlayer, ylayer, "r-", label='Error', markersize=2)
pylab.plot(xlayer, ylayerlayer1, "y-", label='Error', markersize=2)
pylab.plot(xlayer, ylayerlayer2, "g-", label='Error', markersize=2)
pylab.plot(xlayer, oxlayer, "b-", label='Error', markersize=2)
pylab.xlim(myxlimwater)
pylab.ylim(myylimwater)

pylab.ylabel("Water")
ax5.yaxis.set_label_position("right")
#pylab.subplots_adjust(wspace=0,hspace=0)
pylab.tight_layout()
if not os.path.exists("output/images"): os.makedirs("output/images")
pylab.savefig('output/images/'+file1+'fits'+strftime("
%d_%b_%Y_%H_%M", gmtime())+'.png')
#pylab.ion()

#Save to fit to a log
def writelog(filename, paramw, chisq,rchi):
        localtime = time.asctime( time.localtime(time.time()))
        FILE = open(filename,"a") #Open the file in write mode
        FILE.write(file1+'\n')
        FILE.write("-------------------------------------------------
-------------\n")
        FILE.write("FIT LOG:"+localtime+"\nCHISQ:
"+str(chisq)+"\nRed-CHISQ: "+str(rchi)+"\n")
        FILE.write("-------------------------------------------------
-------------\n")
        FILE.write(lf.fit_report(params)+'\n')
        FILE.close

print "Saving image files.."
if not os.path.exists("output"): os.makedirs("output")
writelog('output/'+file1+strftime(" %d_%b_%Y_%H_%M",
gmtime())+'.log', params, chisq, chisq/result.nfree)

#output the results
def writecal(h,k,l, y,e):
  for i in range(len(hnew)):


        if h == hnew[i] and k == knew[i]:
                FILE =
open('output/'+file1+str(hnew[i])[0]+str(knew[i])[0] +strftime("
%d_%b_%Y_%H_%M", gmtime())+'.exp',"a")

FILE.write(str(h)+"\t"+str(k)+"\t"+str(l)+"\t"+str(y)+"\t"+str(e)+"\
n")
                FILE.close
```

```
def writetheo(h,k,l, y):
  for i in range(len(hnew)):
        if h == hnew[i] and k == knew[i]:
                FILE =
open('output/'+file1+str(hnew[i])[0]+str(knew[i])[0] +strftime("
%d_%b_%Y_%H_%M", gmtime())+'.cal',"a")
               # print hnew[i],knew[i]

FILE.write(str(h)+"\t"+str(k)+"\t"+str(l)+"\t"+str(y)+"\n")
                FILE.close

def writewater(x,y1,y2,y,o):
   for i in range(len(hnew)):
        FILE = open('output/'+file1+'watermodel'+strftime("
%d_%b_%Y_%H_%M", gmtime())+'.dat',"a")


FILE.write(str(x)+"\t"+str(y1)+"\t"+str(y2)+"\t"+str(y)+"\t"+str(o)+
"\n")
        FILE.close

for i in range(len(l)):
        writecal(h[i], k[i], l[i], expAx[i], expEx[i])

for i in range(len(ltheo)):
        writetheo(htheo[i], ktheo[i], ltheo[i], finaltheo[i])

for i in range(len(xlayer)):
        writewater(xlayer[i], oxlayer[i],
ylayerlayer1[i],ylayerlayer2[i],ylayer[i])

import datetime
print datetime.datetime.now()

pylab.show()


def model(h,k,l,expA,expE,params, atoms,constants):
        #Different scale factor for specular rod
        import lmfit as lf
        import numpy as np
        import sys
        import scipy
        import os
        import time
        from scipy.integrate import quad
        from scipy.special import erf
        from scipy.special import erfc
        from TF import TF
        from read_data import read_data
        from f_atom_1127A import f_atom
        from read_parameters import read_parameters
        from residual import residual
        global expEy, expAy, amcorr1, fthick, qz,  specular, q, qinp
        from  xmascorr import corr_factors
        #constants
        a = constants[0];

        wavelength=constants[1];
        abslen=3.734e7/(wavelength**3)
        pi = np.pi
```

```
        dwfbulk=constants[2]
        #dwfbulk = params['dwfbulk'].value
        if h == 0 and k ==0:
                l=l*params['shiftl'].value
        if h == 1 and k ==0:
                l=l*params['shiftl1'].value
        if h == 0 and k ==1:
                l=l*params['shiftl2'].value
        #transform recp. unit cell
        #k=0
        h = (h+k)/2
        k = (h-k)/2
        h_cub = (h+k)
        k_cub = (h-k)
        l_cub = l

        hinp=h
        kinp=k
        linp=0

        q = 2*pi*np.sqrt(h_cub**2 + k_cub**2 + l_cub**2)/a
        qinp=2*pi*np.sqrt(hinp**2+kinp**2+linp**2)/a
        qz=2*pi*l/a#/np.sqrt(2)
        #qz = 2*pi*l/(a*1.73205)

        #caluclate scattering factors
        zau = f_atom(q, "Au")
        zcu = f_atom(q, "Cu")
        zcup = f_atom(q, "Cu+")
        zo = f_atom(q, "O")
        zc = f_atom(q, "C")
        zag = f_atom(q, "Ag")
        zna= f_atom(q, "Na")
        #Debye Waller factors
        dwbulk = np.exp(-(q**2 * dwfbulk**2)/2)
        dwl = [0]


        for i in range(1,4):
           if h == 0 and k == 0:
                if i == 3:
                   dwl.append(dwbulk*np.exp(-
(qz**2*params['dwf'+str(i)].value**2)/2))
                  # if h == 0 and k == 0:
                   #     dwl.append(dwbulk*np.exp(-
(qz**2*params['dwfz'+str(i)].value**2)/2))
                else:
                   dwl.append(dwbulk*np.exp(-
(qz**2*params['dwf'+str(i)].value**2)/2))
           else:
                   dwl.append(dwbulk*np.exp(-
(qz**2*params['dwf'+str(i)].value**2)/2))


        #Bulk contribution
        ftot = (f_atom(q,constants[3]))*dwbulk/(1-np.exp(-
pi*1j*(h+k+l)))


        #Commensurate metal layers
        shift = 0
```

```
        fptlayer=0
        beta=params['beta'].value
        betafactor=(1-beta)/np.sqrt(1-beta**2-2*beta*np.cos(2*pi*(-
h/2 + k/2 +l/2)))
       # for i in range(1):
       #         cov = params['coverage'+str(i)].value
       #         shift += params['eps'+str(i)].value
       #         flayer = zcu*dwl[i]*cov*np.exp(2*pi*1j*i*(-h/3 +
k/3 +l/3))
       #         ftot += flayer*np.exp(2*pi*1j*shift*l)
        for i in range(1,4):
                cov = params['coverage'+str(i)].value
                shift += params['eps'+str(i)].value
                if i == 3:
                        flayer = (f_atom(q,
(atoms[2])))*dwl[i]*cov*np.exp(2*pi*1j*i*(h/2+k/2+l/2))
                        #flayer = ((f_atom(q,
(atoms[2])))*dwl[i]*cov*np.exp(2*pi*1j*(h/2)))*(np.exp(2*pi*1j*i*(h/
2+k/2+l/2)))
                if i == 2:
                        #flayer = (f_atom(q,
(atoms[1])))*dwl[i]*cov*np.exp(2*pi*1j*i*(h/2+k/2+l/2))
                        flayer = ((f_atom(q,
(atoms[1])))*dwl[i]*cov*np.exp(2*pi*1j*(h/2)))*(np.exp(2*pi*1j*i*(h/
2+k/2+l/2)))
                if i == 1:
                        flayer = (f_atom(q,
(atoms[0])))*dwl[i]*cov*np.exp(2*pi*1j*i*(h/2+k/2+l/2))
                ftot += flayer*np.exp(2*pi*1j*shift*l)

                #possible water models only for specular fits
        if h == 0 and k == 0:
                #oxygen layers
                shift = 0
                for i in range(1,4):
                        cov = params['Ocoverage'+str(i)].value
                        shift =
params['Oeps'+str(i)].value+(np.sqrt(3)*a)
                        if i == 1:
                                flayer = f_atom(q,
(atoms[4]))*np.exp(-(q**2*params['Odwf'+str(i)].value**2)/2)
*cov#*np.exp(1j*q)
                        else:
                                flayer = f_atom(q,
(atoms[5]))*np.exp(-(q**2*params['Odwf'+str(i)].value**2)/2)
*cov#*np.exp(1j*q)
                        ftot += flayer*np.exp(1j*shift*q)

        ftot=betafactor*ftot
        if h == 0 and k == 0:
                #layered water structure
                if(params['Lcoverage'].value > 0.):
                        #print "LAYERED MODEL INCLUDED!"
                        temp = np.exp(-
(q**2*params['Lsigmabar'].value**2)/2)
                        temp = temp*np.exp(1j*q*params['Lcw'].value)
                        flayer = f_atom(q,
(atoms[4]))*params['Lcoverage'].value*np.exp(-
(q**2*params['Lsigma0'].value**2)/2)*np.exp(1j*(params['Ldist'].valu
e-params['Lcw'].value+(np.sqrt(3)*a))*q)
```

```
                        ftot += flayer/(1-temp)
                if(params['Lcoverage1'].value > 0):
                        #print "LAYERED MODEL INCLUDED!"
                        temp = np.exp(-
(q**2*params['Lsigmabar1'].value**2)/2)
                        temp =
temp*np.exp(1j*q*params['Lcw1'].value)
                        flayer = f_atom(q,
(atoms[5]))*params['Lcoverage1'].value*np.exp(-
(q**2*params['Lsigma01'].value**2)/2)*np.exp(1j*(params['Ldist1'].va
lue-params['Lcw1'].value+(np.sqrt(3)*a))*q)

                        ftot += flayer/(1-temp)
                #error function
                if(params['Ecoverage'].value > 0):
                       # print "ERROR FUNCTION INCLUDED!"
                        flayer =
1j*((zo)*params['Ecoverage'].value)*np.exp(-
((q*params['Esigma'].value)**2/2))/q*np.exp(1j*(params['Edist'].valu
e+(np.sqrt(3)*a))*q)
                        ftot = ftot +flayer

        #calculate complex conjugate
        amp = abs(ftot*np.conjugate(ftot))

        expAy=expA/corr_factors(h,k,l,params,constants)
        expEy=expE/ corr_factors(h,k,l,params,constants)
        return amp* corr_factors(h,k,l,params,constants)


def Qcalc(h,k,l,constants):
        import lmfit as lf
        import numpy as np
        import sys
        import scipy
        import os
        import time
        from scipy.integrate import quad
        from scipy.special import erf
        from scipy.special import erfc
        global expEy, expAy, amcorr1, fthick,   specular
        a = constants[0];
        wavelength=constants[1]
        #abslen=3.734e7/(wavelength**3)
        pi = np.pi
        dwfbulk=constants[2]

        k=0
        h_cub = h#k
        k_cub = k
        l_cub = l

        hinp=h
        kinp=k
        linp=l
        q = 2*np.pi*np.sqrt(h_cub**2 + k_cub**2 + l_cub**2)/a
        qinp=2*np.pi*np.sqrt(hinp**2+kinp**2+linp**2)/a
        qz=2*np.pi/np.sqrt(2)*l/a
        return q,qinp,qz
```

```
def model(h,k,l,expA,expE,params, atoms,constants):
        #Different scale factor for specular rod
        import lmfit as lf
        import numpy as np
        import sys
        import scipy
        import os
        import time
        from scipy.integrate import quad
        from scipy.special import erf
        from scipy.special import erfc
        from TF import TF
        from read_data import read_data
        from f_atom_0619A import f_atom
        from read_parameters import read_parameters
        from residual import residual
        global expEy, expAy, amcorr1, fthick, qz,  specular, q, qinp
        from  slscorr import corr_factors
        #constants
        a = constants[0];

        wavelength=constants[1];
        abslen=3.734e7/(wavelength**3)
        pi = np.pi
        dwfbulk=constants[2]
        #dwfbulk = params['dwfbulk'].value
        if h == 0 and k ==0:
                l=l*params['shiftl'].value
        if h == 1 and k ==0:
                l=l*params['shiftl1'].value
        if h == 0 and k ==1:
                l=l*params['shiftl2'].value
        #transform recp. unit cell
        h_cub = h*2/3 - k *2/3 + l/3
        k_cub = h*2/3 + k*4/3 + l/3
        l_cub = -h*4/3 - k*2/3 + l/3

        hinp=h*2/3-k*2/3
        kinp=h*2/3+k*4/3
        linp=-h*4/3-k*2/3

        q = 2*pi*np.sqrt(h_cub**2 + k_cub**2 + l_cub**2)/a
        qinp=2*pi*np.sqrt(hinp**2+kinp**2+linp**2)/a
        qz=2*pi/np.sqrt(2)*l/a
        #qz = 2*pi*l/(a*1.73205)

        #caluclate scattering factors
       # zau = f_atom(q, "Au")
       # zcu = f_atom(q, "Cu")
       # zo = f_atom(q, "O")
       # zc = f_atom(q, "C")
        zag = f_atom(q, "Ag")
        #zna= f_atom(q, "Na")

        #Debye Waller factors
        dwbulk = np.exp(-(q**2 * dwfbulk**2)/2)
        dwl = [0]


        for i in range(1,5):
           if h == 0 and k == 0:
```

```
                if i == 3:
                   dwl.append(dwbulk*np.exp(-
(qz**2*params['dwf'+str(i)].value**2)/2))
                  # if h == 0 and k == 0:
                   #     dwl.append(dwbulk*np.exp(-
(qz**2*params['dwfz'+str(i)].value**2)/2))
                else:
                   dwl.append(dwbulk*np.exp(-
(qz**2*params['dwf'+str(i)].value**2)/2))
           else:
                   dwl.append(dwbulk*np.exp(-
(qz**2*params['dwf'+str(i)].value**2)/2))


        #Bulk contribution
        ftot = (f_atom(q,constants[3]))*dwbulk/(1-
np.exp(2*pi*1j*((h/3)-(k/3)-(l/3))))


        #Commensurate metal layers
        shift = 0
        fptlayer=0
        beta=params['beta'].value
        betafactor=(1-beta)/np.sqrt(1-beta**2-2*beta*np.cos(2*pi*(-
h/3 + k/3 +l/3)))
       # for i in range(1):
       #          cov = params['coverage'+str(i)].value
       #          shift += params['eps'+str(i)].value
       #          flayer = zcu*dwl[i]*cov*np.exp(2*pi*1j*i*(-h/3 +
k/3 +l/3))
       #          ftot += flayer*np.exp(2*pi*1j*shift*l)
        for i in range(1,4):
                #print i
                cov = params['coverage'+str(i)].value
                shift += params['eps'+str(i)].value
                if i == 4:
                        flayer = (f_atom(q,
(atoms[4])))*dwl[i]*cov*np.exp(2*pi*1j*i*(-h/3 + k/3 +l/3))
                        ftot += flayer*np.exp(2*pi*1j*shift*l)
                if i == 3:
                        flayer = (f_atom(q,
(atoms[2])))*dwl[i]*cov*np.exp(2*pi*1j*i*(-h/3 + k/3 +l/3))
                        ftot += flayer*np.exp(2*pi*1j*shift*l)
                if i == 2:
                        flayer = (f_atom(q,
(atoms[1])))*dwl[i]*cov*np.exp(2*pi*1j*i*(-h/3 + k/3 +l/3))
                        ftot += flayer*np.exp(2*pi*1j*shift*l)
                if i == 1:
                        flayer = (f_atom(q,
(atoms[0])))*dwl[i]*cov*np.exp(2*pi*1j*i*(-h/3 + k/3 +l/3))
                        ftot += flayer*np.exp(2*pi*1j*shift*l)

                #possible water models only for specular fits
        if h == 0 and k == 0:
                #oxygen layers
                shift = 0
                for i in range(1,4):
                        cov = params['Ocoverage'+str(i)].value
                        shift =
params['Oeps'+str(i)].value+(np.sqrt(3)*a)
                        if(cov != 0):
```

```
                                if i == 1:
                                        flayer = f_atom(q,
(atoms[5]))*np.exp(-(q**2*params['Odwf'+str(i)].value**2)/2)
*cov#*np.exp(1j*q)
                                else:
                                        flayer = f_atom(q,
(atoms[6]))*np.exp(-(q**2*params['Odwf'+str(i)].value**2)/2)
*cov#*np.exp(1j*q)
                                ftot += flayer*np.exp(1j*shift*q)

        ftot=betafactor*ftot
        if h == 0 and k == 0:
                #layered water structure
                if(params['Lcoverage'].value > 0.):
                        #print "LAYERED MODEL INCLUDED!"
                        temp = np.exp(-
(q**2*params['Lsigmabar'].value**2)/2)
                        temp = temp*np.exp(1j*q*params['Lcw'].value)
                        flayer = f_atom(q,
(atoms[4]))*params['Lcoverage'].value*np.exp(-
(q**2*params['Lsigma0'].value**2)/2)*np.exp(1j*(params['Ldist'].valu
e-params['Lcw'].value+(np.sqrt(3)*a))*q)

                        ftot += flayer/(1-temp)
                if(params['Lcoverage1'].value > 0):
                        #print "LAYERED MODEL INCLUDED!"
                        temp = np.exp(-
(q**2*params['Lsigmabar1'].value**2)/2)
                        temp =
temp*np.exp(1j*q*params['Lcw1'].value)
                        flayer = f_atom(q,
(atoms[5]))*params['Lcoverage1'].value*np.exp(-
(q**2*params['Lsigma01'].value**2)/2)*np.exp(1j*(params['Ldist1'].va
lue-params['Lcw1'].value+(np.sqrt(3)*a))*q)

                        ftot += flayer/(1-temp)
                #error function
                if(params['Ecoverage'].value > 0):
                       # print "ERROR FUNCTION INCLUDED!"
                        flayer = 1j*(f_atom(q,
(atoms[4]))*params['Ecoverage'].value)*np.exp(-
((q*params['Esigma'].value)**2/2))/q*np.exp(1j*(params['Edist'].valu
e+(np.sqrt(3)*a))*q)
                        ftot = ftot +flayer

        #calculate complex conjugate
        amp = abs(ftot*np.conjugate(ftot))

        expAy=expA/corr_factors(h,k,l,params,constants)
        expEy=expE/ corr_factors(h,k,l,params,constants)
        return amp* corr_factors(h,k,l,params,constants)


def Qcalc(h,k,l,constants):
        import lmfit as lf
        import numpy as np
        import sys
        import scipy
        import os
        import time
        from scipy.integrate import quad
```

```
        from scipy.special import erf
        from scipy.special import erfc
        global expEy, expAy, amcorr1, fthick,   specular
        a = constants[0];
        wavelength=constants[1]
        #abslen=3.734e7/(wavelength**3)
        pi = np.pi
        dwfbulk=constants[2]

        h_cub = h*2/3 - k *2/3 + l/3
        k_cub = h*2/3 + k*4/3 + l/3
        l_cub = -h*4/3 - k*2/3 + l/3

        hinp=h*2/3-k*2/3
        kinp=h*2/3+k*4/3
        linp=-h*4/3-k*2/3
        q = 2*np.pi*np.sqrt(h_cub**2 + k_cub**2 + l_cub**2)/a
        qinp=2*np.pi*np.sqrt(hinp**2+kinp**2+linp**2)/a
        qz=2*np.pi/np.sqrt(2)*l/a
        return q,qinp,qz
def read_parameters(filename):
        global params
        global constants
        global firstatom
        global tol
        import lmfit as lf
        from TF import TF
        params = lf.Parameters()
        line = []
        raw = 1

        f = open(filename, 'r')

        #skip first two lines
        [f.readline() for i in xrange(2)]

        #read parameters from file
        while raw:
                raw = f.readline()
                line = raw.split()
                if len(line) >1 and line[0] == "P":
                        params.add(line[1],   value= float(line[2]),
min=float(line[3]), max=float(line[4]),vary=TF(line[5]))
                if len(line) >1 and line[0] == "M":
                        method = line[1]
                if len(line) >1 and line[0] == "T":   #Tolerences
                        tol = [float(line[1]), float(line[2]),
int(line[3])]
                if len(line) >1 and line[0] == "B":
                        specularrod = float(line[1])
                if len(line) >1 and line[0] == "A":
                        firstatom = line[1]
                if len(line) >1 and line[0] == "K":   #CONSTANTS
                        constants =
[float(line[1]),float(line[2]),float(line[3]),line[4],line[5]]
                if len(line) >1 and line[0] == "E":   #Systematic
Errors
                        syserror = float(line[1])
                if len(line) >1 and line[0] == "F":   #Files
                        filea = line[1]
```

```
                if len(line) >1 and line[0] == "A":    #Atom Types
                        atoms =
[line[1],line[2],line[3],line[4],line[5],line[6]]

        return params, method, tol, specularrod, atoms,
constants,filea,syserror


#Function to calculate the scattering factor using the Crommer Mann
equation




def corr_factors(h,k,l,params,constants):
        import lmfit as lf
        import numpy as np
        import sys
        import scipy
        import os
        import time
        from scipy.integrate import quad
        from scipy.special import erf
        from scipy.special import erfc
        from TF import TF
        from read_data import read_data
        from f_atom_1127A import f_atom
        from read_parameters import read_parameters
        from model001 import Qcalc
        global expEy, expAy, amcorr1, fthick, qz,  specular, q, qinp

        global expEy, expAy,  fthick, qz,  specular, q, qinp
        a = constants[0];
        wavelength=constants[1]
        abslen=3.734e7/(wavelength**3)
        pi = np.pi
        dwfbulk=constants[2]
       brat=0
       fthick=0
       scale=0
       sca=0

        if round(h,2) == 0 and round(k,2) == 0:
                specular = True
                fthick = params['fthick'].value
                scale =2* params['scale'].value
                sca = params['sca'].value
                brat = params['brat'].value
        elif round(h,2) == 1 and round(k,2) == 0:
                specular = False
                fthick = params['fthick1'].value
                scale = params['scale1'].value
                sca = params['sca1'].value
                brat = params['brat1'].value
        elif round(h,2) == 0 and round(k,2) == 1:
                specular = False
                fthick = params['fthick1'].value
                scale = params['scale2'].value
                sca = params['sca2'].value
                brat = params['brat2'].value
        elif round(h,2) == 1 and round(k,2) == 1:
```

```
                specular = False
                fthick = params['fthick1'].value
                scale = params['scale1'].value
                sca = params['sca1'].value
                brat = params['brat1'].value
        elif round(h,2) == 1 and round(k,2) == -1:
                specular = False
                fthick = params['fthick1'].value
                scale = params['scale1'].value
                sca = params['sca1'].value
                brat = params['brat1'].value

#Liquid adsorption
        q,qinp,qz=Qcalc(h,k,l,constants)
        qabs = 8*pi*fthick/(wavelength*abslen)
        absfac=np.exp(-qabs/qz)
        theta=np.arcsin(q*wavelength/(4*pi))
        chi=np.arctan(l/(2*np.sqrt(2)*np.sqrt(h**2+k**2)))
        #acorr1=np.sin(theta)*np.sin(chi)
        angi=np.arcsin((np.sin(theta))*(np.sin(chi)))

        if specular:
                angi=np.arcsin(wavelength*qz/(4*pi))


        #Low angle area correction
        acorr=brat*np.sin(angi)
        if(acorr > 1): acorr = 1

        correction =
abs(absfac)*(acorr/np.sin(angi)**2)*(scale+sca*l)
        return correction
def f_atom(q, atom):


        import lmfit as lf
        import numpy as np
        #coefficents taken from International Tables for
Crystallography Vol C. Ch 6.1
        if atom == "Au":
                #         a1      a2    a3      a4      b1      b2
b3      b4      c
                coeff =
[16.8819,0.4611,18.5913,8.6216,25.5582,1.4826,5.86,36.3956,12.0658]
               f1=-11.370
               f2=3.960

        if atom == "Pb":
                coeff
=[31.0617,0.690200,13.0637,2.35760,18.4420,8.61800,5.96960,47.2579,1
3.4118]
               f1=-11.370
               f2=3.960

        if atom == "Pt":
                coeff =
[27.0059,1.51293,17.7639,8.81174,15.7131,0.424593,5.7837,38.6103,11.
6883]

        if atom == "O":
```

```
                coeff =
[3.0485,13.2771,2.2868,5.7011,1.5463,0.3239,0.867,32.9089,0.2508]
                f1=0.028
                f2=0.017
        if atom == "C":
                coeff =
[2.31,20.8439,1.02,10.2075,1.5886,0.5687,0.865,51.6512,0.2156]
               f1=0.010
               f2=0.005
        if atom == "Cu":
                coeff =
[13.338,3.58280,7.16760,0.247000,5.6158,11.3966,1.6735,64.6126,1.19]
                f1=-0.609
                f2=2.791
        if atom == "Cu+":
                coeff =
[11.94575,3.36690,7.35730,0.227400,6.2455,8.66250,1.55780,25.6126,0.
89]
                f1=0.575
                f2=2.737
        if atom == "Ag":
                coeff =
[19.2908,0.644600,16.6885,7.4726,4.8045,24.6605,1.04630,99.8156,5.17
9]
                f1=-1.143
                f2=1.047
        if atom == "Na":
                coeff =
[3.256,2.66,3.93,6.11,1.39,0.2,1.0032,14.039,0.404]
                f1=-1.143
                f2=1.047
        if atom == "N":
                coeff =
[.2126,0.005700,3.13220,9.89330,2.01250,28.9975,1.16630,0.582600,11.
52]
                f1=0.014
                f2=0.009
        if atom == "H":
                coeff =
[.493002,10.5109,0.322912,26.1257,0.140191,3.14236,0.040810,57.7997,
0.00303]
                f1=-1.143
                f2=1.047
        x=(q/(4*np.pi))**2 # sin(theta)^2/lambda^2
        if x > 1.5:
                print "WARNING: Scattering factor approximation not
vaild at this Q!!"
                quit()

        f = coeff[8]
        for i in range(4):
                f += coeff[i*2]*np.exp(-coeff[i*2+1]*x)

        f +=f1+1j*f2
        return f
def residual(params, h,k,l, expA,expE,specularrod,atoms,constants):
        import lmfit as lf
        import numpy as np
        import sys
        import scipy
        import os
```

```
        import time
        from scipy.integrate import quad
        from scipy.special import erf
        from scipy.special import erfc
        from TF import TF
        from read_data import read_data
        from f_atom_1127A import f_atom
        from read_parameters import read_parameters
        from model001 import model
        points = len(l)
        mod = np.zeros(points)

        for i in range(points):


           if specularrod == 0:
                if h[i] == 1 or k[i] == 1:
                    mod[i] =
model(h[i],k[i],l[i],expA[i],expE[i],params, atoms,constants)
           else:
                mod[i] =
model(h[i],k[i],l[i],expA[i],expE[i],params, atoms,constants)
        return ((expA - mod)/expE)**2
def read_data(filename):

        f = open(filename, 'r')
        line = []
        data = []
        raw = 1

        #skip first line
        f.readline()

        #read parameters from file
        while raw:
                raw = f.readline()
                if len(raw.split()) > 1:
                        data.append(raw.split())

        return data

def TF(tocheck):
        if tocheck == "T":
                return True
        if tocheck == "t":
                return True
        if tocheck == "F":
                return False
        if tocheck == "f":
                return False
        else:
               print "Unrecognised Vary Flag, should be T/F"
        quit()
```

Example parameter file

```
C       PARAMETER FILE
C       ----------------------
C       SYSTEM:
```

```
C
C       Systematic Error on Data Points
C       ------------------------------------------------
E       0.1
C
C       ATOMS
C       ------------------------------------------------
C       METAL1  METAL2  METAL3  ADL1    ADL2    ADL3
A       Au      Au      Au      O       O       O
C
C
C       PARAMETER       VALUE           MIN     MAX     VARY(T/F)
C       ------------------------------------------------
P       scale           0.00063505      1e-10   1e10    f
P       scale1          0.0006389       1e-10   1e10    t
P       scale2          0.00131228       1e-10  1e10    f
P       fthick          0          0    2e7    f
P       fthick1         0         0     2e7   f
P       fthick2         0          0    2e7 f
P       brat            8.95527367          0.0 100     f
P       brat1           3.45660240          0.0 100     f
P       brat2           10               0.0    100     f
P       fitfactor        0.              0.0     300     f
P       sca              0               -0.1    0.1     f
P       sca1             0.00            -0.1    0.1     f
P       sca2             0.000           -.1     .1   f
P       shiftl           1               -2      2       f
P       shiftl1           1              -2      2        f
P       shiftl2          1               -2      2        f
P       beta             0.09       0       .5       f
C
C       CONSTANTS                                       (NO EFFECT)
C       ------------------------------------------------
C       a       wavelength      bulkdwf substrate       Face(111/100)

K       4.078   1.05070         0.124   Au              100
C
C
C       SURFACE METAL LAYERS
C       ------------------------------------------------
P       coverage1       1               0       1.5     f
P       eps1            0.0001     -.2       .2   t
P       dwf1            0.0     0.00    .2      f
C
P       coverage2       0.45246941      0       2       t
P       eps2            0.15627067      -.5     2       t
P       dwf2            0.01     .00    0.2  f
C
P       coverage3       0.42008725      0.0     1.5     t
P       eps3            0.07084495     -.5     2       t
P       dwf3            0.01            0.00    .8      f
P       dwfz3            0.0             0       0.7    f
C
C       OXYGEN LAYERS
C       ------------------------------------------------
P       Ocoverage1      0.0             0       6       f
P       Oeps1           1.9              0      12      f
P       Odwf1           1.32            0.0     3       f
C
P       Ocoverage2      0.0             0.0     2       f
P       Oeps2           11.13           10.5    20      f
```

```
P       Odwf2           0.8             0.0     3       f
C
P       Ocoverage3      .0              0.0     2       f
P       Oeps3           14.06           -.2     20      f
P       Odwf3           1.2             0.0     20      f
C
C       LIQUID MODEL
C       ------------------------------------------------
P       Lcoverage       0.               0      10      f
P       Lsigma0         0.28            0.01    3       f
P       Lsigmabar        1.13           0.01    7       f
P       Lcw             3.5              0      10      f
P        Ldist           2.11             0       18    f
C
P       Lcoverage1      .0               0      10      f
P       Lsigma01        0.33            0.01    3       f
P       Lsigmabar1       1              0.01    7       f
P       Lcw1            4.35             0      10      f
P        Ldist1          3.1              -5      18       f
C
C       Error Function
C       ------------------------------------------------
P       Ecoverage       0               0       2       f
P       Esigma          0.9              0      5        f
P        Edist           15.09           -12      20       f
C       Fitting Settings
C       ------------------------------------------------------------
---
C       Data File
C       ------------------------------------------------
F       n50mV.dat
C       ------------------------------------------------------------
---
C
C       Minimisation method [leastsq/nelder] (least squares or
downhill simplex)
C       [lbfgsb/anneal] (L-BFGS-B algorithm or simulated annealing)
are possible also
C       but not reliable in the current implentation of lmfit-py.
M       leastsq
C       Fitting Tolerences
C       ------------------------------------------------
C       FTOL        XTOL        MAXFEV
T       1.e-17      1.e-17      999999999
C
C       Help:
C       arg     Default Value   Description
C       ------------------------------------------------
C       xtol    1.e-7           Relative error in the approximate
solution
C       ftol    1.e-7           Relative error in the desired sum of
squares
C       maxfev  2000*(nvar+1)   maximum number of function calls
(nvar= # of variables)


C        Please indicate if you want to include the specular rod in
the modelling (Yes: 1, No:0)
B       1
```